

Wear and Friction in a Controllable Pitch Propeller

Proefschrift

ter verkrijging van de graad van doctor
aan de Technische Universiteit Delft
op gezag van de Rector Magnificus prof. ir. K. C. A. M. Luyben,
voorzitter van het College voor Promoties
in het openbaar te verdedigen

op maandag 18 januari te 10.00 uur

door

Milinko GODJEVAC

Naval Architect

Universiteit Belgrado, Servië

geboren te Belgrado, Servië

Dit proefschrift is goedgekeurd door de promotor:

Prof. ir. D. Stapersma

en copromotor:

Dr.ir. H. T. Grimmelius

Samenstelling promotiecommissie:

Rector Magnificus	voorzitter
Prof. ir. D. Stapersma	Technische Universiteit Delft, promotor
Dr. ir. H. T. Grimmelius	Technische Universiteit Delft, copromotor
Prof. dr. ir. C. van Rhee	Technische Universiteit Delft
Prof. Dr. Ing. D. Radojcic,	Belgrade University
Professor J. Carlton, PhD	City University of London
Prof. dr. ir. D. J. Schipper,	Universiteit Twente
ir. T. van Beek,	Wärtsilä Nederland, Drunen

“Wear and Friction in a Controllable Pitch Propeller”

Printed by: Proefschriftmaken.nl

Published by: Uitgeverij BOXpress, Oisterwijk, The Netherlands

ISBN 978-90-8891-136-1

©Milinko Godjevac, 2009. All rights reserved.

All rights reserved. No part of this publication may be reproduced, stored in a retrieval system, or transmitted, in any form or by any means, electronic, mechanical, photocopying, recording or otherwise, without the prior permission of the publisher.

Preface: About “Wear and Friction in a Controllable Pitch Propeller”

The author is a naval architect and this book is his PhD thesis. In this research the author focuses on friction in a controllable pitch propeller (CPP), formation of wear in a CPP system, and their mutual dependence. Instead of going deeply only in tribology aspects, the author tries to get an overall description of the problem incorporating hydrodynamic and mechanical aspects of a CPP. By doing so, the author concludes that total wear is the result of several wear mechanisms but in the first place fretting and sliding wear. An attempt has been made to explain the existence of fretting as a consequence of too high oscillations in the wake speed when the ship is sailing in seaway. Wear experiments presented in this book show fretting wear to be more dangerous than other wear mechanisms in CPP. At the end, based on experiments and previous analysis, the author presents a total wear model for a CPP.

This book is useful for marine engineers to better understand the properties and limits of a CPP in real service conditions. It further can be an example how to use a multi disciplinary approach in solving a specific problem. Also it can be useful for tribology experts to get an impression of the problems the marine people encounter and how these relate to their own expertise.

Keywords: Controllable Pitch Propeller (CPP), Friction, Friction modelling, Wear, Wear experiments, fretting, fretting experiments, sliding wear, sailing in seaway, real service conditions, multi-disciplinary approach

Contents:

Preface: About “Wear and Friction in a Controllable Pitch Propeller”	3
Nomenclature	7
1. Introduction	10
1.1. Tribology	10
1.2. Wear	11
1.3. Friction	12
1.4. Interaction of wear and friction	13
1.5. Controllable Pitch Propeller	13
1.6. Background and motivation	14
1.7. Goal	15
1.8. Description and Methodology	15
1.9. Main contribution of the thesis	17
2. About CPP, failures, wear, and wear failures in a CPP	18
2.1. Advantages of Using a CPP	18
2.2. Assembly of a CPP	21
2.3. Materials used for CPP’s	23
2.4. Historical overview of development of a CPP	24
2.5. Failure mechanisms	25
2.5.1 Body failure mechanisms	26
2.5.2 Surface failure mechanisms	28
2.6. Failures of CPP’s	29
2.7. The investigated CPP	31
2.8. Wear mechanisms	31
2.8.1 Adhesive wear	32
2.8.2 Abrasive wear	33
2.8.3 Fatigue wear	34
2.8.4 Fretting wear	34
2.9. Wear behaviour	36
2.10. Wear failure of a CPP	38
2.11. Wear situation in a blade bearing of a CPP	39
3. Loads	41
3.1. Introduction	41
3.2. Loads in the blade bearing	42
3.2.1 Centrifugal loads	44
3.2.2 Hydrodynamic loads	45
3.2.3 Friction forces in the blade bearing	47
3.2.4 Hydraulic actuating loads	51
3.3. Fretting coefficient	53
3.3.1 Theoretical fretting coefficient	53
3.3.2 Fretting coefficient in the design case	55

3.3.3	Approximation of friction	56
3.3.4	Fretting coefficient for test cases	57
3.4.	Test Cases	59
3.4.1	Example 1	59
3.4.2	Example 2	61
3.4.3	Results.....	62
3.5.	Influence of sea condition on fretting motion.....	63
3.5.1	Influence of wave height in high rpm (overload)	63
3.5.2	Influence of wave height in mid rpm (design).....	64
3.5.3	Influence of wave height in low rpm	64
3.5.4	Influence of rpm in high waves	65
3.5.5	Influence of rpm in medium waves	65
3.5.6	Influence of wave direction	66
3.5.7	Influence of draft on fretting.....	66
3.6.	Discussion	67
3.7.	Conclusions.....	68
4.	Motions.....	70
4.1.	Friction.....	70
4.2.	Friction behaviour.....	71
4.3.	Measurements of friction in a CPP	73
4.4.	Modelling of friction.....	74
4.4.1	Static friction models	75
4.4.2	Dynamic friction model	80
4.5.	Selection of friction model.....	84
4.6.	Modelling of fretting motion	86
4.6.1	Adjusting of the LuGre model	88
4.6.2	Fretting motion in the blade bearing.....	90
4.6.3	Influence of friction model on fretting amplitude.....	91
4.7.	Influence of the design and off-design parameters on fretting motion.....	93
4.7.1	Influence of hydraulic holding pressure on fretting amplitude.....	93
4.7.2	Influence of spindle torque on fretting amplitude.....	94
4.7.3	Natural frequencies of the CPP or influence of the shaft frequency on fretting motion	95
4.7.4	Influence of propeller skew and chord length on spindle torque oscillation.....	95
4.7.5	Influence of backlash on fretting amplitude	99
4.7.6	Influence of cavitation and ventilation on spindle torque oscillations	100
4.8.	Influence of fretting motion on hydraulics	101
4.9.	Discussion	104
4.10.	Conclusions.....	106
5.	Wear experiments	108
5.1.	Introduction.....	108
5.2.	Experiments for wear	109
5.3.	Selection of wear experiments	110
5.4.	Sliding wear experiments.....	110
5.4.1	Testing procedure for Wear Test 1 to Wear Test 6.....	111

5.4.2	Testing procedure for Wear Test 7	112
5.4.3	Results of sliding wear experiments	113
5.5.	Analysis of sliding wear experiments	119
5.5.1	Run-in and run-out behaviour	119
5.5.2	Appearance of wear scar	119
5.5.3	Classification of materials	122
5.5.4	Sudden and temporary increase of wear rate and friction	123
5.5.5	Influence of load	125
5.5.6	Influence of CuNiAl hardness	127
5.5.7	Wear distribution	129
5.6.	Fretting wear experiments	130
5.6.1	Testing procedure for Wear Test 08	130
5.6.2	Testing procedure for Wear Test 9	131
5.6.3	Results of fretting wear experiments	132
5.7.	Analysis of fretting wear experiments	135
5.7.1	Influence of fretting amplitude	135
5.7.2	Influence of lubrication	136
5.8.	Discussion	136
5.9.	Conclusions	138
6.	Field experience and total wear	139
6.1.	Service records on fretting wear	139
6.2.	Total Wear	147
6.3.	Influence of controls on total wear	150
6.4.	Influence of fretting on total wear	152
6.5.	Discussion	153
6.6.	Conclusions	155
7.	In retrospect	156
7.1.	Discussion	156
7.2.	Recommendations	159
	Appendix A: The Project “DYLOPROPS”	160
	Appendix B: Sensitivity analysis of LuGre friction model	164
	Appendix C: Results of the Dyloprops seakeeping tests used in this work	169
	Appendix D: Material properties	177
	Summary	179
	Samenvatting	180
	Reference:	182
	Curriculum Vitae and List of Publications:	186

Nomenclature

– Roman variables:

A	area	m ²
D	propeller diameter	m
D	drag force	N
E	Young's modulus	N/mm ²
F	force	N
H	hardness	GPa
I	moment of inertia	kgm ²
K	wear coefficient	-
L	lift force	N
L	length of contact	m
M	moment	Nm
N	number of cycles	-
N	Normal force	N
R	resultant force	N
R	propeller radius	m
S	sliding distance	m
T	thrust	N
V	volume	mm ³
Q	tangential force	N
Q	torque	Nm
Z	number of blades	-
a	contact width	mm
b	contact width of stick region	mm
b	thickness of blade bearing	m
c	angular spring stiffness	Nm
a, b, c	contribution of thrust, torque, and resultant force to friction	-
d	displacement/amplitude	m
e	eccentricity of pin	m
f	modified fretting coefficient	-
g	arbitrary steady state behaviour of a model	-
h	wear depth	mm
k	fretting coefficient	-
k	blade section	-
k	oil stiffness	N/m
l	length	m
m	mass	kg
n	shaft frequency	1/s
n	exponent for life time of a bearing	-
n	number of voyages, days, years	-
p	pressure	Pa
q	stress per length	N/m
r	radius	m
r'	radius of blade bearing	m
r''	radius of blade carrier	m
t	time	min

u	ratio of force and moment in radial part of blade bearing	-
v	velocity	m/s
w	specific wear rate	mm ³ /Nm
z	internal state of friction model	m
x, y, z	coordinates	m

– **Greek variables:**

α	angle of attack	rad
α	contact angle in axial part of blade bearing	rad
β	bulk oil modulus	N/mm ²
β	Weibull shape factor	
φ	hydrodynamic pitch angle	rad
φ	angle around blade bearing	rad
λ	Weibull scale factor	-
μ	friction coefficient	-
ρ	density	kg/m ³
σ	Stribeck coefficient	-
σ	normal stress	N/mm ²
τ	tangential stress	N/mm ²
θ	pitch angle	rad
υ	Stribeck coefficient	-
ω	natural frequency	1/s

– **Subscripts**

0,1,2	Stribeck coefficients
A	advance
F	caused by force
M	caused by moment
MIMO	mimo behaviour control
R	relative
all	allowable
ax	the axial part of blade bearing
b	blade
ba	break-away
blade	blade
c	Coulomb
cbv	counter balance valve
ce	centrifugal
cg	canter of gravity
ch	hydrodynamic canter
cpg	controllable pitch propeller
crit	critical value
day	day
e	external
fr	friction
fret	fretting
hd	hydrodynamic
hyd	hydraulic
k	blade section

max	maximum
oil	oil
pin	actuating pin
rad	the radial part of blade bearing
s	sliding
s	Stribeck
s	static (break-away)
sp	spindle
ss	steady state
th	threshold
v	viscous
voy	voyage
y	year
yoke	yoke

– **Superscripts**

mean	mean value
other	other contacts in CPP besides blade bearing
reaction	difference from mean value
tot	total
voy	voyage

1. Introduction

The research presented in this thesis is a multi-disciplinary research of wear-related phenomena in a controllable pitch propeller (CPP). In this chapter, the main topics of research, background and motivation for the work undertaken will be presented. The chapter begins with a historical overview of the main disciplines involved in the research and continues with the motivation for the work done. Following this, the goal of the research is stated together with the main hypothesis and research questions. This is followed by the methodology of the work, and the main contributions of the thesis.

1.1. Tribology

With a rising awareness of energy and ecology-related problems, energy efficiency will become the number one topic in the twenty-first century. It is not only the efficient utilization of a machine that is of growing concern, but reliability and conservation throughout the entire life cycle of technical systems. On the one hand, increasing fuel costs accentuate the need for higher performance and better control and for lower friction and wear losses on the other hand. Everything man makes wears out, most often due to the relative motion of interacting surfaces.

The word “tribology” comes from Greek word “τριβω”, which means “to rub”, but also “to wear out”. Throughout the centuries scientists and engineers have been trying to minimize the friction and wear losses. Perhaps the most comprehensive and impressive work on the history of tribology can be found in [Dowson, 1998]. However, not all effects of friction and wear are negative. It is difficult to imagine everyday life without friction, and the wearing process is essential in manufacturing. Figure 1.1 shows an Egyptian drawing of carpenters benefiting from wear and friction by using a bow-drill. Friction is used to rotate the drill, and the hole is made by wearing the surface at a required location.

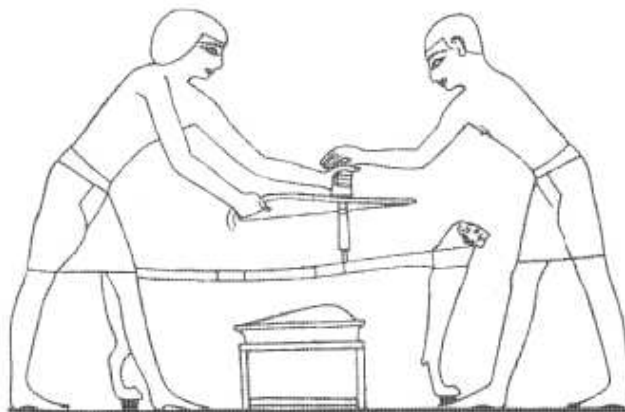


Figure 1.1: Egyptian carpenters drilling holes in a chair. Source: [Dowson, 1998]

Even though tribology aspects had been noticed long ago, only recently have these aspects been explained. For example, the beneficial use of lubricants has long been known, but the physical process which allows reduction of friction and wear have been explored only relatively recently [Reynolds, 1886]. Individual and impressive studies

have been done to explore the specific problems related to friction and wear, but the various aspects of surface interaction call for a somewhat broader overview. The subject of tribology requires the contribution of various specialists, including physicists, chemists, material engineers, mathematicians, mechanical engineers and others. The multi-disciplinary nature of tribology is its strength and its weakness.

1.2. Wear

The most proper definition for engineering purposes defines wear as damage to a surface as a result of relative motion with respect to another substance [Bayer, 1994]. This definition contains all essential elements. In the first place, this is due to the fact that wear is not simply a loss of material from a surface; it is also damage of the surface, which might exist without loss of material. An example of this would be hammering, which causes plastic deformation and therefore change in geometry. The development of cracks and the occurrence of a network of cracks is a mode of wear also included in this definition. This surface damage does not mean any loss in material or changes in geometry.

Older definitions define wear simply as a loss of material [Rabinowicz, 1965], due to contact between two bodies. The more general definition of wear as damage is very natural. It views wear as a change that affects the performance of a certain part. Furthermore, in older definitions wear is said to be caused by the “relative motion of two bodies in contact”. This type of defining wear is quite limiting, since a surface can wear as the result of interaction with other fluids. For example, cavitation can cause wear of propeller blades, which is typical in the marine field that is of interest in this thesis.

It is interesting to consider what wear is not. Typically, when some part cannot perform due to rust or when it is broken, it is said that “the part is worn out”. Reasons for this might include corrosion or that the part is broken in two pieces. These two failure mechanisms are not included in the definition of the wear; corrosion because there is no movement, and fracture because it is a body phenomenon. The corrosion and fracture failures together with wear are considered different failure mechanisms. This is further outlined in Chapter 2.5. However, both corrosion and fracture can definitely be elements of wear. This is because in a wearing situation, the corrosive and fracture elements can influence the wear and contribute to the consequences. Generally, for processes to be considered as wear, there has to be some surface, relative motion and mechanical aspects involved. However, it has been shown that many physical and chemical processes are also involved in wear phenomena.

After defining wear as damage to a surface, it is important to realize that wear is not a material property, but a system property. More on system approach to wear and friction can be found in [Czizhos, 1978]. Wear is influenced by numerous parameters, including the type of contact, type of motion, surrounding circumstances, type of lubricant, etc. One material can be wear resistant with good lubrication, but can have poor wear behaviour if the lubrication is improper, if the pairing material is changed, or if the temperature changes. This leads to another important feature of wear. Transition points in wear behaviour are very pronounced and make wear more of a system response rather than a material property. Typical transition points in wear behaviour can occur in the run-in periods or the initiation of a new wear mechanism.

1.3. Friction

Due to the necessary occurrence of movement, the companion term of wear is friction. Friction and friction-induced phenomena has been the subject of research for centuries. Leonardo da Vinci (1452-1519) was one of the first to study friction (see Figure 1.2). Following him, the important work of Guillaume Amontons (1663-1705) and Charles August Coulomb (1736-1806) contributed to the understanding of friction. They all observed the friction force to be proportional to load, as opposed to motion, and to be independent from the (apparent) contact area. As recently as 1950, Bowden and Tabor [Bowden, 1950] gave a physical explanation for this and found that the true contact area is much smaller than the apparent contact area. True contact is taking place at the tops of the asperities and the area depends on the normal force. This mechanism shows the friction force to be dependant on the true contact area, and it is argued that all friction dynamics takes place at these asperities. Later studies show that friction forces for macroscopic bodies occur due to forces on atomic and nuclear levels, [Persson, 2000].

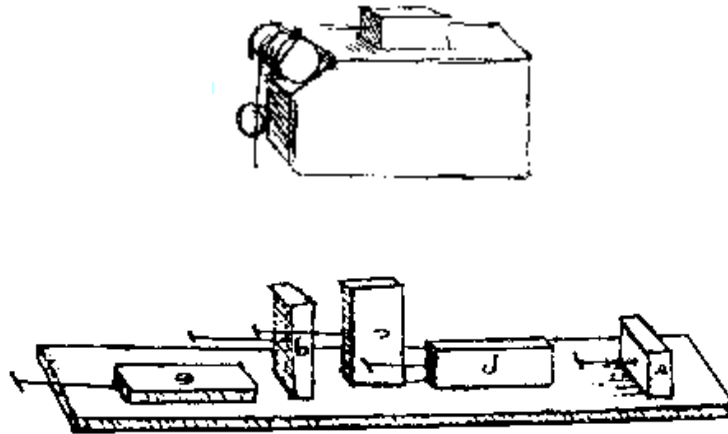


Figure 1.2 : Leonardo da Vinci's sketches from the Codex Atlanticus and the Codex Arundel illustrating friction experiments. Source: www.tribology-abc.com

The research on this topic has been vast and the interest has continued to grow. Often in mechanical systems, friction is considered an impediment that costs energy, and which might induce undesirable phenomena, such as self-sustaining stick slip. There is a wide range of science and engineering disciplines interested in friction, including tribology, mechanical engineering, acoustics, geophysics and seismology. However, tribology is probably the field with the most extensive research on friction and tribologists study friction-generated phenomena in terms of surface interaction, both on the macroscopic and microscopic level. Other research fields are more interested in incorporating friction as part of the entire dynamical system rather than studying the surface contacts in detail. Lubrication engineers and design engineers try to limit the friction in a mechanical system by improving the system itself. They try to achieve this, for instance, with better lubricants or a redesign of the system. In another field, control engineers focus on the modification of the dynamics of a mechanical system by adding a control loop in order to obtain a desirable, closed loop, behaviour. The applied mathematicians and dynamics scientists are primarily interested in the analysis of the nonlinear and discontinuous nature of dynamical systems due to friction.

The increasing interest and research in the class of controlled mechanical systems with friction is mainly due to the increasing demands for these high performance systems. In controlled mechanical systems, friction severely deteriorates the ideal of high performance. In particular, the friction induced negative side effects are increasing tracking errors, large settling time, and stick slip oscillations.

1.4. Interaction of wear and friction

The usual impression is that friction and wear are almost synonymous and that high friction equates to a high wear rate and that low friction equates to a low wear rate. Generally, this is incorrect. Teflon is an example which has the ability to provide a low coefficient of friction ($\mu < 0.1$). However, the wear rate is much larger than in a system using hardened steel, where the friction coefficient is much higher ($\mu = 0.2$) [Bayer, 1994]. In this thesis, the same finding has been confirmed. See Chapter 5.

Interaction between wear and friction is very interesting, as it can be seen that both friction and wear are sensitive to the same parameters and the same general types of phenomena. This is frequently an aid when one is addressing wear problems. For instance, the monitoring of friction behaviour during wear tests can aid in the identification of wear transition. Wear can lead to surface modification, which can influence friction by film formation or roughness changes. Friction can, through heating effects, cause oxide formation, which in turn influences wear. Wear and friction must be considered as related, but not equivalent, phenomena.

1.5. Controllable Pitch Propeller

The main purpose of any propulsion plant is to give acceleration and speed to a certain ship. In all propulsion plants, the majority of propulsors are screw propellers, although there is a niche market for different types of propulsors, such as waterjets. Over time, propellers showed their reliability and efficiency and there is still no substitution for them. Archimedes was perhaps one of the first to propose the use of screws to lift up water. Much later, da Vinci included a screw in his sketch of a helicopter. The later development of the propeller is associated with famous scientists such as Hooke, Bernoulli and Euler [Carlton, 2007]. One of the first applications of a screw propeller was in 1776 on the submarine *Turtle* by David Bushnell. See Figure 1.3.

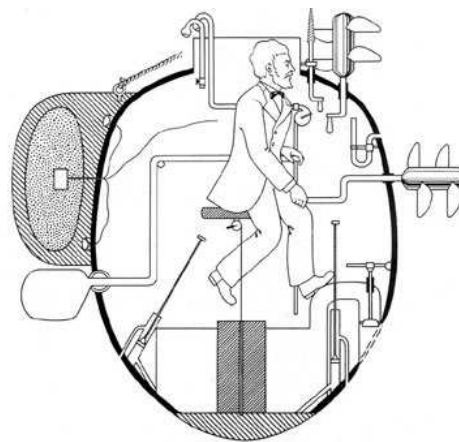


Figure 1.3: Cross section of Bushnell's submarine *Turtle*. Source: www.britanica.com

In the first half of the 19th century, many authors (Francis Pettit Smith, John Ericsson, Josef Ressel, etc) were granted patents for marine application of propellers. However, a proper physical interpretation comes somewhat later with Rankin's momentum theory and Froude's blade element theory.

One of the ways to gain better performance, speed control, manoeuvrability and efficiency is to use propellers where the blades can rotate around an axis normal to the drive shaft. These are controllable pitch propellers (CPP) and the change in pitch is actuated with additional machinery. In the first CPP's, the blades were actuated mechanically. The later demand for increased power in propulsion plants made hydraulic systems necessary. A more detailed description of the CPP mechanism will be given in Chapter 2.

1.6. Background and motivation

There are two main motivations for a more thorough research of wear and friction in a CPP. The first one, the possibilities for more active pitch control of a controllable pitch propeller, has always been challenging. The idea of a high performance control system has been investigated by numerous authors. Vrijdag, in [Vrijdag, 2005], proposes the use of high speed pitch control to limit the occurrence of cavitation. In [Grimmelius, 2001], it has been reported that it may be easier to suppress sea induced variations by pitch control than by fuel rack control. However, all these good theories are uncertain whether a more active and dynamic use of pitch control causes excessive wear and the end result of a total failure of a CPP system. Additionally, in [Bakker, 2006], the friction of a CPP was reported as one of the problems in achieving high performance control.

The second motivation for this research was to better understand wear as a failure mechanism of a CPP in real service conditions. Moreover, it has been observed that some CP propellers are in use for lengthy durations without any wear problems, while other CP propellers show these problems. Please note that the presented thesis is not a failure study of one specific case, but rather a general investigation of wear damage in a CPP, even though it has some elements of a failure study.

Whether one wants to improve the propulsion system by use of a high performance control system or simply to get a better insight into wear damage in a CPP, sooner or later, one has to face the lack of knowledge about wear mechanisms and friction phenomena in a CPP, especially for real service conditions. Despite the fact that vast amounts of work has been done on understanding these phenomena in general applications, there is no adequate model that can be properly and accurately used for estimating the probability of wear occurring in a CPP. This is not even to mention the correlation of wear with real service conditions and blade geometry.

When examining previous experience, two wear situations can be distinguished, namely, sliding wear and fretting wear. While some work has been done on sliding wear [Barbey, 1982], there has not been much work done on a fretting in a CPP. Moreover, practical experience shows that fretting wear, although ship is not manoeuvring so frequently, can have very drastic effects on the performance of a CPP. All these topics will be elaborated on separately, but in this chapter, the goal is only to globally introduce the two main wear situations that play a role in this research, so that the terms used in stating the hypothesis and questions will be clear.

Defining wear as a system property makes wear in a CPP more than just a material problem. In order to tackle the problem of wear in a CPP, extensive and comprehensive

multi-disciplinary research is undertaken. As a result, a better understanding of wear and enlargement of the existing wear database for marine applications will be achieved. Furthermore, future propulsion control strategies can be investigated with wear as another constraint, making it possible to better estimate the reliability of a propulsion system.

1.7. Goal

The main motivations for this thesis are to define the wear limits for highly active pitch control and explain the wear failures of a CPP. In examining the motivation and background, the scope of this thesis can be formulated into one goal:

- The goal is to gain a better understanding of wear as a failure mechanism of bearings in a CPP during service.

In examining the experience of the propeller's manufacturers, one hypothesis can be made. In some cases, it was stated that fretting wear has caused excessive damage of bearings in a CPP. A hypothesis can thus be made that:

- Fretting wear can cause ultimate failure of a CPP.

Raising the following questions should help to structure the work needed to reach the goal:

- Why is it that some CPP's suffer from quick and extensive wear in the blade bearing, while others work fine for ages?
- What is the allowable wear?
- What is the most dominant effect on wear in the blade bearing?
- Can fretting be detected by measuring the hydraulic pressure?
- How can the total wear in a CPP in real service conditions be estimated?
- What is the influence of blade geometry and wake field on the wear of a propeller?

1.8. Description and Methodology

In examining the goal, background, and motivation for the work done, the focus of this investigation is on the bearings of a CPP. Thus, the wear of blades, cavitation and cracking of blades is not within the scope of this thesis. In this investigation, wear will be investigated as a loss of material in the contact area between two bodies in relative motion, (i.e. the blade foot and the blade carrier). Another important characteristic is that the investigation focused on real service conditions. The main elements in any wear investigation are load (pressure) in the contact area, the type of motion in the contact area, material-tribology aspects and surrounding effects. Figure 1.4 shows these four elements and their interaction. At each interaction its subject matter is described in a concise manner. Later in this thesis, each of these will be discussed in detail in a separate chapter. At this point, it is important to have a broad overview of the research and the interaction between different aspects of the subject.

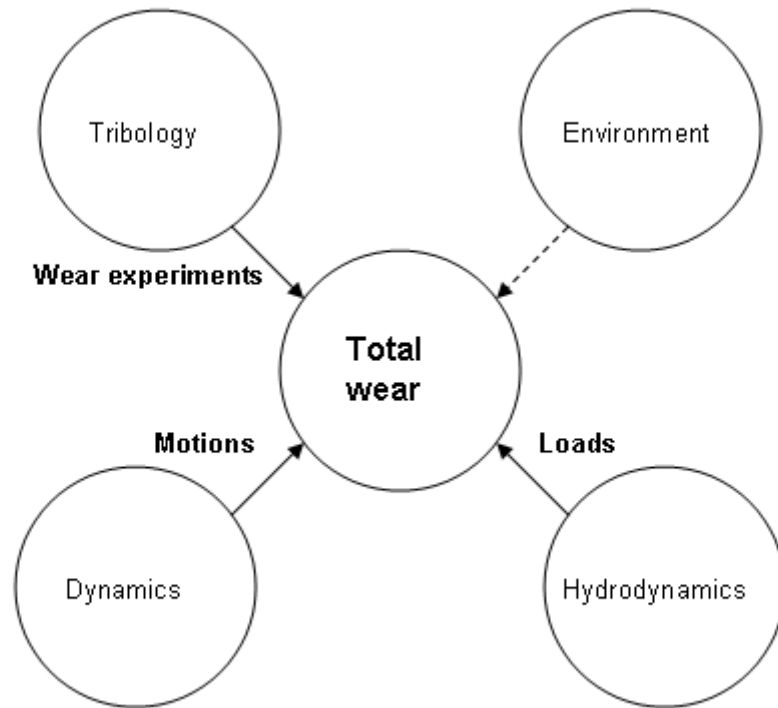


Figure 1.4: Plan of the research.

– Hydrodynamics:

This aspect represents the loads in the bearings induced by the hydrodynamic forces during service. It focuses on the equilibrium of Coulomb friction, hydrodynamic spindle torque, and a non-actuating hydraulic reaction torque. In Chapter 3.3, based on the equilibrium, a coefficient describing the start of fretting motion will be introduced. The hydrodynamic aspects include measured values of thrust, torque and spindle torque during model tests in irregular seas. Using a slightly different (approximated) fretting coefficient, these experiments are systematically investigated in order to draw conclusions on the occurrence of fretting motion in service conditions. However, within the scope of this research, the focus is not on the hydrodynamic nature of the forces acting on the blade, but rather on the effect of these forces on loads in bearings. Therefore, the necessary calculations of hydrodynamic forces are done using existing software. In spite of the fact that the investigated measurements are only for one specific ship, some general and somewhat surprising conclusions will be drawn.

– Dynamics:

The pitch change is normally caused by the actuating system, but small movements can be caused by (too) high oscillations of the hydrodynamic forces. The amount of motion caused by the actuating system is more or less easy to determine, and it depends on the control characteristics. However, the motions caused by the oscillation of the hydrodynamic forces are much more difficult to determine.

The dynamics aspect includes the modelling of friction in the blade bearing and implementing the selected models in a CPP model. In Chapter 4, the dynamics aspect was investigated in order to estimate the small amplitude vibrating motion in bearings of a CPP during a revolution of a blade. This motion occurs within the clearance of bearings, and is caused by seaway and variations in the wake field. Two friction models

are investigated, a dynamic and a static friction model, and together with experiments, an attempt is made to quantify the parameters of friction behaviour.

In this part of the research, the goal was to accurately estimate the motions inside a CPP mechanism during service. Firstly, hydrodynamic loads influence loads in the bearings, and secondly, they influence motions and vibrations inside the bearings.

- Tribology:

The tribology aspect includes a set of wear experiments and their results. The focus is on fretting and sliding wear experiments. Chapter 5 is dedicated to these experiments. The main target is to evaluate the different material combinations and their wear coefficients (rates). In total, nine wear experiments were done on four different test setups. The loads and amplitudes of motions used in experiments were obtained from analysis done in Chapters 3 and 4.

- Environment and surrounding effect:

The environment or surrounding aspects refer to the influence of the environment on total wear behaviour in a CPP. More specifically, it is the influence of sea water on the wear behaviour and lubrication. As no experiments were done on this subject, this aspect is presented only with a dashed line in Figure 1.4.

- Total wear model:

This part combines all known factors that influence wear in the bearing of a CPP, including loads, motions and wear coefficients. Work undertaken in Chapter 6 represents the synthesis of previous work, and investigates the influence of the control regime on wear in a CPP. All aspects must be considered and properly processed in order to get the total wear model.

The research undertaken does not provide all the answers on the questions of wear and wear related failures in a CPP, but in spite of the complexity of wear process in the CPP some answers will be given. Each of the above mentioned aspects deserves special attention and further work. In this research the challenge is twofold in that the work must not oversimplify, but at the same time, it must not go too deeply into only one aspect while neglecting others.

1.9. Main contribution of the thesis

With respect to the goal defined in Chapter 1.7, an effort has been made to gain a better understanding of complex wear phenomena in a CPP. The work done shows the existence of several wear mechanisms and provides useful guidelines in minimizing wear in bearings. Furthermore, it expands the wear database with firm tribology experiments and makes it possible to predict wear in future propeller designs. Additionally, this research is an example for the need of a multi-disciplinary analysis in order to understand a complex phenomenon.

2. About CPP, failures, wear, and wear failures in a CPP

The aim of this thesis is to understand wear in a CPP as one of its failure mechanisms. Before focusing on wear, it is useful to give a general overview of a CPP and failure mechanisms that can lead to the failure of any component. This chapter begins with an introduction to the concept of a controllable pitch propeller by explaining its purpose, working principles, main parts, and historical overview of development. In addition to wear, there are other reasons why a component can fail. After presenting general failure mechanisms, the general failures of a CPP and their frequencies have been presented. In examining the main parts of a CPP, the importance of a blade bearing becomes clear. This bearing is the place where two main (conflicting) functions of a CPP meet. Main wear mechanisms will be presented here as an introduction to the wear experiments carried out in Chapter 5 of this thesis. At the end of this chapter, wear situations and allowable wear in a blade bearing are discussed.

2.1. Advantages of Using a CPP

The main purpose of any propulsion plant is to give acceleration and speed to a certain ship. One of the ways to gain better control, manoeuvrability, performance and efficiency is to use a propeller with controllable pitch (CPP) instead of a propeller with fixed pitch (FPP). The application of a diesel driven fixed pitch propeller has basically only one variable to control the thrust, that is, the number of rpm. However, controlling only the rpm does not allow the use of full power at all conditions that a ship can face. The propulsion plant (engine, propeller, gear box, etc) is optimized for the design conditions as set out in curve 1 in Figure 2.1. However, the operating conditions can change. For example, the hull can get fouled or the ship might encounter heavy seas causing the propeller load to increase from the design conditions, shown in curve 2 in Figure 2.1. Furthermore, the resistance can reduce, for example due to reduced cargo, causing the propeller curve to shift down, curve 3 in Figure 2.1. In both cases, curves 2 and 3, the maximum engine power cannot be delivered.

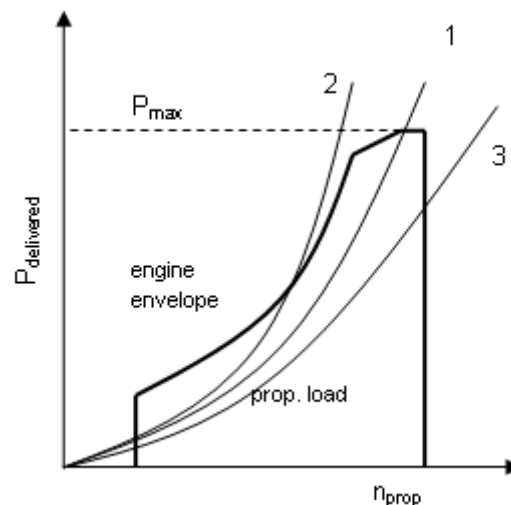


Figure 2.1: Design and off-design conditions of propeller load.

For some other applications, such as fishing vessels, the ship can have more than one operating condition. The difference in operating conditions is even larger than the difference between curves 1, 2, and 3 in Figure 2.1. For ships that have more than one operating condition and use FPP, the maximum power can be delivered for only one operating condition.

It was natural to introduce the mechanical solution that enables the full use of available power. Such a solution was found in the controllable pitch propeller where the propeller load can be changed for different pitch settings. Moreover, in applications where it was not possible to change the direction of the rotation of a propeller, the change of pitch allowed the change of the direction of thrust. This was very important when a turbine was used instead of a diesel engine. The utilization of a CPP is very common and widely used. Figure 2.2 shows examples of ships equipped with a CPP.





Figure 2.2: Four ships equipped with a CPP, from top to bottom: ferry, small tanker, AHTS vessel, and fishing vessel. Source: Wartsila internal photos

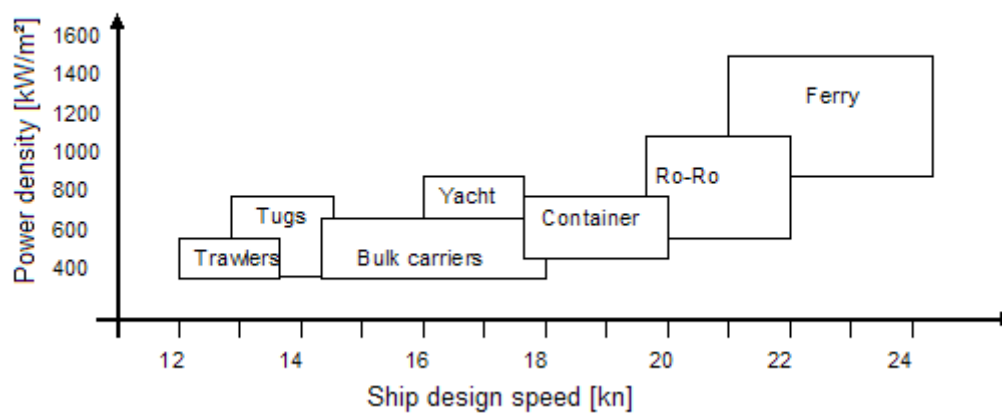


Figure 2.3: Different CPP applications as a function of ship speed, type, and power density (1kn = 0.5144m/s)

On fishing vessels, a CPP is used to deliver full power to the propeller under different operating conditions, including trawling and sailing. A general cargo ship might use a CPP to power the shaft generator. The shaft generator needs a constant rpm and load disturbances are suppressed by the pitch change, while the rpm is kept constant. On ferry vessels, a CPP is used to achieve better manoeuvring and shorten the time between harbours. By using two CPP shaft lines a ferry can operate without the tug's assistance. As a further example of different operating conditions, tug a (or AHTS) uses a CPP to ensure full power for bollard thrust.

However, propellers are not all the same, as the speed and load they operate depends upon the type of application. Figure 2.3 shows available data of different CPP applications as a function of load and ship speed. The load is expressed as a power density, the power delivered to the propeller divided with the disc area of the propeller ($D^2\pi/4$).

2.2. Assembly of a CPP

The two main functions of a CPP are to:

- Give thrust to the ship (from delivered torque); and
- Change the pitch.

There is a natural conflict of interest between these two functions. The transmission of (huge) thrust and torque requires a large force carrying capacity, which means very large parts such as blade carriers and blade bearings. On the other hand, the mechanism to change the pitch also requires a certain amount of space in the hub. However, the hydrodynamic performance of the propeller is influenced by the hub size, wherein a larger hub is less efficient than a smaller hub for the same diameter. The main guidelines for selection of an appropriate hub size are given in [Wind, 1978], and for more details the reader is referred to that paper.

Roughly speaking, the entire system of a controllable pitch propeller can be split into two parts, the rotating and stationary. The rotating part rotates around the shaft axis and consists of the CPP mechanism and shaft (with pipes inside). Most of the rotating part is placed outside the ship, while the stationary part is placed inside the ship. It consists of the hydraulics and controls. Figure 2.4 shows the main components of a CPP system. In general, the rotating part of the system is large, heavy, and simple, while the stationary is small(er), light, and has more parts.

Most of the rotating part of a CPP is shown in Figure 2.5. It is a Wärtsilä C type CPP, which is a result of years of experience and engineering. This hub is replaced with a better and more powerful E hub, but the main components remain the same.

The yoke has a function of a hydraulic piston and it is moved by the hydraulic pressure difference in linear direction along the shaft line. The sliding block is an intermediate part between the yoke and actuating pin. When pitch is actuated, the sliding block slides in the slot of the yoke and it converts the linear motion of a yoke to the rotating motion of a blade carrier. The actuating pin is a part of the blade carrier.

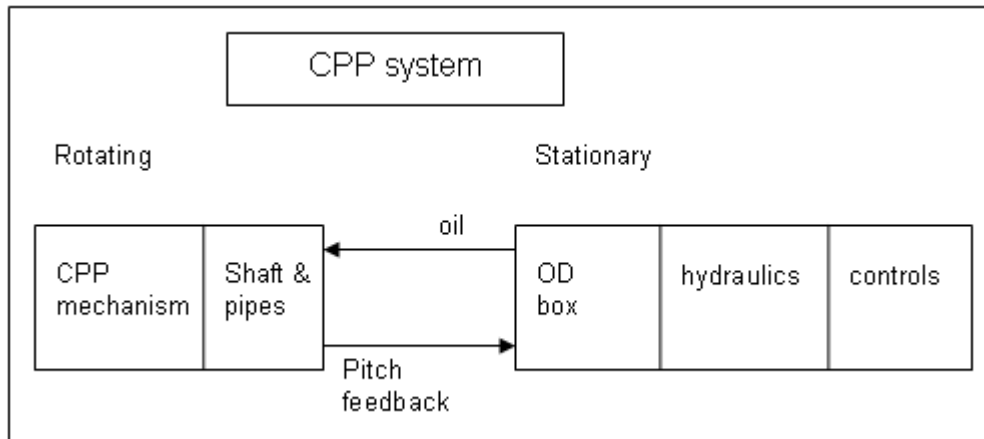


Figure 2.4: Main parts of a controllable pitch propeller system

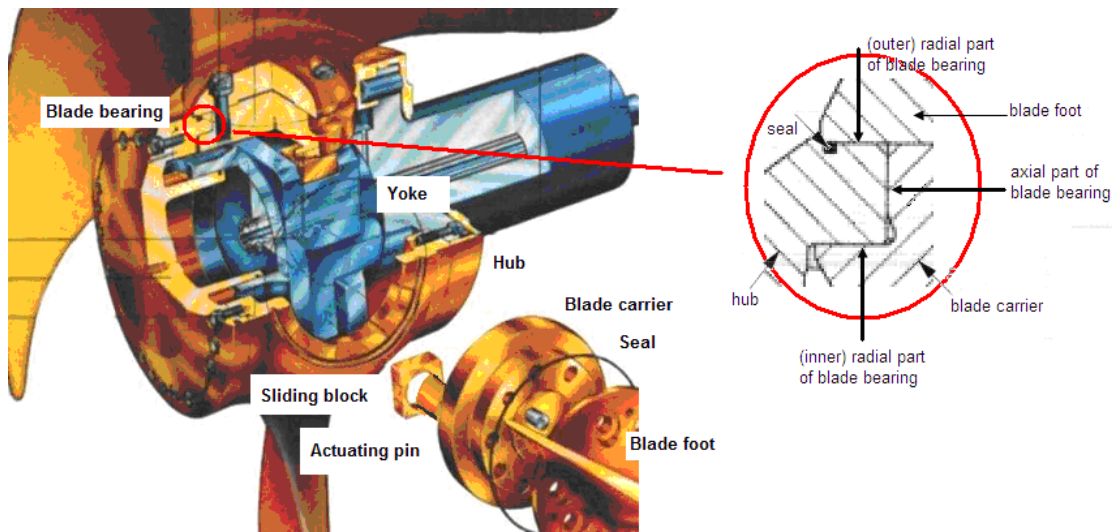


Figure 2.5: Assembly of a CP propeller. Source: Wartsila internal image

The blade carrier together with the blade foot and hub forms a blade bearing. This bearing is very important in CPP design. The importance of the blade bearing reflects in being exposed to the hydrodynamic loads stemming from blade and actuating loads stemming from the hydraulic system. This is the bearing where the two main functions of a CPP meet. The size of the blade bearing has a determining influence on the entire hub size. In addition to the strength/fatigue criteria, a blade bearing has to fulfil the wear criteria, as well. It must be able to withstand the desired number of pitch changes. In this thesis, the wear of a blade bearing is the main topic. A blade bearing of a CPP has a radial and axial part, the radial part has an inner and outer side. For minimizing wear in a blade bearing, the integral part is the seal between the blade foot and hub. In addition to preventing any water from coming in, this seal is also important for environmental reasons, as it prevents any oil from leaking outside of the hub into the sea. As shown, there are other parts, including bolts, which are very important in the construction of a hub. However, for this thesis, they are not the main topic.

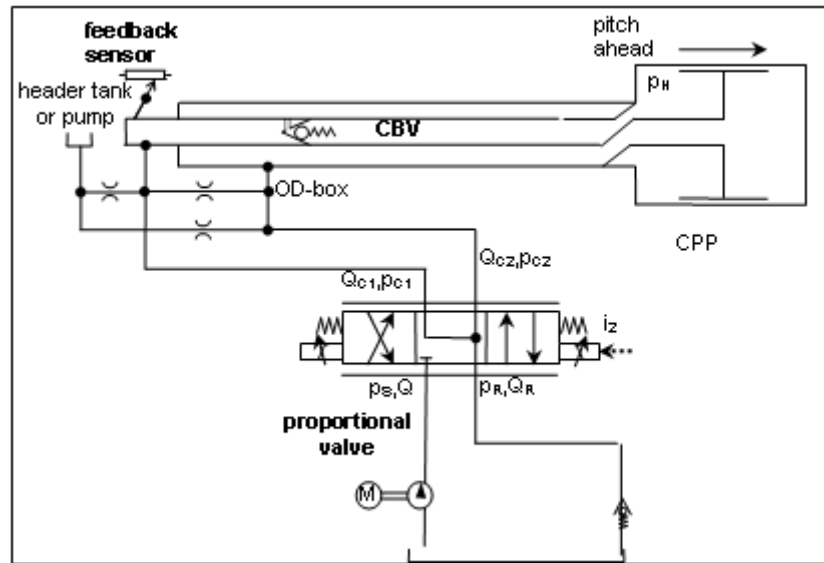


Figure 2.6: Hydraulic scheme of a CPP. Source: Wartsila internal image

In order to change the pitch, a hydraulic pressure must be supplied. Figure 2.6 shows the simplified hydraulic scheme of a modern CPP. A hydraulic power pack supplies the system with a pressure (p_s) and flow (Q_s). Proportional valve is governed by the control system and together they control the pitch. Larger systems have two proportional valves. The oil distribution (OD) box takes care of the connection between the rotating shaft and stationary (oil supply) pipes. The counterbalance valve (CBV) fixes the pitch position in the case of hydraulic power loss and allows depressurization. There are two regimes in which CPP operates, namely when pitch changes (actuating) and when pitch is constant (non-actuating). When pitch does not change, the proportional valve and CBV are closed allowing the system to depressurize, and therefore, no hydraulic power is needed.

2.3. Materials used for CPP's

Optimum material should provide strength, ductility and fracture toughness. It should be resistant to fatigue, corrosion fatigue and wear. In addition, it should be easy to manufacture with low residual stresses, easy to repair and at reasonable cost. The two most common types of materials used for CPP are steel and copper-based alloys. Copper-based alloys such as nickel-aluminium bronze and manganese-aluminium bronze are moderate in their melting temperature and thus easier to produce, lower cost, and easier to machine. Additionally, bronze has good corrosion resistance and it is easy to repair. Chromium-molybdenum steel alloys and stainless steel are attractive for their higher strength, but they have several weak spots, as the risk of cracking increases with size. There is a need for heat treatment for stress relief, sensitivity to fatigue, and pitting corrosion.

Cast Ni-Al bronze is the best and most common solution for hubs and blades. Blade carriers carry large loads and they require the use of high strength alloys such as Mn-Al bronze and Cr-Mo steel. Selection of blade bolts is done based on strength and corrosion resistance, but also on fatigue and corrosion fatigue resistance. Most frequently, the material for blade bolts is stainless steel. When combining two different metals, it is always advisable to check their galvanic compatibility. For example, a low alloy high strength steel and Ni-Al bronze is not a good combination.

The nickel-aluminium bronze is often called CuNiAl for its first letters. The two most common material combinations used in blade bearing are CuNiAl and Mn-Al bronze, or CuNiAl with 42CrMo4 steel.

2.4. Historical overview of development of a CPP

The first CPP mechanisms were developed at the beginning of the twentieth century with the production of mechanically actuated blades. Since then, designers have improved the performance of CPPs, which resulted in less parts, increased reliability, and higher power. A historical overview of the development of the CPP with a special emphasis on the former Lips (now Wärtsilä) propellers runs as follows:

- **1st generation controllable pitch propeller 1955 < 5 MW**
split hub, grease lubricated
mechanical pitch actuation
mechanical pitch feedback
- **2nd generation controllable pitch propellers 1962 < 11 MW**
integral hub, oil lubricated
mechanical pitch actuation
mechanical pitch feedback
- **3rd generation controllable pitch propellers 1972 35 MW**
integral hub, oil lubricated
hydraulic pitch actuation
mechanical pitch feedback
emergency actuating piston
- **4th generation controllable pitch propellers 1983 (C hub) no power limit**
integral hub, oil lubricated
hydraulic pitch actuation
optional electrical pitch feedback
maximum power applied 43 MW, largest size 2.8 m hub diameter
- **5th generation controllable pitch propeller 1989 (CPS hub)**
integral hub, oil lubricated
wearing plates, hub replacement behind the ship
hydraulic pitch actuation
mechanical pitch feedback
- **6th generation controllable pitch propellers 1995 (D hub)**
integral hub, with integrated hub cover
hydraulic pitch actuation
mechanical pitch feedback
- **7th generation controllable pitch propellers 2002 (E hub)**
Integral hub, smaller hub, high strength
No wearing plates, double lip blade foot seal

The mechanical actuated blades were a convenient solution, as most of the mechanism was inside the ship and the pitch was changed via the push-pull rod. This allowed a smaller hub size, but loads on push-pull rods were the limiting factor. It was quickly realized that grease lubrication was not sufficient for ensuring low wear rates of mechanical parts.

The later demand for increased power in propulsion plants made hydraulic actuating systems necessary. By introducing a hydraulic system, the oil lubrication was a natural choice, as the same oil is used for the lubrication and hydraulics. This ensured lower wear rates and lower actuation loads. For a while, mechanical wearing plates were placed in the blade bearing, between the blade carrier and the hub. This was a good option for the maintenance and overhaul of a CPP, but in some cases, plates broke and caused complete failure of the CPP. In the modern, state-of-the-art designs of a CPP, there is no wearing plate and special care is taken of blade foot seals.

The pitch feedback system is essential for proper pitch control. Without it, the control of pitch is not possible. A mechanical pitch feedback was replaced by an electrical feedback signal to improve the overall performance of a CPP.

For the design of CPP hub a modular approach was selected right from early days. The hub was designed for a generic set of requirements suitable for a wide range of vessels. The hub design as a concept was then fixed and hub size was varied such that a power range could be covered. It could be argued that the hub design should be optimized for each ship application. Nevertheless, logistical reasons for the production of controllable pitch propellers necessitate the need for these modular standards.

2.5. Failure mechanisms

In the study of any failure, one must consider a broad spectrum of possibilities or reasons for the occurrence. Often a large number of factors, which are frequently interrelated, must be understood to determine the cause of failure or to prevent it [Wulpi, 1999]. The term “failure” means the inability of a part to perform its intended function for any reason.

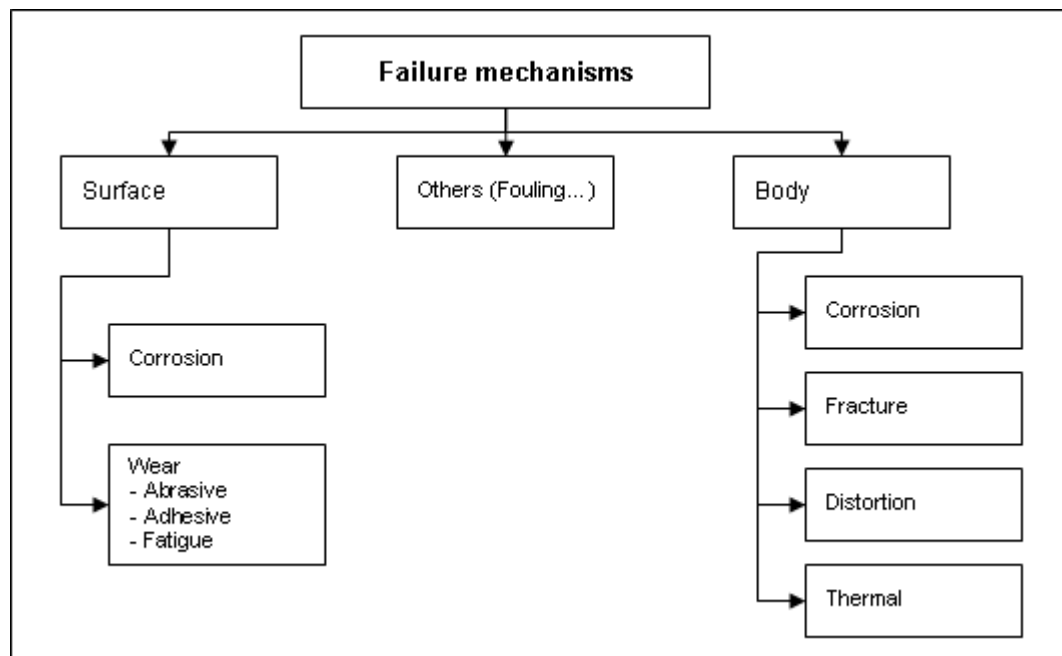


Figure 2.7: Principle types of failure mechanisms

At this point, one should make a clear division between the following terms: failure cause, failure mechanism and failure mode. As stated in [Grimmelius, 2005], a “failure cause identifies the source of the failure”. This means, for instance, the wrong design or wrong thermal preparation of the metal, poor maintenance, etc. A “failure mechanism

is the process that leads to a failure mode”, for example abrasive wear or brittle fracture. A “failure mode is a physical phenomenon which results in loss of functionality”, for example the part is worn out or broken.

Figure 2.7 shows a hierarchical tree of the principle types of failure mechanisms. A failure can occur on the surface of a part or it can be a phenomenon that involves the entire body of a part. Frequently, it is a combination of both. Failure mechanisms that involve the entire body can be divided into distortion, fracture, corrosion, and thermal failure mechanisms. Failure mechanisms that involve the surface of a part can be divided into wear and corrosion related mechanisms.

2.5.1 Body failure mechanisms

Body failure mechanisms can lead to a deformation in shape of the body or to the breaking of a part.

- Distortion:

Distortion failures involve the change in shape and/or size of a part. They are plastic deformations of a part and they can be time dependant or independent. Typical distortion failure mechanisms are creep, yield, and buckling. Creep is a typical example of a time dependant strain occurring under stress. It is a phenomenon that occurs over a considerable time and the temperature may have a significant influence. On the other hand, yield is a distortion failure mechanism that is characterized by a short duration and results in stretching, twisting and bending as a result of the stress exceeding the yield strength. Buckling is a form of distortion similar to yield, the difference being that it is due to instability caused by compressive stress, while normally yield is associated to tensile stress.

- Fracture:

The most drastic type of failure is when a part breaks. At the highest level, there are two modes in which a material can fail by fracture: under single load or under repeated cycle load.

- Single load fracture:

A single load fracture can be ductile or brittle. The difference is caused by the crystal structure of the material. The terms “brittle” and “ductile” are used here to describe the extremes of metal behaviour during a single load. These terms are opposites, like black and white. For many parts, it is desirable to have some “grey” colour.

A ductile fracture results from the application of an excessive force to a metal that has the ability to deform permanently, or plastically, prior to the fracture. The characteristic look of the surface of a ductile fracture is dull and fibrous.

A brittle fracture occurs suddenly and without any plastic deformation. The characteristic look of the metal surface of brittle fracture is bright.

However, several factors determine whether a metal will behave in a ductile or brittle manner. For example, a material can be ductile at room temperature, but it becomes brittle at sub-zero temperatures. For some materials, this transition is sharper than others. The factors and general trends that affect the ductile-brittle relationship are summarized in Table 2.1.

Table 2.1 Factors affecting brittle-ductile relationship. For example, at higher temperature a fracture has ductile trend, at higher stress concentration a fracture has brittle trend, etc.

Factor	Trend	
	Ductile	Brittle
Temperature	Higher	Lower
Rate of loading	Lower	Higher
Geometry	No stress concentration	Stress concentration
Size	Smaller or thinner	Larger or thicker
Strength of metal	Lower	Higher

– Fatigue fracture:

Repeated cycle fractures or fatigue fractures are generally considered the most dangerous type of fractures, because they occur in normal service without any overloads. The fracture occurs after repeated or fluctuating stresses having a maximum value less than the critical strength of a material. There are 3 stages in fatigue fracture:

Stage 1: Initiation: (sub) microscopic initiation of a crack occurs;

Stage 2: Propagation: the cracks grow and intersect;

Stage 3: Final rupture: propagation of cracks continues and the cross-sectional area is reduced until final fracture occurs;

The surface of a repeated cycle fracture is characterized by lines that follow the progression of the crack.

– Corrosion:

Corrosion is a natural process that tries to reverse the chemical action of the refining process. It is a chemical or electrochemical reaction of a metal with the environment. Although corrosion failure usually is not a catastrophic one, it will often cause body and surface changes, and therefore it is placed in both the body and surface failure mechanisms. Research carried out on the cost of corrosion and corrosion prevention shows a value of up to 4.2% of GNP in the United States [Stachowiak, 2005]. These numbers may not be completely accurate, but they suggest an enormous cost of corrosion.

The subject of corrosion is extremely complex. A slight change in metal selection or environment may have a large influence on corrosion. Corrosion must be considered in every failure analysis due to its influence on many fracture and/or wear mechanisms. Therefore, in Figure 2.7, corrosion is placed in both failures that involve the entire body, and those that are constrained to the surface of a part.

– Thermal failures:

Due to the fact that they interact with other failure mechanisms, thermal failures are perhaps the most complex type of body failures. With the rise of temperature, the life of the material is limited, whether under a static or cyclic load. However, a part can fail only due to cyclic thermal stressing. This failure mechanism is known as thermal fatigue. Thermal fatigue is a mechanism that causes cracks in the body due to repetitive changes in temperature when there is not necessarily any applied external force.

2.5.2 Surface failure mechanisms

In Chapter 1.2, wear was defined as the damage to a surface as a result of relative motion with respect to another substance. A further, perhaps even more important feature of wear is that it is a system property and not a material property. In Figure 2.7, corrosion is on the level of wear in failure mechanisms. It is different because it does not directly result in the loss of material, and because it doesn't necessarily include any motion, but damages the surface. Instead, a surface layer forms by corrosion (e.g. iron oxide) and wear occurs by one of three other mechanisms. However, the wear rate is influenced and may even be controlled by corrosion effects.

There are three ways in which wear can be classified. A first classification can be made in terms of the physical mechanism of removing the material. Terms such as abrasion, adhesion and corrosive wear are examples of this classification. A second classification is by the appearance of the wear scar. Terms used in this category include pitted, spalled, scratched, polished, crazed, etc. A third classification is in terms of the circumstances that surround the process of wear or by describing the situation in which the body is wearing. For this classification phrases usually used are lubricated wear, unlubricated, sliding, rolling, impact, etc.

The first classification in terms of physical mechanisms is related to the way material is removed. Terms usually related with physical mechanisms of wear are adhesive, abrasive, and repeated cycle wear. Adhesive wear occurs when two surfaces come into contact and when they adhere to each other. As two surfaces move, wear occurs by one surface pulling material from the other one. Abrasive wear occurs by protuberance (particles thrusting out from a surface), which produces a groove or a scratch. The generic view of repeated cycle wear is that cracks grow and link to form a loss particle. The usefulness of a classification with respect to the physical mechanism would be in guiding the engineer to use proper models to predict wear life and to identify the significance of certain material parameters to the wear. Once the physical mechanism is known, the significance of each parameter can easily be determined in an experiment.

The second classification in terms of appearance can aid in comparing wear situations. This can be illustrated in the wear of gears. "Scuffing" is a term used to describe the appearance of scars produced by sliding with poor lubrication. With gears, different portions of the tooth contact area experience different types of motion. Near the pitch line, it should be pure rolling and in moving out further, sliding will occur. If scuffing is observed near the pitch line, this indicates that sliding occurs at the wrong place and that there may be some problems with alignment. Furthermore, the presence of scuffing may point to a problem of poor lubrication or that the incorrect lubricant is being used. These observations can guide an engineer to resolve the problem.

The third type of classification is potentially the most useful for common engineering practice. It describes a wear situation in terms of things that can be influenced directly by engineers. By giving the description of conditions, a specific list of rules can be identified and used.

Generally, wear is described from these three points of view. But there is no unique classification. Additionally, some terms such as scuffing can be used to describe several phenomena. One author may use this term to describe the appearance on the surface while another author can use it to describe adhesive wear, and a third may use it to describe a sliding process. The conclusion is that classifications are not equivalent nor are interrelations simple, unique or direct. There are numerous ways that material can experience wear and numerous factors have influence on wear. At this point, with

knowledge from tribology, it is not possible to determine a complete connection between operating conditions, wear mechanism and appearance.

2.6. Failures of CPP's

A controllable pitch propeller is a highly loaded system that works in a harsh environment. However, the demand for reliability and endurance is larger than in many other applications. A ship cannot sail without a propeller and repair of a propeller takes a long time and is costly. This means that a ship has to go to a dry dock and it cannot make money. A normal overhaul period for a CPP is five years and a CPP must work properly between two overhauls.

One of most comprehensive investigations done on failures of a CPP, and maybe the most relevant for this investigation, was done in the Barbey case [Barbey, 1982]. In this case, a drastic type of failure occurred, whereby all blade bolts broke and all blades fell off. The report includes a material investigation, laboratory experiments, and on-board measurements of propeller/blade loads. It was concluded that the CPP failed due to overloading during manoeuvring and crash stop test (i.e., stopping the ship at full speed ahead). Luckily, these kinds of failures in the mechanical assembly do not happen frequently, but when happening, they are very drastic.

The always present need for larger and stronger propellers brings new challenges and higher failure rates for propellers with higher power. In a highly loaded and new (larger) installation, problems such as fatigue cracking in the blade carrier, broken blade bolts, cracking in the actuating pin, and wear in the bearings, may be related to an incorrect estimate of the cyclic loadings. With increased experience in designing, the failure rate of a CPP mechanism decreased. Although some serious failures have been considered to be the designer's fault (overstressed components), the majority could have been avoided with a better selection of materials. The hydrodynamic advantage of a stronger material is very attractive (smaller hub and thinner blades), but poor fatigue properties make strong material not the best solution for a propeller. For example, stainless steel has higher yield strength than a bronze alloy. However, the fatigue properties of stainless steel and its notch sensitivity make bronze the preferred material for marine propellers. More frequently, the problems that allegedly were related to selected materials are actually due to bad production, casting and machining.

Additional problems in the CPP mechanism can be caused by poor sealing. Even though oil pressures in the hub are above the surrounding water pressure, the intrusion of sea water is not uncommon. If the sea water intrudes into a CPP mechanism, the lubrication will deteriorate and friction in the system will increase. This will cause high actuating loads and eventually the cracking of the actuating pin. With respect to wear, sea water or a water-oil mixture cause corrosion of parts, accelerates wear, introduces transition in wear behaviour and tribo-corrosion, and causes corrosion-fatigue cracking. A list of possible failures is not limited to this, but major processes that influence wear in blade bearings and leads to progressive deterioration are listed above.

In order to illustrate different types of failures and reliability of a CPP, the available service records have been investigated for a fleet of similar ships with similar operating conditions and all are equipped with a CPP. The investigated ships belong to a series of general cargo vessels, they are similar in size and speed, and their controllable pitch propellers have similar power density.

In order to have a better overview of situation, the failures have been listed in three groups as mechanical, hydraulic and electrical. The majority of failures were electrical-

related failures. Figure 2.8 illustrates different groups of failure as a function of years in operation.

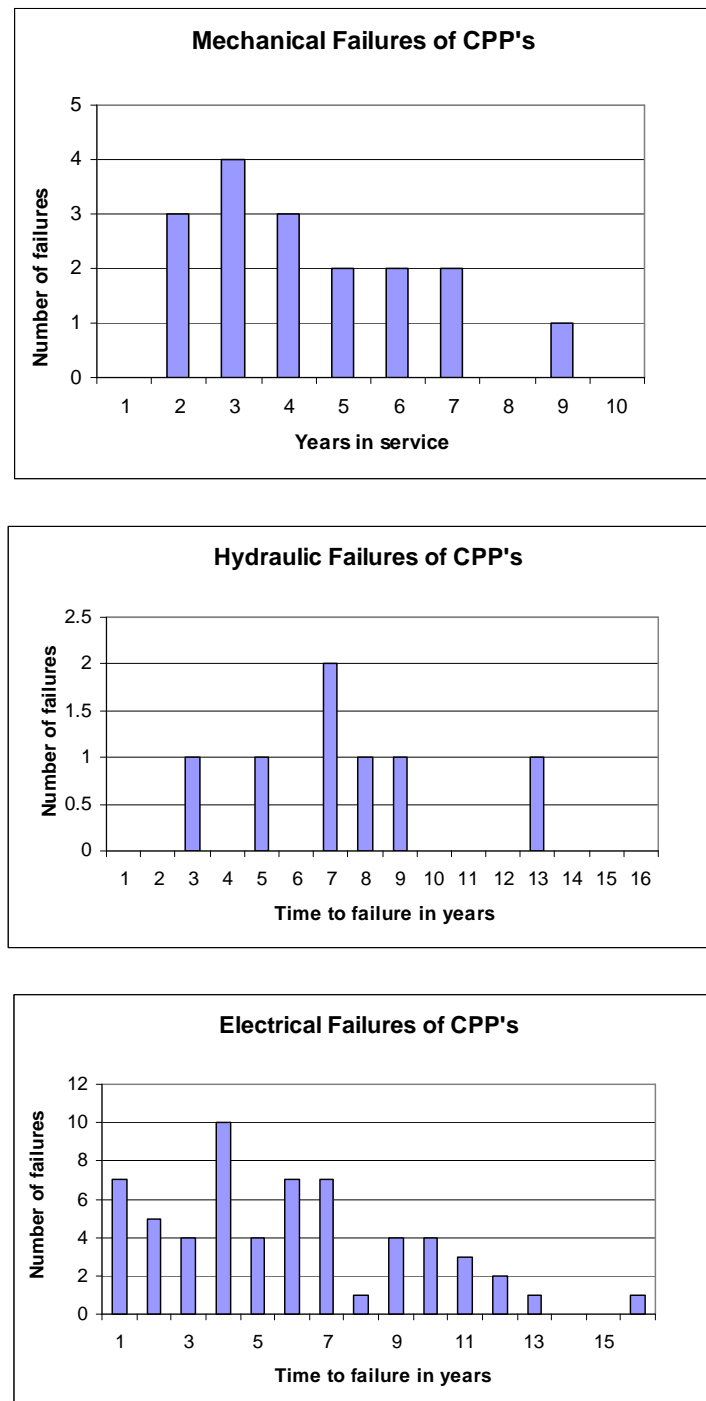


Figure 2.8: Different failures of CPP's as a function of years in service. In total: 17 mechanical, 7 hydraulic, and 59 electrical-related failures.

The electrical failures included all failures of electric and control equipment, including potential meters, and broken wires. As such, electrical failures also included problems related to the proper adjusting of control settings, (i.e. the software of control system). The hydraulic failures were least frequent, and the vast majority is related to OD box failures. The failures of mechanical assembly of a CPP were the most interesting for this investigation. There were no records of the wear related failure of blade bearings,

or any other metal part if a CPP mechanism was in the hub, but approximately half the recorded mechanical failures were related to the seal in the blade bearing. The other half of mechanical failures was related mostly to the shaft bearings.

2.7. The investigated CPP

One CPP is in the focus of this thesis and in the following text it is referred to as the investigated case or the investigated CPP. The investigated CPP was reported to fail due to significant fretting damage in the blade bearing. This thesis is not a failure analysis and as such, does not attempt to validate the reported failure. The thesis treats wear in the blade bearing of a CPP as a general phenomenon. However, the investigated case has been selected as a subject due to its intriguing failure. The goal here is to introduce the investigated case as the subject of following analysis. The investigated CPP is a very large propeller, and it is placed on a 216 m container vessel with 25 knots design speed which is not included in the analysis done in Chapter 2.6. The main data of the propeller is as follows:

Maximum power:	25020	kW
Rotation speed:	95	rpm
Diameter:	7.0	m
Hub diameter:	2.0	m

After the damage occurred, investigation has led to an effective repair of the installation.

2.8. Wear mechanisms

The wear mechanism can be thought of as a material failure mechanism occurring at or near the surface. Major wear mechanisms include adhesion, abrasion, and repeated cycle wear. At this point, a short description of each category of wear will be given and following that, it will be dealt with in more detail. Figure 2.9 illustrates three major wear mechanisms:

- The adhesive wear occurs when two surfaces come into contact and adhere to each other. As two surfaces move, wear occurs by one surface pulling material from the other one.
- The abrasive wear occurs by protuberance (particles thrusting out from a surface), which produces a groove or a scratch.
- The generic view of repeated cycle wear is that cracks grow and link to form a loss particle.

Some authors have defined even more types of wear as typical wear mechanisms [Raboniwicz, 1965]. Over time, with increased knowledge, it was found that these mechanisms can be explained with the other three. For example, fretting which was thought of as a unique mechanism, in the beginning of its occurrence is caused most probably by adhesive wear, and the resulting debris act in an abrasive wear mechanism. Furthermore, repeated cycle wear contributes to making fretting a complex, rather than a single wear mechanism.

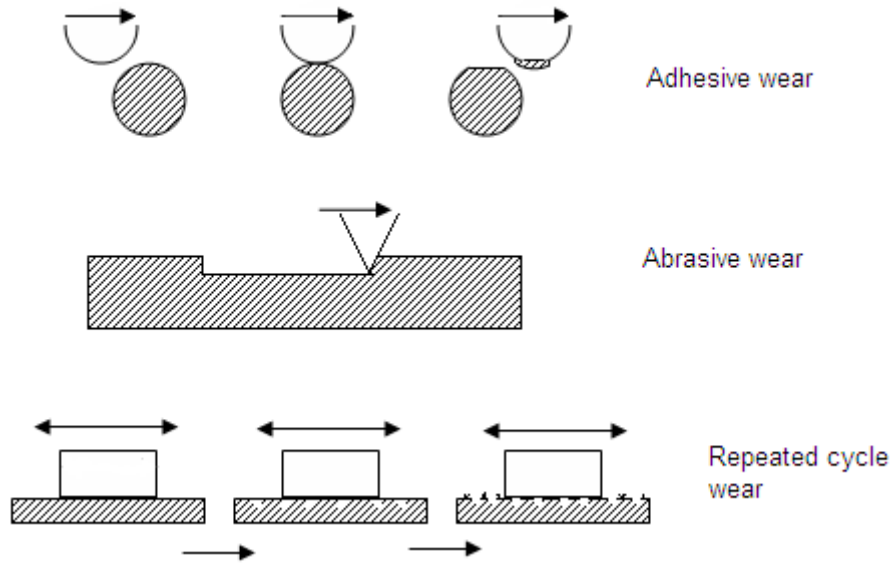


Figure 2.9: Three major wear mechanisms

The main difference between abrasive and adhesive wear on one side and fatigue wear on the other side is that first two wear mechanisms are associated with a single action, while the fatigue mechanism requires more than one cycle. It is important to note that normally in any actual situation more than one mechanism is involved. So, this classification for wear mechanisms is not a classification for wear situations. The simultaneity of these basic mechanisms is the key determinant of wear behaviour. The classification in three modes as presented here is not always complete or undisputed. In the following text, each wear mechanism is explained in more detail. Fretting wear, due to its relevance for this thesis, is also explained in further detail.

2.8.1 Adhesive wear

There are two levels of the nature of interaction between junctions, namely asperity and atomic level. At the asperity level, the deformations can be plastic and elastic. At the atomic level, the interaction in junctions is dictated by the inter-atomic forces. These forces are the most dominant in the adhesive wear. Molecules of one material interact in a different way with different types of materials. Similar materials tend to bond easier than dissimilar materials. That is why the selection of material is crucial for the reduction of adhesive wear. Another way of reducing inter atomic forces between two materials in contact is to use a lubricant.

Actual surfaces, no matter how smooth they are, always have some roughness. Thus, the real physical contact takes places only at few spots. These spots are called junctions. The sum of all junctions is called the real area of contact. The fundamental physical models for adhesive wear are usually based on the real area, while engineering models are based on the apparent area of contact. An interpretation of Archard's equation, see [Archard, 1953], for adhesive wear can be found in [Bayer, 1994]: a proposed model for wear volume (V) lost by adhesive wear is based on normal force (F), hardness (H), wear coefficient (K) and sliding distance (S):

$$V = K \cdot \frac{F}{H} \cdot S \quad (2.1)$$

The main feature of this equation is the dimensionless wear coefficient K . The same source gives the possible values of the coefficient. The two most influential parameters on the value of K are the existence of lubrication and the type of materials in contact. If the materials are the same, and if there is no lubrication, the value for K can increase to 0.2, higher than for any other mechanism. On the other hand, for a pair of dissimilar materials with lubrication, the coefficient can decrease to $9\text{E-}8$. Additionally, the author states the coefficient K to be load dependant. Moreover, the number of junctions and the real contact area also depend upon load.

2.8.2 Abrasive wear

Abrasive wear mechanisms are generally considered to be any mechanism by which hard asperities cause damage in a single action. The damage they produce may be in the form of deformation or in the form of material removal. Terms like “plowing” and “scratching” are often used to describe certain types of abrasive wear. The first one means surface damage and the latter means material removal.

With abrasive wear, there are three possible contact situations, as illustrated in Figure 2.10. The first situation is when asperities of one surface are pressed into another surface. This is often called two-body abrasion. Filing, sanding and grinding are examples of two-body abrasion. The second contact situation is when hard particles are trapped between two surfaces. This is often called three-body abrasion. An example of this is polishing. A third contact situation is when hard particles directly hit the surface. The particles that are hitting the surface are in some stream of fluid. This is called erosion. Some authors classify erosion as a different wear mechanism, but it can be viewed as a sum of single abrasive wear mechanisms.

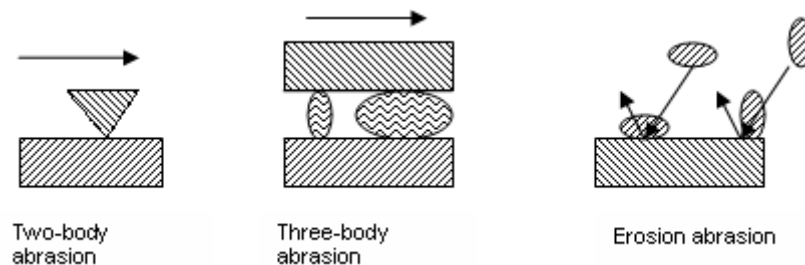


Figure 2.10: The types of abrasive wear

The equation that generally describes two- and three-body abrasion can be developed from the wear produced by a single grain. As sliding occurs, a grain produces a groove of volume equal to the cross section area, times the distance of sliding. One of the proposed models in [Bayer, 1994] for abrasive wear is identical to the adhesive wear model in Equation (2.1).

However, the values for K are different and there seem to be three different trends. The first trend is that the two-body abrasion has higher values for K than three-body abrasion. This is because in the three-body situation, the grain is free and therefore does not always cause wear. The second trend is that when the grains are larger, the value of K is larger, as well. The third trend is in the context of lubrication. an increase in abrasive wear in lubricated systems is explained by the fact that the lubricant flushes the wear debris.

Despite the fact that the hardness is mentioned in both, the adhesive and abrasive wear mechanisms, its influence is somewhat different. In adhesive, the similarity of the materials is much more important, while in abrasive, the “similarity” of hardness is the

determining influence. When the hardness of two materials in contact is similar, the wear decreases, sometimes even dramatically. Some general advice is to not have hardness differences larger than 10%.

2.8.3 Fatigue wear

Fatigue wear occurs as a result of cyclic motion between two bodies in contact at the surface or just below the surface. The exact location will depend upon the location of maximal stress, which again depends on the type of contact. Fatigue wear is somewhat similar to fatigue failure fracture. There are three stages of repeated cycle wear that can be recognized, including incubation period (no cracks), formation of cracks (first cracks appear but no material loss), and loss of material (cracks grow and connect causing the loss of material). During cyclic stressing, cracks propagate creating a network of cracks which then produces the small particles (or flakes) that are easy to remove. For rolling situations, there is a generally accepted empirical relationship between the load and number of revolutions defining the incubating period. The general form of the relation is:

$$N_1 F_1^n = N_2 F_2^n \quad (2.2)$$

Where N_1 is a number of cycles during the incubation period for applied force F_1 , and N_2 for applied force F_2 . The exponent n has a value that is dictated by the contact situation. For point contact, such as at the ball bearing, its value is 3 and for line contact, such as roller bearing, it is 10/3. There have been many studies done on the life of rolling bearings [Zaretsky, 2000], and the general conclusion is that bearing lives limited by fatigue mechanisms are generally viewed statistically, and usually on the basis of Weibull distribution.

2.8.4 Fretting wear

Even though fretting wear can only be considered as a combination of the above mentioned mechanisms, fretting wear will be investigated here in more detail due to its importance for this thesis. Fretting wear is a phenomenon that can occur between two surfaces which have a relative oscillatory motion of small amplitude, typically smaller than 1 mm. Usually, the motion is caused by vibrations of the machinery. The fretting wear can occur at the part of the contact even if there is no gross sliding between two bodies. There are many practical situations (flanges, rivets, couplings) in which fretting can be a problem. Typically, the static joints subjected to vibrations can suffer from fretting.

Fretting wear appears to follow a certain sequence. Firstly, the mechanical actions (vibrations) remove the protective oxide layer and expose the clean and highly reactive metal surface to the environment. This clean surface will then oxidize and vibrations will again remove this new oxide layer. The removed oxide particles may be trapped in the contact and they can introduce abrasive wear because of their higher hardness. The oxide debris made by fretting wear can either escape from the contact or pile up in the contact. If they escape from contact, the contact becomes looser, which means larger vibrations and the increase in wear rate can be expected. If the oxide debris is unable to escape, it can lead to the seizure of the parts in contact. Obviously, the first situation is more dangerous for static joins, while the second situation is more dangerous for parts which are designed to slide or rotate with small clearance such as blade bearings.

The process of entrapment is explained in [Stachowiak, 2005]. One of the special features of fretting wear is the large overlap between fretting amplitude and contact area. For fretting, the amplitude of motion is smaller than the contact length. This results in part of the contact being constantly covered. Within this covered zone, the worn debris remains entrapped. Figure 2.11 shows the concept of overlap for fretting wear and sliding wear.

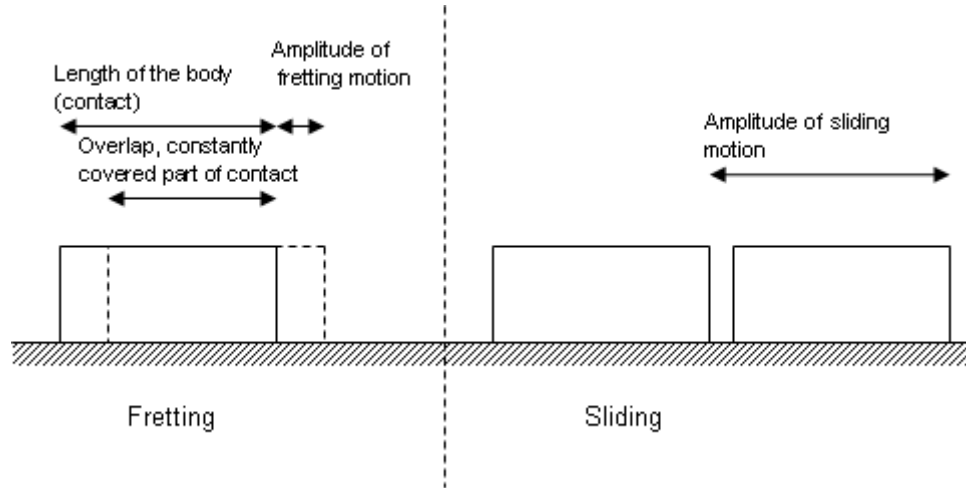


Figure 2.11: Concept of overlap in fretting

Fretting wear can occur even without a gross slip of bodies in contact. In certain circumstances only a part of the contact can exhibit slip while the rest of the contact exhibits no motion. The concept of partial slip will be explained as in [Williams, 1994], for further details the reader is referred to this reference. Figure 2.12 shows the contact situation between two cylinders with parallel axis with the length (L). In this situation, normal force (F) and tangential force (Q) are applied to the contact and there is no gross slip ($Q < \mu F$). The normal load causes Hertzian stress distribution (σ), which results in limiting friction stress determined by the friction coefficient (μ):

$$\tau' = \mu \cdot \sigma \quad (2.3)$$

The tangential stress caused by the tangential force (Q) has an inverse semi-elliptical shape:

$$\tau(x) = \frac{Q}{aL\pi\sqrt{1 - \frac{x^2}{a^2}}} \quad (2.4)$$

It was realized in [Mindlin, 1953] that the no-slip model does not correspond to the real situation. It was proposed that slip would occur wherever the calculated tangential stress (τ) would exceed the limiting frictional stress (τ'), thus causing the partial slip. The tangential stress ($\tau(x)$) rises from some finite value at the middle of the contact up to an infinite value at the edges. However, in the region of slip ($b < x < a$), it was reasoned that the real value of tangential stress is not larger than the limiting frictional stress (τ'). While in the stick region ($x < b$) it was argued that the tangential stress is equal to ($\tau' - \tau$), the limiting frictional stress minus the tangential stress caused by force (Q). Sliding in the contact will occur when the tangential force (Q) overcomes the friction force (μF).

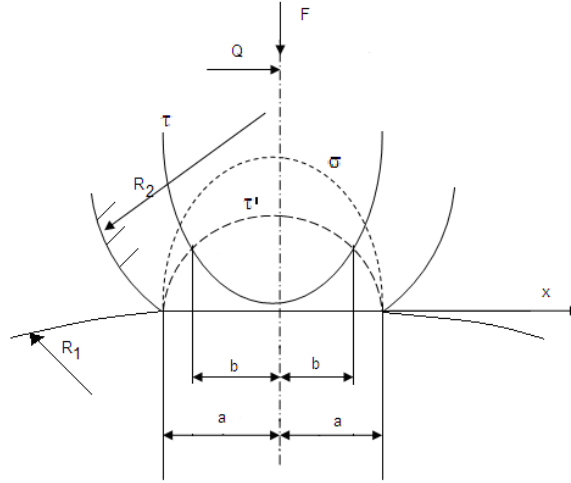


Figure 2.12: Normal and tangential stress distribution for Hertzian contact

The stick and slip regions were confirmed experimentally in the ball against flat experiments, the largest wear was found in the region of maximal tangential stress.

In summation, three different sliding contact situations can exist, namely no slip, partial slip, and gross slip. The fretting wear can be caused by any of these. It is expected [Bayer, 1994] that the partial slip has a much lower wear rate than the gross slip, sometimes to a factor of ten.

2.9. Wear behaviour

The wear behaviour of a material is a complex phenomenon and it involves properties of materials (chemical, physical, mechanical, thermal, etc), operational circumstances (speed, load, temperature, lubrication, etc), and design characteristics (rolling, sliding, material pair, etc). Wear is usually plotted in the form of a graph as a function of time, distance, number of cycles and/or some other parameters such as hardness, temperature, etc. Whichever presentation is used, the designer is looking for transition points, the point where the wear behaviour changes significantly. Wear behaviour is usually represented by the wear rate, a coefficient describing how much volume will be lost for a certain amount of motion and load applied. The specific wear rate (w) is expressed in mm^3/Nm . There are other representations; however this one best suits the above mentioned definition.

$$w = \frac{V}{F \cdot S} \quad (2.5)$$

One of typical transitions in wear behaviour is the run-in transition. When two new parts start running against each other, the initial wear rate is quite high. This period of high wear rate is known as the run-in period. However, as the surfaces become smoother and the largest asperities are flattened, the wear rate decreases and mild wear behaviour occurs. Figure 2.13 shows the typical wear behaviour over the life of a component. The run-in period is followed by the low wear rate regime. This regime is maintained through the operational life of a component. When the fatigue processes and repeated cycle wear becomes dominant, the wear rate rises again and this rise usually marks the end of life of a component.

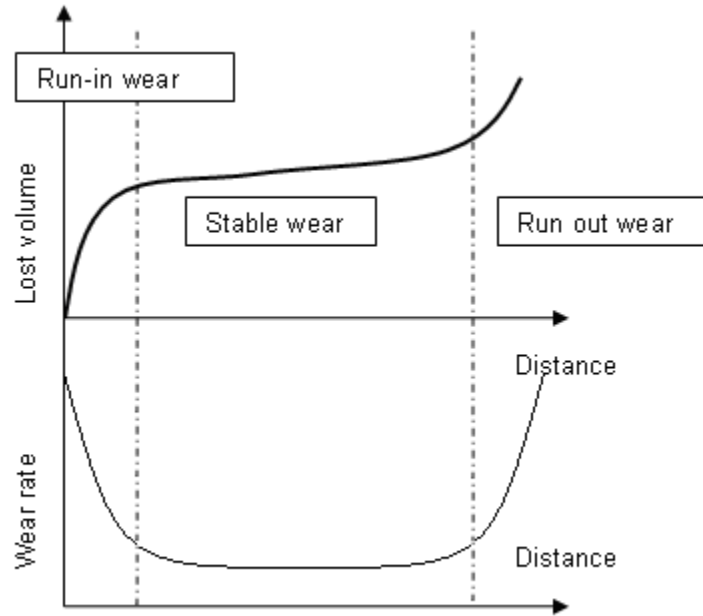


Figure 2.13: Transitions in wear behaviour as a function of time or sliding distance

It is interesting to consider how the interaction of two wear mechanisms can influence the total wear behaviour. There are two ways in which the wear mechanisms can interact. The first one is when they occur parallel to each other. In this case, the overall wear behaviour is the sum of those two. For example, in sliding wear, the damage can be made by both abrasive and fatigue wear. The total volume lost is therefore:

$$V_{\text{total}} = V_{\text{abrasive}} + V_{\text{fatigue}} \quad (2.6)$$

The second type of interaction between wear mechanisms is when individual mechanisms interact in a sequential fashion, giving rise to each another. Fatigue wear can cause the formation of cracks, which will increase abrasive wear. Mathematically, the wear may be described by the equation for abrasive wear, where the wear coefficient is now dependent upon fatigue parameters.

$$V_{\text{total}} = K(V_{\text{fatigue}}) \frac{F}{H} \cdot S \quad (2.7)$$

An additional overall observation can be made with respect to the selection of material combination based on their wear behaviour. Suppose there are two combinations of materials in contact; material A in contact with material B with superior wear properties in conditions $p < p_{\text{critical}}$, but not very robust, (i.e. very sensitive to the change in parameter p), and the combination of material A in contact with material C which does not have characteristics as good as the combination A and B with respect to design parameters, but it is very robust against parameter p . Figure 2.14 shows the wear rate of material combinations A and B and A and C as a function of parameter p . In this example, parameter p can be the percentage of sea water in the lubrication of a CPP. The material A can be some Ni-Al type of bronze, (stainless) steel, while material B can be some (stainless) steel, and material C Mn-Al type of bronze. Often, a more expensive material does not necessarily mean a better material. The designer must know the sensitivity of materials with respect to many parameters.

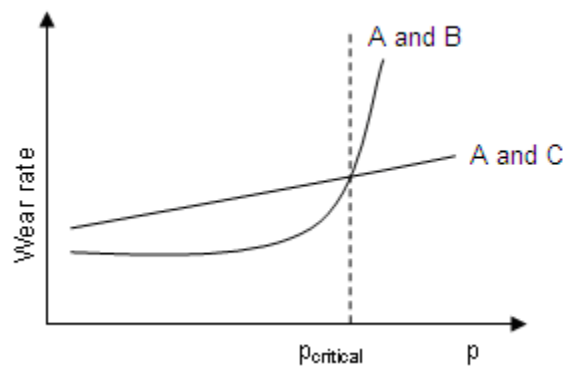


Figure 2.14: Wear behaviour of two different materials

Here, some general trends on wear behaviour will be briefly mentioned.

- In general, higher material *hardness* reduces wear. However, a large difference in hardness combined with higher roughness can cause significant abrasive wear.

- The *ductility* (or brittleness) can have an influence on single cycle wear mechanisms. Usually, ductile materials tend to experience less wear in single cycle wear mechanisms.

- The *temperature* in the contact and surrounding can have an influence on oxidization and strain rate, and in drastic cases, it can change the structure of material. Additionally, it can reduce oil viscosity and lower the effect of hydrodynamic lubrication.

- Velocity* can increase hydrodynamic lubrication, but in dry contacts it can increase friction and contact temperature.

- Roughness* can influence the formation of the lubricant film and can influence the wear of material. If the allowable wear is larger than roughness, roughness usually plays only a limited role in the life of the component. In [Barbey, 1982], it was documented that the roughness only has an influence on the run-in period, and the higher roughness decreases the time of the run-in period.

2.10. Wear failure of a CPP

There are two possibilities in which a blade bearing of a CPP can fail due to wear. The first possibility is that the total amount of wear is higher than the allowable wear. The second possibility is the seizure of the actuating mechanism.



Figure 2.15: 4D1000 hub and blade carrier after 10 years service

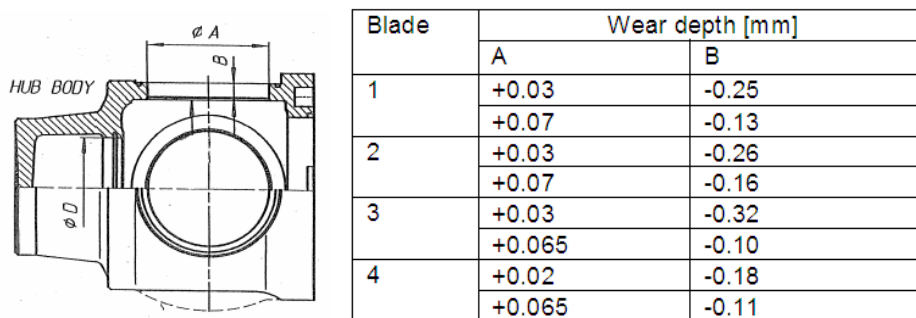


Figure 2.16: measured dimensions of the 4D1000 hub and blade carrier after 10 years service

For blade bearings, the maximal wear that is allowed is equal to the sum of manufacturing tolerances of all parts involved in pitch actuation, approximately 200 μ m. However, field experience shows some propeller suffered from significantly higher wear, even up to 500 μ m, but they were still operational. Figure 2.15 shows a photo of wear scars on a D-hub after 10 years service. The hub is CuNiAl and blade carrier is made of MnAl bronze. The propeller came to the workshop for an overhaul and there was no record of any complaints on the propeller's performance. The maximum calculated load was 21N/mm² on the inner side of the blade bearing. The total amount of wear for this D-hub was between 100 and 320 μ m, depending on a blade number. Figure 2.16 shows the measured dimensions of CPP parts. It is important to mention that large water marks have been observed in the hub. The presence of water has a large influence on the wear regime. It is possible to conclude that wear of 200 μ m does not represent a problem for a CPP system and this value is selected as the allowable wear of blade bearing of a CPP.

In addition to the total amount of wear, another wear related failure mode that may happen in the blade bearing is the seizure of the system. It is possible to foresee three reasons that can lead to the seizure, namely lack of lubrication, entrapment of debris, and drastic change of surface roughness due to wear. The lack of lubrication refers to circumstances that can deteriorate the lubrication of the bearing, for example insufficient amount of lubricating oil and/or intrusion of sea water. The entrapment of debris has been explained in Chapter 2.8.4; worn out debris can stay trapped in the bearing and consume clearance required for normal performance.

Wear process can change the contact situation in the blade bearing so much that is not possible for the hydraulic system to change the pitch. This has been observed in practice. In some rare cases, it was not possible to change the pitch of a CPP, even though there was nothing wrong with the hydraulics. The pitch was simply stuck. Some propellers suffered from seizure of the mechanism even though the total wear was lower than 200 μ m.

2.11. Wear situation in a blade bearing of a CPP

Any wear situation is dictated by loads and motions of bodies in contact and influenced by the surrounding environment. It must be noted that sometimes the surrounding environment can dictate the amount of wear. The wear situation of a blade bearing of a CPP is no exception. The environment of a CPP can have a large effect on the wear of the blade bearing. The lubrication of a blade bearing is achieved from the inner side of the bearing. Under design conditions, the lubrication of the bearing is good and

sufficient. However, the conditions on the outer side of a blade bearing are very harsh. In addition to sea water, there can also be some ice, fish nets, sand, etc. Any intrusion of these elements may lead to lack of lubrication, increased friction and ultimately to the failure of the blade bearing and a CPP.

Loads in a blade bearing are large and oscillatory, as the entire thrust of a blade is transmitted to the ship by the blade bearing! The basic motion in the blade bearing is caused by the hydraulics and is a main feature of a CPP (i.e. to change the pitch). Additionally, oscillations in the wake field and orbital velocities caused by waves may lead to load variations and additional motions in the blade bearing. These additional motions are more frequent and have smaller amplitudes than the basic motion. It is to be expected that the motion caused by hydraulics has a sliding nature, while the motion caused by oscillating hydrodynamic forces has a fretting nature.

All three mechanisms (abrasive, adhesive, and fatigue) can be expected in the wear behaviour of a blade bearing of a CPP. The blade carrier and blade bearing are sliding relative to each other with relatively large surfaces and low velocities. In the present use of pitch control in ships, the blade bearing spends a lot of time in a (relative) stand-still position, (i.e. no pitch actuation). This situation can easily lead to adhesive wear, and careful material selection is essential. Investigation will indicate whether adhesive wear is present in the form of galling, scuffing, and pitting.

Due to the long lifetime of a CPP (up to 20 years), it is normal to expect effects of fatigue wear in the form of spalling, pitting or cracks. Despite the fact that a significant amount of attention has been paid to the surface finishing of the bearings, it is normal to expect some abrasive wear, as well. Two types of abrasion may be present, two- body and three-body abrasion. Particles removed by fatigue wear can react with the environment and act as a third body abrasion. Investigation will indicate whether abrasion has a scratching, scoring, or plowing form.

3. Loads

This chapter focuses on the forces acting in a controllable pitch propeller (CPP) mechanism and the equilibrium of Coulomb friction, hydrodynamic spindle torque, and a non-actuating hydraulic reaction torque in the blade bearing. The disruption of this equilibrium will lead to the fretting motion in the blade bearing. An attempt has been made to define the circumstances leading to fretting in a CPP and to describe the influence of sea state on fretting behaviour. Using hydrodynamic tools it is possible to determine the theoretical conditions for fretting. A combination of theoretical and experimental results provides a better understanding of the fretting phenomenon in a CPP. The first part of the chapter gives an introduction to the working regimes and forces acting on a CPP. In the second part the presence of fretting is defined based on the calculation of forces and moments during one revolution of a blade in the non-actuating regime for the design condition of a specific propeller. The third part investigates self propulsion tests in irregular seas and hydrodynamic forces acting on a CPP in those conditions. The results indicate a decrease of fretting in higher waves and higher speeds. It has been shown that it is not wise to look only at the load mean value as design criteria.

3.1. Introduction

A lot of work has been done on understanding the hydrodynamic loads on propeller blades, such as thrust and torque, but little is known about their effect on the mechanism of a CPP and potential vibrating motion in the bearings. In contrast to the sliding motion over relatively large distances, fretting motion is defined as small amplitude and frequent oscillating motion. The fretting motion may result in fretting fatigue, fretting wear or increased friction coefficient. Fretting motion of the pitch in a CPP may be caused by a change in hydrodynamic forces or by improper control setting. The second possibility will not be investigated here; the focus is rather on fretting motion caused by oscillations in hydrodynamic forces due to the change in wake field during one revolution. Instead of looking at the total mean values of loads acting on all four blades, the accent is on the prediction of fretting motion based on instantaneous values of the forces acting on one blade. Moreover, by looking at modelled and measured results of loads acting on a propeller of a single screw vessel, an attempt is made to get more insight in the influence of sea condition on the fretting motion in a CPP. The measurements of loads acting on a CPP were presented in [Dallinga, 2006] for various sailing conditions and the results will be used here. This chapter however, does not make an attempt to quantify the damage due to fretting motion. The chapter will contribute to safe application and avoidance of fretting in the design of CPP.

On the left side of Figure 3.1 a simplified hydraulic scheme of a CPP is shown. The hydraulic power pack supplies the system with a pressure (p_s) and a flow (Q_s). A proportional valve is governed by the control system and together they control the pitch, larger systems have two proportional valves. An oil distribution (OD) box takes care of the connection between the rotating shaft and the oil supply pipes. A counterbalance valve (CBV) fixes the pitch position in case of an hydraulic power loss and allows depressurization.

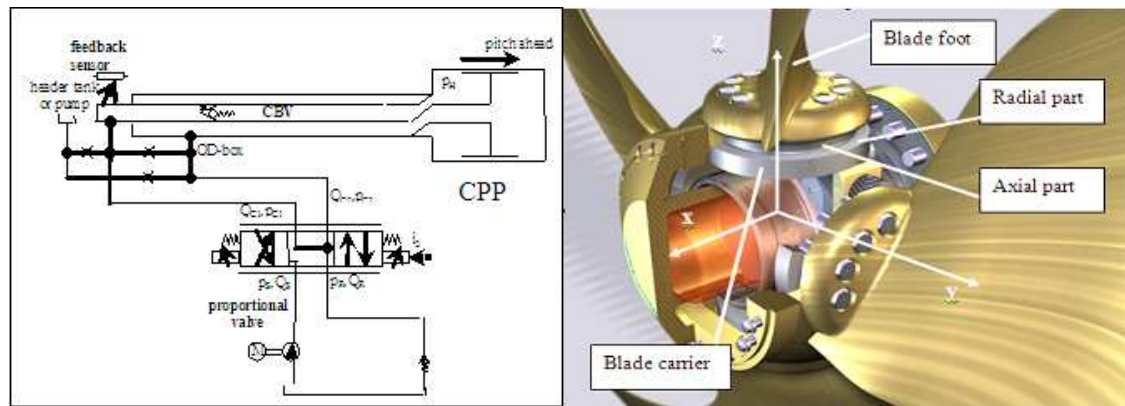


Figure 3.1: Hydraulic scheme of a CPP (left) and its main parts (right). Blade bearing is the bearing that connects the blade foot, blade carrier and hub. Blade bearing has the radial and axial parts. Radial part of blade bearing has the inner side (closer to x axis) and outer side. Source: Wartsila

There are two regimes in which a CPP operates: when the pitch changes (actuating) and when the pitch is constant (non-actuating). When the pitch does not change the proportional valve and CBV are closed. This chapter will investigate only the non-actuating regime.

On the right side of Figure 3.1 the x , y , and z axis are used to describe the forces and moments acting in a blade bearing. It also shows the radial and axial part of the blade bearing. Only a rotation around the z axis will be considered and no elastic deformation around the z axis will be included, so the fretting will be first manifested in the blade bearing. Other components of a CPP might also be affected by fretting (for example the actuating pin) but the motion will start in the blade bearing. The blade foot and the blade carrier are fastened with bolts and no relative displacement between the blade foot and blade carrier will be assumed.

The critical moment for the beginning of fretting motion is when the spindle torque overcomes the friction torque. Since the thrust and torque of a blade are changing during one revolution, the Coulomb friction in the blade bearing changes as well during one revolution. Looking at the Coulomb friction in the blade bearing and spindle torque of the corresponding blade, it is possible to describe the occurrence of fretting motion.

After this introduction, the loads acting in the blade bearing will be described in the second part of this chapter. In the third part of this chapter the fretting coefficient is introduced. There is an ideal theoretical fretting coefficient, however some modification is necessary. This is due to the type of measurements done to investigate the dynamic loads on the propeller in service. The fourth part gives the results for the modified fretting coefficient from measurements. The influence of sea conditions on the fretting coefficient is in the fifth part, which is followed with discussion and conclusions.

3.2. Loads in the blade bearing

There are three more or less external sources of loads (forces) acting on a CPP:

- Hydrodynamic
- Inertial (Centrifugal)
- Hydraulic.

The hydrodynamic forces acting on a blade result in thrust, torque, and spindle torque. The rotation of a propeller will result in centrifugal forces. Gravitation forces acting on a propeller blade are much smaller than the centrifugal force. A hydraulic pressure difference actuates the pitch. If the valves are closed there remains a pressure difference in the CPP; so in this case the hydraulic system creates a non-actuating force. The mechanism of a CPP consists of several parts and the above listed forces will result in reaction forces in the contacts between different parts. These in turn will induce a friction force opposing the motion (or tendency to move) in the contacts and bearings.

In the non-actuating regime the mean spindle torque around the z axis is in equilibrium with the friction forces and the non-actuating hydraulic force. However, variation in hydrodynamic spindle torque can disturb the equilibrium and may cause fretting motion. Friction force, that is opposing the motion, can be “consumed” by the spindle torque and/or hydraulics. Here the best case scenario will be assumed, the motion starts when friction force is completely consumed by the spindle torque. When the hydraulic valves are closed, the non-actuating hydraulic force cannot prevent oscillations around an equilibrium point (it can only give an offset to the oscillations). Once it moves, the amplitude of oscillations is influenced by the friction force, spindle torque and oil compressibility. Also, if it occurs, most of the fretting motion happens within the clearances in the bearings. The change in hydrodynamic forces during one revolution of a blade will have an effect on the forces trying to move the blade (the spindle torque) and on the Coulomb friction. The starting point of fretting motion in a blade bearing is when the spindle torque overcomes friction force.

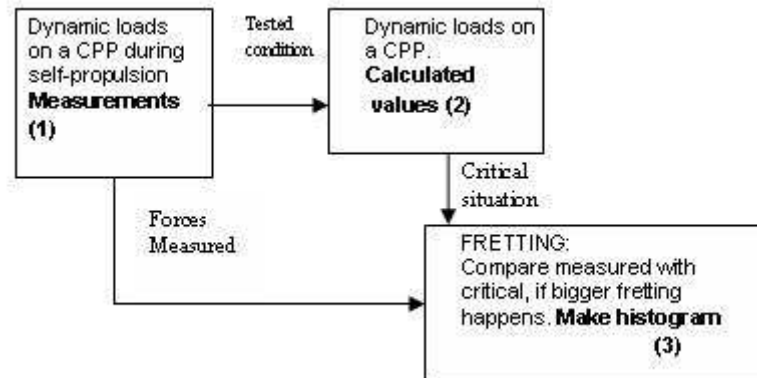


Figure 3.2: Procedure for investigation of fretting in blade bearing during sailing

The critical conditions, necessary for the occurrence of fretting in the blade bearing, are defined by the ratio of spindle torque and friction torque. Investigation of fretting during sailing is done by looking at the measured values of the hydrodynamic forces and the critical condition. The measurements of loads acting on a CPP were presented in [Dallinga, 2006] for various sailing conditions. Figure 3.2 shows the procedure for investigation. Model measurements of hydrodynamic forces for a propeller have been conducted for a single screw vessel sailing in different sea conditions. Measurements include thrust and torque of the propellers and spindle torque of one blade for different ship speeds, sea states, draughts, etc. (Figure 3.2, block 1) on model scale. The critical ratio of hydrodynamic forces leading to fretting will be calculated using a hydrodynamic software tool for each tested condition (Figure 3.2, block 2). The software tool calculates hydrodynamic forces and moments using the boundary element

method. It is possible to calculate friction in the CPP when the hydrodynamic and centrifugal forces are known. A comparison of measured and calculated values (Figure 3.2, block 3) investigates the occurrence of fretting.

3.2.1 Centrifugal loads

Rotation of a propeller creates centrifugal forces of related masses. The centrifugal force is a function of the masses of propeller, blade foot and blade carrier, and further of shaft speed and the position of the centre of gravity with the respect to the shaft and spindle axis. The centrifugal force contributes to a spindle torque and friction torque by an axial and radial force and a bending moment at the blade bearing. Gravity causes a sinusoidal varying force on the blade bearing which is much smaller comparing to the centrifugal force and will be neglected. Figure 3.3 shows centrifugal force stemming from rotation of a propeller. The centrifugal forces and moments are defined as:

$$F_{ce,x} = 0 \quad (3.1)$$

$$F_{ce,y} = 4\rho\pi^2 n^2 \iiint y dx dy dz \quad (3.2)$$

$$F_{ce,z} = 4\rho\pi^2 n^2 \iiint z dx dy dz \quad (3.3)$$

$$M_{ce,x} = 0 \quad (3.4)$$

$$M_{ce,y} = 4\rho\pi^2 n^2 \iiint xz dx dy dz \quad (3.5)$$

$$M_{ce,z} = 4\rho\pi^2 n^2 \iiint xy dx dy dz \quad (3.6)$$

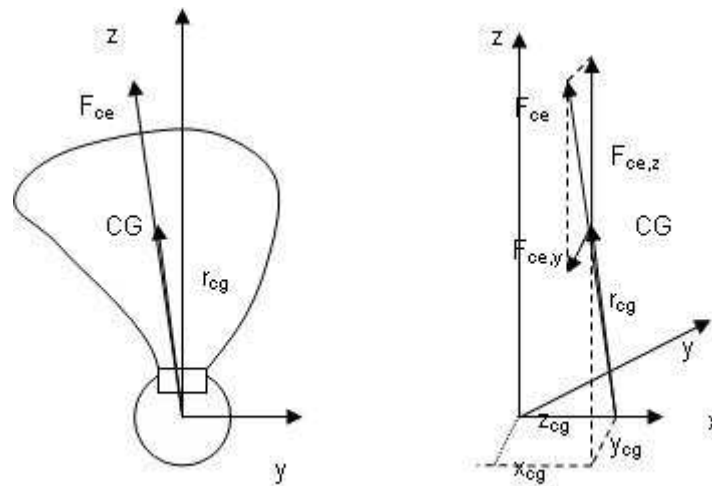


Figure 3.3: Centrifugal force acting on a CPP blade

Centrifugal forces and moments have been calculated for the design condition, and presented in non-dimensional values. The centre of gravity is made dimensionless with the 0.7 radius ($R_{0.7}$). Forces are made dimensionless with $\rho_{sw} n^2 D^4$ where ρ_{sw} is the density of sea water, n is the number of revolutions per second, and D is the diameter of the propeller. Moments are made dimensionless with $\rho_{sw} n^2 D^5$.

-Centre of gravity:

$$[x_{cg}; y_{cg}; z_{cg}] = [0.15; -0.08; 0.75] \quad (3.7)$$

-Centrifugal force:

$$[F_{ce,x}; F_{ce,y}; F_{ce,z}] = [0; -13.5; 131.7] \quad (3.8)$$

-Centrifugal moments:

$$[M_{ce,x}; M_{ce,y}; M_{ce,z}] = [0; -6.2; -3.5] \quad (3.9)$$

3.2.2 Hydrodynamic loads

The pressure field on the blade surface induces a hydrodynamic load on the propeller blade. Different theoretical methods of predicting these loads are presented in [Carlton, 1994]. In order to show their effect on the blade bearing, the hydrodynamic forces will be presented using airfoil theory. However in the following work, the hydrodynamic forces are calculated using a software tool. A propeller blade is divided in different sections, each with its own lift (L_k), drag (D_k) and pitching moment (M_k) around the spindle axis. Thrust (T_k) and torque (Q_k) of the blade's k -th section are determined using the hydrodynamic pitch angle (β) as it is shown in Figure 3.4.

$$T_k = L_k \cdot \cos \beta_k - D_k \cdot \sin \beta_k \quad (3.10)$$

$$Q_k = r_k \cdot D_{k,z} = r_k(L_k \cdot \sin \beta_k + D_k \cdot \cos \beta_k) \quad (3.11)$$

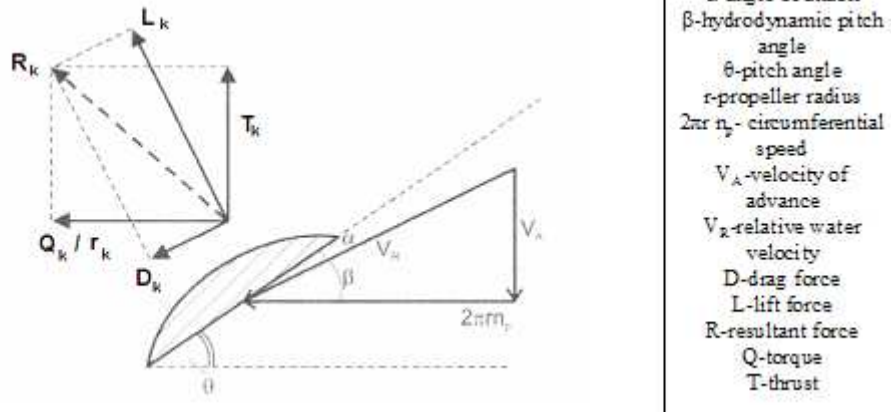


Figure 3.4: Propeller blade section

The resultant lift and drag forces are assumed to act in the hydrodynamic centre (x_{ch} , y_{ch}). Then forces and moments acting on the shaft line (Figure 3.5) are:

$$F_{hd,x} = \sum T_k = T \quad (3.12)$$

$$F_{hd,y} = \sum Q_k / r_k = Q / r \quad (3.13)$$

$$M_{hd,x} = F_{hd,y} \cdot z_{ch} \quad (3.14)$$

$$M_{hd,y} = F_{hd,x} \cdot z_{ch} \quad (3.15)$$

$$M_{hd,z} = F_{hd,x} \cdot y_{ch} + F_{hd,y} \cdot x_{ch} \quad (3.16)$$

The sum of all forces in the x direction will result in a total thrust (T) and the sum of all forces in the y direction will result in tangential force (Q/r). The hydrodynamic spindle torque ($M_{hd,z}$) and bending moments $M_{hd,x}$, $M_{hd,y}$ are resulting torques of the hydrodynamic forces acting around the x , y and z axis.

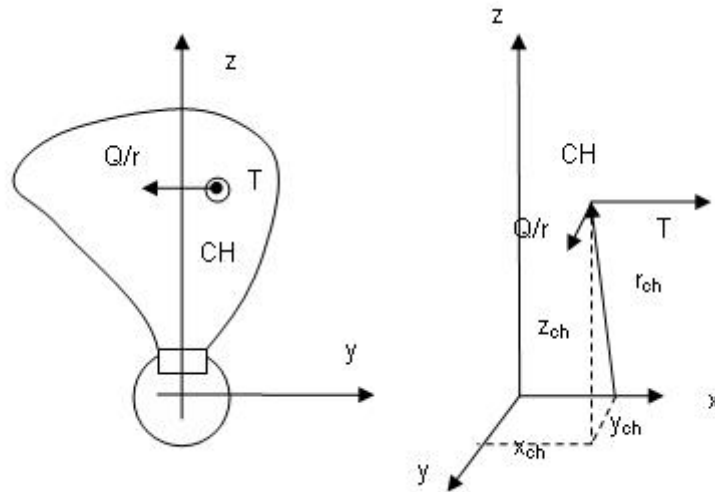


Figure 3.5: Hydrodynamic forces acting on the hydrodynamic centre (CH) of a CPP blade

The hydrodynamic forces on the blade induce forces, bending moments and a spindle torque at the blade bearing. The thrust and torque will act on the axial part of blade bearing ($F_{hd,x}$, $F_{hd,y}$), while the bending moments ($M_{hd,x}$, $M_{hd,y}$) will affect the radial part of the bearing (see Figure 2.5).

During one revolution, the hydrodynamic forces will change due to the change in the wakefield of a propeller, Figure 3.6 shows the investigated nominal wakefield. The angle of attack (α in Figure 3.4) will change as the blade rotates through the wakefield causing oscillations of thrust and torque. Oscillations of thrust and torque of a single blade are rpm dependent and oscillations of thrust and torque of the entire propeller are dependent on the number of blades times the rpm.

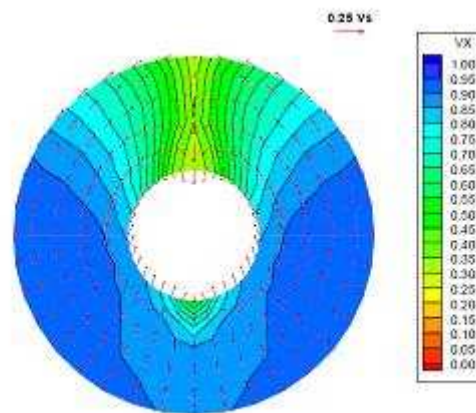


Figure 3.6: Nominal wake for investigated propeller Source: Wartsila internal report

As mentioned before, Equations (3.10)-(3.16) are used to illustrate effects of hydrodynamic forces on the blade bearing. In following analysis a software tool will be used to calculate the forces and moments acting on a blade. Theoretical and computational tools allow the investigation of conventional and unconventional propellers in realistic working conditions. Two methods, vortex-lattice method and boundary element method, have been in the focus of numerous investigations. The overview of the development of numerical design and analysis methods for propulsors is given in [Meshabi, 2005]. Figure 3.7 shows the comparison of three different methods with the measured value of the dimensionless spindle torque around the z axis.

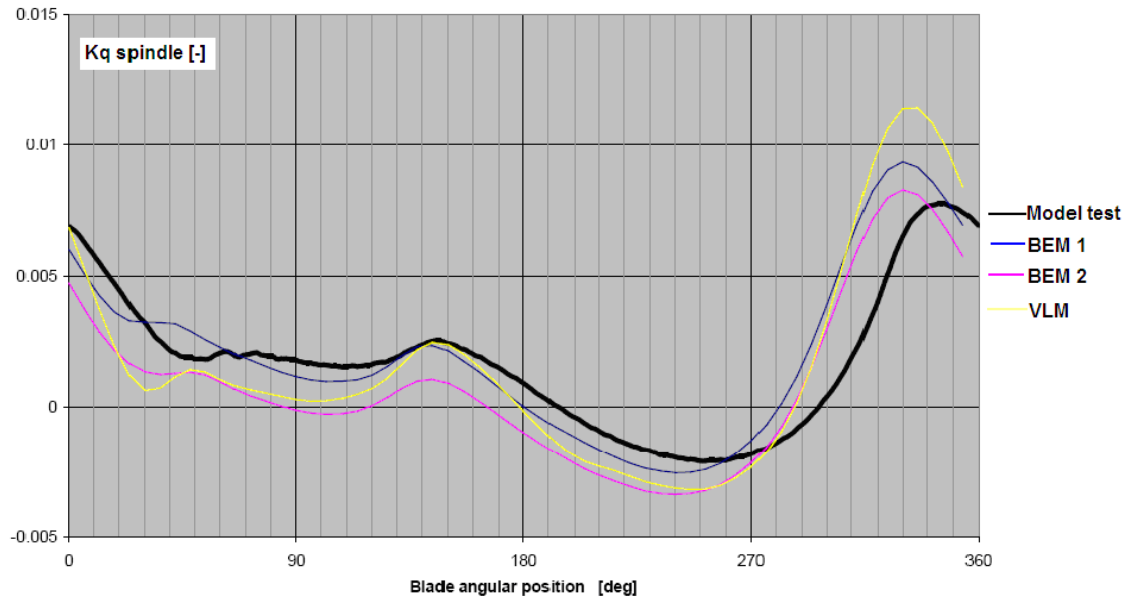


Figure 3.7: Comparison of calculated blade spindle torque with the measurements for design conditions
Source: Wartsila internal report

Three methods have been compared (Figure 3.7): an unsteady panel code 1 (or BEM 1), an unsteady panel code 2 (or BEM 2), and an unsteady vortex lattice method (or VLM). In this analysis BEM2 will be used; it is a practical method to examine a lot of different cases and it gives a good correlation with the measured results. Moreover, estimated maximal values match with the measured values. The BEM2 uses a panel method, sometimes also called boundary element method and it is based on potential flow theory. The forces follow from integration of pressure over the blade surface together with some empirical expressions for friction shear stress on the blade. Mean values of the hydrodynamic loads are also presented in the same way as the non dimensional centrifugal loads. The BEM2 predicts a small force in the z direction; this could be the result of the rake of the blade.

$$F_{hd,x}; F_{hd,y}; F_{hd,z} = [-72.8 \quad 44.2 \quad 7] \quad (3.17)$$

$$M_{hd,x}; M_{hd,y}; M_{hd,z} = [15.2 \quad 24.4 \quad 1.9] \quad (3.18)$$

3.2.3 Friction forces in the blade bearing

The blade bearing supports the propeller blade in the axial and radial direction. Here the friction forces will be derived for each part separately. The resulting force (F_{rad}) and

bending moments ($M_{rad,x}$, $M_{rad,y}$) in the radial part of blade bearing can be found by considering the force and moment equilibrium:

$$\sum F_z = 0 \Rightarrow F_{ce,z} + F_{rad} + F_{hd,z} = 0 \Rightarrow F_{rad} = -F_{ce,z} - F_{hd,z} \quad (3.19)$$

$$\sum M_x = 0 \Rightarrow M_{hd,x} + M_{rad,x} = 0 \Rightarrow M_{rad,x} = -M_{hd,x} \quad (3.20)$$

$$\sum M_y = 0 \Rightarrow M_{hd,y} + M_{ce,y} - M_{rad,y} = 0 \Rightarrow M_{rad,y} = M_{hd,y} + M_{ce,y} \quad (3.21)$$

The resulting moment M_{rad} in the radial part of the blade bearing is determined with:

$$M_{rad} = \sqrt{M_{rad,x}^2 + M_{rad,y}^2} \quad (3.22)$$

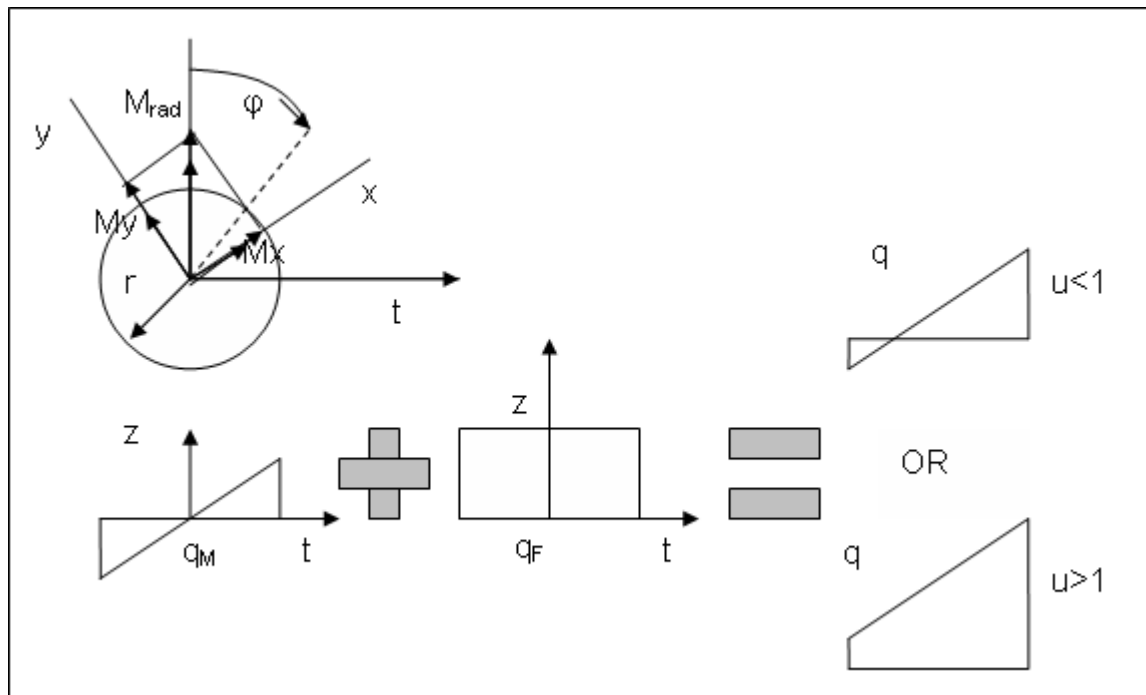


Figure 3.8: Distribution of bending moments and centrifugal force over radial part of blade bearing

The radial force (F_{rad}) will be uniformly distributed (q_F) while the reaction of the resulting moment will be non-uniformly distributed (q_M) around the blade bearing. The sum of these two load distributions will result in a total load distribution (q), shown in Figure 3.8. The distributed load around the radial part can be written as a function of angle ϕ :

$$q = q_F + q_M = \frac{F_{rad}}{2\pi r} + \frac{2M_{rad} \sin\phi}{r \cdot 2\pi r} \quad (3.23)$$

where r is a radius of blade bearing. Tangential friction force ($F_{fr,rad}$) on a radial part can be written as:

$$F_{fr,rad} = \int \mu \cdot q \cdot r \cdot d\phi \quad (3.24)$$

The value of friction coefficient μ is 0.1, more about the friction coefficient of a blade bearing can be found in Chapter 4.3. The total friction torque can be written as:

$$Q_{fr,rad} = r \cdot F_{fr,rad} = r \cdot \int_0^{2\pi} \mu \cdot q \cdot r \cdot d\phi \quad (3.25)$$

The final equation for the total friction torque in radial part of the blade bearing will depend on the value for u , where u is a coefficient that describes the ratio of the radial force and the maximum force ($2M_{rad}/r$) resulting from the bending moment (see Figure 3.8):

$$u = \frac{F_{rad} r}{2M_{rad}} \quad u = \begin{cases} > 1 \text{ if } q_F > \max(q_M) \\ < 1 \text{ if } q_F < \max(q_M) \end{cases} \quad (3.26)$$

The radial part of a blade bearing has two sides, one side (inner side) is closer to the shaft line and other side (outer side) is closer to the sea. Figure 3.8 shows two possible load distributions over the radial part of a blade bearing. If the load caused by the radial force (F_{rad}) is higher than the load caused by the bending moment (M_{rad}), then only the inner side will be loaded. The total friction torque in that case will be:

$$Q_{fr,rad} = r \cdot \int_0^{2\pi} \mu \cdot q \cdot r \cdot d\phi = r \cdot \mu \cdot F_{rad} \quad \text{for } u > 1 \quad (3.27)$$

Opposite to this, both sides will be loaded if the maximum load caused by the bending moment is higher than the load caused by the radial force. The total friction torque in the radial part of the blade bearing is the sum of friction torques in the inner and outer part of a radial blade bearing. The angle ϕ_0 where the load (q) equals zero is:

$$\frac{F_{rad}}{2\pi r} + \frac{2M_{rad} \sin\phi_0}{2\pi r^2} = 0 \Rightarrow \phi_0 = -\arcsin\left(\frac{F_{rad} r}{2M_{rad}}\right) = -\arcsin(u) \quad (3.28)$$

The friction torque can be found by integrating:

$$Q_{fr,rad} = -2\mu r^2 \int_{-\pi/2}^{\phi_0} q d\phi + 2\mu r^2 \int_{\phi_0}^{\pi/2} q d\phi \quad (3.29)$$

Substituting q from Equation (3.23) in Equation (3.29) and integrating gives:

$$Q_{fr,rad} = \frac{4}{\pi} \cdot \mu \cdot M_{rad} (\cos\phi_0 + u \cdot \arcsin(u)) \quad (3.30)$$

or:

$$Q_{fr,rad} = \frac{4}{\pi} \cdot \mu \cdot M_{rad} (\sqrt{1-u^2} + u \cdot \arcsin(u)) \quad \text{for } u < 1 \quad (3.31)$$

The friction in the axial part of the blade bearing depends on the resultant force of all forces in the axial direction:

$$F_{ax} = \sqrt{F_{ax,x}^2 + F_{ax,y}^2} \quad (3.32)$$

$$\sum F_x = 0 \Rightarrow F_{hd,x} - F_{ax,x} \Rightarrow F_{ax,x} = F_{hd,x} \quad (3.33)$$

$$\sum F_y = 0 \Rightarrow F_{hd,y} + F_{ce,y} - F_{ax,y} = 0 \Rightarrow F_{ax,y} = F_{hd,y} + F_{ce,y} \quad (3.34)$$

The resultant torque in the axial bearing is the torque around the z (spindle) axis of a blade:

$$\sum M_z = M_{hd,z} + M_{ce,z} - Q_{fr,rad} - Q_{fr,ax} = M_{sp} - Q_{fr} \quad (3.35)$$

The total friction torque in the axial part of the blade bearing can be calculated according to [Faraz, 2001]. The contact situation for the axial part of the blade bearing is the same as for the revolute joint (Figure 3.9); there is only one degree of freedom. Contact between blade carrier and hub is considered to be elastic and an approximate model to predict the friction force is made based on an elliptic load distribution over the contact surface. The authors of [Faraz, 2001] report that the equilibrium equation cannot be solved analytically since it is an elliptic integral. They use a series expansion and curve fitting to ensure less than 1% deviation. The final expression for the friction torque in the axial part of the blade bearing is:

$$Q_{fr,ax} = F_{ax} \cdot r' (1 + 0.0477 \sin^2 \alpha + 0.5744 \sin^4 \alpha - 1.051 \sin^6 \alpha + 0.6982 \sin^8 \alpha) \cdot \frac{\mu}{\sqrt{1 + \mu^2}} \quad (3.36)$$

$$\alpha = \arcsin \left(\sqrt{\frac{2.31 F_{ax}}{E b \sqrt{1 + \mu^2}} \cdot \frac{r' / r''}{r' - r''}} \right) \quad (3.37)$$

- E- Young's modulus of elasticity [N/mm²]
- b- Thickness of blade bearing [m]
- r' - radius of blade bearing [m]
- r'' - radius of blade carrier [m]

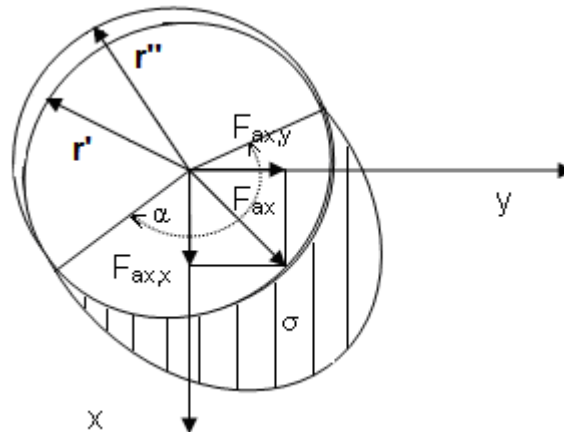


Figure 3.9: Contact situation in axial part of blade bearing (the clearance is exaggerated for illustration purpose)

Although a comparison is difficult in general friction torque will be higher if only one side of the radial bearing is loaded ($u > 1$). Also the stresses in the bearing would be higher. A lower friction force is advantageous for lower hydraulic pressures. On the other hand, when the load is distributed to both sides it will result in a region of very low friction force in the blade bearing. This low friction zone will be exposed to partial sliding (micro-movement in the part of the contact). The usual design practice is to make hydrodynamic and centrifugal spindle torque such that the mean value of their sum is close to zero. Also, the load distribution factor (u) is smaller than one in usual design practice. This ensures lower actuating hydraulic pressures. It means that by careful design one can change the properties of a CPP. For example a more stiff and rigid design will be more resistant to disturbances from the sea but on the other hand it will be more difficult to change pitch (hence, a bigger hydraulic power pack, a stronger hub, a rise in costs, etc). The other approach could be to make a more flexible CPP, for example when the mean value for spindle torque is made zero. This type of CPP is easier to move, has a smaller power pack, requires less hub strength, but has a bigger potential risk of causing vibrations and fretting.

3.2.4 Hydraulic actuating loads

The loads created by the hydraulic system during pitch actuation are called actuating loads. There are several mechanical solutions how to change the pitch. The illustration of actuating loads will be made only for the design that applies to the investigated case. This design is contemporary and most of modern CPPs have it. For other solutions reader is referred to [Beek, 1976].

Figure 3.10 shows a blade carrier in a blade bearing. The actuating pin is part of the blade carrier and it is placed in the sliding block which is placed in the slot of a yoke. The yoke is hydraulically moved in linear direction. Thanks to the pin's eccentricity (e) the linear motion of the yoke is converted into the pitch rotation.

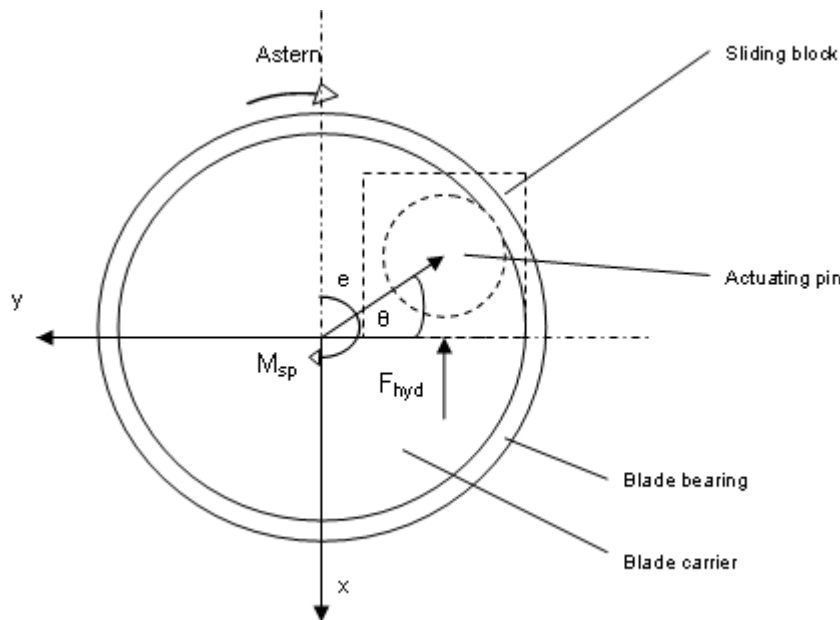


Figure 3.10: hydraulic force actuating pitch towards ahead

Figure 3.10 shows the situation when a hydraulic force (F_{hyd}) is moving the pitch (θ) ahead during free sailing ahead. The hydraulic force creates a hydraulic moment (M_{hyd}):

$$M_{hyd} = F_{hyd} \cdot e \cdot \cos \theta \quad (3.38)$$

The moment created by the hydraulic force is opposed by the spindle torque and friction. When actuating pitch ahead, the sum of moments around the z axis for one blade is:

$$\sum M_z = M_{sp} + Q_{fr} - M_{hyd} \quad (3.39)$$

The spindle torque and friction change during rotation of the blade. The sum of spindle torques for all blades is the sum of four (number of blades) signals with 90 degrees phase difference and as such is almost equal to the sum of four mean values. The same principle applies to friction torque. The total hydraulic force (F_{hyd}^{cpp}) needed to change the pitch is equal to the sum of the mean spindle torque and friction times the number of blades (Z), in this case $Z = 4$, plus friction force in other parts of a CPP (F_{fr}^{other}) such as pin-slot, yoke-hub and other contacts.

$$F_{hyd}^{cpp} = \frac{Z \cdot (\overline{M}_{sp} + \overline{Q}_{fr})}{e \cdot \cos \theta} + F_{fr}^{other} \quad (3.40)$$

The total hydraulic pressure (p_{hyd}) depends on the yoke's area (A_{yoke}) and it is increased by an additional back pressure (p_{cbv}) needed to open the counter balance valve (CBV).

$$p_{hyd} = \frac{F_{hyd}^{cpp}}{A_{yoke}} + p_{cbv} \quad (3.41)$$

Figure 3.11 shows the total hydraulic pressure as a function of pitch position for free sailing ahead for pitch values close to design pitch. The upper line represents the pressure needed to change the pitch to ahead and the lower line to astern. The middle line represents the sum of four mean spindle torque values. This pressure is a holding (non-actuating pressure), it is a reaction to spindle torques, and it can have any value between upper and lower line.

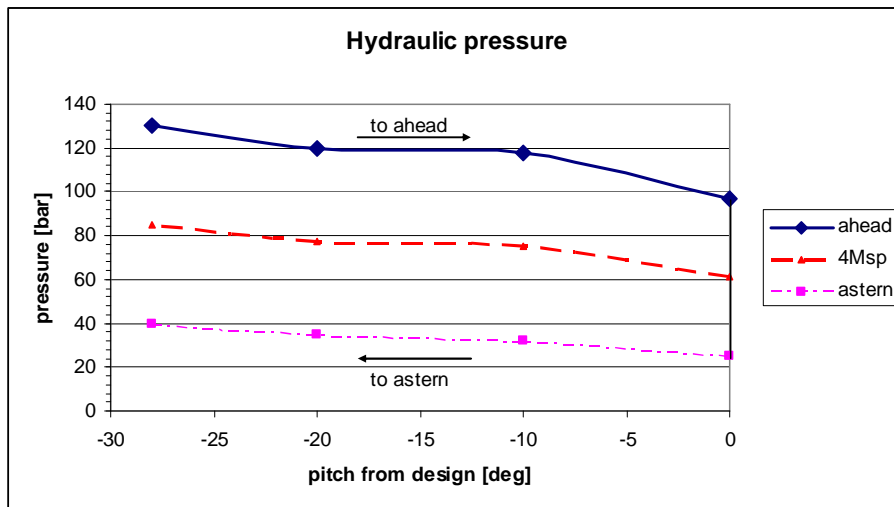


Figure 3.11: Hydraulic pressure needed to actuate pitch assuming the constant and maximal rpm

3.3. Fretting coefficient

This investigation considers the non-actuating regime and the aim is to define the conditions leading to fretting motion in the blade bearing during service. Fretting motion, just as any other motion, starts when the sum of forces trying to move the body overcomes the friction force. Moreover, the broader definition of fretting includes also pre-sliding regime (micro movement in the contact prior to the real sliding). More about fretting can be found in Chapter 2 of this thesis but general characteristics of fretting motion involve pre-sliding, small amplitude sliding (up to 1 mm), and frequent reciprocating (back and forth) motion. In this paragraph the critical moment for the start of fretting motion is described by introducing a new coefficient.

3.3.1 Theoretical fretting coefficient

As mentioned in the Chapter 3.2 of this document, the hydraulic system has very limited influence on the pitch oscillations around the equilibrium point in the non-actuating regime. In contrast to Equation (3.39), the fretting motion starts when the spindle torque overcomes the friction and hydraulic torque. In equilibrium point (point when the sum of forces is zero) around the z axis:

$$\sum M_z = M_{sp} - Q_{fr} - M_{hyd} = 0 \quad (3.42)$$

Where M_{hyd} is the moment around the z axis created by the hydraulic system, or as previously defined by the non-actuating hydraulic force. Motion starts when the sum of forces trying to move the body overcomes the friction force:

$$\sum M_z > 0 \Rightarrow M_{sp} - M_{hyd} > Q_{fr} \quad (3.43)$$

It will be assumed $M_{hyd} = 0$; therefore motion starts when:

$$M_{sp} > Q_{fr} \quad (3.44)$$

Most of the motion will happen within the clearance of the bearing and fretting motion will happen when the blade spindle torque becomes higher than the friction torque. Of course it could be argued that M_{hyd} can reduce the spindle torque. However, it should be kept in mind that the spindle torque has a negative part during one revolution as well (Figure 3.7). Then spindle torque would not be able to move the blade in positive direction but it would be much easier (smaller oscillation is needed) to move it in the negative direction. Figure 3.12 shows a hypothetical case of spindle torque (dash-dot line), Coulomb friction torque (two symmetrical lines around zero) and hydraulic torque (flat dash line) in one blade bearing during one revolution of a shaft. The marked line in Figure 3.12 is the difference of the hydraulic and spindle torque. The Coulomb friction in the bearing represents a threshold for fretting motion, if the forces trying to move the blade are lower than the limiting friction force than there is no motion. It can be seen, the line representing the difference of spindle and hydraulic torque gets above the threshold value and causes fretting motion in the region 216 to 264 degrees rotation of the shaft. On the other hand if M_{hyd} is zero, no fretting motion would occur. However, if the spindle torque variations increase somewhat, than the influence of M_{hyd} (and assumption $M_{hyd}=0$) very much determine the occurrence of fretting, for instance

whether fretting occurs at one or both sides (i.e. for positive and/or negative spindle torque). If the spindle torque oscillations increase drastically than fretting motion will occur on both sides and the total fretting time is hardly dependant on M_{hyd} . So the assumption of $M_{hyd}=0$ seems reasonable, although an assumption of M_{hyd} equal to the mean value of M_{sp} would be equally right. In fact, in “real life” the value of M_{hyd} can have any value between upper and lower threshold value due to internal leakage, pressure adjustment, control strategies, etc. Chapter 4.7.1 will look into this matter in more details.

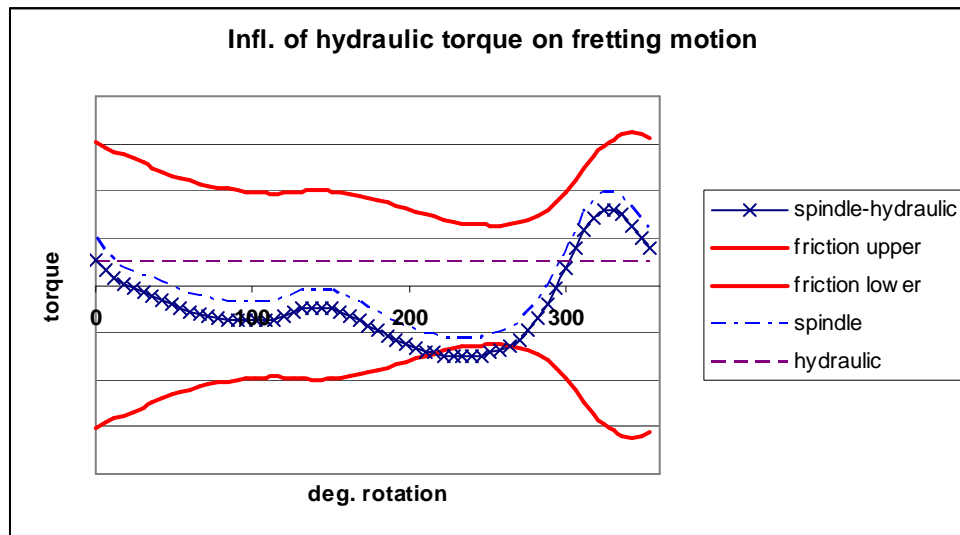


Figure 3.12: Spindle torque, Coulomb friction and hydraulic torque in a blade bearing

In order to investigate the fretting motion in a CPP, the relation between friction torque and spindle torque will be examined during one revolution. Parameters that will change during one revolution are the parameters that are influenced by the hydrodynamic forces. Thus, the hydrodynamic spindle torque and both components (axial and radial) of friction torque will change while the centrifugal spindle torque is constant (rotational speed is assumed constant).

Apart from the hydrodynamic and centrifugal force, the total friction force will be also influenced by the design characteristics such as radius of the blade bearing (r), the friction coefficient (μ) and material properties. Therefore, the fretting motion in a blade bearing (of one single blade) during its revolution can be described as a function of the hydrodynamic, operational and design conditions:

$$\text{Fretting} = f(T_{blade}, Q_{blade}, M_{sp}, r, \mu, \text{material}, rpm, m) \quad (3.45)$$

Ideally, fretting motion could be determined by the ratio of spindle torque and friction torque in the blade bearing: if the ratio is larger than unity there is motion. Now defining a fretting coefficient (k_{fret}) as the ratio of the spindle torque of one blade and the total friction torque of the corresponding blade bearing:

$$k_{fret} \stackrel{\text{def}}{=} \frac{M_{sp}}{Q_{fr}} \quad (3.46)$$

The oscillation of a spindle torque is caused by the variation of hydrodynamic forces in the wakefield of a propeller. In real service conditions these variations can be different from the variations expected in the design case (no waves). Following analysis starts from the design case and continues with the investigation of results made in self-propulsion tests in different sea conditions.

3.3.2 Fretting coefficient in the design case

If the aim of this chapter would be to analyze only the theoretical aspects of fretting, than the analysis of fretting coefficient would end here. To illustrate the fretting coefficient defined in Equation (3.46), Figure 3.13 shows the total friction torque in the blade bearing and the spindle torque of one blade during one revolution. Blade spindle torque follows from BEM2 calculations and friction torque has been calculated according to Equations (3.19-3.37). In order to get a somewhat clearer overview of the situation, Figure 3.14 shows the friction torque multiplied with the sign of the spindle torque. This is done to show the regions where spindle torque exceeds friction torque in the blade bearing: those regions are marked as fretting regions.

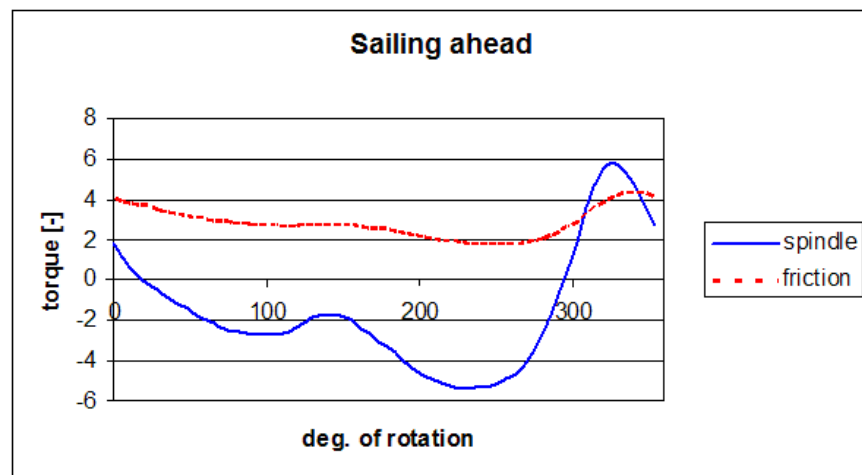


Figure 3.13: Spindle and friction torque for sailing ahead condition

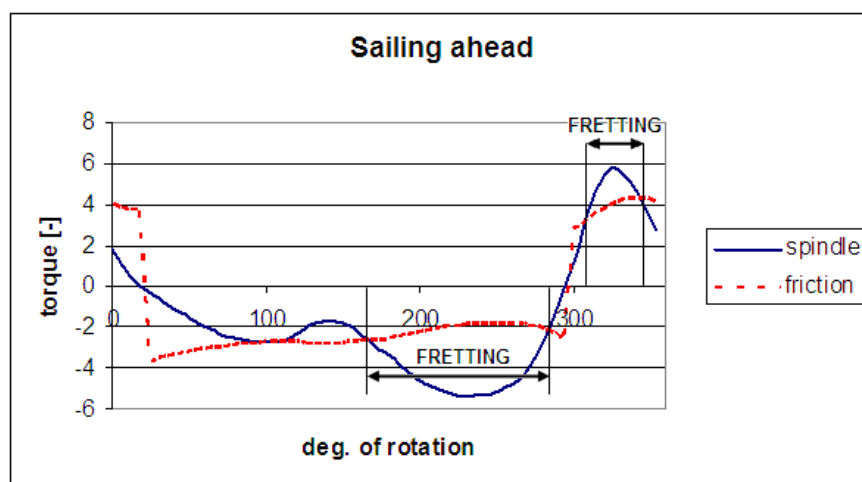


Figure 3.14: Spindle torque and friction torque multiplied with sign (M_{sp})

Looking at the Figure 3.14 it is possible to determine the angle of rotation at which the spindle torque exceeds the friction torque. The spindle torque is larger than the friction torque between 174 and 282 degrees, and between 310 and 344 degrees of rotation. For

the investigated propeller, fretting motion could be expected to happen within these angles in design conditions. Extreme values of the fretting coefficient are -2.98 at 246 degrees and 1.44 at 324 degrees of rotation.

3.3.3 Approximation of friction

Measurements that will be used in this investigation contain (only) the values of the total thrust and total torque of the propeller instead of preferred values of thrust and torque for a single blade. Thus the loads needed to calculate the friction torque in a single blade bearing were not known. This made it practically impossible to find out the exact friction torque and to use the fretting coefficient as defined in Equation (3.46). It is difficult but not necessary to know all parameters to find the change in friction torque during one revolution. During one revolution it is assumed that only hydrodynamic forces can influence the change in friction (i.e. centrifugal forces are constant). So when the friction torque is calculated, the change in friction torque can be estimated by the measured change in thrust and/or torque. In order to investigate the fretting motion in service conditions, some solution for friction torque is necessary.

An assessment of fretting motion in service conditions can be made based on the relation of measured spindle torque of a single blade and measured total thrust and/or torque. To find which of three parameters: total thrust (T), total torque (Q) or resultant total force (R_k in Figure 3.4) can correlate the best with the calculated friction (Q_{fr}), three parameters are defined as:

$$\begin{aligned} \text{-the total thrust and friction torque} \quad a &= \frac{T \cdot R_{0.7}}{Q_{fr}} \\ \text{-the total torque and friction torque} \quad b &= \frac{Q}{Q_{fr}} \\ \text{-the sum of total thrust and torque and friction} \quad c &= \frac{\sqrt{T^2 R_{0.7}^2 + Q^2}}{Q_{fr}} \end{aligned}$$

The selection should be made based on the smallest difference between the average and the maximal values of coefficients a , b , and c during one revolution. The ideal coefficient would have the constant value. Figure 3.15 shows the coefficients a , b , and c during one revolution. Table 3.1 shows the average and maximal values of a , b , and c . The maximal values are presented in relative manner as the percentage of their average values. As it can be seen, there is no big difference among these three coefficients.

Table 3.1: Average and maximal values of coefficients a , b , and c

Coefficients	Average [-]	Maximal [% avg]
a	60.07	156.4
b	35.67	155.5
c	69.86	156.2

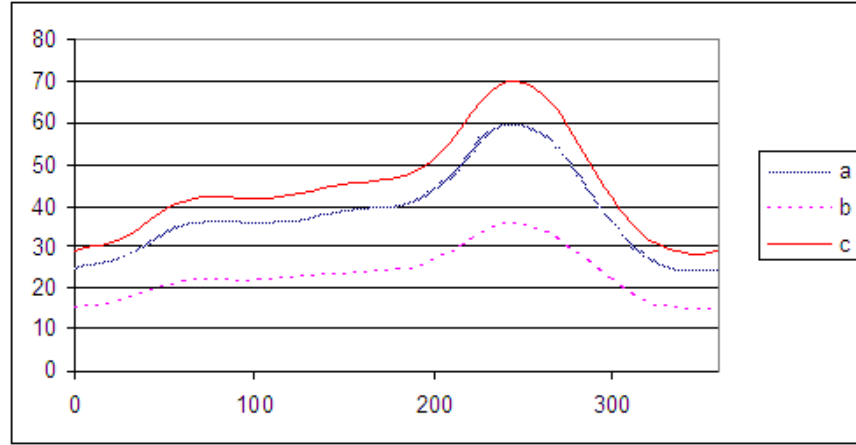


Figure 3.15: Coefficients a, b, and c during one revolution

Looking at Figure 3.15 it seems that none of the proposed parameters can describe the friction torque in the blade bearing in a satisfying manner. It is obvious that the measurements of forces per blade are necessary for a real quantitative analysis. Nevertheless, the ratio of the spindle torque and total thrust can give a first estimate whether the hydrodynamic forces will rotate the blade around its z axis. Thrust has been chosen because the values in Equations (3.17) and (3.18) indicate bigger loads in the bearing to be caused by the hydrodynamic forces acting in the direction of the x axis. As it will be shown, this ratio and its distribution are influenced by the sea conditions. The authors will show that in some situations hydrodynamic forces acting on a blade can have a less favourable distribution causing more fretting motion (and other way around).

3.3.4 Fretting coefficient for test cases

In the following investigation the ratio of thrust and spindle torque will be used to get an assessment of fretting motion in the blade bearing during service. The fretting coefficient has been defined in Equation (3.46) but it will be changed to:

$$f_{\text{fret}} = \frac{Z \cdot M_{\text{sp}}}{T \cdot R_{0.7}} \quad (3.47)$$

Since the thrust belongs to the entire propeller, the spindle torque of one blade (M_{sp}) is multiplied with the number of blades ($Z=4$ in this case). And in order to keep the dimensionless form, the thrust is multiplied with the 0.7 radius of the blade ($R_{0.7}$).

As a transition from the theoretical aspects of fretting in a blade bearing to fretting in a real service condition, an analysis of design conditions will be made here. The propeller that is investigated is a CP propeller on a single screw ship. The calculation of forces and moments acting on the blade bearing is done using software tools and the calculation of the friction force is done according to Equations (3.19-3.37). Figure 3.16 shows the fretting coefficient as defined in Equation (3.47) for the design conditions. The critical values of the fretting coefficient are the values at which the spindle torque overcomes the friction torque. Looking back at Figure 3.14, the critical values of fretting coefficient are the values at 174 and 310 degrees:

$$\begin{aligned}
- \quad f_{fret_critical} &= \frac{4M_{sp}}{T \cdot R_{0.7}} = 0.13 \text{ for positive spindle torque} \\
- \quad -f_{fret_critical} &= \frac{4M_{sp}}{T \cdot R_{0.7}} = -0.11 \text{ for negative spindle torque}
\end{aligned}
\tag{3.48}$$

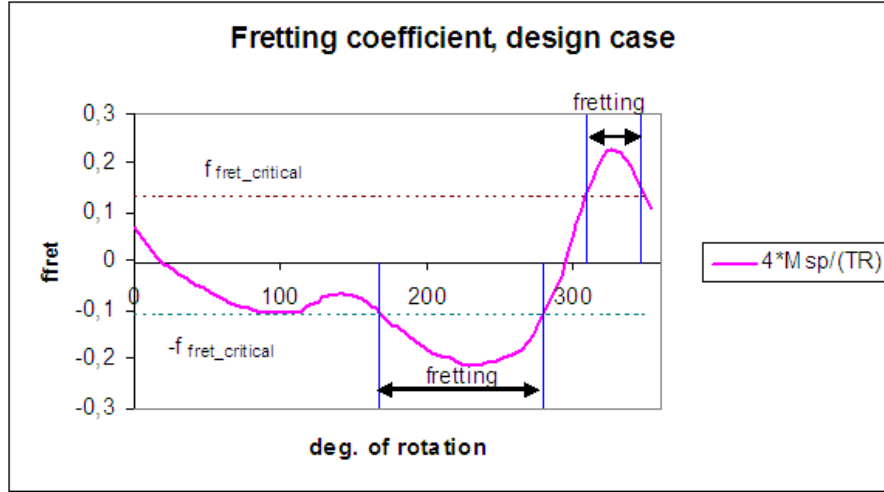


Figure 3.16: Fretting coefficient for design conditions

To demonstrate the accuracy of the approximation, also the thrust per blade (which in this case is from BEM2 calculation) is used to determine the fretting coefficient. Replacing the total thrust (T) in Equation (3.47) with the thrust of one blade (T_{blade}), the fretting coefficient will be:

$$f_{frett_b} = \frac{M_{sp}}{T_{blade} R_{0.7}} \tag{3.49}$$

Figure 3.17 shows the coefficient f_{frett_b} during one revolution of the blade and the critical value is ± 0.115 . There is a satisfying match between this value and the value in Equation (3.48).

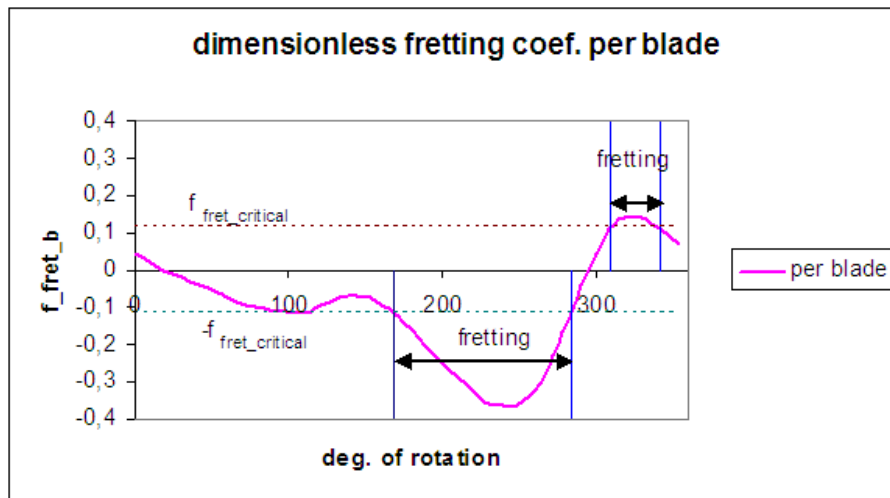


Figure 3.17: Fretting coefficient per blade

3.4. Test Cases

Here an attempt will be made to make a connection between fretting and a sea condition using the available self-propulsion tests in irregular seas. The fretting coefficient calculated from the ratio of measured spindle torque per blade and total thrust measured (f_{fret} in Equation (3.47)) will be compared with the critical (theoretical) fretting limit ($f_{fret_critical}$ in Equation (3.48)). The value of fretting coefficient will be calculated for maximum (positive and negative) values of blade spindle torque per each blade rotation. Afterwards, a distribution of maximal fretting coefficient will be made. It is reasoned that fretting occurs if the absolute value of maximal fretting coefficient is greater than the corresponding critical value. More about the course of action can be found in Figure 3.2. A review of the main parameters of self-propulsion tests in irregular seas and the tested conditions can be found in Table 3.3 and Appendix A. The goal is to expand formula in Equation (3.45) to:

$$\text{Fretting} = f(T, Q, M_{sb}, rpm, d, \mu, \text{material}, \text{sea state}) \quad (3.50)$$

Analysis will be completely shown only for two cases; the rest of the cases will be presented in table form. These two cases have been selected in order to illustrate the procedure when fretting is expected and when fretting is not expected.

3.4.1 Example 1

In this test the ship speed was 24.4 knots and the shaft speed 111 rpm. For these conditions the calculated values for spindle torque and friction torque in the blade bearing are shown in Figure 3.18.

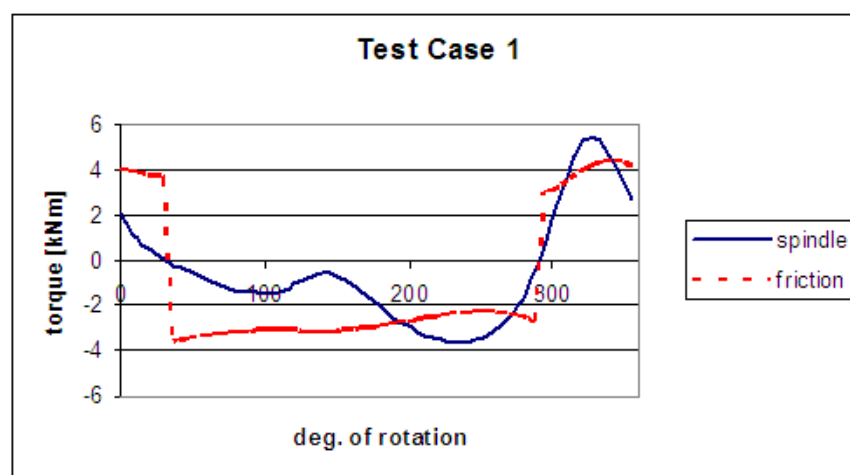


Figure 3.18: Calculated spindle torque and friction torque for Test Case 1

Figure 3.19 shows the fretting coefficient for Test Case 1; the critical values of fretting coefficient are the values at 192 and 308 degrees and it appears the limit has changed somewhat:

$$\begin{aligned} - f_{fret_critical} &= \frac{4M_{sp}}{T \cdot R_{0.7}} = 0.14 \text{ for positive spindle torque} \\ - f_{fret_critical} &= \frac{4M_{sp}}{T \cdot R_{0.7}} = -0.095 \text{ for negative spindle torque} \end{aligned} \quad (3.51)$$

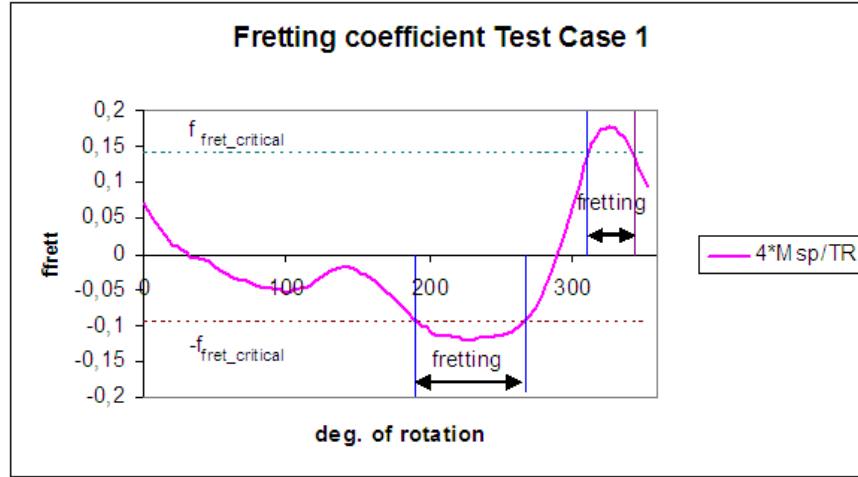


Figure 3.19: fretting coefficient for Test Case 1

This test was done in irregular seas with waves heading from 180 deg, a peak period of 7.6 seconds and a significant wave height of 2.9 meters. All results are given as scaled values for real ship. Figure 3.20 shows the measured (dimensionless) thrust and spindle torque for Test Case 1 in the first 50 seconds. Using Equation (3.47), the fretting coefficient has been calculated for each revolution of the propeller at extreme values (positive and negative) of spindle torque. Figure 3.21 shows their distribution in Test Case 1. The dash line in Figure 3.21 marks the critical value of fretting coefficient from Equation (3.51) and the border of the fretting danger region. For negative spindle torque, the danger of fretting motion exists if the value of the fretting coefficient is smaller than the critical value, and vice versa for positive spindle torque.

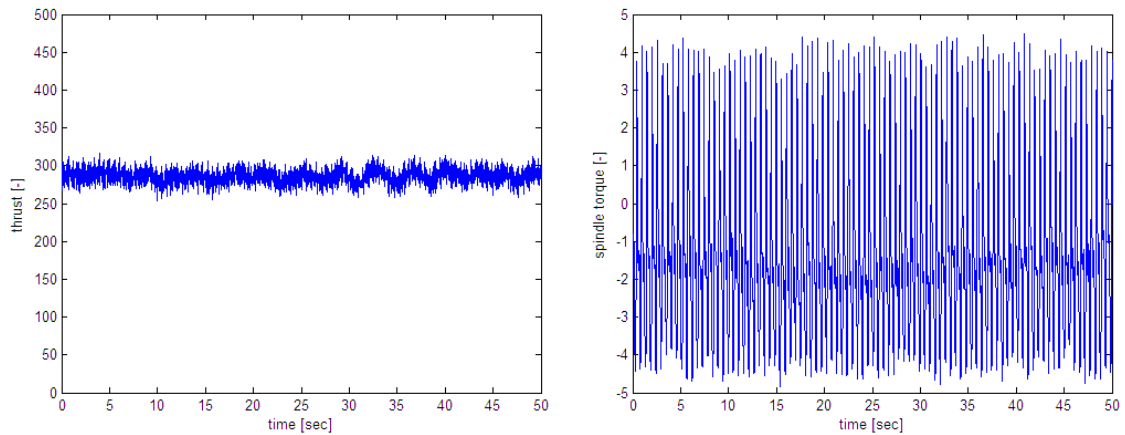


Figure 3.20: Measured thrust (left) and spindle torque (right) in Test Case 1

The fit curve (Figure 3.21) was made in *MatLab* environment using the generalized extreme value distribution. Similar to extreme value distribution, this distribution is used to model the large sets of maximum and minimum values of the measured parameter. Other option was to use the lognormal distribution but this was possible only for the positive values. Since measurement was made for roughly 760 cycles it follows that fretting happened in each cycle. The fretting coefficient for negative spindle torque is always smaller than -0.095 and for positive (almost) always larger than 0.14.

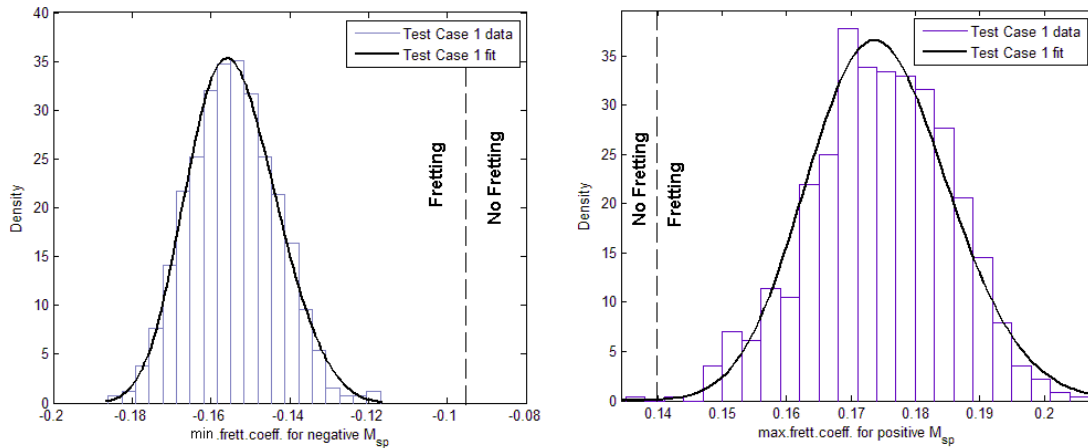


Figure 3.21: distribution of measured fretting coefficient for negative (left) and positive (right) spindle torque; dash line is the fretting border. Both fit curves are in the fretting zone

Table 3.2: Conditions and results of Test Case 1

Test Case	Wave head	Wave height	Speed [kn]	rpm	Fretting predicted	Fretting measured	Critical $f_{x,z}$
1	180	2.90	24.4	111	Yes	100%	-0.095; 0.140

The fit curve on Figure 3.21 can easily be plotted as a cumulative probability function to see the percentage of fretting measured. Table 3.2 shows the conditions in Test Case 1 and results of previous analysis: the fretting motion is predicted as on Figure 3.18, during measurements fretting coefficient exceeded the critical values (-0.095, 0.140) in all cycles (fretting measured almost 100%).

3.4.2 Example 2

The investigation of Test Case 3 will be shown to illustrate the case when fretting motion was not predicted but the measured values of thrust and spindle torque indicate fretting motion. In this test the ship speed was 19.8 knots and the shaft speed 106 rpm. For these conditions the calculated values for spindle torque and friction torque in the blade bearing are shown in Figure 3.22. The results of calculated blade spindle torque, calculated friction torque, calculated fretting coefficient, and measured fretting coefficients are given in Appendix C for all test cases.

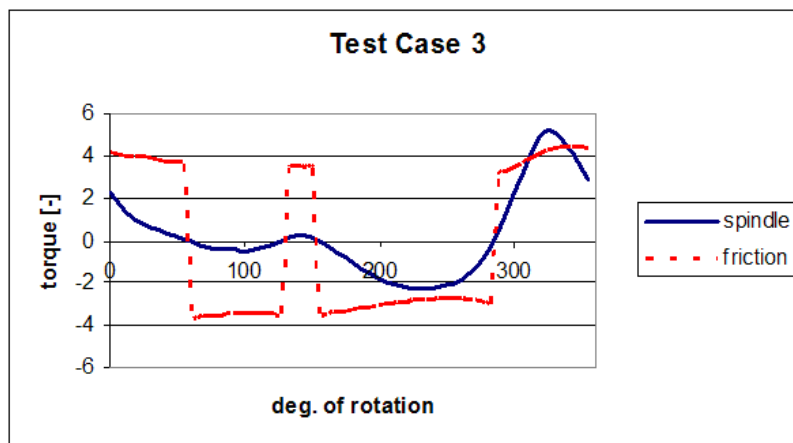


Figure 3.22: Calculated spindle torque and friction torque for Test Case 3

According to this figure there is no fretting because the negative spindle torque does not exceed the friction torque. However, it is possible to calculate the maximal value of the spindle torque and the related fretting coefficient to overcome the friction torque. If the spindle torque is increased by 25% (only for negative values) then the limiting value of friction coefficient is:

$$-0.085 > f_{frett} > 0.125 \quad (3.52)$$

Test Case 3 was done in irregular seas with waves heading from 180 deg, a peak period of 9.8 seconds and a significant wave height of 4.85 meters. Following the procedure in Test Case 1, Figure 3.23 shows the distribution of fretting coefficient. Even though the fretting motion was not predicted, the density distribution of the measured fretting coefficient indicates the existence of fretting for approximately 42.5% of the distribution.

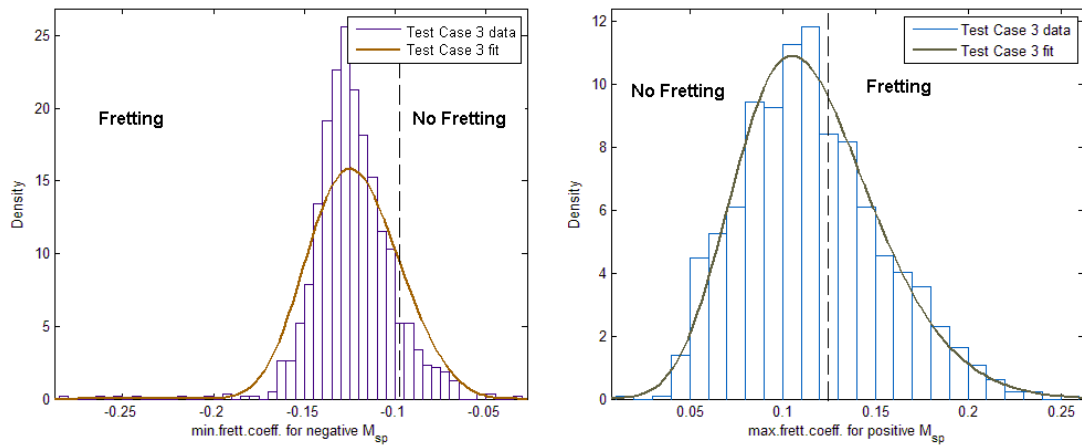


Figure 3.23: Test Case 3; fretting coefficient for negative (left) and positive (right) values for spindle torque

3.4.3 Results

The conditions and results of tests done are presented in Table 3.3. Waves heading from 180 degrees are bow waves are 0 degrees are stern waves.

Table 3.3: The results and conditions of tests done

Test Case	Wave Heading	Wave Height	Speed	rpm	Fretting predicted	Fretting Probability	Critical fretting coefficient $f_{frett_critical}$
1	180	2.90	24.4	111	Yes	100 %	-0.095; 0.140
2	180	4.85	22.2	106	Yes	77.5 %	-0.085; 0.133
3	180	7.45	19.8	106	No	42.5 %	-0.085; 0.125
4	180	4.85	17.1	83.3	Yes	56.5 %	-0.089; 0.132
5	180	7.45	15.8	89.5	No	45 %	-0.086; 0.119
6	180	4.85	7.6	42.6	No	75 %	-0.087; 0.131

7	180	7.45	6.9	46.5	No	47.5 %	-0.091; 0.119
8	180	7.45	12.4	69.7	No	36.2 %	-0.086; 0.118
9	0	7.45	20.6	89.1	Yes	77.5 %	-0.099; 0.118
10	45	7.45	19.7	92	Yes	73 %	-0.093; 0.117
11	60	7.45	20.2	88.1	Yes	72 %	-0.097; 0.117
12	90	7.45	20.0	90	Yes	99 %	-0.096; 0.114
13	135	7.45	16.4	87.1	No	70 %	-0.085; 0.114
14	180	7.45	25.1	107.4	Yes	100 %	-0.099; 0.120

3.5. Influence of sea condition on fretting motion

An investigation of results presented in Table 3.3 will be done here. First, the influence of wave height on fretting motion will be investigated for three different rpm ranges. Second, the influence of rpm will be investigated for two different wave heights. Third, the influence of wave direction will be considered. Fourth, the influence of draft will be investigated.

3.5.1 Influence of wave height in high rpm (overload)

Test Cases 1, 2, and 3 will be considered to investigate the influence of wave height on fretting motion. All tests are done with similar rpm and different wave heights. Figure 3.24 shows the distributions of the fretting coefficient in the investigated cases. As it can be seen, with the increase in wave height the distribution gets wider and mean value moves towards zero.

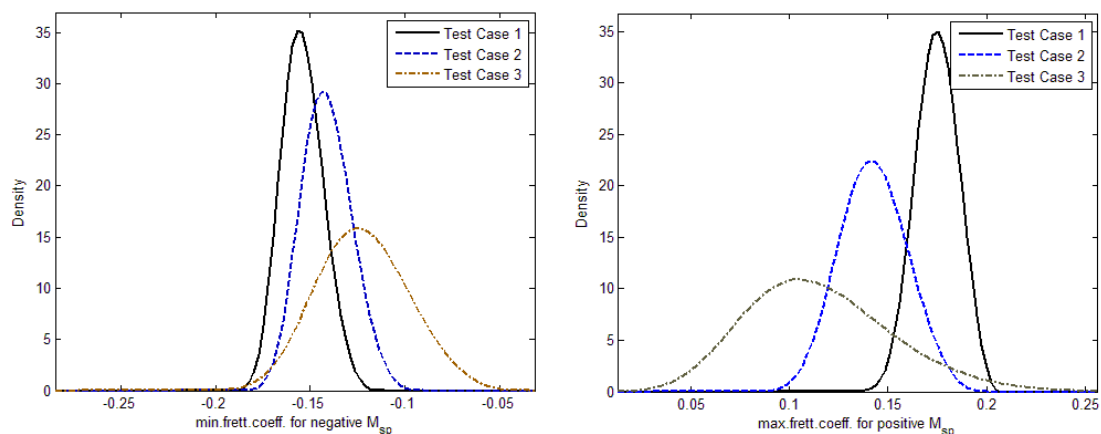


Figure 3.24: Distribution of fretting coefficients for different wave height in high rpm.

3.5.2 Influence of wave height in mid rpm (design)

Test Cases 4 and 5 will be considered for influence of wave height on fretting motion with rpm somewhat lower than in Chapter 3.5.1. Figure 3.25 shows the distribution of the fretting coefficients. The influence of wave height on fretting for shaft speeds close to the design value corresponds to the influence for high shaft speeds and the analysis in Chapter 3.5.1. With increase in wave height the distribution of fretting coefficient gets wider and mean value moves towards lower values.

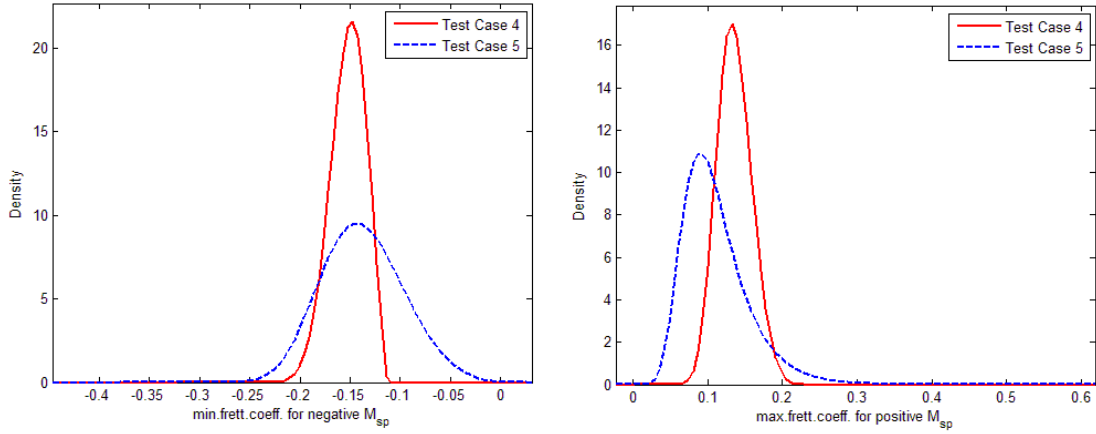


Figure 3.25: Distribution of fretting coefficients for different wave height in mid rpm

3.5.3 Influence of wave height in low rpm

Figure 3.26 shows the distribution of the fretting coefficients for Test Case 6 and 7. Note that the negative fretting limit for Test Case 6 is smaller than for Test Case 7, this being opposite to other cases. Maybe this is due to big difference in shaft speed (10%). In other cases there is a much smaller difference in rpm. However, the trend is same as in Chapter 3.5.1 and 3.5.2, the distribution gets wider with increase in wave height.

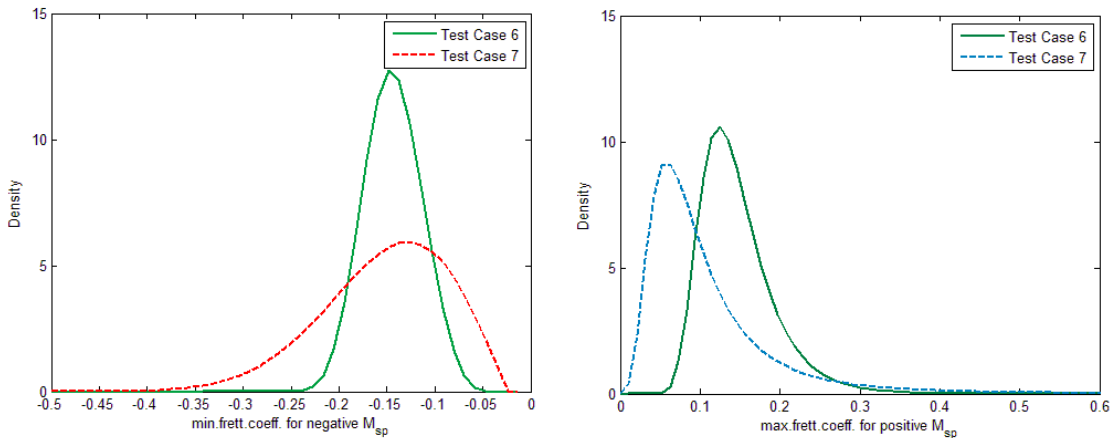


Figure 3.26: Distribution of fretting coefficients for different wave height in low rpm.

3.5.4 Influence of rpm in high waves

In this analysis the ship speed and the shaft rpm change but the sea condition remains the same. Waves are 7.45 meters high with a peak period of 12.2 and in head seas (180 degrees). Figure 3.27 shows the distribution of the fretting coefficient for the investigated cases. It seems that the probability of fretting rises with a decrease of speed and that the distribution of the fretting coefficient gets wider. The mean value of the fretting coefficient changes hardly.

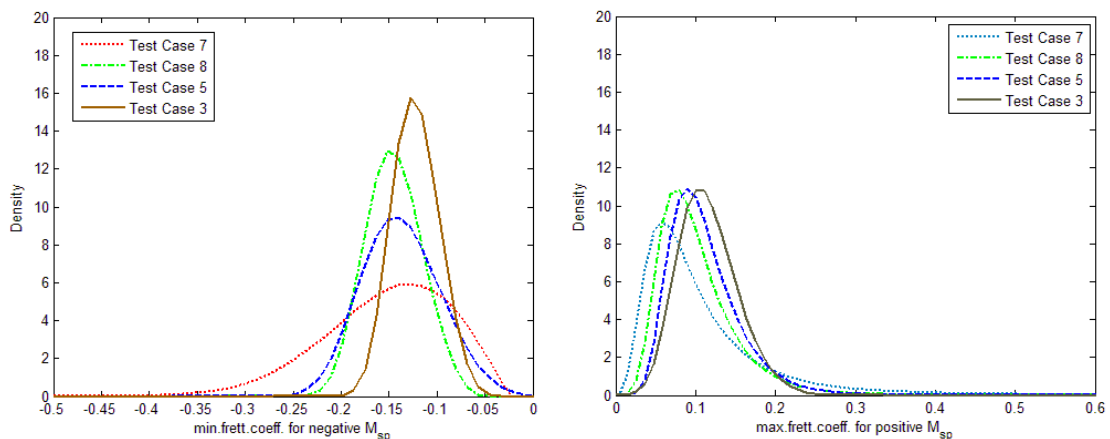


Figure 3.27: Distribution of fretting coefficients for different rpm.

3.5.5 Influence of rpm in medium waves

In this analysis the ship speed and shaft rpm change but the sea condition remain the same. In Chapter 3.5.4 it was done for high waves and here the analysis is for waves of 4.85 meters high with a peak period 9.8 and in head seas (180 degrees). Figure 3.28 shows the distribution of the fretting coefficient. The results match with Chapter 3.5.4, the distribution of the fretting coefficient gets wider with a decrease of speed.

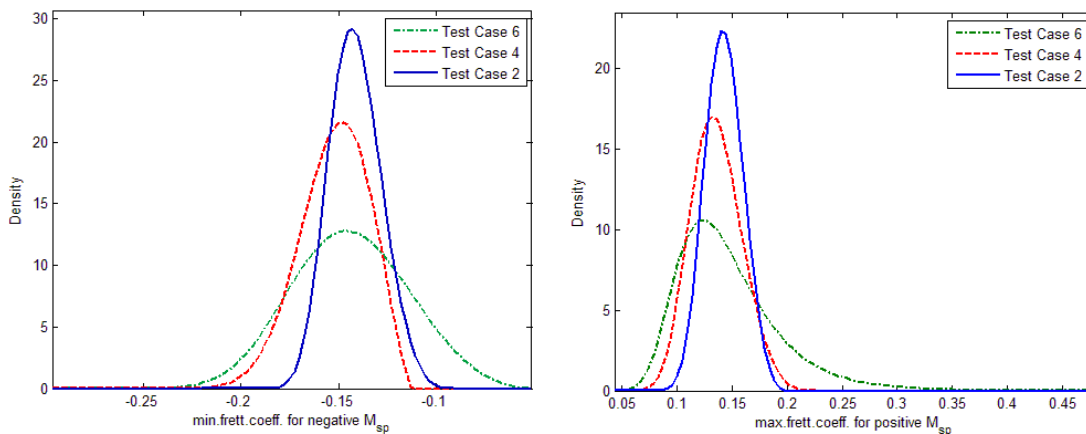


Figure 3.28: Distribution of fretting coefficients for different rpm.

3.5.6 Influence of wave direction

In this analysis the ship speed and shaft rpm are about the same, the wave height is the same (7.45 m), but the direction of wave changes. Figure 3.29 shows the distribution of fretting coefficients. It is difficult to draw a solid conclusion but it seems that waves coming from aside (Test Case 12) give the biggest percentage of fretting motion.

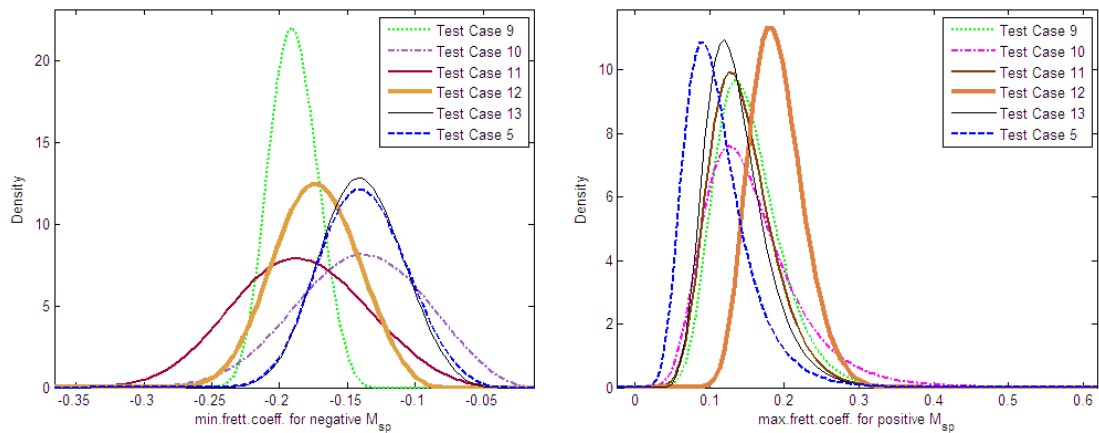


Figure 3.29: Distribution of fretting coefficients for different wave direction.

3.5.7 Influence of draft on fretting

In this analysis the ship speed and shaft rpm are about the same, the wave height (2.90 m) and wave direction is the same, but the draft of the ship is different. Figure 3.30 shows the distribution of the fretting coefficient for the Test Case 1 and 14. The distribution of the fretting coefficient for a reduced draft is much wider and above the fretting limit.

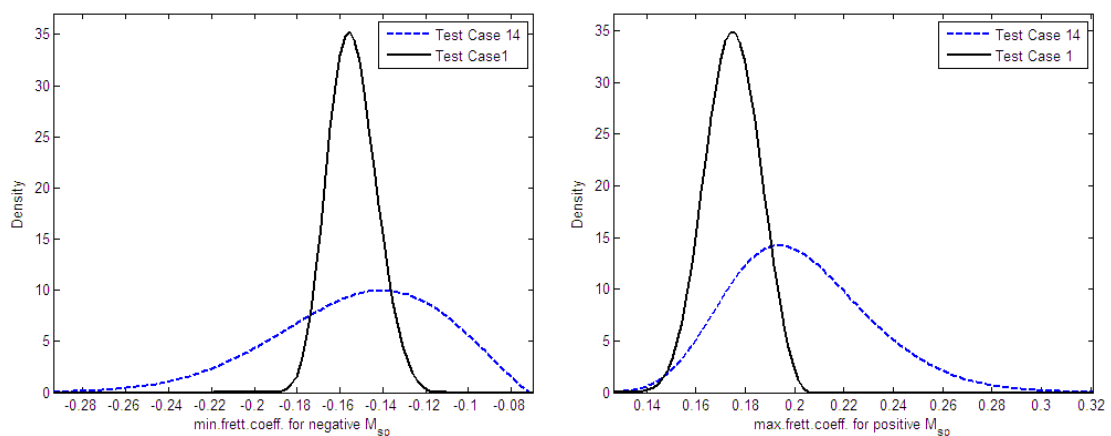


Figure 3.30: Distribution of fretting coefficients for different draft.

3.6. Discussion

The goal of this investigation was to say more about the fretting behaviour (motion) in a CPP in service conditions. There were two main questions that were answered. First, when does the fretting motion start in a CPP and second what is the influence of service conditions (sea state, rpm, and draft) on the fretting motion.

The equilibrium point and force balance was investigated in order to determine the start of small fretting motions. Problems involving friction are complicated, especially when involving the transition from stop to go. As a first assumption it was proposed to take the hydraulic force to be zero. The author is aware that the assumption is not perfect but definitely it is not wrong. As a result it is possible to determine the start of fretting motion. This motion starts when the total spindle torque overcomes the friction force in the blade bearing of a CPP.

In order to fully understand the fretting motion it is necessary to have the experiments where all forces would be measured for one single blade (i.e. spindle torque per blade, thrust per blade, and torque per blade) of a CPP. Since measurements of only total thrust and torque were available some approximation of the friction force was required. Since a good approximation turns out to be very difficult (see Chapter 3.3), the ratio of the spindle torque and total thrust was chosen and this can give a first estimate of the fretting behaviour of a CPP. In the first place, the interest was in the relative change between different sailing conditions. Using software tools, it was possible to determine the benchmark, or critical fretting coefficient, and say whether the change is going into good or bad direction.

It is clear now that when discussing fretting in a CPP the real issue is actually the distribution and probability of fretting. The situation where fretting motion does not occur has a distribution of the fretting coefficient lying below the critical fretting coefficient. In general, a good distribution would be narrow and (at least the mean value) would be below the critical fretting coefficient. A wider distribution means a wider spread of the fretting coefficient and therefore a higher probability of fretting motion. Together with values above the critical value of the fretting coefficient this means a bad distribution of the fretting coefficient. In the following paragraph the analysis made through Chapter 3.5.1 to Chapter 3.5.7 will be discussed keeping in mind these criteria for a good and bad distribution.

Table 3.4: Fretting coefficients and its distribution coefficients.

Test	Wave	Fretting	mean value		sigma	
Case	height	prob.	Positive	negative	positive	negative
1	2.90	100 %	0.175	-0.154	0.011	0.011
2	4.85	77.5%	0.143	-0.142	0.017	0.013
3	7.45	42.5%	0.116	-0.123	0.038	0.021

Looking at Chapter 3.5.1 it can be observed that for higher waves the mean value of the fretting coefficient is smaller and the spread of the fretting coefficient gets wider (Table 3.4). The drop in mean value can be explained by the increased thrust and a wider spread is expected for heavy seas (in high waves hydrodynamic forces oscillate more than in calm sea). The analysis carried out in Chapter 3.5.2 and 3.5.3 shows similar trends for increase in wave height at medium and low rpm. Since the analysis done predicts fretting in low waves (Test Case 1) the increase of wave height reduces the fretting motion for the investigated propeller. However for another propeller, with a

low prediction of fretting motion, the increase in wave height may cause fretting due to a wider distribution of the hydrodynamic forces.

Looking at Chapter 3.5.4 and 3.5.5 it can be observed that reducing the rpm increases the chance of fretting. The mean value of the fretting coefficient stays around a constant value but the distribution of the fretting coefficient is much wider for low rpm. This can be explained by a simple sensitivity analysis of the fretting coefficient k :

$$f_{\text{frett}} \cong \frac{M_{\text{sp}}}{T} \Rightarrow \frac{\delta f_{\text{frett}}}{f_{\text{frett}}} = \frac{\delta M_{\text{sp}}}{M_{\text{sp}}} - \frac{\delta T}{T} \quad (3.53)$$

Looking at Figure 3.20, the oscillations in thrust are much smaller comparing to their mean value, while oscillations in spindle torque are much bigger. Therefore, the second part of equation (3.53) can be neglected since it is much smaller than the first part. Than:

$$\delta f_{\text{frett}} = \frac{\delta M_{\text{sp}}}{T} \quad (3.54)$$

Since for the same sea state the oscillations in spindle torque are the same and thrust drops with decrease of rpm, the distribution of fretting coefficients gets wider for lower rpm. Due to lower rpm the thrust and centrifugal forces go down; this reduces the friction in a blade bearing and fretting motion is more probable at lower rpm.

Looking to Chapter 3.5.6 it was not possible to draw any solid conclusion for the influence of wave direction: the largest risk of fretting has been observed in waves coming from 90 degrees.

Looking at Chapter 3.5.7 it is clear that a reduced draft has a big influence on fretting behaviour. The mean value of the fretting coefficient increases and the distribution becomes wider at reduced draft. The explanation for this is the same as for reducing the rpm.

3.7. Conclusions

- This chapter shows the importance of maximal values as design criteria. If only mean values of spindle torque are considered everything looks nice and firm. This analysis shows there is much small movement in the mechanical assembly of a CPP.
- Fretting motion in the blade bearing is caused by a combination of wakefield distribution and blade design. A wakefield with high variations in the wake factor is more probable to cause fretting motion, such as is the case for large single screw vessels. Nicely balanced blades with a low value of mean spindle torque are easier to move around their z axis than blades with higher mean spindle torque.
- To completely avoid fretting, the variations of spindle torque must be lower than the Coulomb friction torque.
- Risk of fretting decreases with increased wave height for the investigated propeller. For other propellers the trend may be different.

- In heavy seas it is much better to reduce the pitch than the shaft speed. Reduction of shaft speed leads to a reduction of the centrifugal part of the friction force and this leads to an increase in fretting.
- Low draft situations are very dangerous for fretting in a CPP.
- The proposed fretting coefficient can be used to predict the fretting motion in a CPP. However, there is still awareness that the proposed fretting coefficient is not a final proof that fretting (wear) actually occurs although it seems the best available method so far.

4. Motions

The amplitude of fretting motion is one of the decisive factors in determining the total amount of fretting wear. The blade bearing of a CPP is exposed to loads and moments resulting from hydrodynamic, centrifugal, and actuating (hydraulic) forces. Motions in a blade bearing can occur due to the change of pitch by a hydraulic system, or due to vibrations generated from an oscillating hydrodynamic spindle torque. Here, the investigation focuses on the motion caused by an oscillating hydrodynamic spindle torque. It is reasoned that this motion has a vibrating/fretting nature, or in other words, a small amplitude and high frequency. The effects of an oscillating spindle torque on motions in the blade bearing are not fully clear or fully understood. While Chapter 3 “Loads” describes when the fretting motion starts, this chapter investigates what happens after the process begins. The amplitude of the fretting motion is the focus and the parameters influencing the amplitude are discussed.

This chapter begins with an overview of general friction behaviour and friction models. It continues with experiments of the friction behaviour of materials used in a CPP. These experiments provided useful information about the presence of static friction. Additionally, results were used as an aid in selecting the most suitable friction model. A simple model of a CPP mechanism was developed in *Matlab Simulink* environment. Answers to the above stated questions are given by implementing the selected friction models into the model of a CPP mechanism. Results indicated the existence of a fretting motion with an amplitude lower than 1 mm for the investigated case.

4.1. Friction

Friction is a complex phenomenon, characterized by transitions in its behaviour, and at the same time, it is dynamic and non-linear. In [Olsson, 1997], it was stated that friction forces are the result of different mechanisms that depend on contact geometry and topology, properties of the bulk and surface materials of the bodies, displacement and relative velocity, and the presence of lubrication. For physical explanation of friction, in [Persson, 2000], it was stated that: *“The friction forces observed for macroscopic bodies are ultimately due to the electromagnetic forces between the electrons and nuclear particles. Thus, an exact treatment of the interaction between two solids would consider coupling between all the electrons and nuclei using microscopic equations of motion for these particles (quantum electrodynamics).”* Since wear and friction are related terms, this explanation for friction force is of essential importance in understanding not only the friction phenomena, but wear phenomena as well. This is why the simple wear models are not correct. This will be elaborated more in Chapter 7. Real contact between two surfaces is achieved only at the asperities in contact. The asperities each carry a part of the normal load. In sliding contacts between flat surfaces, which are of interest for this investigation, friction can be modelled as elastic and plastic deformation forces of asperities in contact [Bowden, 1950]. For each asperity contact the tangential deformation is elastic until the applied shear stress exceeds the shear strength of the contact, whereby it becomes plastic.

4.2. Friction behaviour

Friction is influenced by many different parameters and characterized by a variety of behaviour aspects. As such, friction is very difficult to model. A perfect friction model would contain all behaviour aspects and include all relevant parameters. The main aspects of the complex friction behaviour are presented here.

- Different lubrication regimes:

Figure 4.1 shows friction forces in a lubricated journal bearing as a function of velocity, lubricant viscosity and pressure in the bearing, combined in a non-dimensional, Stribeck number. This curve is known as the Stribeck Curve [Stribeck, 1903] and it shows three different lubrication regimes. In this investigation, due to low speeds and high loads, it is always a boundary lubrication regime.

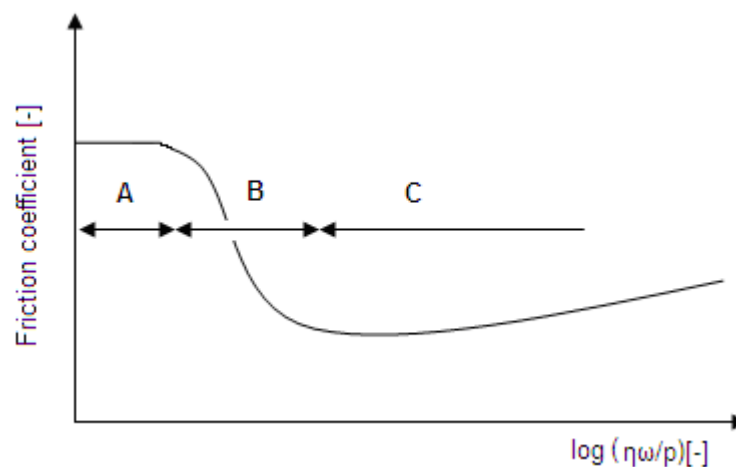


Figure 4.1: The Stribeck curve: Different lubricating regimes as a function of the rotation velocity (ω), lubricant viscosity (η), and pressure (p): A) Boundary, B) Mixed, and C) Hydrodynamic.

- Static and kinematic friction:

More relevant for this investigation is another type of transition in friction behaviour. The force needed to initiate a motion is (often) higher than the force needed to maintain the motion of two bodies in contact. Thus, friction can be divided into two main regimes, namely, pre-sliding and gross sliding regimes. In the pre-sliding regime, friction is characterized by displacement.

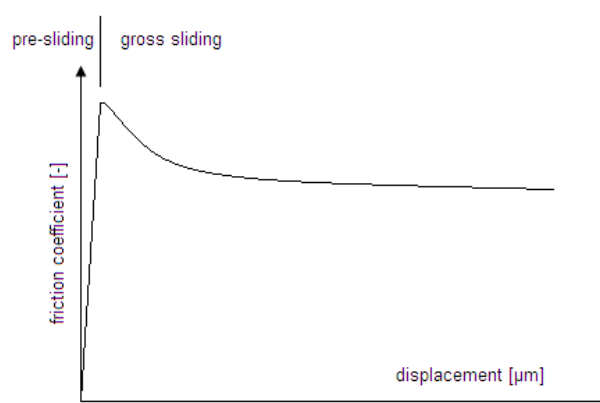


Figure 4.2: Experimental results in [Rabinowicz, 1951].

Instead of presenting friction force as a function of velocity, in [Rabinowicz, 1951] the author presented friction force as a function of displacement as shown in Figure 4.2. Friction during the pre-sliding regime is called static friction, and friction during the gross sliding regime is called kinematic friction. The force required to overcome static friction and initiate motion is called the break-away force.

In [Johannes, 1973] it was experimentally found that the break-away force depends on the rate of applied (tangential) force. The break-away force was measured for different rates of tangential force. Figure 4.3 is the summation of results from those experiments. On the x axis, the force rate is shown as a function of the tangential force rate divided by the normal force (\dot{F}_{tan} / N). Higher break-away forces for low rates of tangential force are explained by an increased true contact area. However, in the pre-sliding regime, the adhesive forces are dominant [Al-Bender, 2004]. Adhesive forces refer to all tangential forces resisting the motion arising from a variety of sources, independent of forces arising from geometrical deformation of asperities in the tangential direction. It is highly likely that the force rate has an influence on the adhesive part of the friction force.

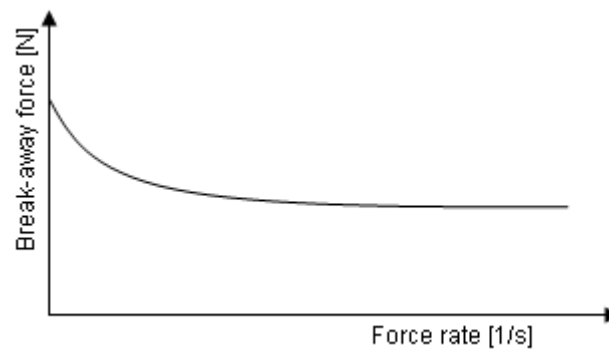


Figure 4.3: Break-away force as a function of the rate of application of the tangential force

Behaviours shown in Figure 4.2 and Figure 4.3 will not be explored in detail in this investigation. They are presented here solely to show the complexity of friction. For further explanation, the reader is directed to [Persson, 2000]. Having said this, behaviours shown in Figure 4.2 and Figure 4.3 have certain relevance for this investigation. Theoretically, it is possible to delay the unwanted fretting motion by choosing the contact situation (materials and lubrication) with higher static friction coefficients, and by applying a low rate of external forces (spindle torque). Implications of this solution are discussed later in Chapter 4.9.

– Pre-sliding displacement:

The microscopic motion that occurs before the gross sliding is called the pre-sliding motion. As long as the applied (tangential) force is below the break-away force and kept constant, the displacement will remain constant as well. Some parts of the contact will exhibit micro slip, while some parts will remain unbroken. When the applied force is decreased back to zero, not all the displacement will be recovered. This hysteretic character of the pre-sliding regime is shown in Figure 4.4. It can be seen that the displacement deviates from the elastic line (dashed). The pre-sliding displacement is a sum of two displacements, the elastic (reversible) and plastic (irreversible). The dash-dot line shows what would happen if applied force continued to rise until the gross slip occurs.

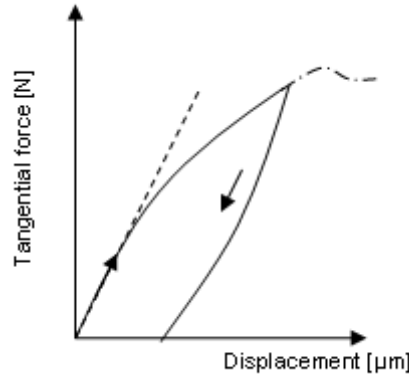


Figure 4.4: pre-sliding displacement during the increase and decrease of applied tangential force

Many authors, including [Worden, 2007] and [Parlitz, 2004], explore the pre-sliding problem by combining it with experiments and different modelling techniques. For further information on the identification and modelling of the pre-sliding regime, the reader is directed to those references. Here, the pre-sliding regime is presented to aid in understanding partial slip as a fretting mechanism.

– Friction hysteresis:

Figure 4.5 shows three possible hysteretic behaviours of friction force. The first curves show only the pre-sliding regime, while the third curve shows pre-sliding and gross sliding regimes. In Figure 4.5a, there is no plastic deformation, and pre-sliding displacement is purely elastic. The second curve, Figure 4.5b, shows a friction hysteresis during the pre-sliding regime, with the effect of plastic deformation. The third curve, Figure 4.5c, shows gross slip regime, and has a previously mentioned drop in friction force. These three curves are typical for three types of fretting motion and fretting wear; no slip, partial slip, and gross slip.

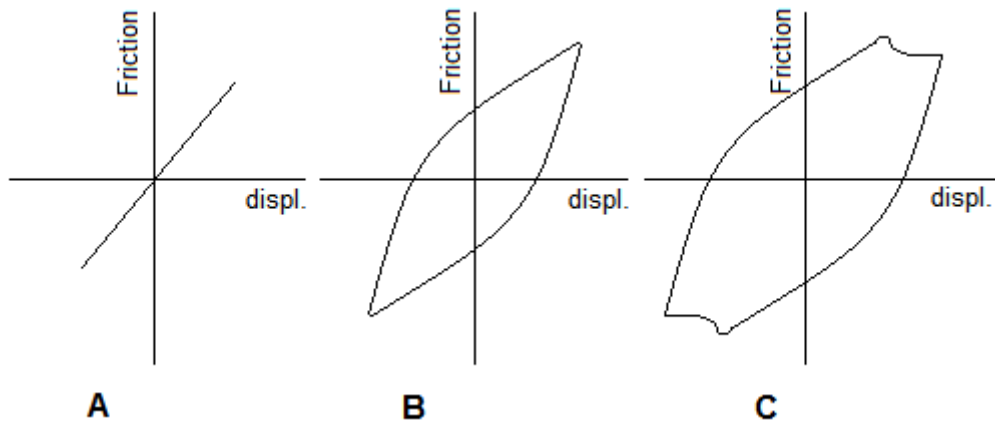


Figure 4.5: different hysteresis loops of friction force as a function of displacement: a) elastic, b) partial slip, and c) gross slip

4.3. Measurements of friction in a CPP

It is difficult to determine the pre-sliding displacement due to the fact that a sophisticated test apparatus is needed [Worden, 2007]. Here, an attempt is made to capture the transition from pre-sliding to gross sliding with the apparatus and specimens as described in Chapter 5.4.1, Sliding Wear. A set of experiments was

undertaken in which the hydraulic pressure in the actuator slowly increased until the motion began. Figure 4.6 shows the measured friction coefficient and angular displacement during one of the experiments.

The investigated material pair was 42CrMo4 steel and CuNiAl bronze, with a lubricated contact, exposed to a 48N/mm^2 load. The highest friction coefficient is 0.115 at 0.25 degrees of angular displacement, or $100\mu\text{m}$ of linear displacement. The value of the kinematic friction coefficient is 0.1.

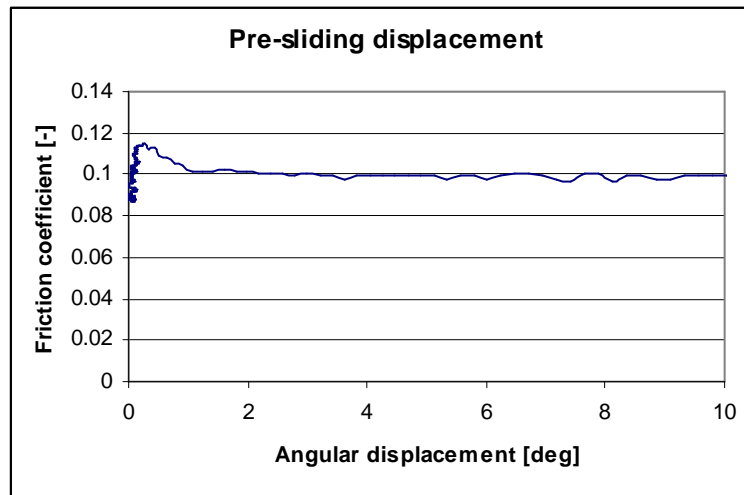


Figure 4.6: change from no sliding to sliding for a steel and CuNiAl material pair with a load of 48N/mm^2

The rate of increase of tangential force was approximately 0.003 N/sN , which was extremely low. According to [Johannes, 1973] it is in the range of increased break-away force. To compensate for the low rate effect of the tangential force, a value of 0.11 is selected for the static friction coefficient in the following investigation.

Unfortunately, the apparatus was not adequate for more sophisticated experiments, which would determine the pre-sliding hysteresis. Nevertheless, valuable information about the frictional behaviour of materials used in a CPP were obtained. However, in [Pronk, 1980] the actuating pressures of a CPP were measured at the OD box and the results indicated no drop in the actuating pressure, (i.e. the maximum static friction is equal to the kinematic friction).

4.4. Modelling of friction

Various mathematic models try to capture and describe the practically observed and complex friction phenomenon. The most suitable model depends upon the purpose of it, but it is preferable to have a model that accurately describes all aspects of friction. Here, the focus is on the amplitude of fretting motion in the blade bearing of an investigated CPP.

The main division of friction models is between static and dynamic friction models. Frictional memory is a delay between a change in sliding velocity or normal force and the consequent change in friction. The static friction models fail to describe friction memory, while the dynamic friction models try to describe it with additional dynamics. For static friction models, the friction force is a static function of velocity. For dynamic friction models, the friction force is described by introducing additional state variables.

Experiments from Chapter 4.3 are used in selecting the appropriate models and its coefficients for this investigation. Figure 4.7 shows a body with mass m , an actuating force of F , and resisting friction force F_{fr} as in experiment in Chapter 4.3. Note that in all friction models, friction is modelled as a force resisting the motion and therefore has negative sign in the equation of motion. The normal pressure from the friction experiment is 48N/mm^2 , which corresponds to 27 kN normal force (N) for the contact area of samples described in Chapter 5.4.1 in Figure 5.2. When the body is moving, the Coulomb friction force F_c is:

$$F_c = \mu \cdot N \quad (4.1)$$

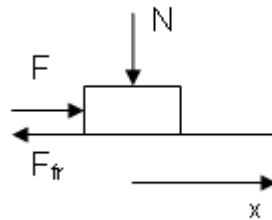


Figure 4.7: the situation as in experiment in Chapter 4.3, here represented for linear motion

In order to explore different friction models, a simple *Simulink* model has been made. This model shown in Figure 4.8 simulates the configuration described in the friction experiment for different friction models. An actuating force (F) is represented as a constantly increasing signal. Friction in the system is represented as a block that has three inputs, namely actuating force, Coulomb friction and velocity. The actuating force and friction force are summed up, divided for mass of the body and twice integrated to get the displacement of the body. Notice the dead zone block before the integration of velocity is used in one specific friction model.

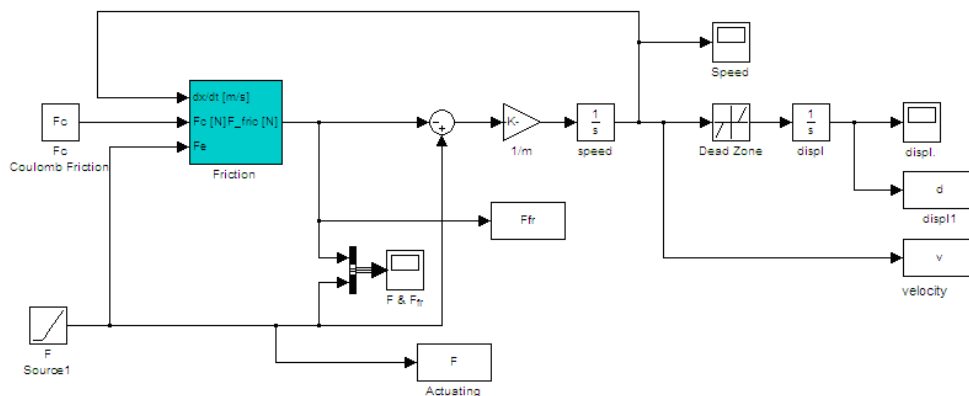


Figure 4.8: Model used to investigate and compare the behaviour of different friction models

Friction force is modelled according to the selected friction model. Different friction models are tested using the simulation model shown in Figure 4.8. By doing so, the advantages and disadvantages of each mentioned model are illustrated.

4.4.1 Static friction models

Figure 4.9 shows four levels of modelling the friction force by use of static friction models. Figure 4.9a shows the simplest model. This model captures the basic behaviour

of friction. It describes friction as a function of Coulomb friction and direction of motion. Coulomb friction is proportional to normal load (N). The friction is modelled as an ideal relay model. Friction force (F_{fr}) is equal to Coulomb friction (F_c), except when the velocity (\dot{x}) is zero. Then friction can have any value between $-F_c$ and F_c .

$$F_{fr} = F_c \operatorname{sgn}(\dot{x}) \quad (4.2)$$

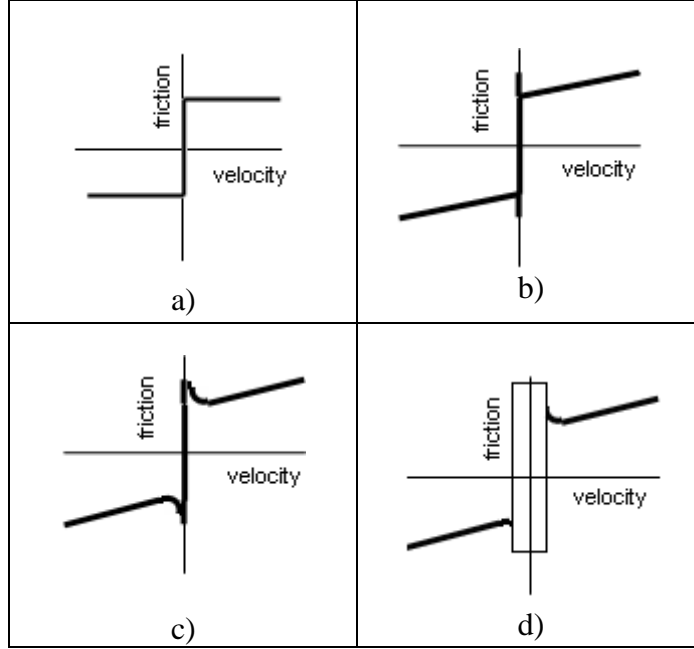


Figure 4.9: Four different levels of interpretation of static friction models

Figure 4.9b shows friction behaviour, including the effects of static friction and viscous friction. By introducing the sum of external forces (F_e), it is possible to extend the friction model and describe the break-away force (F_s). When velocity is zero, the friction force can have any value between $-F_s$ and F_s . Equation (4.3) includes the effects of the break-away force and viscous friction (F_v):

$$F_{fr}(\dot{x}, F_e) = \begin{cases} F_c \operatorname{sgn}(\dot{x}) + F_v & \dot{x} \neq 0 \\ F_e & \dot{x} = 0; |F_e| < F_s \\ F_s \operatorname{sgn}(F_e) & \dot{x} = 0; |F_e| \geq F_s \end{cases} \quad (4.3)$$

where viscous friction is usually a linear function of speed:

$$F_v = f(\dot{x}) \quad (4.4)$$

However, the transition between break-away friction and kinematic friction is not as immediate as in the real application. Figure 4.9c shows friction decreasing continuously from break-away friction to kinematic friction, as proposed by Stribeck:

$$F_{fr}(\dot{x}, F_e) = \begin{cases} (F_c + (F_s - F_c) \cdot e^{-|\dot{x}/v_s|^2}) \cdot \operatorname{sgn}(\dot{x}) + F_v(\dot{x}) & \dot{x} \neq 0 \\ F_e & \dot{x} = 0; |F_e| < F_s \\ F_s \operatorname{sgn}(F_e) & \dot{x} = 0; |F_e| \geq F_s \end{cases} \quad (4.5)$$

where v_s is called the Stribeck velocity. Furthermore, in using Equation (4.5), the friction force can have any value between $-F_s$ and F_s for zero velocity.

To overcome the discontinuity between static and kinematic friction, Karnopp in [Karnopp, 1985] proposed a zero velocity interval defined by a very low threshold speed (v_{th}). Inside this interval ($|\dot{x}| < v_{th}$), the “output” velocity is maintained at zero by a dead-zone. Within the dead zone interval, the friction force is a saturated version of the external force ($\max(F_s, F_e)$). Figure 4.9d illustrates the Karnopp model. Equation (4.5) therefore changes into:

$$F_{fr}(\dot{x}, F_e) = \begin{cases} (F_c + (F_s - F_c) \cdot e^{-|\dot{x}/v_s|^2}) \cdot \text{sgn}(\dot{x}) + F_v(\dot{x}) & |\dot{x}| \geq v_{th} \\ F_e & |\dot{x}| < v_{th}; |F_e| < F_s \\ F_s \text{sgn}(F_e) & |\dot{x}| < v_{th}; |F_e| \geq F_s \end{cases} \quad (4.6)$$

The discontinuity at zero velocity may lead to non-unique solutions of the equations of motion and numerical problems when it is used in simulation. To illustrate this, a comparison between the Karnopp model and Equation (4.5) is done. For both models the actuating force increases from a negative value to a positive value. The velocity of the body will change from negative to zero and then to positive value. On the left side, Figure 4.10 shows the actuating force and friction force modelled according to Equation (4.5) and, on the right side the resulting velocity. The problem of non-unique solutions for friction force and velocity is visible. In contrast to Figure 4.10, Figure 4.11 shows the actuating force and friction force modelled using the Karnopp model described in Equation (4.6). Using the Karnopp model the problem of non-unique solution is solved.

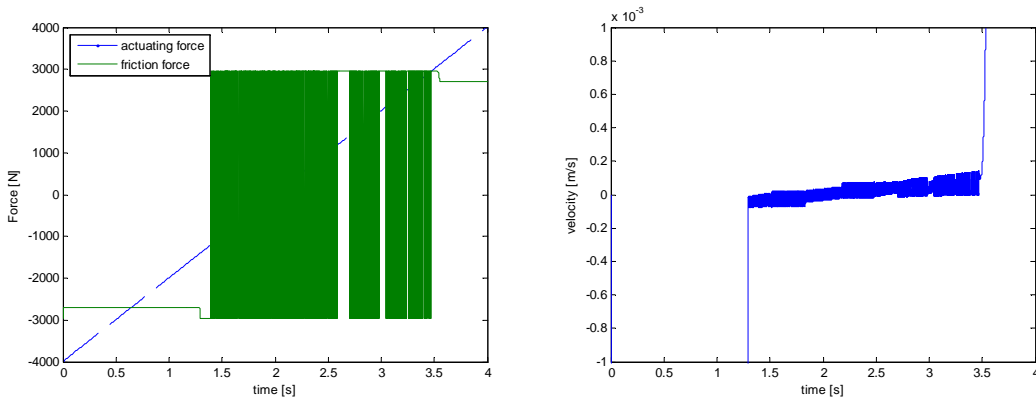


Figure 4.10: Actuating force and friction force modelled using Equation (4.5), left, and the resulting velocity, right.

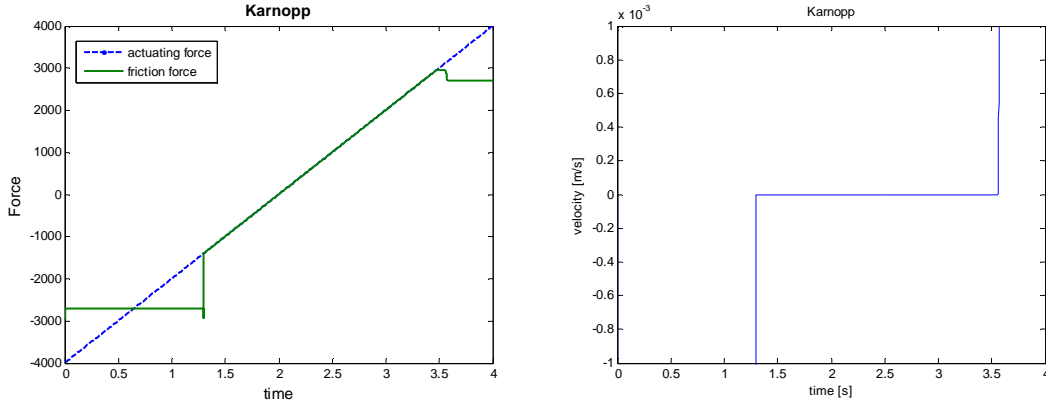


Figure 4.11: Actuating force and friction force modelled using Karnopp model, left, and the resulting velocity, right.

The drawback of the model in Equation (4.6) is that it is strongly coupled with the rest of the system. In addition, there is no pre-sliding displacement in using the Karnopp model.

Another approach in overcoming the discontinuity is to approximate the friction force by a curve of a finite slope in the vicinity of zero velocity. Within this region, friction force is assumed to be linearly proportional to velocity. Figure 4.12 shows friction behaviour using Equation (4.7).

$$F_{fr}(\dot{x}) = \begin{cases} (\dot{x}/v_{th}) \cdot (F_c + (F_s - F_c) \cdot e^{-|\dot{x}/v_s|^2}) \cdot \text{sgn}(\dot{x}) + F_v(\dot{x}) & |\dot{x}| \leq v_{th} \\ (F_c + (F_s - F_c) \cdot e^{-|\dot{x}/v_s|^2}) \cdot \text{sgn}(\dot{x}) + F_v(\dot{x}) & |\dot{x}| > v_{th} \end{cases} \quad (4.7)$$

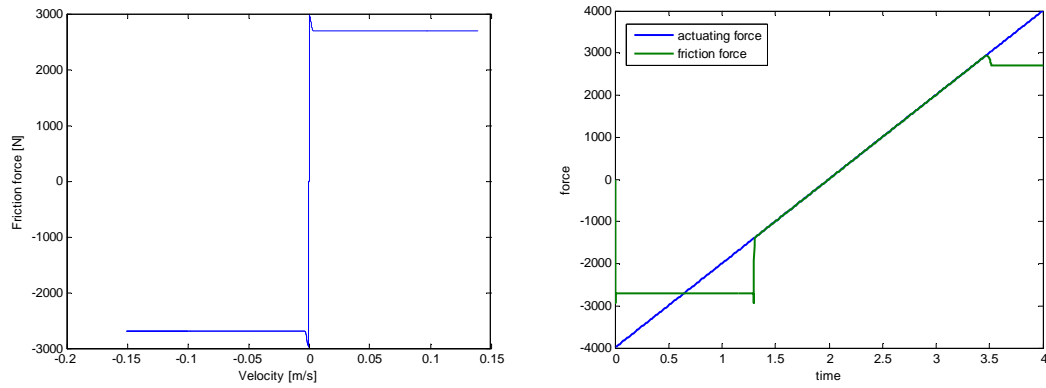


Figure 4.12: Friction force as a function of velocity (left) using Equation (4.7), resulting from an actuating force that changes direction (right).

Using Equation (4.7), it is possible to simulate the results of the experiment. On the left side, Figure 4.13 shows the actuating force and calculated friction force together, and on the right side, it shows the resulting pre-sliding displacement. The exact amount of pre-sliding displacement depends upon a threshold speed.

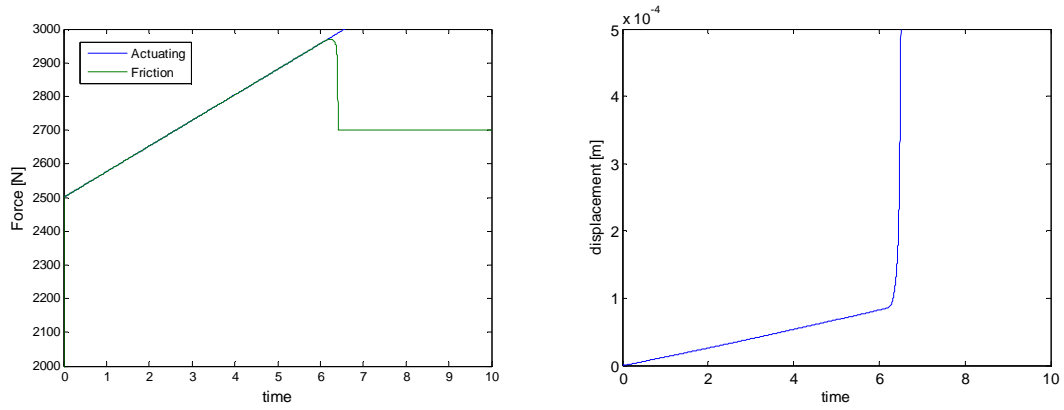


Figure 4.13: Calculated friction force (left) and displacement (right) using Equation (4.7)

The list of static friction models does not end here. There are other static friction models, such as in [Olsson, 1997], and new static friction models can be made by combining the above mentioned models. For example, a coarse solution is to neglect the Stribeck effect but keep the finite slope of friction force in vicinity of zero velocity. Furthermore, for this investigation, the effect of viscous friction is not relevant and can be excluded from the friction model. In that case, Equation (4.7) can be combined with Equation (4.2). Figure 4.14 shows the resulting friction behaviour defined as:

$$F_{fr} = \begin{cases} \text{sgn}(\dot{x}) \cdot (F_c) \\ \frac{\dot{x}}{v_{th}} \text{sgn}(\dot{x}) \cdot (F_c) \end{cases} \quad \begin{cases} |\dot{x}| \geq v_{th} \\ |\dot{x}| < v_{th} \end{cases} \quad (4.8)$$

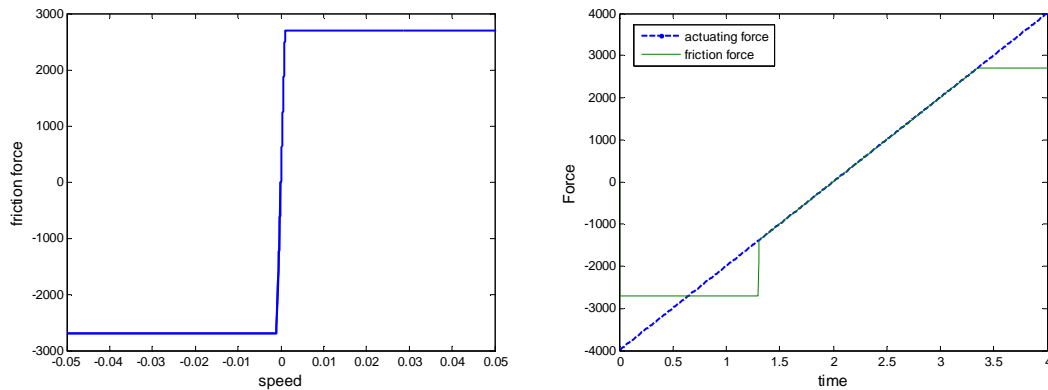


Figure 4.14: friction force as a function of velocity (left) and using Equation (4.8) resulting from an actuating force that changes direction (right).

Notice the friction force calculated with Equations (4.8) or (4.7) does not stop relative motion when an acting force drops below the break-away force. The bodies will creep relative to each other with a relative velocity. Figure 4.15 shows the body slowly drifting under a constant actuating force below the break-away force. On the other hand, the Karnopp friction model will not have this drawback, but it will have zero pre-sliding displacement.

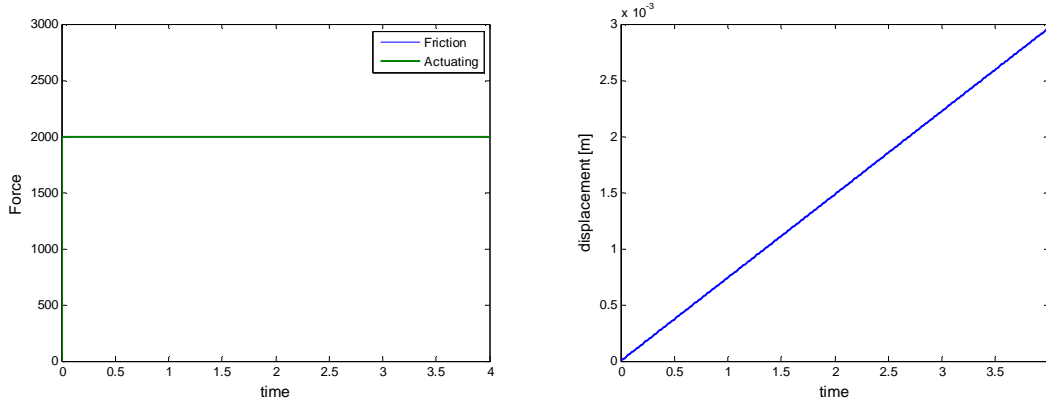


Figure 4.15: non-physical drift of a body (right) exposed to a constant tangential force lower than the break-away force (left).

One of major disadvantages of static friction models is their limited richness, which will result in inaccurate friction models for certain regions of interest, including the region of pre-sliding displacement. This lack of accuracy can be a serious problem for advanced control systems. The practical need for advanced friction models, combined with the scientific curiosity, resulted in dynamic friction models.

4.4.2 Dynamic friction model

In order to capture the dynamic behaviour of friction, a dynamic friction model describes friction with an additional state variable defined by a set of differential Equations. A very good overview of friction models can be found in [Olsson, 1997]. The starting point of dynamic friction models is the Dahl model [Dahl, 1968] which is based on a stress-strain curve for brittle material from solid mechanics. In Figure 4.16 the stress-strain curve can be transformed into a friction force-displacement curve by:

$$F_{fr} = F_c \left(1 - e^{-\frac{\sigma_0}{F_c} x} \right) \text{sgn}(\dot{x}) \quad (4.9)$$

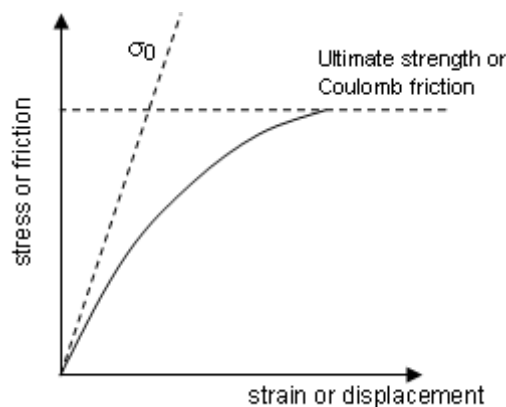


Figure 4.16: Analogy between friction-displacement curve and a stress-strain curve

Differentiating it for x , it yields:

$$\frac{dF_{fr}}{dx} = \sigma_0 \left(1 - \frac{F_{fr}}{F_c} \operatorname{sgn}(\dot{x}) \right) \quad (4.10)$$

where σ_0 is the stiffness coefficient (in N/m) of the asperity junctions at $F_{fr}=0$, and x is the displacement. To obtain a differential equation in the time domain:

$$\frac{dF_{fr}}{dt} = \frac{dF_{fr}}{dx} \cdot \frac{dx}{dt} = \sigma_0 \cdot \dot{x} \cdot \left(1 - \frac{F_{fr}}{F_c} \operatorname{sgn}(\dot{x}) \right) \quad (4.11)$$

Introducing internal state z , the friction force can be defined as:

$$F_{fr} = \sigma_0 \cdot z \quad (4.12)$$

Then:

$$\dot{z} = \dot{x} - \frac{\sigma_0 \cdot |\dot{x}|}{F_c} \cdot z \quad (4.13)$$

Notice that the Dahl model describes friction only as a function of displacement and neglects the Stribeck effect. As a further development of dynamic model, the LuGre model [Canudas de Wit, 1995] is related to the asperity interpretation of friction. When a tangential force is applied, the asperities in contact will deflect as springs, which will result in a displacement. As the displacement increases, more and more junctions will break until gross sliding occurs. The randomness of displacements originates from the random distribution of asperities. The internal state (z) can be interpreted as an average deflection of asperities in contact, and friction can be visualized as a force produced by bending asperities, which are behaving like springs. In order to introduce the Stribeck effect, Coulomb friction in Equation (4.13) is replaced by an arbitrary steady state behaviour $g(\dot{x})$:

$$g(\dot{x}) = F_c + (F_s - F_c) e^{-(|\dot{x}|/v_s)^2} \quad (4.14)$$

In the LuGre model, friction force is defined as a function of variable z and velocity as:

$$F_{fr} = \sigma_0 \cdot z + \sigma_1 \cdot \dot{z} + \sigma_2 \cdot \dot{x} \quad (4.15)$$

During pre-sliding, the actuating force is cancelled by a spring-damper system ($\sigma_0 \cdot z$ and $\sigma_1 \cdot \dot{z}$). For a very small (pre-sliding) velocity, the first part in Equation (4.15) corresponds to hysteresis behaviour of the friction force and for gross sliding, it corresponds to the Stribeck behaviour. The second term of Equation (4.15) avoids undamped vibrations during the pre-sliding regime, and it vanishes for gross sliding. To visualize it, the average bending of asperities has a constant value ($z=\text{const.}$) for gross sliding. The third term of Equation (4.15) corresponds to viscous friction. In this work viscous friction is assumed zero due to high load and low speed, i.e. $\sigma_2=0$.

The LuGre model is very attractive because it describes friction in a continuous way and because of its richness. It captures pre-sliding, the Stribeck effect, friction

hysteresis and it is rate dependant. However, the behaviour of the model is strongly influenced by the value of parameters (σ_0 , σ_1 , v_s) used in the model. This is especially notable during pre-sliding, when any change in one parameter can have unrealistic consequences on the overall friction behaviour. For example, it is possible to adjust the pre-sliding displacement by increasing the stiffness of asperities (σ_0), but this will result in high vibrations of friction force, especially during the transition from go to stop. In [Worden, 2007] and [Hensen, 2002], different techniques have been used to select the most appropriate values for parameters in the LuGre model. In this work, values for parameters of the LuGre model are chosen by doing a sensitivity analysis, (see Appendix B), where the influence of each parameter was investigated. After investigating the friction behaviour for a number of different values of LuGre parameters, the final values were chosen as a best match between the results of the experiment and the reasoned friction behaviour. Figure 4.17 (left) shows friction force using the final values from Table 4.1, under conditions as set out in the experiment. The resulting displacement is shown in Figure 4.17 (right).

Table 4.1: parameters of the LuGre model that are used in following analysis

Parameter	Value	Unit
σ_0	1e9	[N/m]
σ_1	4e5	[Ns/m]
σ_2	0	[Ns/m]
F_s	$1.1 \cdot F_c$	[N]
v_s	0.0008	[m/s]

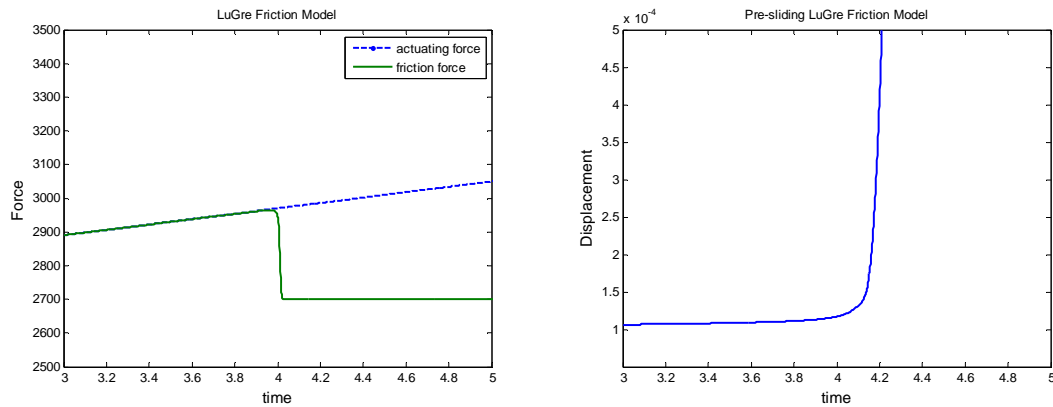


Figure 4.17: Left: Results of friction force and displacement using the LuGre model (Table I). Right: The pre-sliding displacement is $140\mu\text{m}$.

Since the goal for later stages is to model a reciprocating motion of a very small amplitude, it is important that the friction force is modelled without too many vibrations. Figure 4.18 (left) shows friction under an oscillating actuating force. It is important to note that the rate of actuating force is much higher than in the experiment, it is corresponding to typical wake variations. Looking at the Figure 4.18, the behaviour of the friction model is relatively smooth and continuous. Vibrations in the LuGre model can be reduced by increasing σ_1 , but this would lead to a smaller pre-sliding displacement.

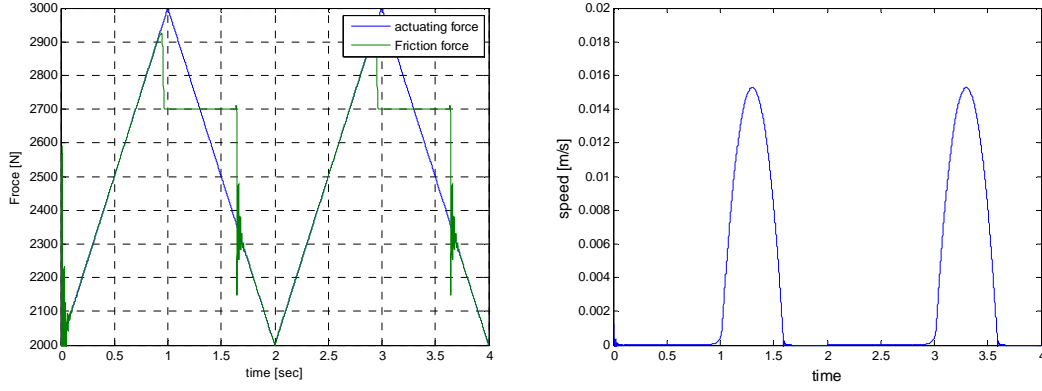


Figure 4.18: Friction force under an oscillating actuating force (left) and the resulting speed of the body (right)

One of the drawbacks of the LuGre model is the so-called drifting phenomenon. This occurs when it appears as if the body is slowly moving (drifting) even though the actuating force never overcomes the break-away force. Figure 4.19 (left) shows the oscillating actuating force with an amplitude below the break-away force. Therefore, no motion is expected. However, Figure 4.19 (right) shows a displacement. It seems that the body is slowly drifting. In increasing the pre-sliding displacement, the drifting will increase as well.

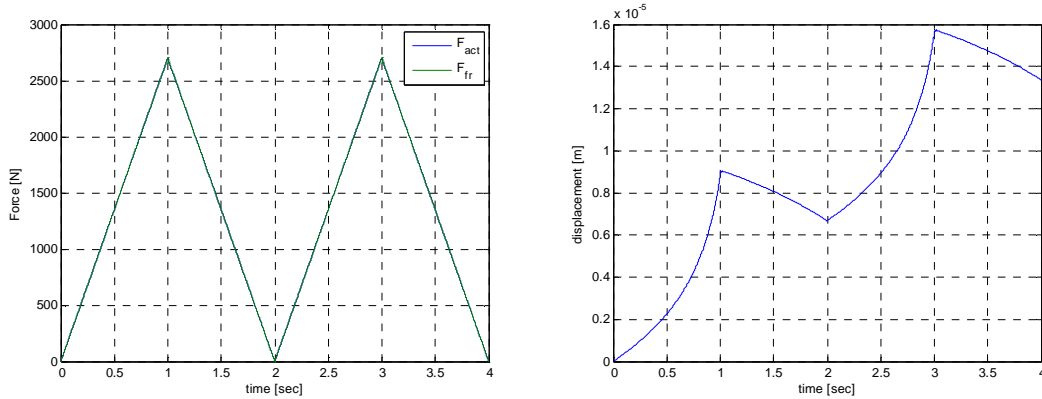


Figure 4.19: Oscillating actuating force is the same as friction force (left) and the body appears to move (right)

It is possible to reduce the drift by introducing a new parameter α . In [Dupont, 2002], a new elasto-plastic model is proposed. The LuGre model exhibits a nonphysical drift phenomenon, which results from modelling the pre-sliding as a combination of elastic and plastic deformation. In elasto-plastic models, the pre-sliding is divided into an elastic and plastic displacement. It is first purely elastic and then transitions to plastic. The asperity displacement (z) has its steady state value (z_{ss}) that corresponds to steady sliding at certain velocity. A break-away displacement (z_{ba}) is defined such that the model behaves elastically for $abs(z) < z_{ba}$. Equation (4.13) for elasto-plastic model states:

$$\dot{z} = \dot{x} - \alpha(z, \dot{x}) \cdot \frac{|\dot{x}|}{g(\dot{x})} z \quad (4.16)$$

$$\alpha(z, \dot{x}) = \begin{cases} 0 & |z| \leq z_{ba} \\ \alpha_m & z_{ba} < |z| < z_{ss}(\dot{x}) \\ 1 & |z| \geq z_{ss}(\dot{x}) \end{cases} \left\{ \begin{array}{l} \text{sgn}(\dot{x}) = \text{sgn}(z) \\ \text{sgn}(\dot{x}) \neq \text{sgn}(z) \end{array} \right. \quad (4.17)$$

With

$$\alpha_m(z, z_{ba}, z_{ss}) = 0.5 + 0.5 \sin\left(\pi \frac{z - (z_{ba} + z_{ss})/2}{z_{ss} - z_{ba}}\right) \quad (4.18)$$

And

$$0 < z_{ba} \leq z_{ss} \quad (4.19)$$

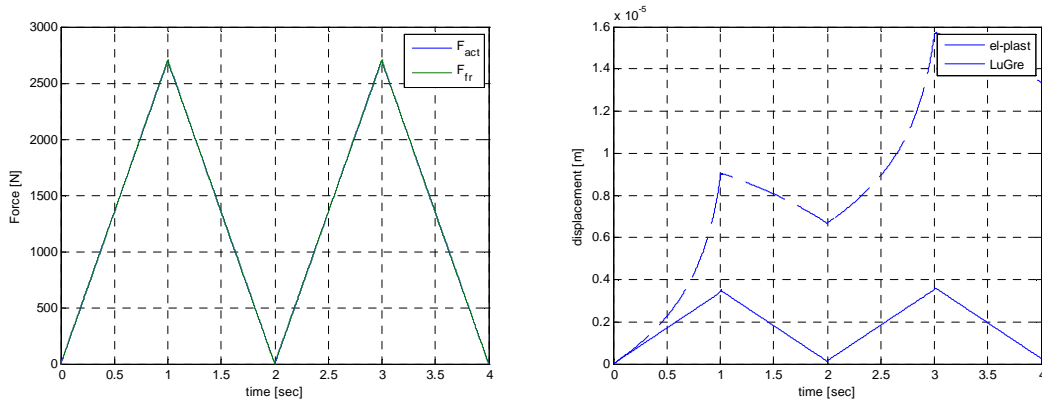


Figure 4.20: Reduction of drift achieved by using the single state elasto-plastic friction model

Figure 4.20 shows the comparison of drift between the two models. The elasto-plastic model makes it possible to completely eliminate drifting when $z_{ba}=z_{ss}$. In that case, pre-sliding is purely elastic.

4.5. Selection of friction model

The experiment in Chapter 4.3, Figure 4.6 clearly shows the Stribeck effect for materials and loads used in a CPP. However, this experiment alone is not sufficient to properly validate a friction model. Nevertheless, it can be used as a useful guideline. Most important is that the selection of a friction model should be made according to its purpose. Here, the goal is to estimate the amplitude of fretting motion and validate assumptions made in Chapter 3 “Loads”. In Chapter 3, it is obvious that for the investigated propellers, the total spindle torque overcomes the total friction torque (for positive and negative values), and therefore, the fretting regime is most likely the gross sliding.

Static models fail to describe friction in a physically accurate way, but they are relatively simple to use. In addition to the non-physical interpretation of friction, they have few other drawbacks. Main problem of static models is their discontinuity at zero velocity. As illustrated in Figure 4.10, some static models are not suitable for zero velocity. The pre-sliding behaviour is also lacking. It is possible to simulate the pre-sliding displacement by introducing a coarse threshold speed, but it is more of a way to

overcome the discontinuity than true hysteretic behaviour. Figure 4.15 shows a large drift of a static friction model when the actuating force is below the break-away force. All these disadvantages make static friction models difficult to use for solving the problems that are closely related to pre-sliding behaviours. However, for gross sliding problems, the static friction models are very convenient. Their simplicity makes them easy to use and certainly suitable for quality analysis of gross fretting motion. Moreover, they are found in a wide range of applications that involve gross sliding.

Dynamic friction models describe friction in a physically realistic way. They do not have problems with discontinuity, but can exhibit problems related to drifting. In this chapter, the LuGre model was presented in detail as a typical dynamic friction model. Of course there are other models, such as in [Bliman, 1995], but they all originate from Dahl's model, and the difference among them is not too expansive for the scope of this investigation. Dynamic friction models are superior over static friction models for pre-sliding behaviour. However, their complexity can be challenging. The selection of the right parameters is often crucial and difficult. It requires advanced modelling techniques and sophisticated measurement equipment to verify the results. In this work, fretting motion in the blade bearing is investigated for real values of Coulomb friction, actuating force and inertia. Since real forces in the blade bearing are much higher than in the experiment, some adjustment of parameters, as listed in Table 4.1 are needed.

In the following chapter, the amplitude of the fretting motion will be investigated using a mass-spring model of a CPP. Two friction models are selected in order to eliminate/reduce any uncertainty of results caused by a selection of the correct friction model. One model is a static friction model and other is a dynamic friction model. The selected dynamic friction model is the LuGre model, as defined in Equations (4.13), (4.14) and (4.15):

$$\begin{aligned} F_{fr} &= \sigma_0 \cdot z + \sigma_1 \cdot \dot{z} + \sigma_2 \cdot \dot{x} \\ g(\dot{x}) &= F_c + (F_s - F_c)e^{-(|\dot{x}|/v_s)^2} \\ \dot{z} &= \dot{x} - \frac{\sigma_0 \cdot |\dot{x}|}{g(\dot{x})} \cdot z \end{aligned}$$

Since selection of the right parameters in LuGre is achieved in a rough way, the static friction model is used as an additional check of results obtained from the LuGre model. The selected static friction model is from Equation (4.8):

$$F_{fr} = \begin{cases} \text{sgn}(\dot{x}) \cdot (F_c) & |\dot{x}| \geq v_{th} \\ \frac{\dot{x}}{v_{th}} \text{sgn}(\dot{x}) \cdot (F_c) & |\dot{x}| < v_{th} \end{cases}$$

The selected static model does not include the Stribeck effect. In order to investigate the relevance of including the Stribeck effect, results obtained with the selected static model can be compared with the results obtained using Equation (4.7). By comparing results obtained with the LuGre model and the Equation (4.8) model, it is certain that the trends (of results) are correct and assumptions from Chapter 3 can be checked.

4.6. Modelling of fretting motion

The CPP mechanism is described in Chapter 2. Here, a somewhat simplified model is used to estimate the amplitude of the fretting motion and provide answers on questions stated in the beginning of this chapter. Figure 4.21 shows one blade of a CPP and its actuating pin, yoke in the hub, and hydraulic oil. As shown in Chapter 3, the fretting motion in a blade bearing can be caused by an oscillating spindle torque, and is opposed by the friction force and hydraulic force. The friction force acts on the blade bearing and the hydraulic force acts on the yoke.

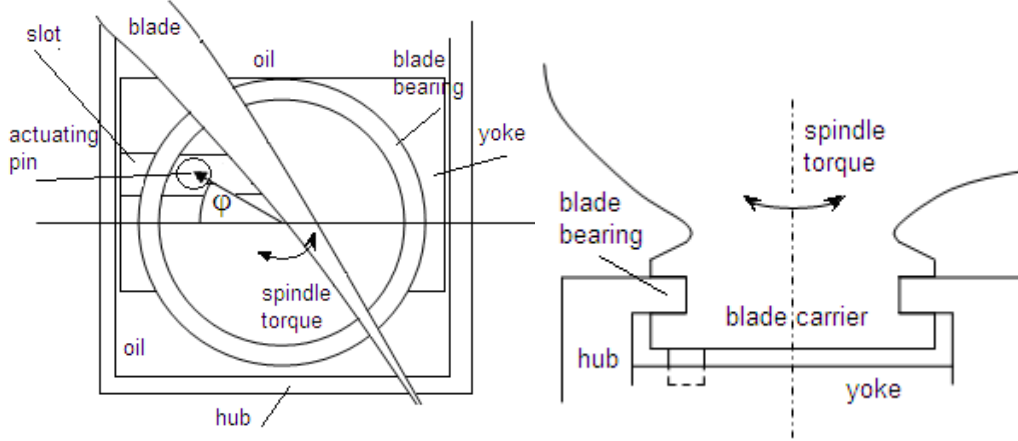


Figure 4.21: Simplified drawing of a CPP without proper scaling of components.

The yoke and the blade are connected via a pin-slot mechanism, whereby the pin of the blade carrier is located in the slot of a yoke. The pin of the blade carrier and the blade carrier are one body and no elastic deformations are assumed. Furthermore, it is assumed that the blade carrier and blade are one rigid body, (i.e. no elastic deformations and no slip between blade and blade carrier). The motion of the blade carrier over the blade bearing is considered as the motion in a blade bearing. Moments acting on a blade (for a non-actuating regime) can be described by:

$$I_{\text{blade}} \ddot{\phi} = M_{\text{sp}} - Q_{\text{fr}} - M_{\text{hyd}} \quad (4.20)$$

where the inertia of the blade includes a water entrained effect. Oil in the hydraulic system can be presented as a spring with the stiffness k . The oil bulk modulus is defined as the pressure increase needed to gain the relative change in volume:

$$\beta = -V \frac{\partial p}{\partial V} \quad (4.21)$$

For the oil used in a CPP the bulk modulus is estimated to be approximately $1.5 \times 10^9 \text{ N/m}^2$. The oil volume in the hub is estimated at approximately 250 liters and the yoke area is 0.95 m^2 . This gives the length of the oil spring in the hub as 0.25 meters. The expression in Equation (4.21) can be modified to:

$$\beta = -V \frac{\partial p}{\partial V} \Rightarrow \partial p = \frac{\beta}{V} \partial V \quad (4.22)$$

If it is assumed that the oil is much more compressible than the bronze around it, and any change in pressure can be represented as a change in the length of the oil spring:

$$\frac{\partial F}{A} = \frac{\beta}{A \cdot l} A \cdot \partial l \Rightarrow \partial F = \beta \frac{A}{l} \partial l \Rightarrow k_{oil} = \beta \frac{A}{l} \quad (4.23)$$

Therefore, the oil compressibility in this case is estimated to be approximately 5.7e9N/m. Figure 4.22 illustrates the mass-spring model of a CPP, spindle torque causes rotational motion of the blade carrier and pin (ϕ), which is then converted into a linear motion of the yoke (x_{yoke}), which subsequently deforms the oil spring. Please note that, as in Chapter 3, all elastic deformations are neglected. Moreover, blade, blade carrier, and pin are assumed as one rigid body.

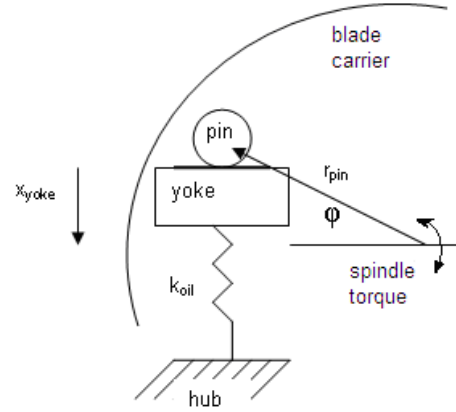


Figure 4.22: Illustration of the mass-spring model used in Equation (4.21), (4.22), and (4.23).

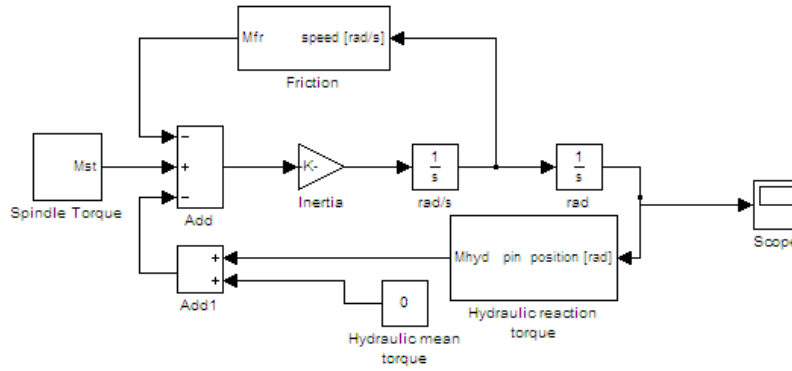


Figure 4.23: Matlab Simulink model of Figure 4.22

Figure 4.23 shows the Matlab Simulink model of the physical model shown in Figure 4.22. The spindle torque is opposed by the friction torque in the blade bearing and by the hydraulic reaction. The hydraulic moment in Equation (4.20) can be divided into its mean value and reaction value:

$$M_{hyd} = M_{hyd}^{mean} + M_{hyd}^{reaction} \quad (4.24)$$

The mean value of hydraulic pressure is the same as a holding or non-actuating hydraulic pressure. The reaction part of the hydraulic moment can be written as:

$$M_{hyd}^{reaction} = F_{hyd}^{reaction} \cdot r_{pin} \cdot \cos \phi \quad (4.25)$$

The force generated by the oil spring can be written as:

$$F_{\text{hyd}}^{\text{reaction}} = \Delta x_{\text{yoke}} \cdot k_{\text{oil}} \quad (4.26)$$

$$\Delta x_{\text{yoke}} = r_{\text{pin}} \cdot (\sin \varphi - \sin \varphi_0) \quad (4.27)$$

Where φ_0 is the angle where $F_{\text{hyd}}^{\text{reaction}}$ is zero. Figure 4.24 shows the design values of spindle torque and Coulomb friction in the blade bearing. In order to better illustrate the ratio of the spindle torque and friction, the friction torque is multiplied with the sign of the spindle torque. In the following analysis, these loads are used, if not otherwise stated. These are the same loads as set out in Chapter 3 for the design case.

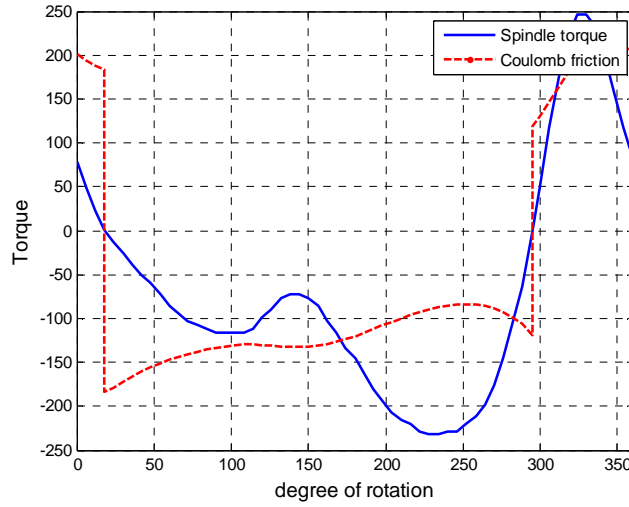


Figure 4.24: Design total spindle torque and Coulomb friction torque in the blade bearing of the investigated CPP. Friction force is multiplied with the sign of spindle torque.

4.6.1 Adjusting of the LuGre model

In order to describe friction in blade bearing for design conditions, there are two reasons why the values of LuGre model from Table 4.1 need certain adjustments. Firstly, all values in Table 4.1 are given for translating model, but the simulation uses Equation (4.20), made for rotating motion. Therefore, all values in Table 4.1 must be multiplied with radius of the blade bearing. Secondly, coefficients of LuGre model depend on value of Coulomb friction which was much lower for Table 4.1 than for the design conditions. One way to select a proper value for σ_0 is to assume that the steady state asperity deflection (z_{ss}) is equal for conditions in Table 4.1 and for design conditions. Since there is no viscous friction, it will be assumed that the total friction force for steady velocity is equal to the Coulomb friction. Then the steady state asperity deflection for steady velocity is:

$$z_{ss} = \frac{F_{fr}}{\sigma_0} \quad \text{when } (|\dot{x}| > 0) = \frac{F_c}{\sigma_0} \quad (4.28)$$

This gives $z_{ss} = 2.7 \mu\text{m}$ for the value of Coulomb friction in the experiment and for σ_0 as in Table 4.1. However, in the design conditions, in Figure 4.24, Coulomb friction oscillates significantly. Therefore, the average value of Coulomb friction in design conditions is used as a reference value. For $z_{ss} = 2.7 \mu\text{m}$ and an average value of design Coulomb friction, the new asperity stiffness for the rotating model is $5e10 \text{ N/rad}$. The difference between the break-away force and kinematic friction coefficient will remain the same. The Stribeck coefficient changes only for rotation velocity, where the value of v_s in Table 4.1 is divided by the radius of the blade bearing.

Since the asperity stiffness of the LuGre model has increased, it is also necessary to increase the damping factor σ_1 . The damping coefficient (σ_1) must be corrected for more than just a rotation effect. Correction is undertaken for design conditions so that the damping of the friction force is sufficient, but also takes into effect the pre-sliding displacement. Figure 4.25 shows the influence of the damping coefficient (σ_1) on the modelled friction force for design of this Coulomb friction. On the left side, σ_1 is the same as in Table 4.1, and on the right, σ_1 has a new value (all other parameters have the same values). It can be seen that the old value of σ_1 does not damp the vibrations of the LuGre model. The new value of σ_1 has been selected so that the vibrations are sufficiently damped. The final values of the parameters describing the LuGre model are listed in Table 4.2, and these values are used in the following analysis.

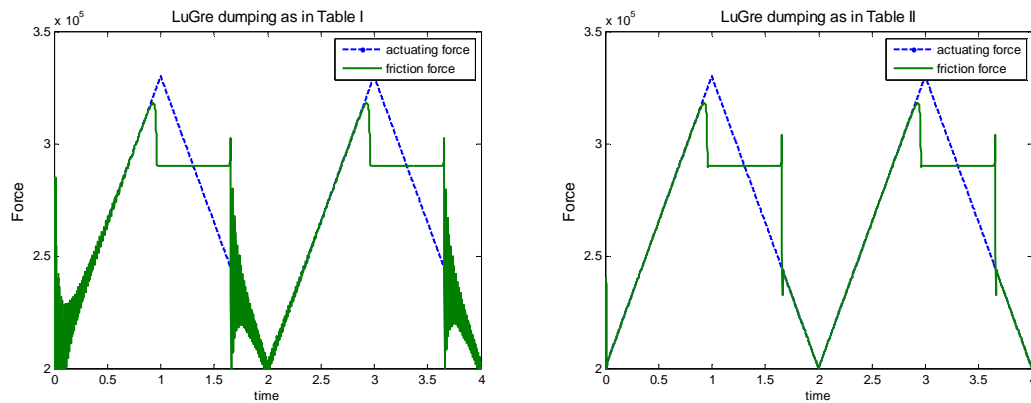


Figure 4.25: Influence of damping factor σ_1 on friction behaviour. Left: σ_1 is as in Table 4.1. Right: σ_1 is increased until vibrations are damped.

Table 4.2 Adjusted parameters of the LuGre model for analysis of (rotating) fretting motion in the blade bearing in design conditions.

Parameter	Value	Unit
σ_0	$5e10$	[N/rad]
σ_1	$1e8$	[Ns/rad]
σ_2	0	[Ns/rad]
F_s	$1.1 \cdot F_c$	[N]
v_s	0.002	[rad/s]

However, the values from Table 4.2 will result in a lower pre-sliding displacement. Figure 4.26 shows the influence of σ_1 on a pre-sliding displacement for situations similar to those in the experiment, i.e. with the same rate of tangential force. The only difference is in Coulomb friction, where it is as set out for the design conditions (which

is much higher than in the experiment). The final pre-sliding displacement is slightly lower than 40 μm .

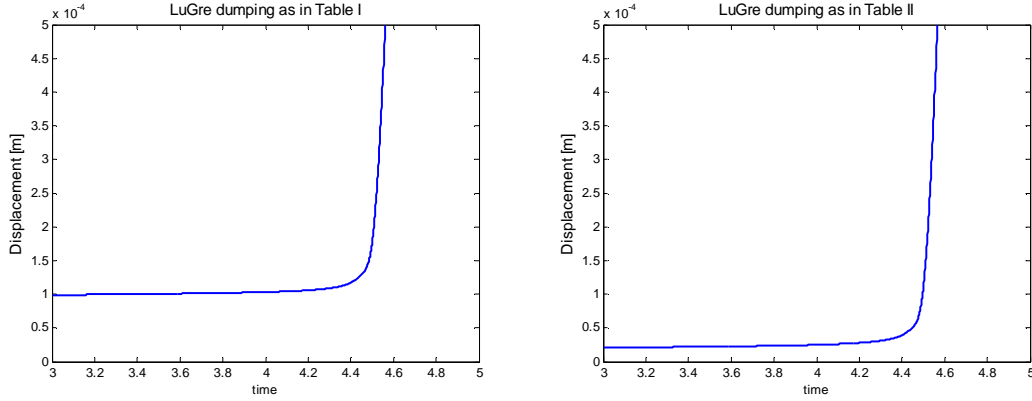


Figure 4.26: Influence of damping factor σ_1 on the pre-sliding displacement. Left: σ_1 is as in Table 4.1. Right: σ_1 as in Table 4.2. Note that the conditions are similar to Figure 4.17 but for the design case.

It would be very difficult to actually verify experimentally these values for a real CPP, as the Coulomb friction is high, parts are huge, and mass and loads are enormous. The results of experiment are useful to estimate how accurate the parameters in Table 4.2 are. The compromise between the pre-sliding and gross sliding aspects has been made, the pre-sliding displacement is relatively similar to the one from experiment and the vibrations of friction force for oscillating actuating force are low.

4.6.2 Fretting motion in the blade bearing

The motion of the blade carrier in the blade bearing is modelled as in Equation (4.20):

$$I_{\text{blade}} \ddot{\varphi} = M_{\text{sp}} - Q_{\text{fr}} - M_{\text{hyd}}$$

The calculation is done for the design conditions, with values of spindle torque and Coulomb friction torque as shown in Figure 4.24. Note that it is assumed that the mean hydraulic moment is zero. Therefore, Equation (4.20) can be written as:

$$I_{\text{blade}} \ddot{\varphi} = M_{\text{sp}} - Q_{\text{fr}} - M_{\text{hyd}}^{\text{reaction}} \quad (4.29)$$

Figure 4.27 shows the modelled motion of the blade carrier, under design conditions, using the LuGre friction model. The motion is shown on the left side as a function of the blade position with 0 degree as the blade's top position. In order to have a better look at the start of the motion and how it continues, the motion is shown for 540 degrees (1.5 rotations of the blade) together with the Coulomb and spindle torque on the right. The pre-sliding motion is from 0 degree to 175 degrees blades position. The gross sliding motion starts at the 175 degree position, when spindle torque overcomes the friction torque. For a short moment, the difference between the spindle torque and friction torque is compensated by the reacting hydraulic torque (i.e. spring) and it stops briefly at 198 degrees. Since the difference continues to grow, the motion continues and it has a maximum negative displacement (85 μm) at 225 degrees. The spindle torque then suddenly drops and the sign changes. The leading edge of the blade enters the wake peak region (see Figure 3.6) and the suction pressure in the leading edge

increases. The blade carrier is pushed back by the hydraulic torque (i.e. spring) and soon the spindle torque (again) overcomes the friction torque in the positive direction.

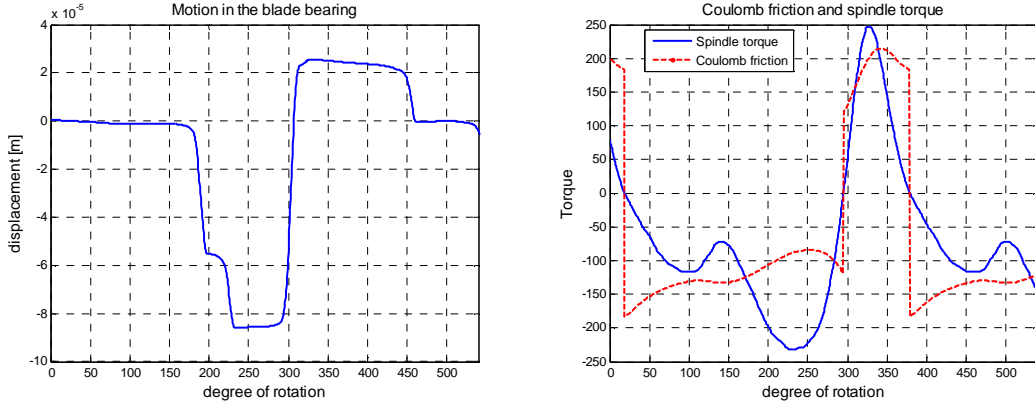


Figure 4.27: The fretting motion in the blade bearing (left) caused by the oscillating spindle torque (right)

The maximum spindle torque is when the suction pressure in the leading edge is highest, just before the blade's top position. This results in the maximum positive displacement (25μm) at 325 degrees. After this, the spindle torque starts dropping quickly, and the blade carrier begins to move back in the pre-sliding regime. As the blade comes full circle, the blade carrier is still in the pre-sliding regime. The gross sliding toward zero position will occur after the spindle torque changes the sign (and “consumes” friction) at 450 degrees. The blade carrier then begins moving back to zero position and later, at 535 degrees, the fretting cycle starts again.

Figure 4.27 indicates a reciprocating small amplitude motion in the blade bearing caused by the oscillating spindle torque. As such, this motion can be called the fretting motion. The total amplitude of fretting motion in the blade bearing is approximately 110μm for design case. There are many aspects that can have an influence on the (estimated) fretting amplitude. They are investigated in the following paragraphs.

4.6.3 Influence of friction model on fretting amplitude

The estimation of fretting amplitude can be influenced by a selection of the friction model. Figure 4.28 shows the modelled fretting motion of the blade carrier, under design conditions, using two different friction models. On the left, friction is modelled using a dynamic friction model and on the right, friction is modelled using a static friction model. The selection of friction models was done in Chapter 4.5. The LuGre friction model was selected for a dynamic model, and Equation (4.8) was selected for a static model:

$$F_{fr} = \begin{cases} \text{sgn}(\dot{x}) \cdot (F_c) & |\dot{x}| \geq v_{th} \\ \frac{\dot{x}}{v_{th}} \text{sgn}(\dot{x}) \cdot (F_c) & |\dot{x}| < v_{th} \end{cases}$$

Figure 4.28 shows only a slight difference of the (modelled) fretting motion related to the selection of the friction model. In both examples, the fretting amplitude is approximately 110μm. Furthermore, both models indicate the periods of gross sliding. However, the richness of the LuGre model is visible, as Figure 4.28 (right) shows no pre-sliding behaviour. It appears that for this investigation, there is no added value in

describing the pre-sliding motion. Moreover, the LuGre friction model required a difficult process of selecting the correct parameters as shown in Chapter 4.6.1.

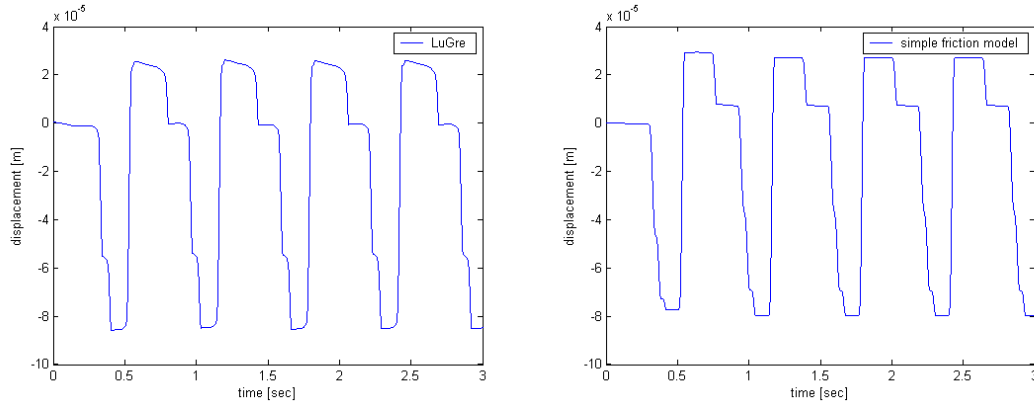


Figure 4.28: Results for amplitude of fretting motion obtained using the LuGre model (left) and static model from Equation (4.8) (right). Amplitude is presented in meters due to its influence on fretting. A distance of 100 μ m corresponds to 0.02 degrees pitch change.

The selected static model does not include the Stribeck effect. Another static friction model was tested in order to investigate the relevance of including the Stribeck effect in the static friction model. Figure 4.29 shows the fretting motion in the blade bearing, where friction is modelled as in Equation (4.7):

$$F_{fr}(\dot{x}) = \begin{cases} (\dot{x} / v_{th}) \cdot (F_c + (F_s - F_c) \cdot e^{-|\dot{x}/v_s|^2}) \cdot \text{sgn}(\dot{x}) + F_v(\dot{x}) & |\dot{x}| \leq v_{th} \\ (F_c + (F_s - F_c) \cdot e^{-|\dot{x}/v_s|^2}) \cdot \text{sgn}(\dot{x}) + F_v(\dot{x}) & |\dot{x}| > v_{th} \end{cases}$$

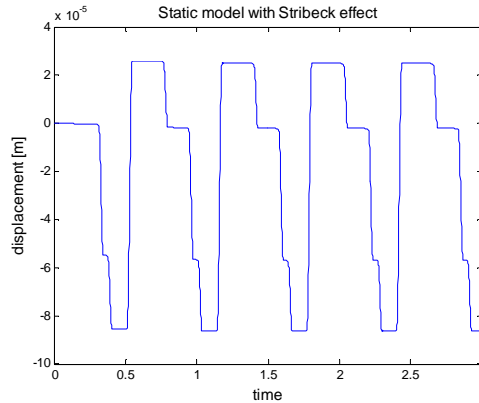


Figure 4.29: Fretting motion in the blade bearing under design loads where friction is modelled as a static model including the Stribeck effect, i.e. Equation (4.7)

The result did not change much when using the static friction model with the Stribeck effect. The amplitude is the same. In comparing Figure 4.29 and Figure 4.28 (right), the only difference is when the spindle torque is negative but lower than the friction torque, a period of between 390 and 535 degrees in Figure 4.27 (right). During that period, the displacement is zero when using the model that includes the Stribeck effect, while for the model without the Stribeck effect, the displacement is slightly above zero (around 10 μ m).

It was shown that for this investigation the selection of friction model is not influential. With all tested models, the fretting amplitude is almost the same. Implications of the selected friction model are discussed elaborately in Chapters 4.9 and 4.10.

4.7. Influence of the design and off-design parameters on fretting motion

Fretting motion in the blade bearing of a CPP is influenced by the many design and off design parameters. It was shown that the investigated propeller exhibits a fretting motion in the blade bearing with 110 μ m amplitude in design conditions. Here, the general influence of design, off design, and operational parameters on fretting amplitude is explored. The analysis is done for the investigated propeller, but the trends are general. Implications of analysis done in this chapter are discussed elaborately in Chapters 4.9 and 4.10.

4.7.1 Influence of hydraulic holding pressure on fretting amplitude

In Chapter 3, it was assumed that the hydraulic mean (holding) pressure has no influence on fretting amplitude. The same assumption was made in Chapter 4.6.2. Here, an evaluation of that assumption is made. In order to investigate the influence of external (holding) hydraulic pressure on the fretting displacement, a constant pressure was added in a form of constant hydraulic torque. Therefore, in Equation (4.20), the mean hydraulic torque ($M_{\text{hydraulic}}^{\text{mean}}$) will have values different from zero, while the spindle torque and Coulomb friction torque are as set out in Figure 4.24:

$$I_{\text{blade}} \ddot{\phi} = M_{\text{sp}} - Q_{\text{fr}} - M_{\text{hyd}}^{\text{mean}} - M_{\text{hyd}}^{\text{reaction}} \quad (4.30)$$

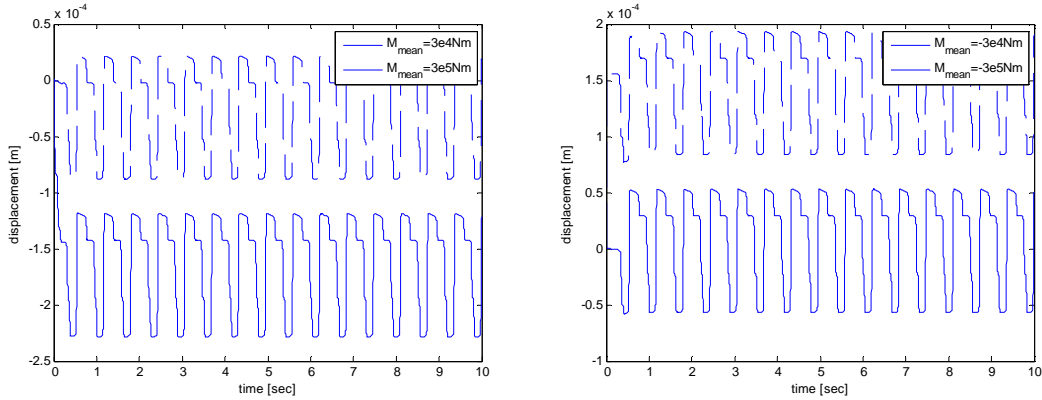


Figure 4.30: effect of positive (left) and negative (right) hydraulic holding pressures on fretting amplitude. (3e4Nm is approximately 1 bar)

Figure 4.30 shows the effect of the mean hydraulic torque on the fretting amplitude. In Figure 4.30 (left), $M_{\text{hyd}}^{\text{mean}}$ has positive values (3e4Nm and 3e5Nm), and in Figure 4.30 (right) negative values (-3e4Nm and -3e5Nm). It can be seen that the mean (external) hydraulic torque has no effect on the amplitude of displacement. However, the external hydraulic torque gives an offset to the vibrations, (i.e. CBV keeps the demanded pitch).

In fact, mean hydraulic holding pressure can be considered as a reaction (force) to the spindle torque. During a non-actuating regime, the CBV is closed and a pressure is created between the yoke and CBV by the spindle torque. In fact, the pressure is created from all blades, and therefore, it is equal to the sum of (mean) spindle torques, or in this case, four blades.

4.7.2 Influence of spindle torque on fretting amplitude

The ratio of spindle torque and friction torque has a major influence on the fretting motion in the blade bearing. The detailed analysis of spindle and friction torque was discussed in Chapter 3. In order to determine how sensitive the fretting motion is on their ratio, the value of spindle torque was changed and the value of Coulomb friction torque kept as its original (design) value. Original (design) values of spindle and Coulomb friction torque are shown in Figure 4.24. Figure 4.31 (left) shows the spindle torque decreased for 20% of the original value and Coulomb friction as its original value. The resulting displacement, Figure 4.31 (right), is 25% smaller than in Figure 4.28

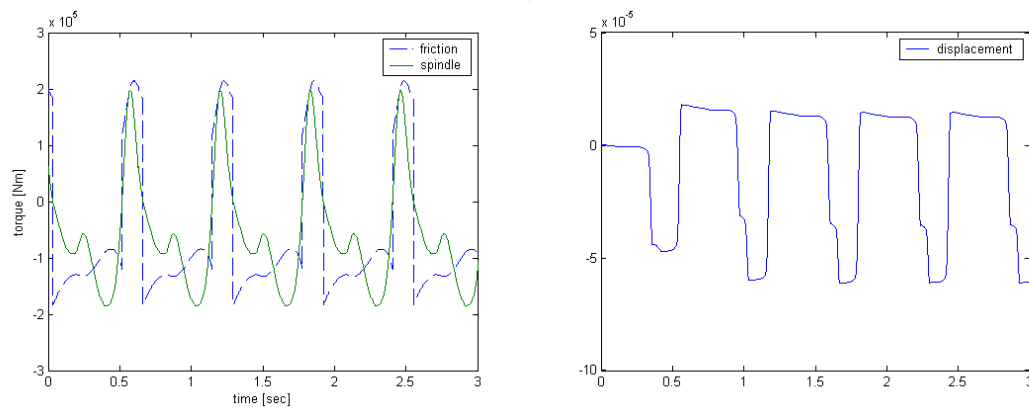


Figure 4.31: resulting fretting motion (right) for 0.8 design spindle torque (left)

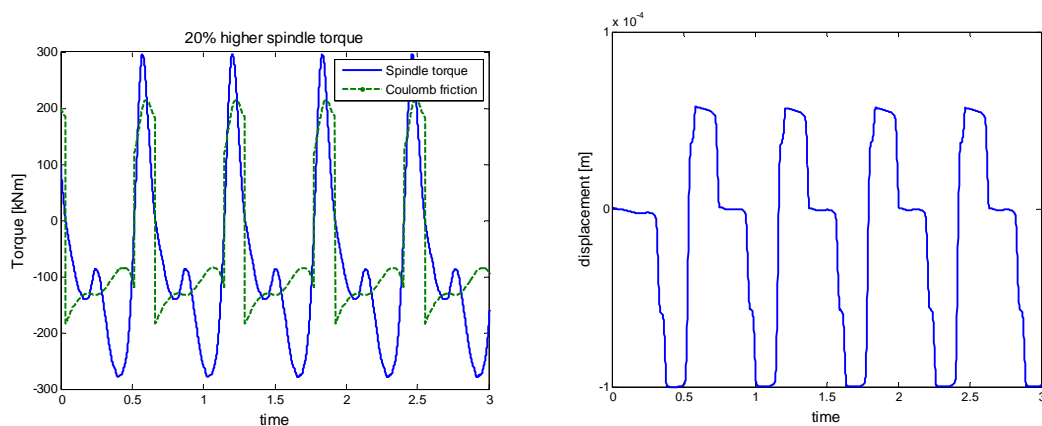


Figure 4.32: resulting fretting motion (right) for 1.2 design spindle torque (left)

Figure 4.32 (left) shows the spindle torque increased for 20% of its original value (in Figure 4.24) and Coulomb friction as its original value. The resulting displacement, Figure 4.32 (right), is 25% larger than in Figure 4.28.

As explained in Chapter 3, the spindle torque oscillation depends on many parameters, and it is affected by the wake field, which is affected by the form of a ship. Clearly, the

oscillation of the blade spindle torque has a strong influence on the amplitude of fretting motion.

4.7.3 Natural frequencies of the CPP or influence of the shaft frequency on fretting motion

The fretting amplitude could be higher if the spindle torque frequency matched the natural frequency of the system. Moreover, it could lead to resonance and catastrophe of the system. Since the CPP is modelled as a mass-spring system, it is interesting to look at the natural frequencies of the system. The calculation of natural frequency (ω_0) is rather simple for the model of four blades, a yoke and oil spring in the hub:

$$\omega_0 = \sqrt{c/I} \quad (4.31)$$

where c is the angular spring stiffness calculated using the stiffness (k_{oil}), from Equation (4.23), and design pitch (ϕ):

$$c = k_{oil} \cdot (r_{pin} \cdot \cos \phi)^2 = 0.65e9 \text{ Nm} \quad (4.32)$$

Total inertia of the system is the sum of all individual inertial moments. The blade inertia includes entrained water:

$$I = 4 \cdot I_{blade} + I_{yoke} = 1.6e5 \text{ kgm}^2 \quad (4.33)$$

The calculated natural frequency is:

$$\omega_0 = 10.1 \text{ Hz} \quad (4.34)$$

The operating frequency of the system (ω) is the blade frequency, i.e. four times the shaft frequency:

$$\omega = 4 \cdot n/60 = 6.33 \text{ Hz} \quad (4.35)$$

It is beneficial that the operating frequency is lower than the natural frequency. However, there is one issue that can easily change the situation and decrease the natural frequency. The value of natural frequency can decrease if the spring stiffness (k) drops. As reported in [Jelali, 2003], the bulk modulus of oil will decrease with the presence of air in the oil, and this will lead to a reduced stiffness (k) and as explained to a risk of resonance.

4.7.4 Influence of propeller skew and chord length on spindle torque oscillation

The following text explores the possibility of reducing the spindle torque oscillations by controlling one design parameter of a propeller, the skew or chord length. The investigation in Chapter 3 raised a concern for other CP propellers in addition to the one investigated. In order to investigate how frequent the fretting motion is in CPP applications, a comparison of spindle torque and friction torque was done for the investigated CPP and similar propellers. The results, as shown later in Chapter 6.1, indicate the risk of fretting being proportional to the skew angle of a propeller.

In [Carlton, 2007], the skew angle of a propeller is defined as the greatest angle, measured at the shaft centre line, in the projected plane, which can be drawn between lines passing from the shaft centre line through the mid-chord¹ position of any two sections. The propeller skew tends to be classified in two types, balanced and biased skews. Figure 4.33 shows a skew angle, a propeller skew, and two types of propeller skews (balanced and biased skew). The investigated case belongs to the balanced type of skewed propellers and in comparing them to other similar CP propellers it has the highest propeller skew.

The influence of propeller skew on the performance of a propeller was investigated in [Bosswell, 1971] and [Oossanen, 1970]. They have measured and calculated open water diagrams (thrust, torque and efficiency) for a propeller with 4 different skews. However, open water diagrams show the mean values of investigated parameters. As shown in Chapter 4.7.2, the fretting motion is highly dependent upon the oscillation of the spindle torque during one revolution of the blade. If the spindle torque oscillation decreases, it is expected that the fretting amplitude will also decrease.

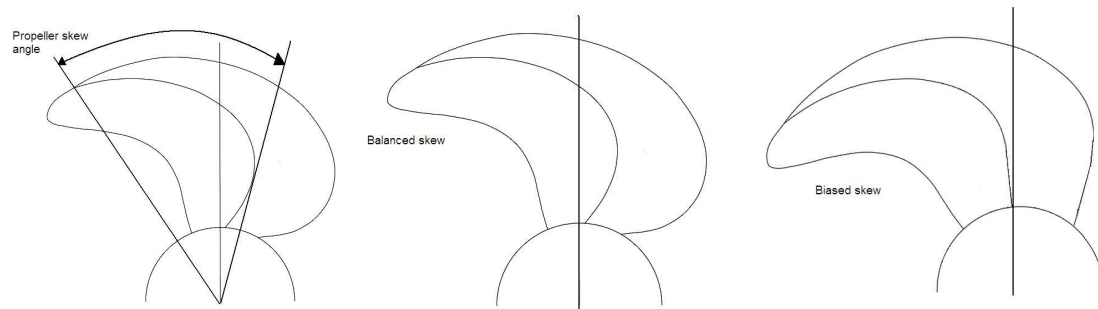


Figure 4.33: Definition of a propeller skew angle and two types of skews.

The influence of the skew angle on the spindle torque of the propeller was explored for design conditions. The skew angle was varied, keeping the balanced skew type of the propeller. Forces and moments acting on the blade were calculated using the same tool as in Chapter 3, the BEM2. Table 4.3 shows the difference between the maximum and minimum value of spindle torque during one revolution as a function of propeller's skew. Furthermore, the average value of spindle torque is given in the same table. Figure 4.34 shows blades investigated in Table 4.3 while Figure 4.35 shows only their skew lines.

Table 4.3: Spindle torque oscillations as a function of propeller skew

Skew [deg]	Spindle torque [kNm]			
	max	min	max-min	average
52.3	259	-225	484	-56.7
49.2*	247	-232	479	-65.8
45.9	235	-240	475	-77.6

*-Design skew

¹ A mid-chord is mid-point on the line between the leading and trailing edges.

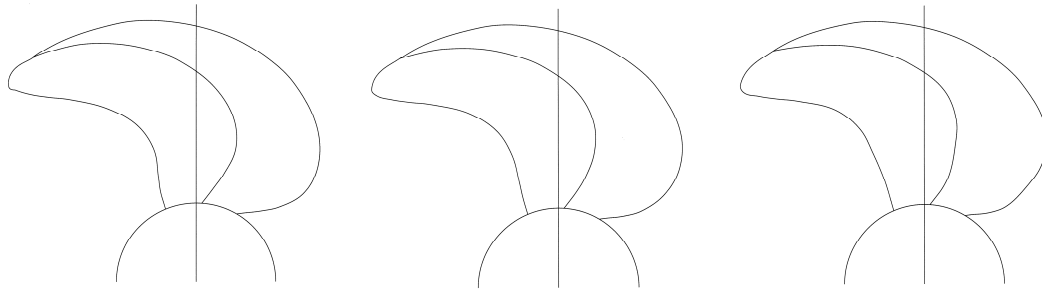


Figure 4.34: Investigated skew angles: left 52.3 degrees, centre 49.2 degrees (design), right 45.9 degrees

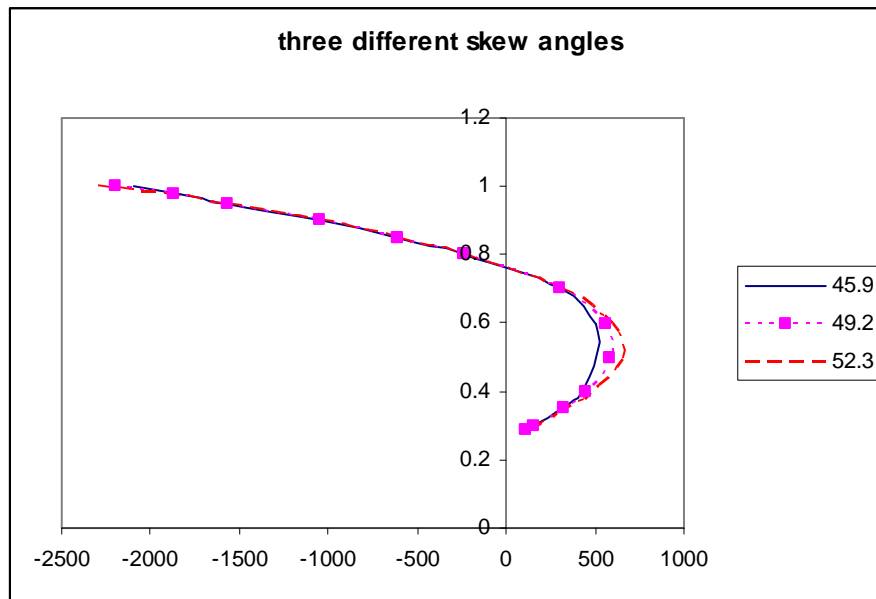


Figure 4.35: Investigated skew angles; x axis shows position of mid-chord point from spindle axis in projected plane; y axis shows radius of the blade

Skew is an influential parameter of a propeller's performance, especially with respect to load distribution and pressure pulses. Propellers with a high skew have a less varying load (more even hydrodynamic pressure distribution) over the blade's surface than propellers with a low skew angle. Results in Table 4.3 show another important aspect of skew. During one revolution, the spindle torque of a high skew propeller oscillates more than the spindle torque of a low skew propeller for the same wake variation. However, the average value of spindle torque is higher for propellers with a low skew angle.

Besides the skew angle, the type of skew was also varied. The biased type of skew is not favourable for a CPP due to high mean values of the blade spindle torque, which will result in high actuating pressures. In the following example the skew angle was not changed but the propeller skew was rotated around the shaft axis. The skew of investigated propeller was rotated for five degrees in positive and negative direction, where positive direction corresponds to a more biased type of skew. Table 4.4 shows the difference between the maximum and minimum value of the spindle torque during one revolution as a function of propeller's skew type. Furthermore, the average value of spindle torque is given in the same table. Figure 4.36 shows the investigated blades while Figure 4.37 shows only their skew lines. As it can be seen from Table 4.4, the type of skew has a high influence on spindle torque behaviour. The biased type of skew tends to create high mean values but lower oscillations of the blade spindle torque during one revolution.

Table 4.4: Spindle torque oscillations as a function of skew type

Rotation of skew [deg]	Spindle torque [kNm]			
	max	min	max-min	average
+5	182	-263	445	-113
Design	247	-232	479	-65.8
-5	317	-199	517	-19.8

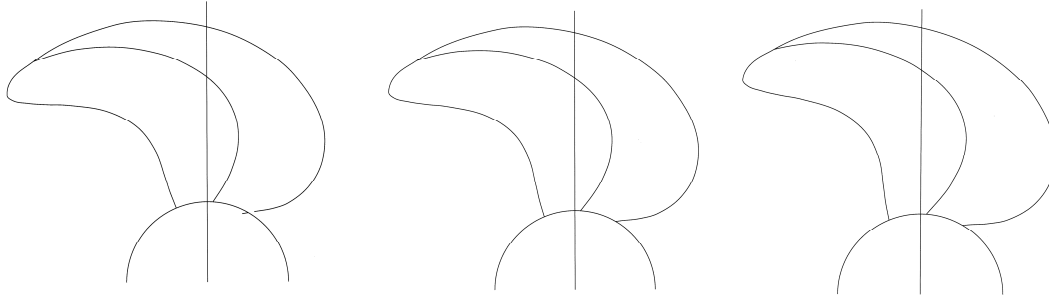


Figure 4.36: Investigated skew types; left: skew rotated for +5 degrees to give more biased skew type, centre: design condition, right: skew rotated for -5 degrees to give more balanced skew type.

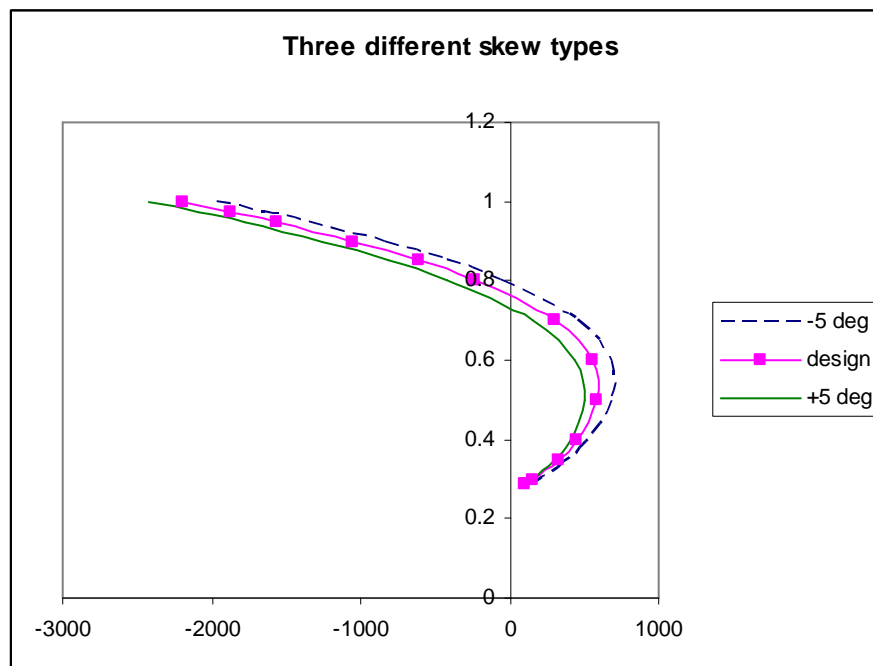


Figure 4.37: Investigated skew types; x axis shows position of mid-chord point from spindle axis in projected plane; y axis shows radius of the blade

The influence of chord length on blade spindle torque was investigated for three different chord lengths. The chord length is defined as the distance between the leading and trailing edge. In Table 4.5 the chord length at each blade section was increased and reduced with 10%. Figure 4.38 shows blades with three different chord lengths. The chord length also has an influence on the spindle torque, blades with higher chord length values (larger blade area) have lower average values of the spindle torque and larger spindle torque oscillations during one blade revolution than the blades with lower chord length values (smaller blade area).

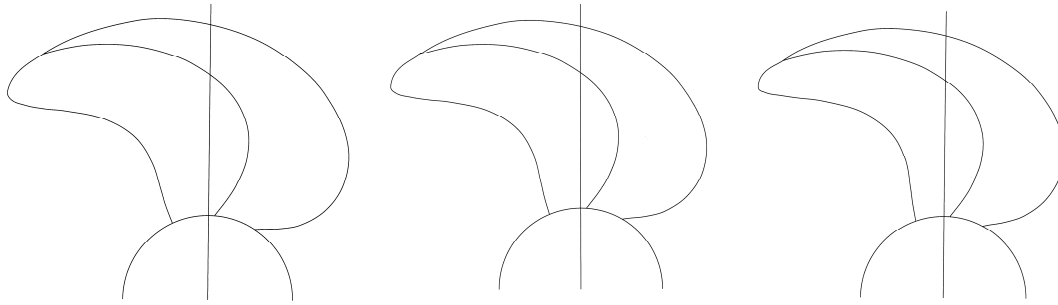


Figure 4.38: Investigated chord lengths; left: chord length increased for 10%, centre: design condition, right: chord length decreased for 10%.

Table 4.5: Spindle torque oscillations as a function of chord length

Chord length	Spindle torque [kNm]			
	max	min	max-min	average
+10%	311	-232	543	-46.2
Design	247	-232	479	-65.8
-10%	193	-230	423	-89.5

For a CPP the mean value of the blade spindle torque plays an important role; lower values of mean spindle torque will lead to lower actuating pressures. It should be remembered that the values of blade spindle torque highly depend on the wake field of the propeller. The analysis done in this chapter is made for the wake field shown in Figure 3.6. From the above made analysis it appears that factors which contribute to a more even load distribution, such as the larger skew angle and blade area, are favourable for lower mean values of blade spindle torque but have a higher variation of the spindle torque during one revolution. A higher variation of blade spindle torque is not favourable for avoiding the fretting.

4.7.5 Influence of backlash on fretting amplitude

All parts in the CPP mechanism are machined with a certain tolerance. These tolerances will result in a clearance/backlash between the actuating pin and slot in the yoke. For fretting motion, this means that for a small part of displacement the yoke and the oil spring are not in contact. The maximal total backlash was estimated at 200 μ m in Chapter 2.10. In the following example, the backlash is modelled as a dead zone, wherein the effect of the oil spring is zero for the displacement of the actuating pin between -100 μ m and 100 μ m.

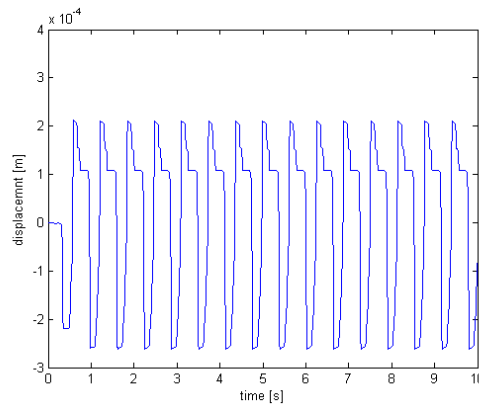


Figure 4.39: The presence of backlash drastically increases the fretting motion

Figure 4.39 shows the fretting motion for design conditions (see Figure 4.24), but includes the effect of backlash. Figure 4.39 indicates a total fretting amplitude of approximately $500\mu\text{m}$. The backlash of $200\mu\text{m}$ leads to an increase of fretting amplitude of $400\mu\text{m}$. This is a drastic increase of the fretting amplitude.

4.7.6 Influence of cavitation and ventilation on spindle torque oscillations

As shown in Chapter 4.7.2 any increase or decrease of spindle torque will have an influence on the amplitude of fretting motion in the blade bearing. In contrast to Chapter 4.7.4, where the possibility of reducing the oscillations of spindle torque was explored, here circumstances leading to the increase of spindle torque oscillations are explored.

The pressure distribution on the blade is affected by the occurrence of cavitation and ventilation. Consequently, spindle torque is affected as well. Cavitation will occur when the hydrodynamic pressure drops below the water vapour pressure. Ventilation occurs when a large amount of air is sucked in by blade rotation. Ventilation may occur at reduced draught, heavy seas, and even without the blade tip protruding above the water surface. The influence of cavitation on the mean value of the blade spindle torque was investigated in [Pronk, 1980]. In [Beek, 2006], the influence of cavitation and ventilation on the variation of spindle torque was studied. Experiments were carried out for the investigated propeller and the following parametric variations were systematically studied:

- the effect of the ambient pressure;
- the effect of the propeller immersion;
- the effect of the propeller loading; and
- the effect of the rudder angle.

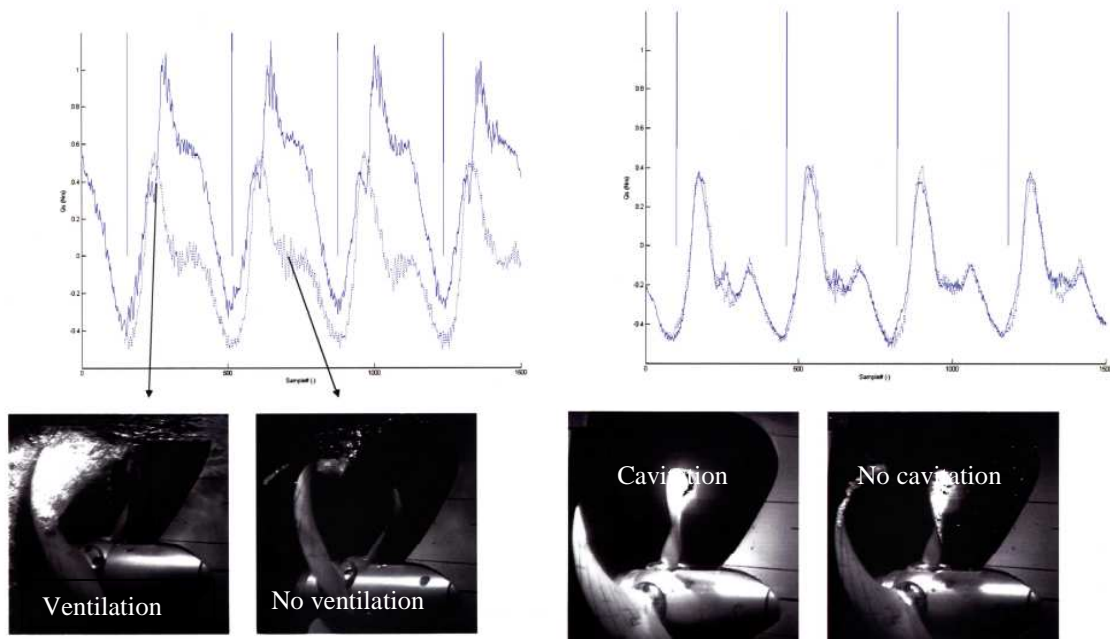


Figure 4.40: Effect of ventilation on blade spindle torque, accomplished by different propeller immersions in atmospheric pressure. Right: Effect of cavitation on blade spindle torque, accomplished by different surrounding pressures. Source: [Beek, 2006]

Results show the blade spindle torque to be strongly affected by ventilation. Figure 4.40 (left) shows the influence of ventilation on the blade spindle torque. However, for the investigated propeller, the blade spindle torque is not affected by cavitation. Figure 4.40 (right) shows the influence of cavitation on the blade spindle torque. In the same work, one interesting finding is that cavitation has “a strong damping effect” on the ventilating spindle torque. Oscillations of spindle torque are much lower when the propeller is affected by both cavitation and ventilation, than when the propeller is only affected by ventilation.

4.8. Influence of fretting motion on hydraulics

In heavy seas ventilation can cause increase of spindle torque and fretting in the blade bearing. Detecting the presence of fretting motion in the blade bearing could be used to detect propeller ventilation and prevent protruding of the blade tip. In heavy seas the presence of fretting could be a signal to the captain to reduce speed. One way to detect fretting motion in the blade bearing is to measure the pressure pulses generated by the fretting motion. Additionally, the same principle might be used to detect fretting motion for design conditions. Figure 4.41 shows the pressure oscillations caused by the motion in a blade bearing of only one blade for design conditions. It is the same as in Figure 4.28 (left), only instead of displacement, the resulting pressure oscillations are shown.

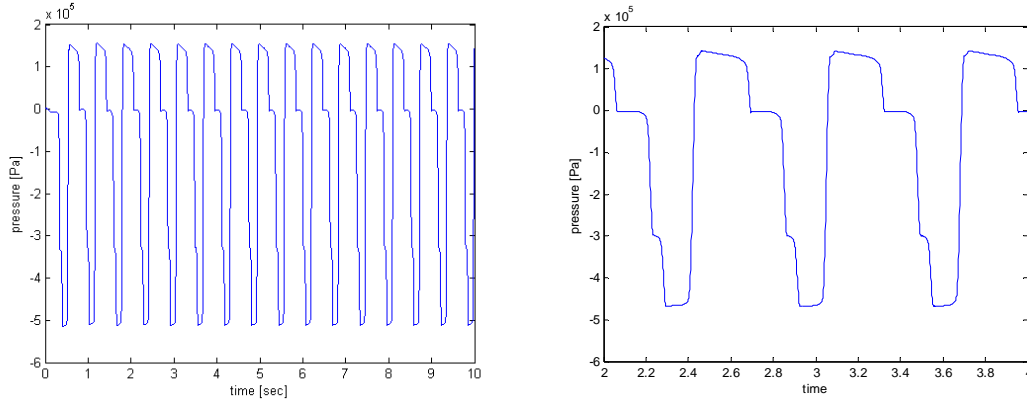


Figure 4.41: Pressure pulses caused by fretting motion using the LuGre model. On the right, zoom between 2nd and 4th second of the simulation.

In fact, the pressure pulses in the hydraulics could be caused by the yoke motion, which is created by fretting motion in all blade bearings. Since the yoke of investigated CPP holds four blades, it is necessary to include all four blades in order to investigate pressure pulses in the hydraulics. To investigate the effect of four blades on pressure pulses in hydraulics, the force acting on the yoke is presented as a sum of four resulting forces, with a 90 degrees phase difference. Each line in Figure 4.42 represents the difference of the spindle and Coulomb friction torque for each blade (bearing). Figure 4.42 (left) shows four forces acting on the yoke, from each blade, and Figure 4.42 (right) shows their sum.

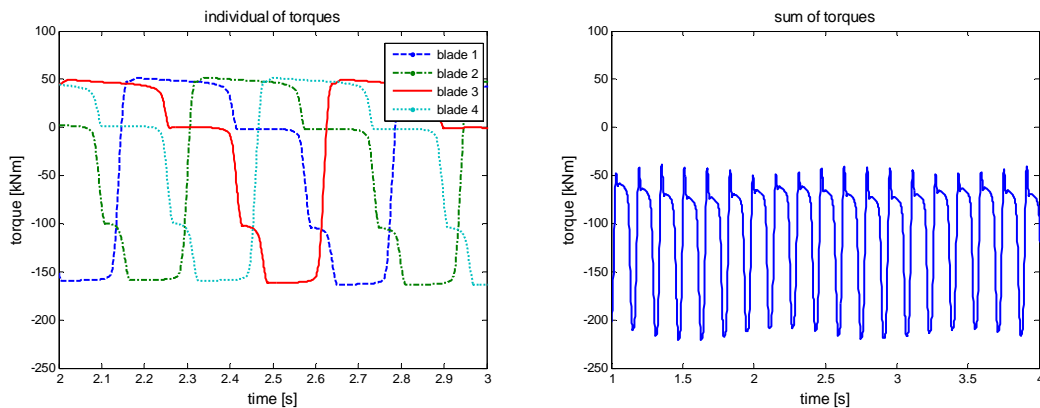


Figure 4.42: Motion in four different blade bearings (left) and their resulting sum (right).

Figure 4.43 shows the comparison of pressure pulses estimated with the LuGre and Equation (4.8) friction model. The input force for estimated pressure pulses is the sum of torques shown in Figure 4.42 (right). In both cases, amplitude is relatively similar. Using the LuGre friction model, it appears as if there is a slow fluctuation of the amplitude of the pressure pulses, while with the Equation (4.8) model, there is no such fluctuation. This is probably a swaying effect of the LuGre friction model which is introduced by additional spring stiffness in the model (σ_0).

The opposite blades will reduce the resulting force and this is reflected in lower amplitude of pressure pulses in Figure 4.43 than in Figure 4.41, where pressure pulses were estimated only for one blade. Important to mention is that these figures do not include friction in other parts of the CPP mechanism, for example pin-slot, yoke-hub, etc. The friction in other parts will reduce the pressure pulses even further. Having said this, there are numerous practical obstacles to detect pressure pulses in the hydraulics

caused by fretting. For example, one of the problems is where to position the sensors. If pressure sensors are put at the end of the shaft it is probable that the pressure pulses will suffer from attenuation (the gradual loss of intensity).

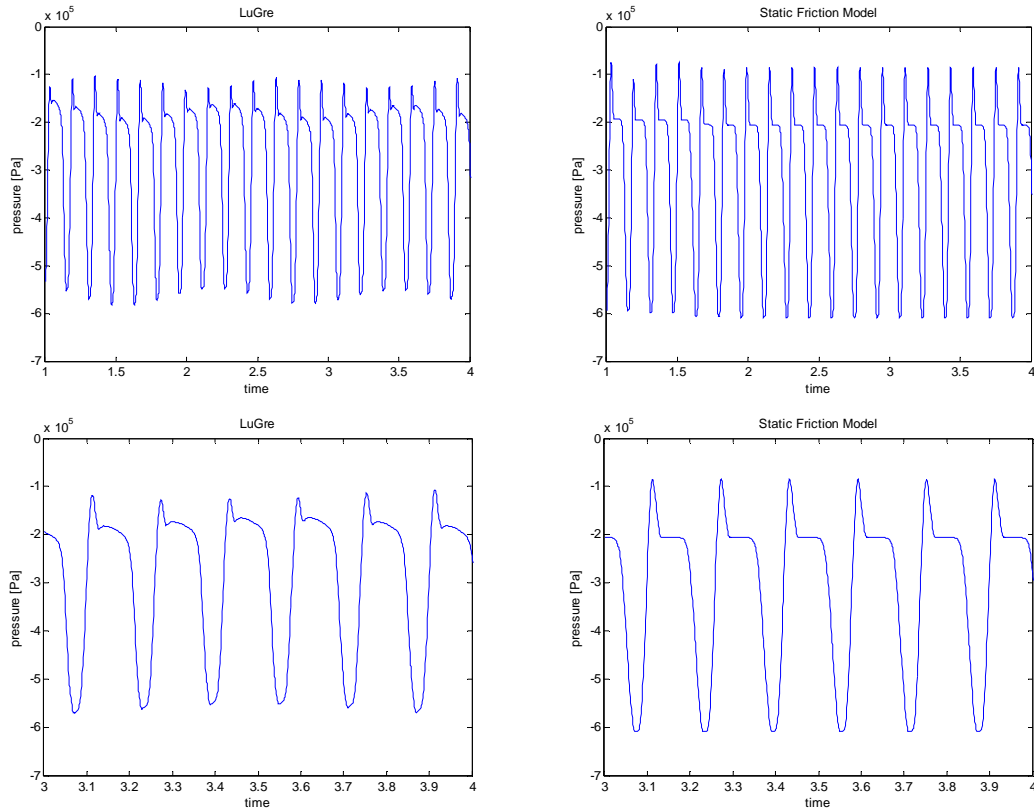


Figure 4.43: Up: pressure pulses estimated by the LuGre model (left) and static model (right). Bottom: zoomed between 3rd and 4th second of the simulation using LuGre model (right) and static model (left)

A mistake could be made if the resulting torque is calculated as a sum of four spindle torques and friction torques. By doing so the spindle torques of opposite blades, blades with 180 degrees phase difference, would compensate each other and the sum of spindle torques would appear to be lower the sum of friction torque. Figure 4.44 shows the sum of four spindle torques and four coulomb friction torques. It appears that the sum of friction torques is higher than the sum of spindle torques (in absolute values). Thus, it appears that there would be no motion, but this is not correct because: the calculation must firstly be done per blade and resulting force on the yoke is the sum of four force differences.

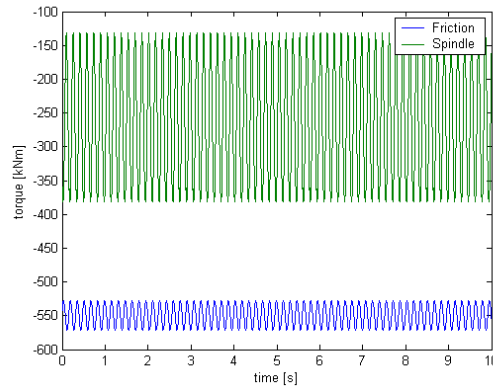


Figure 4.44: Four spindle torques with 90 phase difference have been added (green line) and they appear to be lower than the sum of four Coulomb friction torques (blue line).

The pressure pulses estimated in Figure 4.43 are based on a relatively rough analysis. The situation is much more complex and it calls for a multibody analysis. Additional influence, on the pressure pulses, may come from the backlash. The backlash in the CPP mechanism will mean that not all blades are in the contact with the yoke. Potentially this can lead to 16 different contact situations (one blade and yoke in contact, two blades and yoke in contact, etc). Moreover, motion in backlash causes impacts when bodies get in contact and impacts could cause additional vibrations in the system. How big these additional vibrations will be, depends on the impact and how elastic the impact is. This remains for future investigations.

4.9. Discussion

The ratio of spindle torque and friction in the blade bearing determines the existence of fretting motion. In order to avoid fretting, two options exist - to decrease the spindle torque or increase the friction force. For example, it is possible to increase the friction by increasing the Coulomb friction and/or break-away force. The Coulomb friction can be increased by increasing the normal load or friction coefficient. However, these options are not recommended as they imply higher loads. The break-away force can be increased by a lower rate tangential force, and by doing so, it is expected that the fretting motion would be delayed and possibly reduced. However, the rate of tangential force, spindle torque in this case, is too high to make this solution feasible.

The only sound solution to reduce the fretting motion is by reducing the oscillations of spindle torque. In Chapter 4.7.4, the relation of spindle torque oscillations to the skew angle of the propeller was investigated. In a practical way, it was shown how to reduce the spindle torque oscillations for a given wake field. As a result of relatively even pressure distribution, high skew propellers are easier to rotate around their spindle axis. As seen in Table 4.3, the average value of a spindle torque is lower for a high skew blade. The low value of average mean spindle torque makes it easier to change the pitch, and it reduces the actuating hydraulic pressures. This is very important for a CPP. On the other hand, such a highly mobile situation is favourable for the fretting motion in a blade bearing. In Table 4.4 and Table 4.5 the influence of the type of skew and blade area on the behaviour of spindle torque was presented. From Chapter 4.7.4 it appears that factors which contribute to a more even load distribution, such as the larger skew angle and blade area, are favourable for lower mean values of blade spindle torque but have a higher variation of the spindle torque during one revolution. There are

other parameters of blade geometry which might have an influence on the spindle torque. It is recommended to investigate their influence in future research.

Of course, oscillations of spindle torque are initially influenced by the wake field of the propeller. As the leading edge of the blade enters the wake peak region, the suction pressure in the leading edge increases and the blade spindle torque increases sharply. The hull form of a ship has an influence on a ship's motions in heavy seas. The experiments done in [Beek, 2006] indicate strong effect of ventilation on spindle torque. Oscillation of spindle torque can increase twice with the presence of ventilation. Ventilation occurs at low draught or it can be induced by the ship's motions when the propeller tip gets close to the water surface. As a result of ventilation, fretting motion in a blade bearing can occur even in cases where the design spindle torque is below the Coulomb friction torque. The form of a ship does not only influence fretting by the wake field, but also by ship motions in heavy seas.

The measurements of friction described in Chapter 4.3 clearly recorded the presence of the Stribeck effect. It is estimated that the difference between break-away force and kinematic friction is approximately 10 percent. The same value of dynamic friction coefficient was also measured on a different test setup presented in Chapter 5. Moreover, the measured value of the dynamic friction coefficient is in line with the design and service experience.

The model of one blade and oil spring is very simple, but useful. Much effort has been put into the selection of the appropriate friction model. The results of the fretting amplitude were compared for two different friction models, one static and the other dynamic. The selected dynamic model, the LuGre model, shows very complex behaviour, but it takes significant effort to select the right parameters. On the other hand, the static model is not as complex, as it does not describe pre-sliding in a detailed way. However, the fretting amplitude is not affected by the selected friction model. With both friction models, the amplitude of the fretting motion is estimated to 110 μ m. For the investigated propeller, both models show the fretting motion to be the gross sliding fretting motion. Here, an additional remark can be made by looking at the load distribution around the blade bearing in Chapter 3, and fretting wear as explained in Chapter 2. There is always a part of blade bearing exposed to partial slip fretting motion if the both sides of the blade bearing (inner and outer) are loaded. However, the specific wear rate is lower for partial slip than for gross sliding. The model in Chapter 4.6 has no damping effect, and oil is modelled only as a spring. However, in [Bakker, 2005], a strong dependence of actuating pressure on actuating (pitch) speed was recorded. This leads to the conclusion that the viscous friction and damping are very pronounced. If the damping effect is present in a CPP, it can be expected that it would have positive effects, and that the fretting amplitude should be smaller, and the danger of resonance reduced. In Chapter 4.7.3, the importance of natural frequency for large CPP's was illustrated. Due to the large inertial moments, the operating frequency of a large CPP is close to its natural frequency, and the danger of resonance is present. In this case, in the author's opinion, these two frequencies are too close. It should be remembered that the presence of air in oil has a significant influence on oil compressibility. The small presence of air can change the compressibility by a factor of 10, and brings the operating and natural frequency to the same value. In addition to damping, there is another question related to the model presented in Chapter 4.6. The hub of the CPP was selected as a ground point. However, oil in the hub and oil in the

pipe are connected. Following the same calculation as in Equations (4.21), (4.22) and (4.23), the stiffness of the oil spring in the pipe is much lower than the stiffness of the oil spring in the hub. If the end of the shaft (CBV is there) is selected as the ground point, the mass of the hub and shaft should probably be taken into the calculation of natural frequency.

In addition to the spindle torque itself, the most significant influence on fretting motion is clearance in the bearing (backlash). In Chapter 4.7.5, it was shown that most of the motion will occur within the backlash of a CPP mechanism. In fact, a fretting motion for a mechanism with the backlash ($500\mu\text{m}$) is larger than the sum of the fretting motion for a mechanism without backlash ($110\mu\text{m}$), and the backlash ($200\mu\text{m}$). This leads to a conclusion that the blade picks up additional momentum within the backlash. The first instinct to reduce the fretting motion is to have smaller tolerances. However, the tolerances of a system are very important for preventing the seizure of a system. The danger of seizure is present if worn out particles oxidise and stay stuck in between two parts. In this work, the backlash is modelled as a dead zone and impact between the actuating pin and the yoke is purely plastic. In real situations, it might be possible that some amount of elastic impact occurs and creates some additional vibrations. This is especially true if involved masses and forces are extremely large. The issue of backlash and multi-body dynamics is very complex and requires some future attention.

In Chapter 4.8, it was shown that if fretting occurs, pressure pulses in the hub are expected. Pressure pulses created by all four blades are smaller than the pressure pulses created by only one blade due to the phase difference between blades. However, the situation is much more complex and it requires future multi body investigation which will include effects of backlash. The potential of this issue is larger than only detecting the existence of fretting wear. Theoretically, the same principle could be used to detect ventilation and indicate to the captain to reduce the ship speed in heavy seas. It is not clear if it is really feasible to detect these pressure pulses at the other end of the shaft, where the CBV is. In examining the measurements done in [Pronk, 1980] and [Bakker, 2005], the behaviour of the actuating pressure at the CBV is somewhat different than expected. They recorded no Stribeck effect and have a very strong presence of viscous friction. Most likely, it is necessary to measure the hydraulic pressure directly in the hub to be able to detect the fretting motion in the blade bearing.

4.10. Conclusions

The fretting motion in the blade bearing of a CPP occurs when spindle torque of the blade overcomes the friction torque in the bearing. Other parameters that can significantly increase the fretting motion (maybe even become governing factors) are draught, skew, mass (size), ship form, and backlash in the mechanism.

Here, the goal was to provide answers to questions stated in the beginning. In that respect, it can be stated that:

- The amplitude of fretting motion in the blade bearing for the investigated propeller is approximately $100\mu\text{m}$ for design case;
- The hydraulic holding pressure cannot oppose the fretting motion. However, it is possible that additional friction could be generated by the hydraulic holding pressure, namely in the pin-slot bearing and axial part of the blade bearing. The hydraulic holding pressure will hold the demanded pitch;

- Theoretically, fretting motion in the blade bearing should create the motion of yoke and pressure pulses. However, it is not likely to be able to detect them in the OD box;
- The influence of backlash on amplitude of fretting motion is large. Amplitude increases not only for the clearance in the bearing (backlash is 200 μ m), but the body picks up additional speed and gives a total fretting amplitude of 500 μ m; and
- Ventilation increases the spindle torque drastically, and as such, can introduce fretting motion.

Additional remarks that can be made:

- The type of friction model was not important in evaluating fretting amplitude of gross slip motion;
- The natural frequency of the investigated system is dangerously close to the working frequency;
- The influence of spindle torque on fretting motion is direct. A low oscillating spindle torque is beneficial for reducing the fretting motion;
- The skew angle, skew type, and chord length of a propeller have an influence on load distribution over the blade's surface. As such, they can influence the mobility of a blade around its spindle axis; and
- Reducing the backlash will help in reducing the fretting motion. However, in the case where fretting motion results in fretting wear, the worn debris of material can get stuck in the bearing, where it can oxidize and cause seizure of the bearing.

5. Wear experiments

Wear as a failure mechanism can lead to two failure modes of a blade bearing, namely worn-out and seizure. Wear experiments contribute to a better understanding of wear and friction in the blade bearing of a CPP as a failure mechanism. The main parameters needed for experiments, such as load, motion, and materials, have been defined in previous chapters of this thesis. In this chapter, in accordance with the main goal of the thesis, 9 experiments were carried out on 4 different test setups with more than 70 test samples. The following text presents the testing procedure, results and discussion of the experiments done.

5.1. Introduction

In order to present the parameters for tests done in this chapter, a short overview of the previous findings is presented here.

In Chapter 2, materials and mechanism of a CPP are presented. It was stated that the focus of this investigation is on the blade bearing of a CPP due to its high loads and its influence on the size of the hub. In turn, the hub size has an influence on the hydrodynamic efficiency of the propeller. Failures occurring in a CPP that are of interest for this investigation are the total amount of wear exceeding the allowable wear (worn out CPP) and seizure of a CPP mechanism. The materials used for a blade bearing are usually a CuNiAl and Mn-Al bronze combination or a CuNiAl and Ni-Cr steel combination for high load application. Additionally, despite the fact that it is known that PTFE (Teflon) coatings have bad wear resistance characteristics, two types of PTFE coating are tested because of their attractive friction characteristics.

In Chapter 3, loads in the blade bearing were analyzed. While loads during pitch actuation (actuating regime) are straightforward, the loads in blade bearings during the non-actuating regime yielded more interesting results. High oscillations of hydrodynamic spindle torque, in combination with a well-balanced blade, can lead to a fretting motion in the blade bearing. Moreover, in examining the practical experience with CPPs, there are reasons to suspect that fretting wear may occur in some cases and the damage caused by it may be significant.

In Chapter 4, the amplitude of the fretting motion was analyzed. It was shown that the amplitude of the fretting motion depends upon the clearance in the mechanism, but that it is less than 1mm. The frequency of the fretting motion was shown to depend upon the shaft rotational speed.

In addition to the fretting motion, there is a gross sliding motion in the blade bearing. For the sake of completeness, it should be stated that it is possible to make a subdivision of gross motions generated by the hydraulic system into large and small amplitude sliding motions. Large amplitude sliding motion is caused by the hydraulic system and has a low frequency. The largest amplitude of sliding motion is from full-pitch ahead to full-pitch astern, for example during the crash-ahead manoeuvre. The large adjustments in pitch may occur only a few times a day for large ships, and a few times an hour for tug boats. The small amplitude sliding motions would be the small pitch adjustments, they are relatively frequent (every 10 to 120 seconds) and have amplitude of between 0.5 and 5 degrees. The exact figures depend upon many things, such as leakage, sealing, control strategy, etc.

5.2. Experiments for wear

The reason for performing a wear test is to provide data that can be applied in a way to increase life, reduce cost and maintenance, and increase reliability. Of course, in addition to this end result, the test should provide the data about a wear mode, wear behaviour, wear coefficients, as well as identify the transition points, etc. As discussed previously, the nature of wear is very complex. There are several mechanisms of wear, each of them sensitive to numerous parameters and not necessarily in the same way. There is no single, unique and universal parameter that can be used to characterize wear behaviour. As a consequence, there is no single, unique and universal wear test. Also, as mentioned previously, wear is not a material property, and wear tests do not provide us with definite material characteristics that can be related directly to all possible applications of tested materials. As a result of several wear mechanisms and numerous parameters, a question that arises is which wear test is the most appropriate. The key to the relevance of any wear test to the application lies in the degree to which the application is simulated in the test. However, increasing the realism of the test increases costs and decreases the control over the experiment and the overall understanding of experiment.

There are several levels of wear experiments. In each wear experiment, the intention is to simulate a wear situation up to a certain level. The most basic level (first level) is a simulation in terms of the general nature of a wear situation. The first level simulation is concerned with representing the basic facts of the wearing process, such as the type of motion (sliding, rolling, and impact), lubricated or un-lubricated, two- or three- body abrasion, erosion, etc. The second level simulation is related to the values of the key parameters in the wear situation and the range of those key values. Examples of these parameters are speed, load, stress, and temperature. The third level simulation replaces the actual wear situation, while all parameters and features are similar, if not identical to those in the application. The highest level of wear tests would be taking results from the field and measuring the wear within the actual machines that have been in use.

For wear processes that are not fully understood, it is beneficial to begin with the higher level simulations to gain the perspective of the overall wear behaviour. After the second or third level simulation, it is possible to define critical mechanisms and parameters. Then, the critical mechanisms and parameters can be tested in a well-controlled first level simulation. The general recommendations for any wear test are to:

- carefully specify the reasons to perform the test;
- select tests that will provide closest possible resemblance;
- ensure that the correct wear mechanism is being tested; and
- select a test which is quick, controllable and low cost.

Different authors have different interpretations about the number of test levels, but the trend is the same. Most simple tests (level one simulation), such as pin on disc or ball on a flat surface, provide a good understanding of wear mechanisms, but their correlation with the real application is not as clear. On the other hand, increasing the simulation level will result in better correlation, but the understanding of the wear situation will decrease. The repeatability and control of experiments is higher for low level simulations than for high level simulations.

5.3. Selection of wear experiments

In accordance with the goal of the thesis and previous findings, two types of wear experiments are selected:

- 1) Sliding wear experiments;
- 2) Fretting wear experiments.

The goal of these experiments is to explain the circumstances that might lead to the seizure of a blade bearing, quantify the wear behaviour of the blade bearing for different material combinations, and evaluate the influence of fretting wear.

Sliding wear experiments will describe the wear behaviour of a blade bearing during the large change in pitch. In order to cover the interaction of different wear mechanisms, the second level simulation is selected for sliding wear experiments. The main difference from the real application is in the load distribution. In the experiments it is simplified and only one side of the bearing will be uniformly loaded, while in the real application, bending moments create a non-uniform load distribution on both sides (see Figure 3.8: the coefficient u is larger than 1 in the experiment). However, other parameters such as load, lubrication, speed, amplitude of motion, surface finishing, and temperature will be the same as in the real application. Sliding wear experiments are done on two different set-ups in order to confirm results. In total, seven experiments were done which include four different material pairs and 61 tested samples. The sliding wear experiments are named Wear Test 1 to Wear Test 7.

Fretting wear experiments describe the wear behaviour of a blade bearing during fretting motion. Experiments were done on two different set-ups and the selection of fretting wear experiments was based on the goals of experiments. In order to determine the influence of fretting amplitude on the total amount of fretting, first order experiments were selected. More precisely, the ball on flat surface experiment was selected. The influence of lubrication on fretting wear was also investigated in a first order simulation, but on a different set-up. Wear Tests 8 and 9 include ten fretting experiments, five for different fretting amplitudes and five for influences of lubrication.

5.4. Sliding wear experiments

Sliding wear experiments (Wear Tests 1 through 6) are done on the test setup specifically designed for these experiments in order to simulate the actual wear situation as accurately as possible. Sliding wear experiment Wear Test 7 was done on a different setup, which is described further on. Figure 5.1 shows the cross-section of a CPP and the blade bearing that was investigated. In sliding wear experiments, a blade bearing was simulated with two parts, a bush and ring. The contact situation is shown in Figure 5.1 (right). The bush part will represent a blade carrier and the ring part will represent the hub. In experiments, the wear situation is simulated by applying the load and a reciprocating rotating motion on the bush.

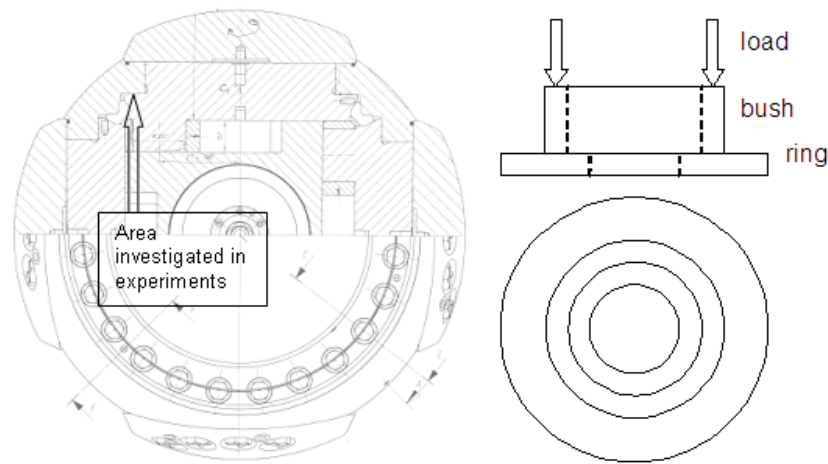


Figure 5.1: Sliding wear experiments are focused on the wear of the blade bearing, typically on the inner side where the loads are higher.

5.4.1 Testing procedure for Wear Test 1 to Wear Test 6

Two parts, the bush and the ring, were positioned in a specially designed testing rig, Figure 5.2, and were submitted to a sliding motion load. The testing rig was designed in such a way as to simulate sliding wear in the propeller blade bearing during the change of the pitch. This was accomplished by rotating the bush over a limited angle. The ring and bush are compressed by a pendulum construction and supported by two axial roller bearings. Five separate rows are available for two specimen pairs, allowing ten specimen pairs to be examined simultaneously. Sample pairs are named according to the row they are placed in, for example 1a means sample pair A in row 1, 3b means sample pair B in row 3, etc. A pneumatic cylinder with an adjustable air pressure loads the pendulum. The wear is measured continuously at the top of the pendulum, with a displacement transmitter with an accuracy of 0.1 mm. The pendulum ratio is 1 to 10, which gives an accuracy of 0.01 mm for the measured wear depth over the two surfaces. Experiments included different material combinations under different loads. The dimensions of the bush and ring used in the test are also shown in Figure 2.

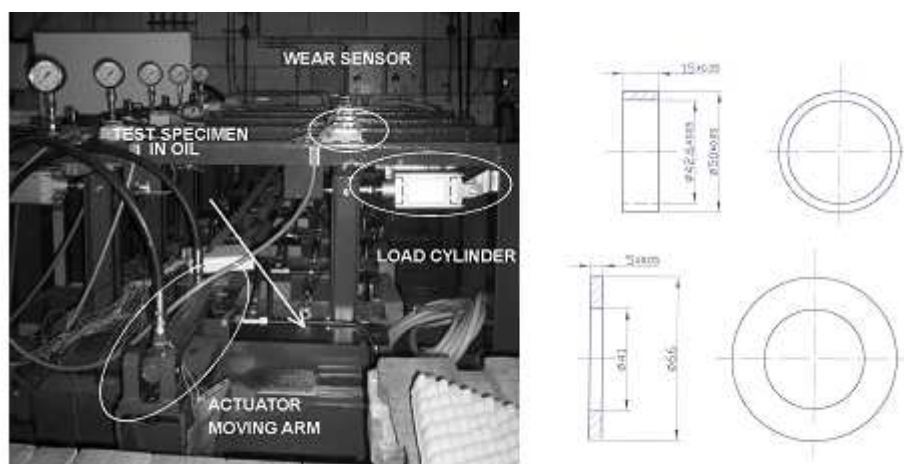


Figure 5.2: Test rig and the geometrical properties of test specimens: (a) bush (top) and (b) ring (bottom)

Table 5.1 shows a list of material pairs used in Wear Tests 1 through 6 and all loads tested during one experiment. Materials DU and DP-4 are materials used in journal bearings, and have a layered structure. The base is made of steel, with an additional layer of PTFE (Teflon) applied. The PTFE layer has a low friction coefficient, which was interesting in this application and was therefore included in the wear analysis. Materials used for the bush were a 42CrMo4 steel and a MnAl bronze. Materials used for the ring were an alloy CuNiAl, DU and DP 4. Material properties of 42CrMo4 steel, CuNiAl, and MnAl bronze can be found in Appendix D.

Table 5.1: Variable parameters in sliding wear tests

Test	Material	Load [N/mm ²]	Distance [m]
Wear Test 1	DU-42CrMo4 steel	15.7, 31.9, 48, 64.1, 80.3	5009
Wear Test 2	DP4-42CrMo4 steel	15.7, 31.9, 48, 64.1, 80.3	8746
Wear Test 3	CuNiAl-MnAl bronze	15.7, 31.9, 48, 64.1, 80.3	9431
Wear Test 4	CuNiAl-42CrMo4 steel	15.7, 31.9, 48, 64.1, 80.3	9502
Wear Test 5	CuNiAl-42CrMo4 steel	15.7, 31.9, 48, 64.1, 72	8839
Wear Test 6	CuNiAl-42CrMo4 steel	48 for all specimens	10800

The examined loads were typically 15.7, 31.9, 48, 64.1 and 80.3 N/mm². Each load corresponds to one row in the test apparatus so that samples 1a and 1b have lowest load and samples 5a and 5b highest load. It should be noted that in normal conditions, the maximum load in the blade bearing was around 25 N/mm². However it was decided to test materials for higher loads as well. In each row, two test pairs are exposed to the same amount of pressure. During Wear Test 5, it was not possible to achieve the maximum air pressure and therefore, the maximum load is somewhat lower. In Wear Test 6, all test pairs are exposed to the same pressure.

The invariable experimental parameters Wear Test 1 through 6 included:

- Speed: angular speed was kept constant at 15 deg/s.
- Motion: motion oscillated back and forth, with an amplitude of 60 degrees.
- Surface finishing properties: the average surface roughness was the same for all test specimens.
- Oil properties: viscosity and type of oil highly influences the wear behaviour. Oil used in the experiment was gear oil, ISO VG 46, and there was no forced lubrication.
- Temperature: experiments were performed at room temperature (25-30 deg C).

5.4.2 Testing procedure for Wear Test 7

The test set-up used in this experiment has better control over motion and load distribution than the set-up used in Wear Tests 1 through 6. However, the maximum possible load was much lower. This test was performed in an outsourced facility by the order of the author. The contact geometry of the sample in Figure 5.3 had to be significantly reduced to create 50 N/mm² contact load. This load was selected in order to be comparable with Wear Test 6. The tested material combination is CuNiAl and 42CrMo4 steel in the same lubricant as in Wear Test 6. In Wear Test 7, wear was not

measured continuously, but friction was measured as torque at the holder. At the end of experiment, the depth of the wear scar was measured by a profilometer.

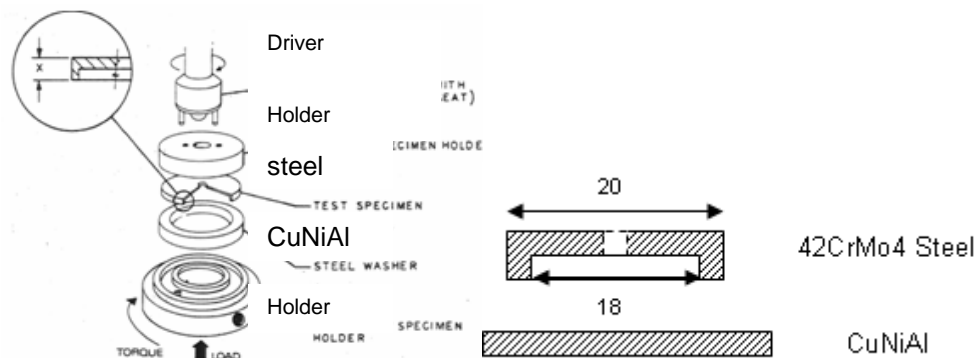


Figure 5.3: Test bench for Wear Test 07 (left) and test specimen (right)

5.4.3 Results of sliding wear experiments

Several material pairs were investigated for different loads in Wear Test 1 to 6. Wear was measured continuously during sliding as a wear depth. The total sliding difference was not the same in all experiments, as for DU and DP4 pairs it was somewhat shorter. Figure 5.4 through 5.7 show the wear behaviour for Wear Tests 1 through 4. Curves presented in these figures are average values of the two specimens subjected to the same load.

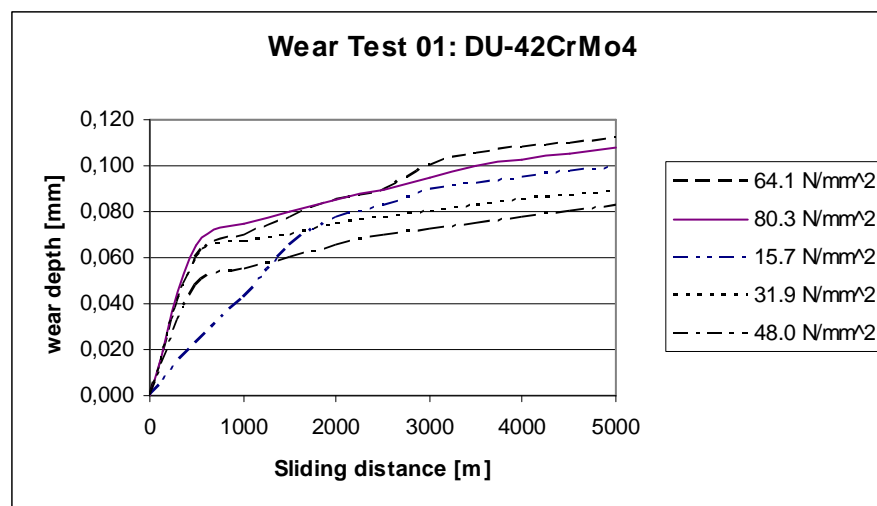


Figure 5.4: Wear curves for the DU-42CrMo4 pair

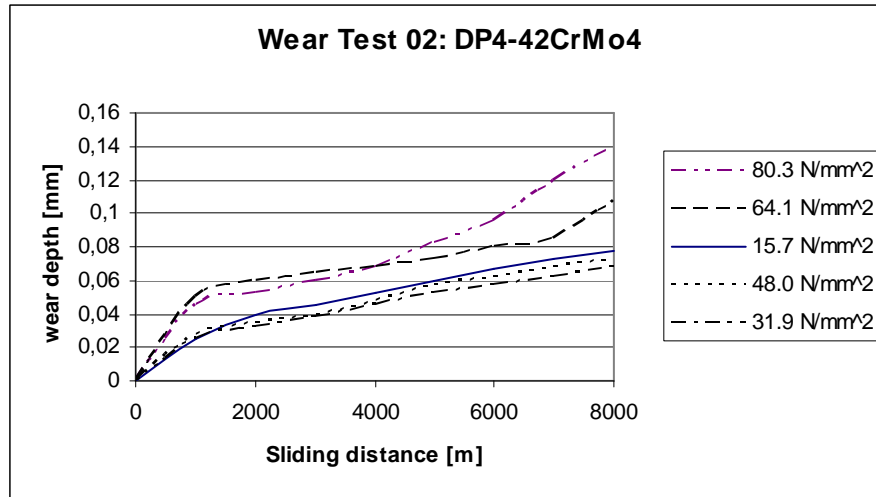


Figure 5.5: Wear curves for the DP4-42CrMo4 pair

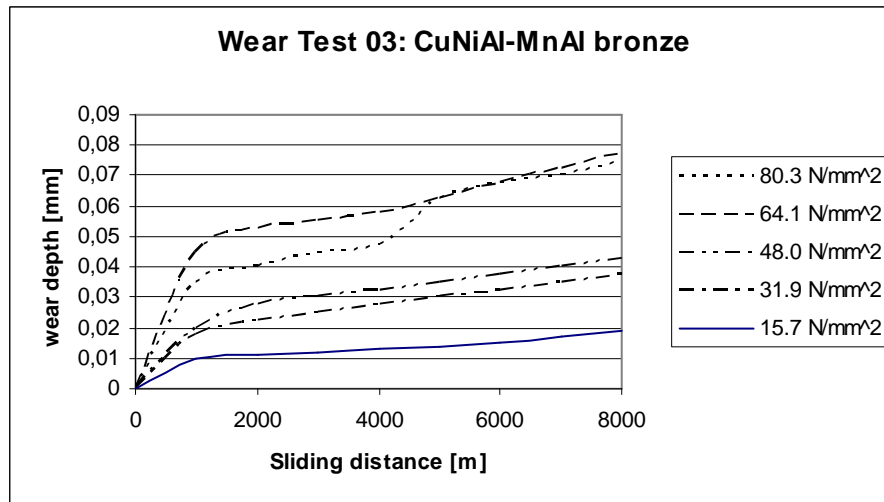


Figure 5.6: Wear curves for the CuNiAl-MnAl bronze pair

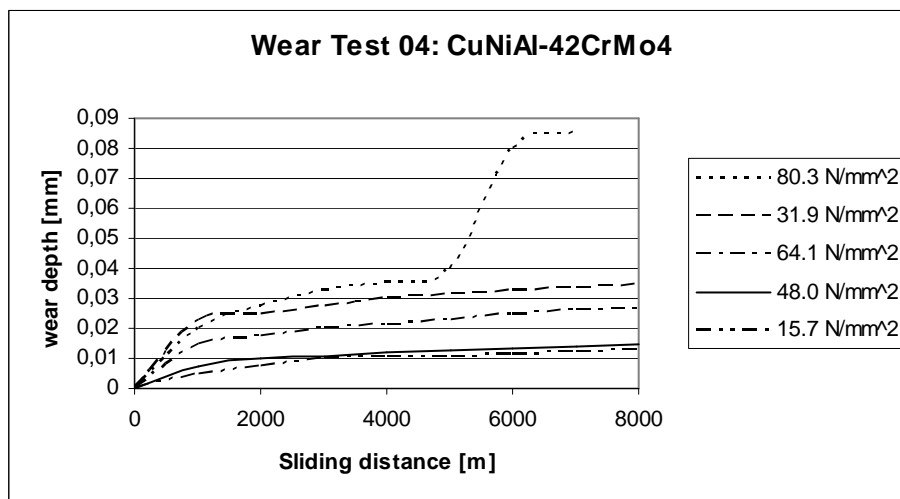


Figure 5.7: Wear curves for the CuNiAl-42CrMo4 pair

One of the first observations made after the first four tests was the difference in the total amount of wear between the two samples subjected to the same load. Figure 5.8 shows results from Wear Test 3. The difference in the measured amount of wear is

evident. Materials without a coating exhibited a smaller difference in the total wear than materials with coatings.

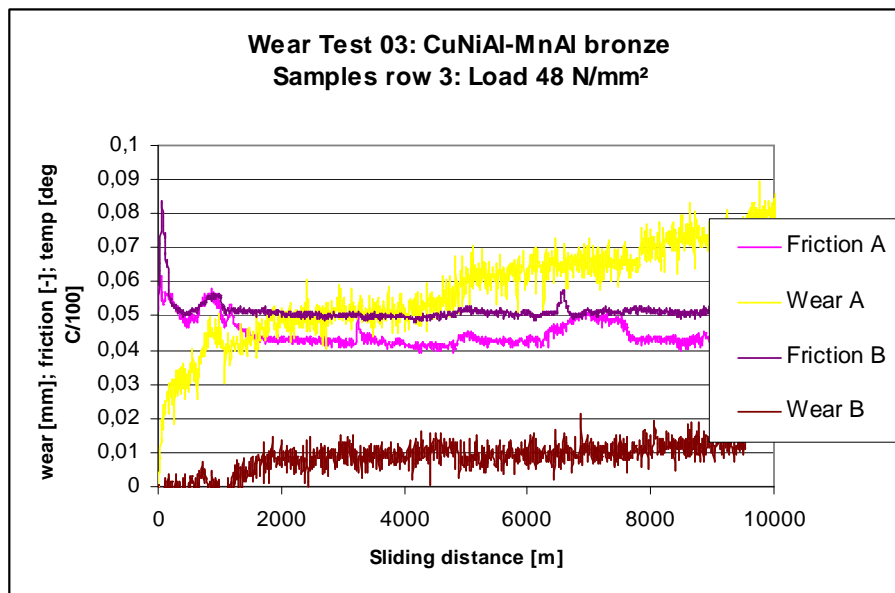


Figure 5.8: results from Wear Test 3, two samples of the same material combination, subjected to the same amount of load and sliding, show different amounts of wear

In order to check the repeatability of results, Wear Test 4 was repeated in Wear Test 5. Further information with respect to repeatability can be found in Chapter 5.5.7. In Wear test 5, the tested material pair is CuNiAl and 42CrMo4 steel. However, it turned out that the CuNiAl specimen in Wear Test 5 had a lower hardness than in Test 4. This was noticed after the test was done. Further information with respect to the influence of hardness can be found in Chapter 5.5.6. Figure 5.9 shows results of Wear Test 5.

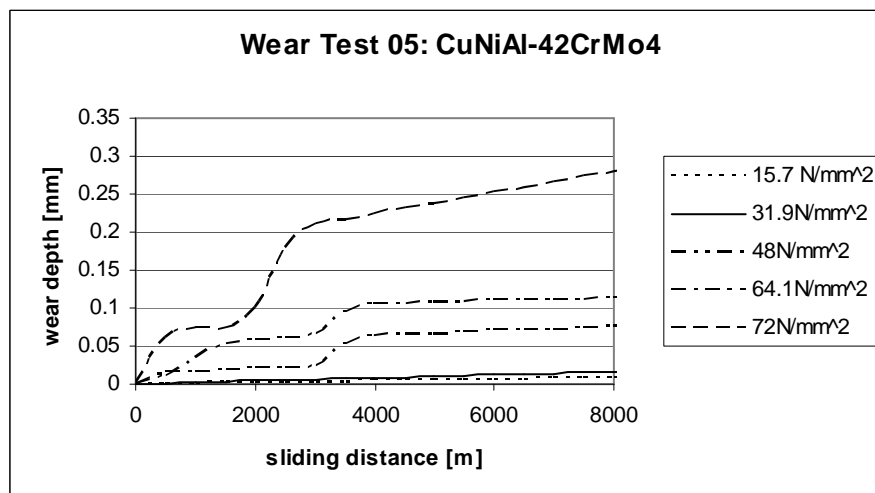


Figure 5.9: Wear curves for the CuNiAl-42CrMo4 pair

As an additional check, the weight of the test sample was measured before and after Wear Test 5. Figure 5.10 shows the comparison of the measured weight loss of CuNiAl part and wear depth at the end of the experiment. Despite the fact that the results do not correlate 100%, the similarity in trends is obvious. The x axis on Figure 5.10 represents the samples number.

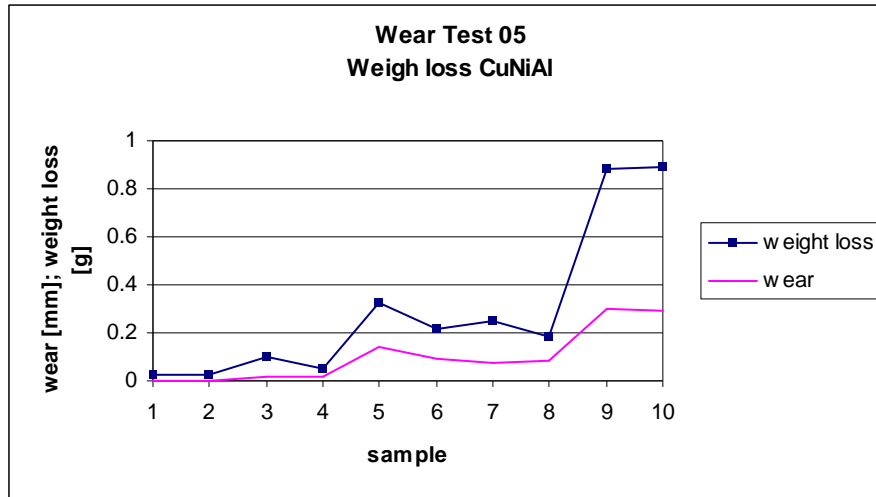


Figure 5.10: The comparison of measured weight loss and wear depth at the end of Wear Test 05. Test sample 1a (15.7N/mm²) is sample 1 on x axis, 1b is sample 2, 2a (31.9N/mm²) is sample 3, and so on, until 5b (72Nmm²) is sample 10 in x axis

It is interesting to note the weight loss of the 42CrMo4 steel part. The steel part has much lower wear and Figure 5.11 shows the weight loss of the steel part. Samples 5a and 5b (or numbers 9 and 10 in Figure 5.10) are exposed to the highest load. These samples have recorded an increase in weight at the end of Wear Test 5. The increase in weight is visible on the samples, as well. There is also evidence of material transfer from CuNiAl to the steel contact surface on samples 5a and 5b. This can be explained by the (high) presence of adhesive wear at high loads. As mentioned previously in the chapter on adhesive wear, this type of wear has a very high wear rate, and this may be the cause for the drastic increase in wear at high loads.

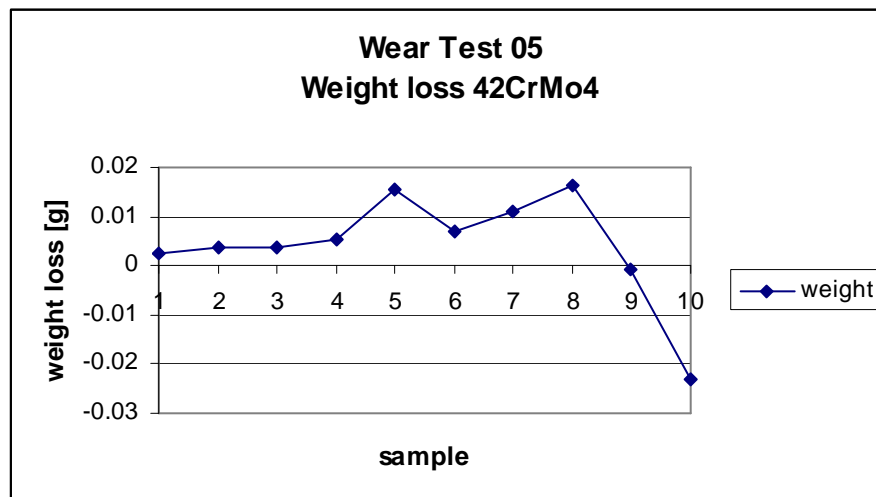


Figure 5.11: The change in weight of 42CrMo4 steel bush after Wear Test 05

When examining Figure 5.6, 5.7, and 5.9 the certain jumps in wear can be noticed. Explanations for these effects can be found in Chapter 5.5.4. It should be noted that by the end of Wear Test 5, the rig began to show signs of wearing out. Some of bearings showed signs of wear and some sensors failed. Therefore, it was decided to do one more test and to do a similar test in a different set-up. The last test on the rig was conducted with all samples subjected to the same load.

The results of Wear Test 6 are used to get the distribution of wear for the same load (48 N/mm^2) and after the same sliding distance (10800 m). Due to the fact that in Wear Test 6 all samples are exposed to the same load, it was difficult to show wear curves from Wear Test 6, as in Figure 5.4 through 5.7 since they overlap. Instead, Figure 5.12 shows the comparison of the total measured wear depth at the end of the experiment and the measured weight loss of the CuNiAl part. The steel counterpart had a very small change in weight (Figure 5.13) and a transfer of bronze material was present.

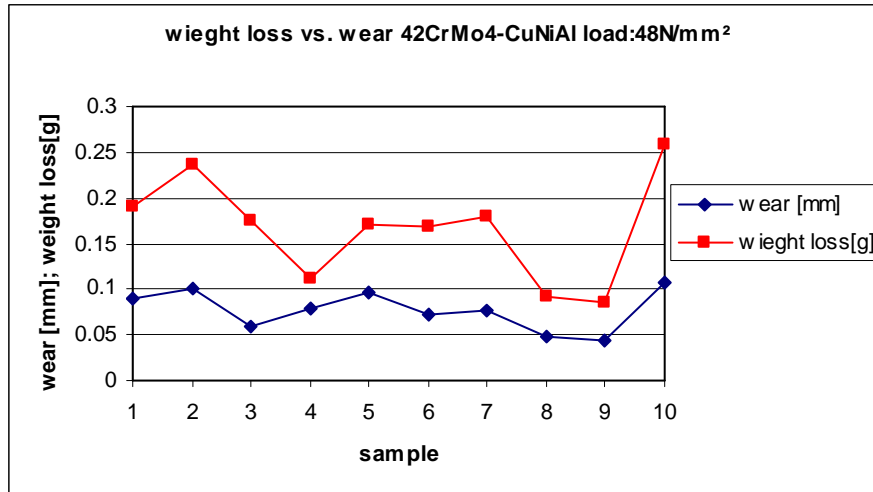


Figure 5.12: The comparison of measured weight loss and wear depth at the end of Wear Test 06

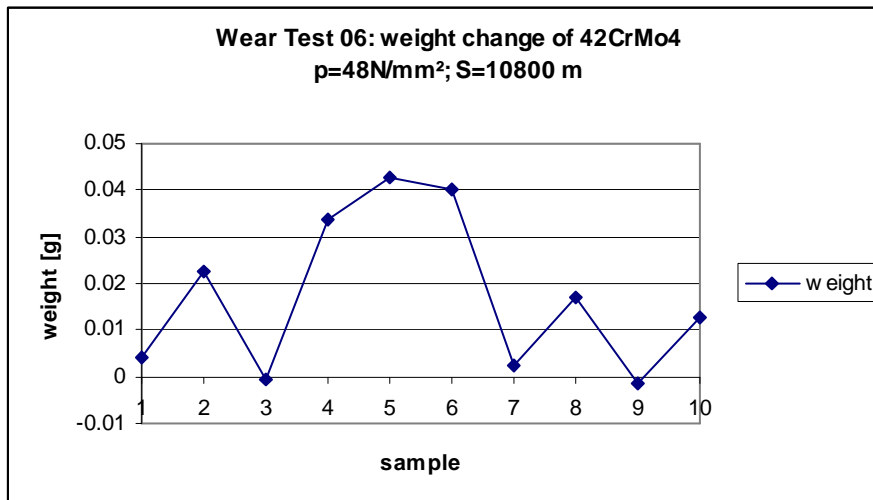


Figure 5.13: The change in weight of 42CrMo4 steel bush after Wear Test 06

Wear Test 7 is similar to Wear Test 05 and 06 since the same material combination was used (CuNiAl-42CrMo4). However it was done with a different apparatus, which is shown in Figure 5.3. The load in the experiment was 50 N/mm^2 . The goal was to compare results from two different apparatuses, as well as the wear scar morphology. Figure 5.14 shows the results for friction in Wear Test 07. Unfortunately, an overly high sampling rate caused only initial data to be recorded. During these 25.000 seconds, the measured friction coefficient is in correlation with other sliding wear tests.

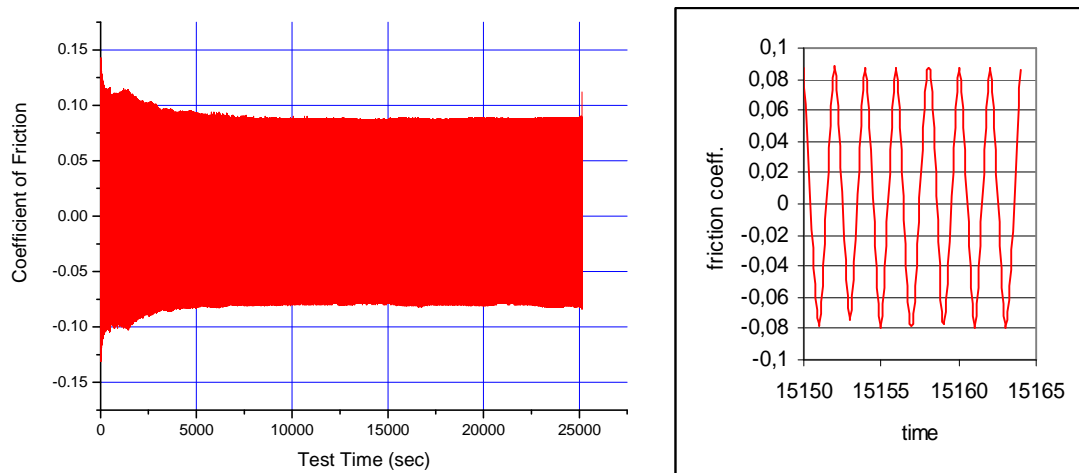


Figure 5.14: Measured friction coefficient in Wear test 07

In Wear Test 7, the wear depth was measured at the end of the experiment by an outsourced institution. The profile of the wear scar on the CuNiAl part was measured with a profilometer (Taylor Hobson Stylus) at 4 positions around the wear scar and Table 5.2 summarizes the results. The total measured wear depth in Wear Test 7 is similar to the wear depth measured in Wear Test 6, for example, with samples 2a, 4b and 5a (see Figure 5.12).

Table 5.2: Measured wear depth of CuNiAl sample at the end of Wear Test 07

Wear Test 07	CuNiAl
Depth Meas. 1 (μm)	51
Depth Meas. 2 (μm)	33
Depth Meas. 3 (μm)	47
Depth Meas. 4 (μm)	30
Depth Average (μm)	40

As an additional control of wear measured using the setup in Figure 5.2, the depth of the wear scar was measured using profilometry as was done for the 3a CuNiAl sample from Wear Test 05. Table 5.3 shows values measured using the same profilometer as in Table 5.2. This value can be compared with the value for sample 5 in Figure 5.10.

Table 5.3: Measured wear depth of CuNiAl sample at the end of Wear Test 5

Wear Test 05	CuNiAl
Depth Meas. 1 (μm)	130
Depth Meas. 2 (μm)	115
Depth Meas. 3 (μm)	45
Depth Meas. 4 (μm)	70
Depth Average (μm)	90

5.5. Analysis of sliding wear experiments

The experiments are not discussed in chronological order; rather the following discussion is structured along the main observed trends after all experiments were completed.

5.5.1 Run-in and run-out behaviour

The run-in effect is visible in the tests for all material combinations. Following the initial period of high wear rate, the wear rate decreases to a lower value and enters a stable (wear) period. In the experiments done, this transition occurred typically between 1000 and 2000 meters sliding distance. During the run-in period, the friction also is higher. Figure 5.14 confirms the effect of run-in in Wear Test 7, whereby the coefficient of friction begins at a higher value of 0.14 and decreases fairly quickly to 0.08. There is also an evident influence of load on run-in behaviour. The transition from the run-in to stable wear is much more evident for higher loads than for lower loads. However, the influence of the load on the duration of the run-in period is only visible in Wear Test 1. Figure 5.4, it can be seen that for higher loads, the run-in period is shorter. For other tests, it appears that the load has no influence on the length of the run-in period. The run-in behaviour is of course known and was a.o. reported in [Barbey, 1982] for materials used in CPP. It was stated that roughness had a limited influence on the length of the run-in period and rougher surfaces were reported to enter stable wear more quickly than smooth surfaces.

The run-out wear is recorded in one test. Figure 5.5 shows the wear behaviour of DP4 against the 42CrMo4 steel from Wear Test 2. The ring in 5b specimen subjected to the highest load broke by the end of the experiment. The curves for the two highest loads (64.1 and 80.3 in Figure 5.5) show the end of life behaviour at longer sliding distance. Typically for run-out behaviour (see Figure 2.13), the wear rate was high probably due to dominant effect of fatigue wear. There is also a difference in the sliding distance needed for run-out wear to occur, wherein run-out begins earlier for higher loads.

5.5.2 Appearance of wear scar

Photos in this chapter are made by an external institute under the order of the author. Firstly, the wear scars from Wear Test 7 were examined. Figure 5.15 shows the steel part in Wear Test 7 after 200.000 cycles. The dominant wear mechanism is scoring, as seen in the formation of severe scratches in the direction of sliding that resulted from abrasive wear. In enlarged photos, there is also the presence of pitting, and the separation of particles in the form of flakes. Pitting can result from fatigue wear. The transfer of CuNiAl to the steel counter surface is evident. Figure 5.16 shows the wear scar of the CuNiAl part in Wear Test 7. The same two wear mechanisms are present, with the dominant mechanism being scoring. The presence of pitting is also visible.

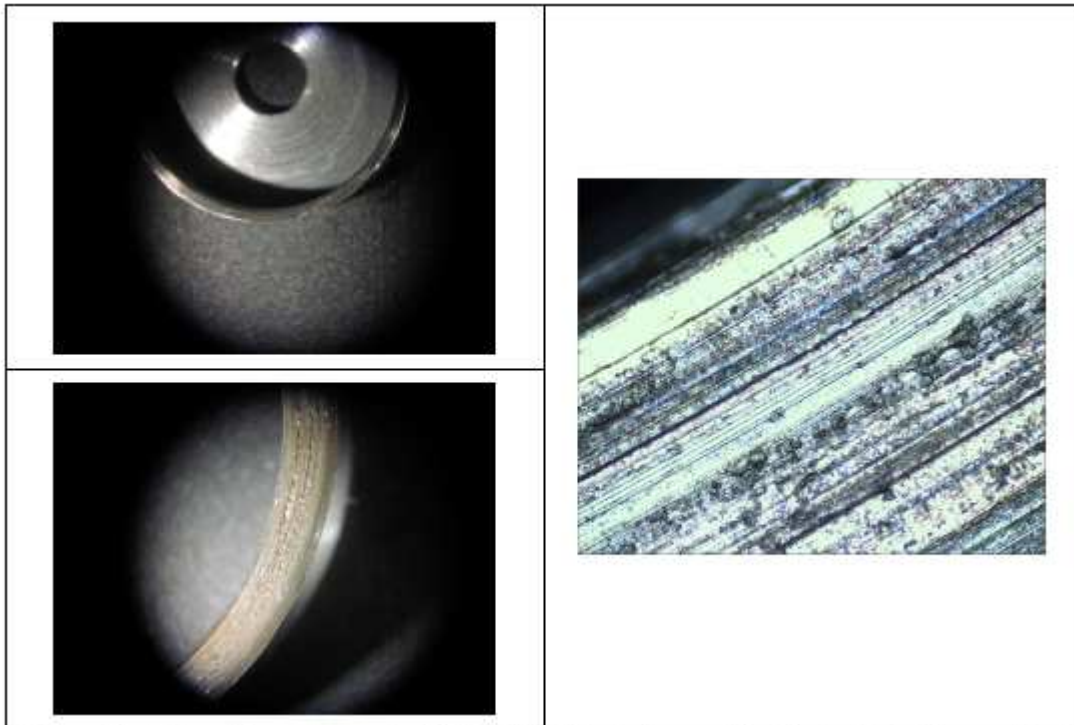


Figure 5.15: photos of wear scar on the 42CrMo4 steel part: 8x magnification top left, 50x magnification bottom left, and 200x magnification right; pictures taken by Falex

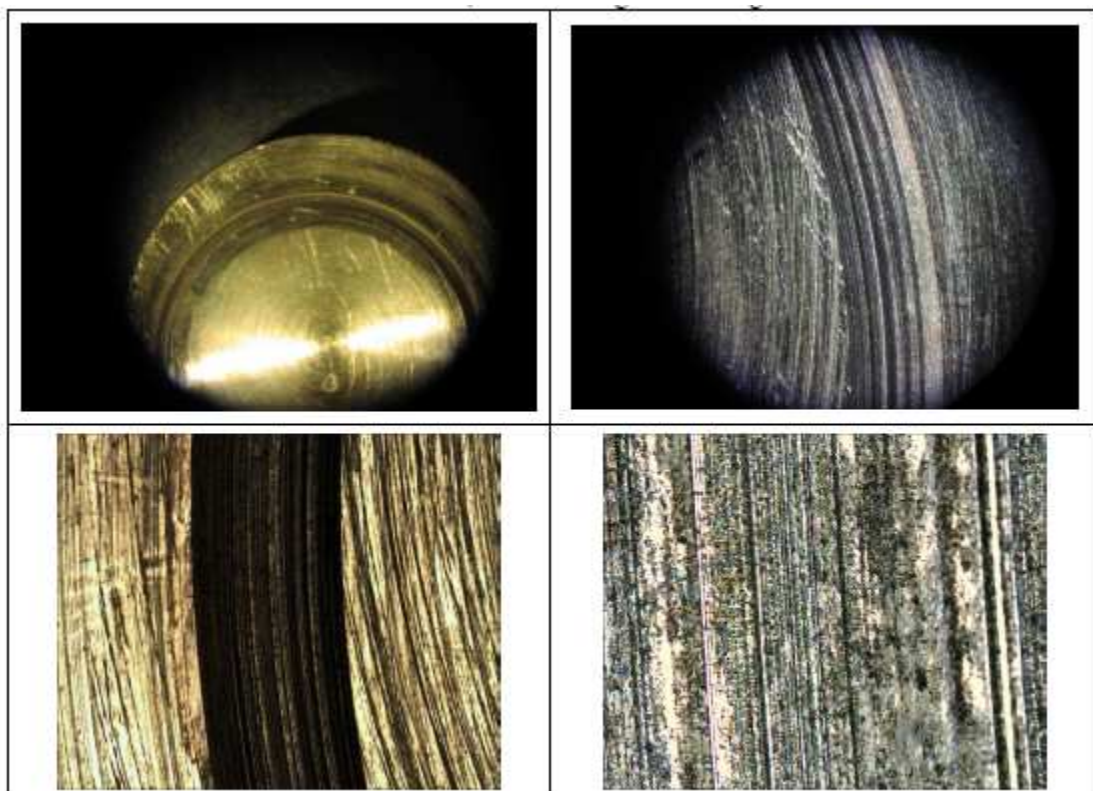


Figure 5.16: photos of wear scar on the CuNiAl part from Wear Test 7: 8x magnification top left, 45x magnification bottom left, 50x top right, and 500x magnification right; pictures taken by Falex

The morphology of a test sample from Wear Test 5 has been inspected with a microscope as well. Figure 5.17 shows the wear scar of the CuNiAl 3a sample in Wear

Test 5. Again there are two wear mechanisms, scoring and pitting. Figure 5.18 shows the 3a steel counter sample for Wear Test 5 with evidence of scoring and pitting.

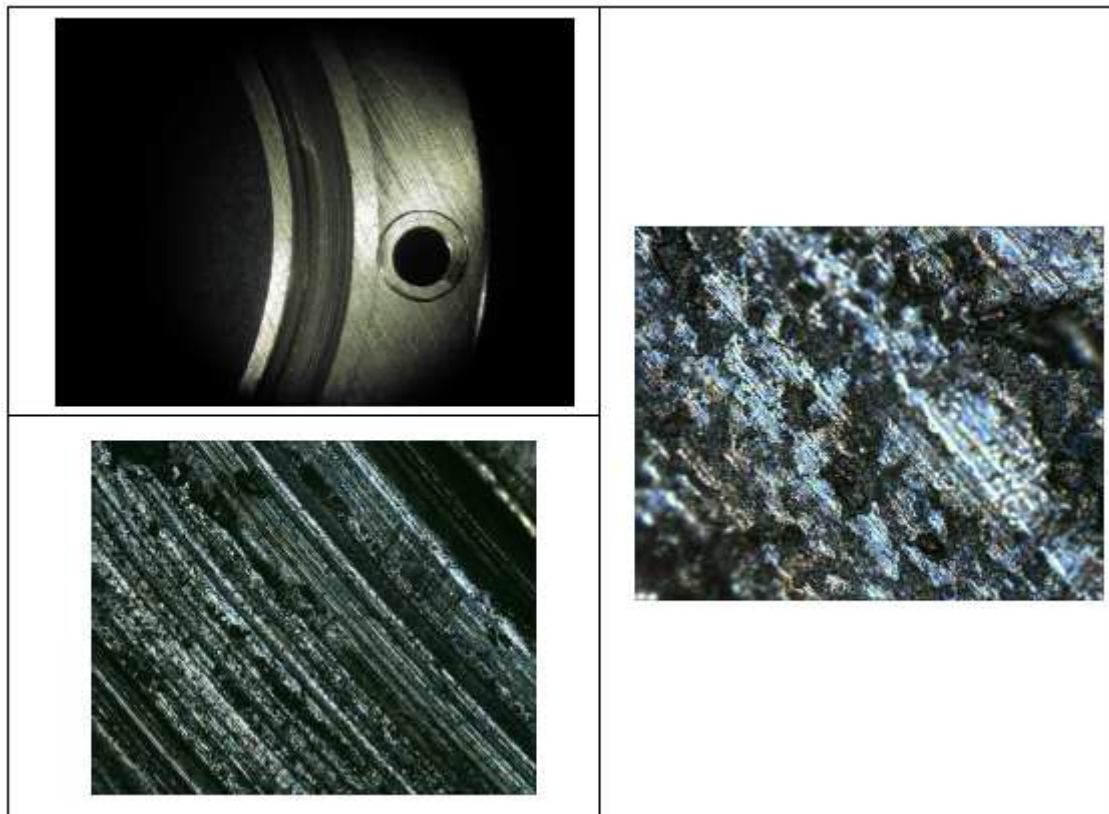


Figure 5.17: photos of wear scar on the CuNiAl part from Wear Test 05: 8x zoom top left, 45x zoom bottom left, and 500x zoom right; pictures taken by Falex

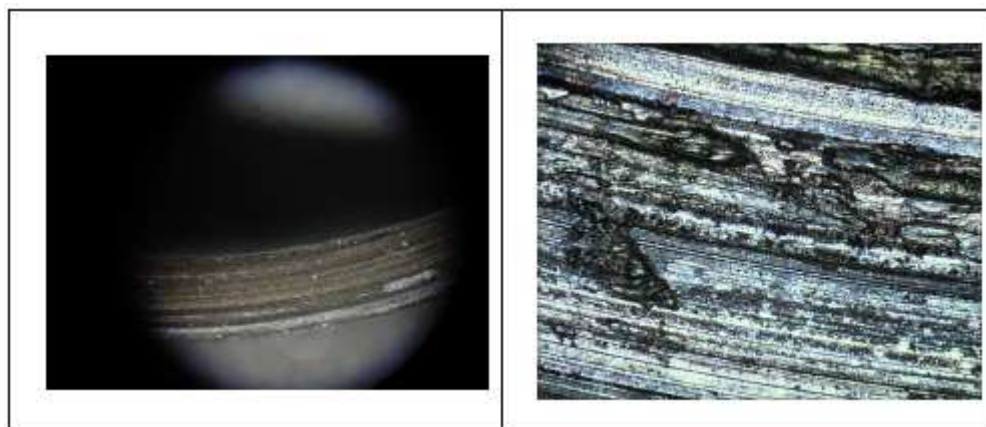


Figure 5.18: photos of wear scar on the 42CrMo4 steel part from Wear Test 05: 8x magnification left and 500x magnification right; pictures taken by Falex

In examining the figures made for Wear Test 7, the presence of scoring is dominant over pitting. Looking at Figure 5.17 and Figure 5.18, it is difficult to definitively say which of the two mechanisms, scoring or pitting, is more dominant in Wear Test 5. Having said this, it can be stated accurately that there is a higher presence of pitting in the samples from Wear Test 5 than in the samples from Wear Test 7, Figure 5.15 and Figure 5.16. The reason for this could be in the difference in the size of the samples. The samples in Wear Test 5 and 6 are much larger, therefore the total sliding distance is

larger and the contacting surface is larger. The larger contact surface is more difficult to lubricate and poor lubrication can increase the presence of pitting.

A comparison of scars from Wear Test 7 with Wear Tests 5 and 6 shows important similarities. The two main wear mechanisms, scoring and pitting, are present on both samples.

5.5.3 Classification of materials

Four different material combinations were tested. Wear rates of each material pair, as defined in Chapter 2.9, Equation (2.5), will be determined to illustrate the wear behaviour of the tested materials. The comparison of wear rates will be made for a stable wear period (2000-5000 m) and for a 48N/mm² load. This load was selected because the amount of wear was accurately measurable; the accuracy of the measured wear was 0.01 mm. Values for wear rates (w) are taken from Wear Tests 1 to 4 and presented in Table 5.4.

Table 5.4: wear rates of tested material pairs for stable wear periods

Test	Material pair	w [mm ³ /Nm]	Wear class
Wear Test 2	DP4-42CrMo4	1.56E-7	3
Wear Test 1	DU-42CrMo4	1.25E-7	3
Wear Test 3	CuNiAl-MnAl bronze	5.21E-8	2
Wear Test 4	CuNiAl-42CrMo4	2.08E-8	2

The specific wear rate is classified into several categories, as outlined in Table 5.5. The least wearing class has a value zero, while a material is classified as hard wearing (hard to wear) when the wear rate has a class of 3 or smaller.

Table 5.5: Classification of wear rate as in [Beek, 2004]

w [mm ³ /Nm]	Wear Class
1E-10 to 1E-9	0
1E-9 to 1E-8	1
1E-8 to 1E-7	2
1E-7 to 1E-6	3
1E-6 to 1E-5	4
1E-5 to 1E-4	5
1E-4 to 1E-3	6
1E-3 to 1E-2	7

In addition to presenting the specific wear rate during the stable wear period, the results for overall wear rate will be presented as well. There are several reasons for this. Firstly, the designer may be interested in knowing the total wear in order to schedule maintenance period. However, the main reason is that overall wear rate will be used in later analysis. Table 5.6 shows the overall wear rates of the tested materials for total sliding distances between 0 and 5000 meters and a 48N/mm² load.

Table 5.6: Overall wear rate

Test	Material pair	W [mm ³ /Nm]	Wear class
Wear Test 1	DU-42CrMo4	0.35E-6	3
Wear Test 2	DP4-42CrMo4	0.24E-6	3
Wear Test 3	CuNiAl-MnAl bronze	0.15E-6	3
Wear Test 4	CuNiAl-42CrMo4	0.05E-6	2

Coated materials exhibit the highest wear rates. Moreover, the coated material was completely worn out at the end of the test. Tests for coated samples were run only up to a maximum of 8000 meters, and some of the samples eventually broke.

The material pair of CuNiAl and 42CrMo4 steel exhibited the best wear characteristics, and is followed by the material pair of CuNiAl and MnAl bronze. It is suspected that adhesive wear is the reason why the pair of two bronze materials (CuNiAl and MnAl) has a higher wear rate. However, for these two combinations (CuNiAl-steel and CuNiAl-MnAl), a strange temporary increase in wear rate was observed for higher loads, which will be discussed in the following text.

5.5.4 Sudden and temporary increase of wear rate and friction

When examining wear curves for the highest loads in Figure 5.6, 5.7, and 5.9 one notices a sudden rise of wear curves for the highest loads. Figure 5.19 shows the results of the test specimen subjected to the highest load in Wear Test 4. After 5500 meters sliding distance, a sudden and temporary increase in wear rate accompanied with a higher friction period was detected. In another example, Figure 5.20 shows measured wear and friction for the sample exposed to the highest load in Wear Test 5. In both Figure 5.19 and Figure 5.20, the high wear rate period is temporary. After a while, wear and friction decrease to values typical for the steady wear period.

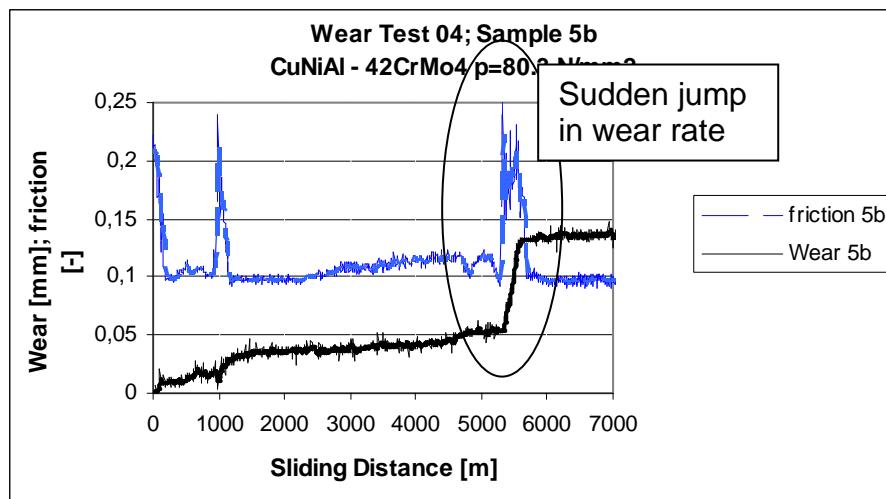


Figure 5.19: Sudden and temporary jump in wear rate and friction, recorded during Wear Test 04 on sample 5b

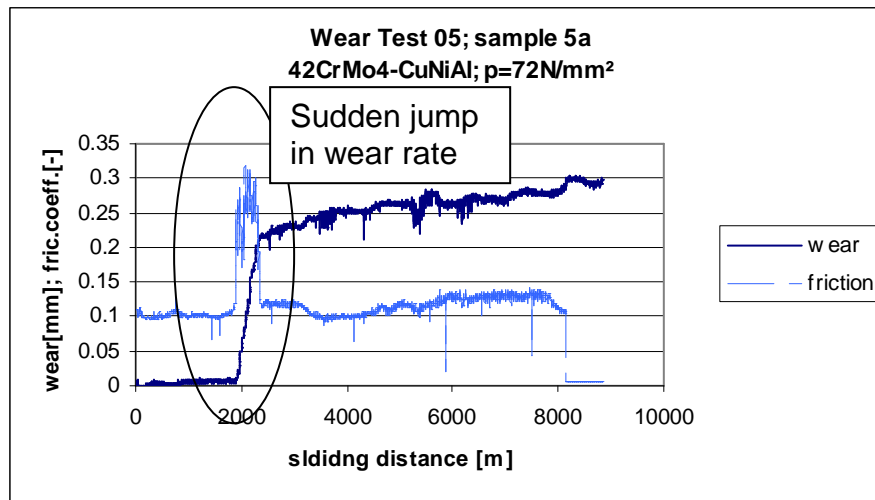


Figure 5.20: Sudden and temporary jump in wear rate and friction, recorded during Wear Test 05 on sample 5a

Wear Test 6 was done in order to investigate the temporary increase in friction and wear rate and the repeatability of results. In Wear Test 6, all samples were exposed to the same load of 48 N/mm^2 , and the investigated material combination was again 42CrMo4 against CuNiAl. Figure 5.21 shows the sudden jump in wear rate observed on sample 4a. It lasted for 50 meters or 1000 cycles. On the right side, Figure 5.21 shows wear, friction and temperature magnified during a period of high friction. It can be seen that the friction reaches maximum at around 5750 meters sliding distance and then wear starts to increase, friction increases before the wear rate increases. The jump in wear and friction is accompanied by a jump in temperature, as represented by the green line in Figure 5.21. Additionally, almost as a warning sign, prior to the jump in wear and friction at around 5600 meters sliding distance, there is a small temporary increase in friction.

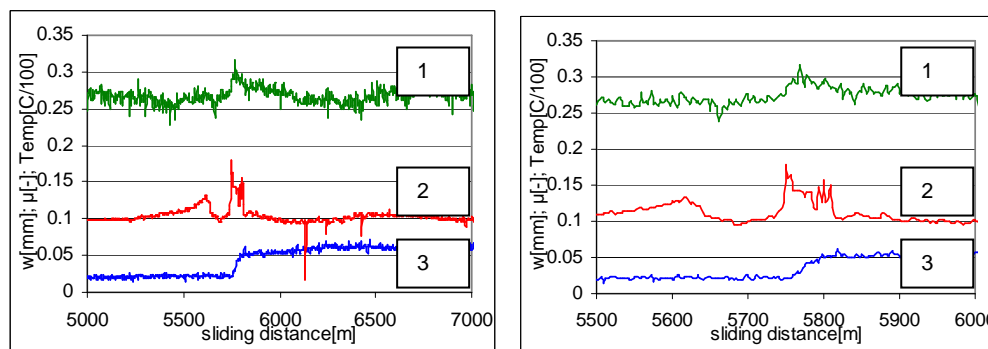


Figure 5.21: jump in wear rate on sample 4a during Wear test 06. Legend: 1-temperature (green), 2-friction (red), 3-wear (blue).

The probable order of events is that first there is abrasive wear during the run in period. Next, the run-in period is over and the contact enters a stable wear period. As bodies come into contact, some of the lubricant gets squeezed out of the contact, and this enables metal to metal contact. This dry contact is a favourable situation for adhesive wear and there is jump in wear rate.

The increase in friction is either due to a lack of lubrication or due to an increase of normal stress. For CPP application another possibility is that the worn out debris remain entrapped in the contact area and react with the environment (sea water) causing

a volume increase of the debris in a fixed space. In the end, this can create seizure in the bearing causing a high wear rate and high friction.

Although not all information are reported, when examining the results, it can be seen that in Wear Test 3, a sudden increase occurred once, in Wear Test 4 it also happened once and in Wear Test 5 it occurred on six samples. In Wear Test 6, where all samples were exposed to the same load, four samples suffered from a sudden and temporary increase in wear rate and friction. During this period of increased friction and wear rate, the friction coefficient is doubled and wear rate is significantly higher than during the stable wear period. There seems to be no rule when these jumps occur and they usually last for 50 meters sliding distance for the load investigated in Wear Test 6. Prior to the jump of wear rate, there is an increase in friction force. One trend is noticeable: these jumps and the number of occurrence of jumps increase with higher loads. For lower loads, there are rare jumps in the friction coefficient and mild jumps in wear rates. With increased loads, jumps in wear rate are more frequent and more drastic, and always accompanied by a high friction coefficient.

5.5.5 Influence of load

In this section, a comparison of wear and load will be given for the results in Wear Tests 1 to 5. Figure 5.22 through 5.25 show the wear depth as a function of load, based on the same results as Figure 5.4 through 5.7. Each line is made after a certain sliding distance for investigated materials.

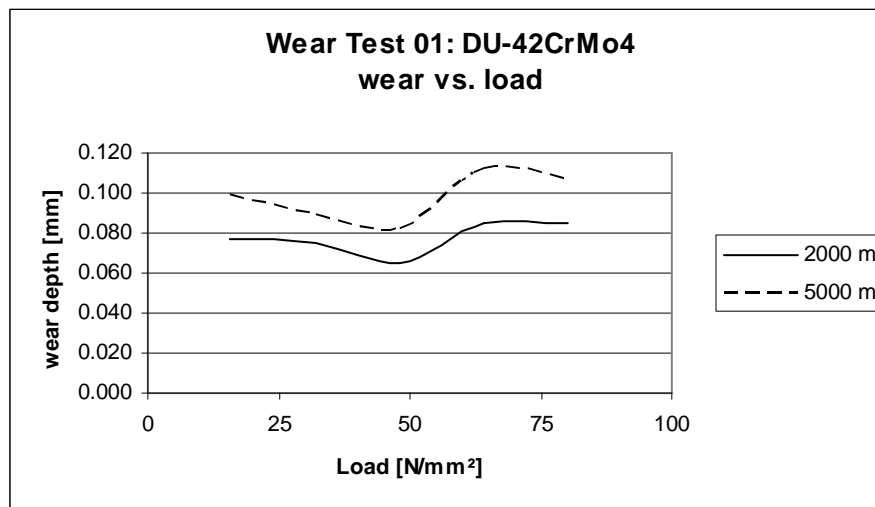


Figure 5.22: Wear as a function of load after 2000 and 5000 meters sliding distance in Wear Test 1

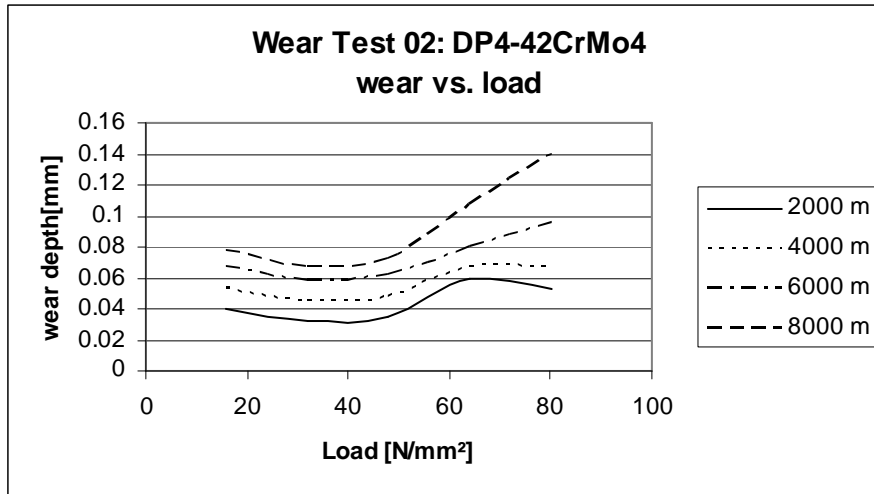


Figure 5.23: Wear as a function of load after 2000, 4000, 6000, and 8000 meters sliding distance in Wear Test 2

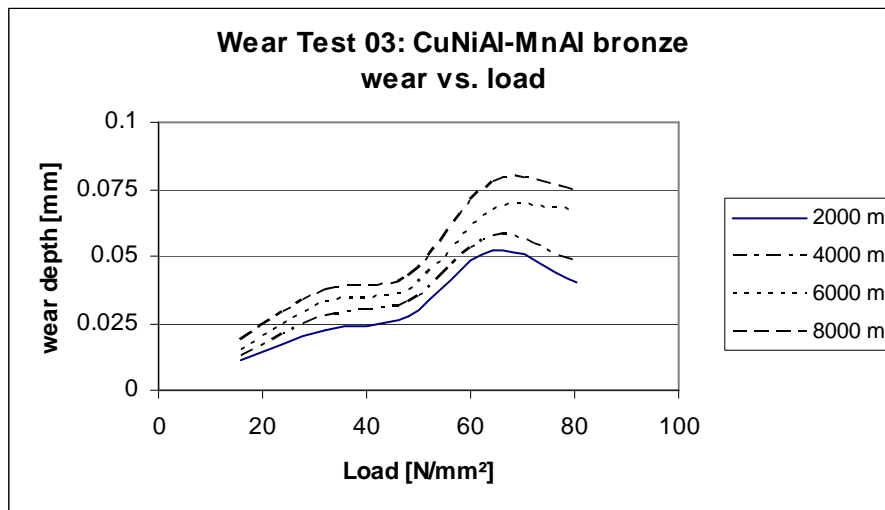


Figure 5.24: Wear as a function of load after 2000, 4000, 6000, and 8000 meters sliding distance in Wear Test 3

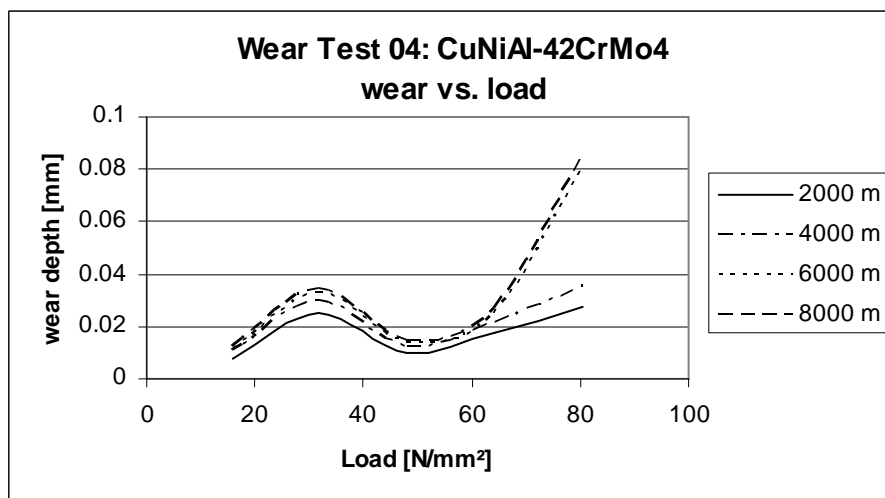


Figure 5.25: Wear as a function of load after 2000, 4000, 6000, and 8000 meters sliding distance in Wear Test 4

Same as discussed in Chapter 5.5.1, Figure 5.23, DP against 42CrMo4, shows the effect of run-out wear on the wear behaviour of the tested material pair. The higher load end of the wear curves increases with an increase in sliding distance. However, before the fatigue wear (or run-out) period, there is only a limited influence of load on the total wear. Another coated sample, DU against 42CrMo4 in Figure 5.22, also shows only a limited influence of load on the total wear. In Figure 5.24, for the pair of CuNiAl against MnAl bronze, the wear depth grows almost linearly with the increased load. In Figure 5.25, CuNiAl against 42CrMo4, the situation is somewhat more complicated. The higher load end of wear curves for the two longest sliding distances increases steeply with an increased load. However, this is not due to wear out behaviour. It is due to the temporary increase in wear rate, observed at a higher sliding distance, as discussed in Chapter 5.5.4. In Wear Test 5, also CuNiAl against 42CrMo4, wear as a function of load shows similar trends as Wear Test 4.

In both tests the sudden increase in wear rate, which occurs at higher loads, gives an almost exponential rise of the higher load end of wear curves.

In Figure 5.26, an exponential trendline has been added to the results. The thick line in Figure 5.26 represents the trendline of a wear curve for 7000 meters. The exponential line is added to illustrate the border of recommended load in order to avoid sudden jumps in wear rate rather than to give the real trend to wear behaviour. In order to avoid sudden jumps in wear rate, it is not advisable to have loads higher than 40 N/mm².

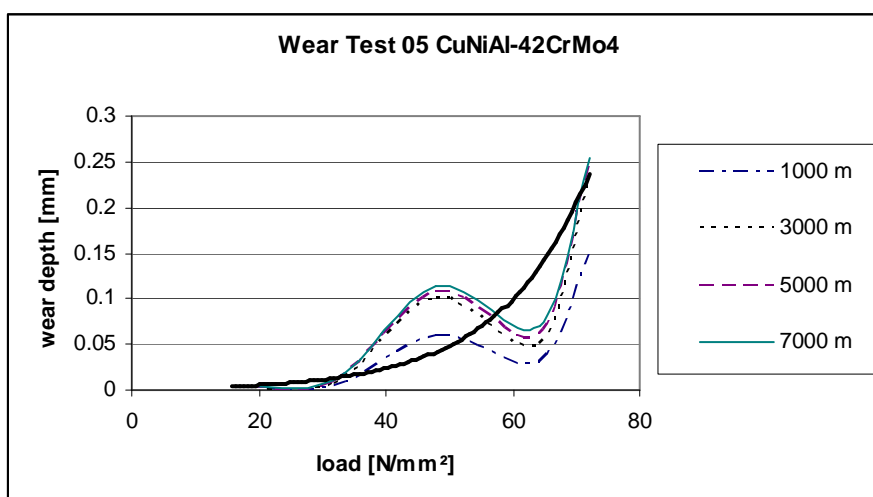


Figure 5.26: Wear as a function of load after 1000, 3000, 5000, and 7000 meters sliding distance in Wear Test 5

It should be remembered that this exponential dependency of wear on load is caused by the temporary increase in wear rate as discussed in Chapter 5.5.4. The temporary increase in wear rate is more likely to occur for higher loads and longer distances.

Looking at Figure 5.25 and Figure 5.26 another thing can be noticed; in experiments the higher load did not always cause the higher wear. This is probably more of a spread in measurement than the real tribological phenomena. The reasons for this could be the accuracy of sensors (0.1 mm) and spread of results shown in Figure 5.8.

5.5.6 Influence of CuNiAl hardness

Despite the fact that it was not planned to investigate the influence of CuNiAl hardness, this was done coincidentally. Figure 5.27 shows the comparison of measured wear depth after 8000 meters in Wear Tests 4 and 5. The goal of Wear Test 5 was to check

results for the best material pair from previous tests. However, after Wear Test 5 was done and the results compared with Wear Test 4, a substantial difference in results was noticed. After checking the hardness of the CuNiAl samples, it was realized that the hardness was much lower for the samples in Wear Test 5. It should be noted that in first set of experiments, Wear Tests 1 through 4, the sampling rate was approximately 10 meters per sample, and in Wear Tests 5 and 6, it tripled to approximately 3.3 meters per sample.

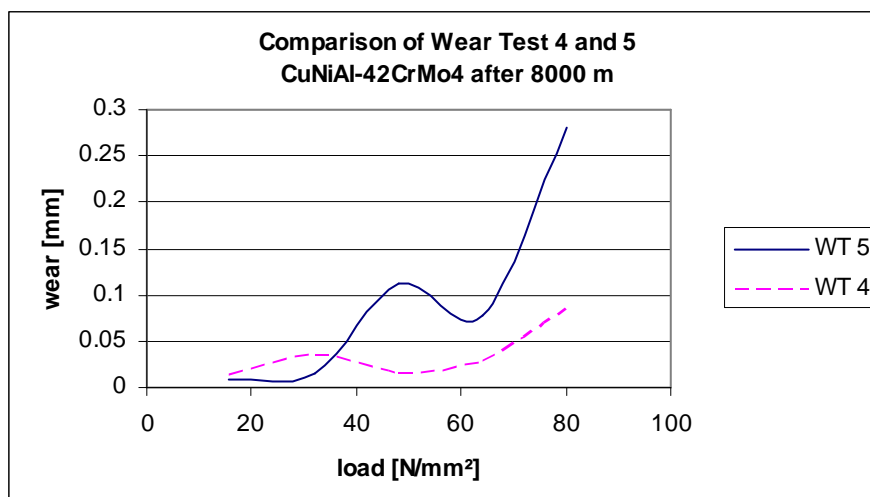


Figure 5.27: The comparison of results from Wear Tests 4 and 5 after 8000 meters sliding distance. The hardness of CuNiAl part was different; 127 HB in WT5 and 143 HB in WT4.

In examining Figure 5.27, the results indicate a relatively substantial difference between values in Wear Tests 5 and 4. The hardness is presented in the Brinell scale: in Wear Test 5, the hardness was 127 HB, while in Wear Test 4 it was 143 HB. The hardness of the 42CrMo4 steel part is 220 HB in all tests. It should be noted that in Wear Test 6, the hardness of the CuNiAl sample was the same as in Wear Test 5.

The poor correlation can be attributed to the difference in hardness. One thing remains unclear, as in Figure 5.27 can be seen that the softer material has lower wear for low load. Wear Test 4 shows higher values of wear for low loads (15.7 and 31.9 N/mm²), while Wear Test 5 shows higher values for high loads (48, 64.1, and 72 N/mm²). It should be noted that the sensibility of the wear sensor is 0.01 mm (in the best case scenario) and any wear measured lower than 0.01 mm is questionable.

It appears that the lower hardness of CuNiAl causes higher (more frequent) presence of jumps in wear rate and friction. In Wear Tests 5 and 6, the presence of jumps was much more frequent than in Wear Test 4.

It is not clear how such a large difference in the hardness occurs. The difference might have been caused by the different material composition and/or by manufacturing. It is less likely that the difference is due to the material composition since melted material has been taken from real propeller. The only difference in the preparation was that instead of pouring melted material into a regular mould, the material was poured into a different type of mould made for this occasion. This also caused a different cooling time (for samples in Wear Test 5 and 6) from those measured in standard practice. It must be stressed out that the low hardness of CuNiAl in Wear Test 5 and 6 is not acceptable for propeller design.

5.5.7 Wear distribution

The results of Wear Test 6 can be used to get the wear probability function. In Wear Test 6, all samples were exposed to the same load. In [Weibull, 1939], the author proposes the distribution as an appropriate analytical tool for modelling the variation of breaking strength of materials. The Weibull distribution has the form:

$$f(x; \beta, \lambda) = \frac{\beta}{\lambda} \cdot \left(\frac{x}{\lambda} \right)^{\beta-1} \cdot e^{-(x/\lambda)^\beta} \quad (5.1)$$

Where β is the shape factor, and λ is the scale factor. Later, [Palmgren, 1945] applied the same distribution for modelling fatigue wear and afterwards, it was used by many authors [Zaretsky, 2000] for predicting the lifetime of bearings. The current usage of the Weibull distribution includes reliability modelling as well. The Weibull distribution is more flexible than the exponential. It makes a reasonable assumption that the hazard rate increases with time, which is not the case with exponential distribution.

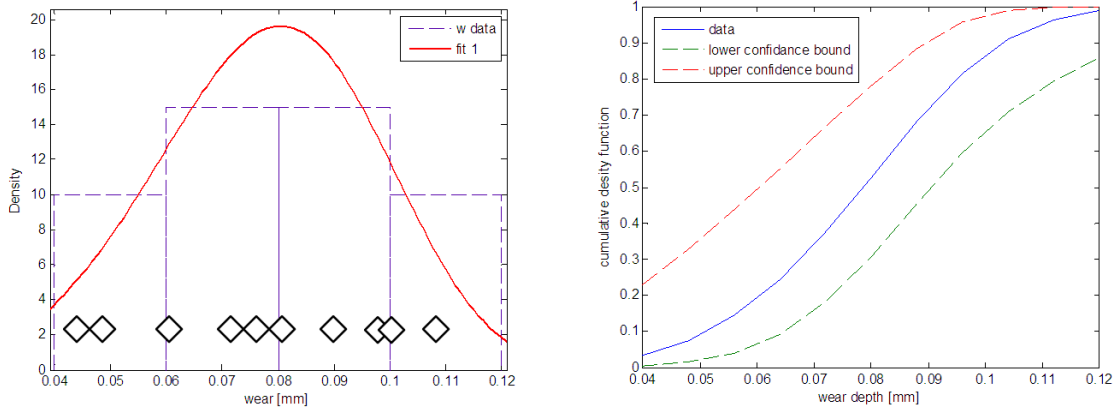


Figure 5.28: Left: Distribution of the total wear in Wear Test 6 : 0.09; 0.10; 0.06; 0.08; 0.097; 0.073; 0.077; 0.048; 0.043, 0.107 mm; Right: cumulative probability of wear depth 95% and confidence bounds

Based on the results of Wear Test 6, a distribution of the total amount of wear can be made. Figure 5.28 shows the density of the end results (wear after 10800 meters sliding distance) from Wear Test 6 and the Weibull fit. In Equation (5.1), x is wear depth in mm and the estimated values of the Weibull distribution are:

$$\beta = 4.43$$

$$\lambda = 0.085$$

The β coefficient of Weibull fit indicates somewhat large spread in the distribution. Practically, it is a normal distribution. The probability and the implications of the distribution on the total amount of wear will be discussed in Chapter 6. The Weibull distribution in Figure 5.28 is very wide. In Figure 5.28 right, confidence bounds are shown for the 95% confidence level. In order to gain more confidence in the results, it is recommended that more measurements are taken. Nevertheless, this wide distribution points out the need to address wear in terms of probability.

More general interpretation of Figure 5.28 can be made if the wear depth is replaced with a wear rate. The specific wear rate can be calculated for each value of measured

wear depth in Wear Test 06 using the load and sliding distance in the experiment. The specific wear rate (w), defined in Equation (2.5), can be written as:

$$w = \frac{h}{\sigma \cdot S} \quad (5.2)$$

Where h is the wear depth, σ is the normal load (48 N/mm²), and S is total sliding distance (10800 m) from Wear Test 6.

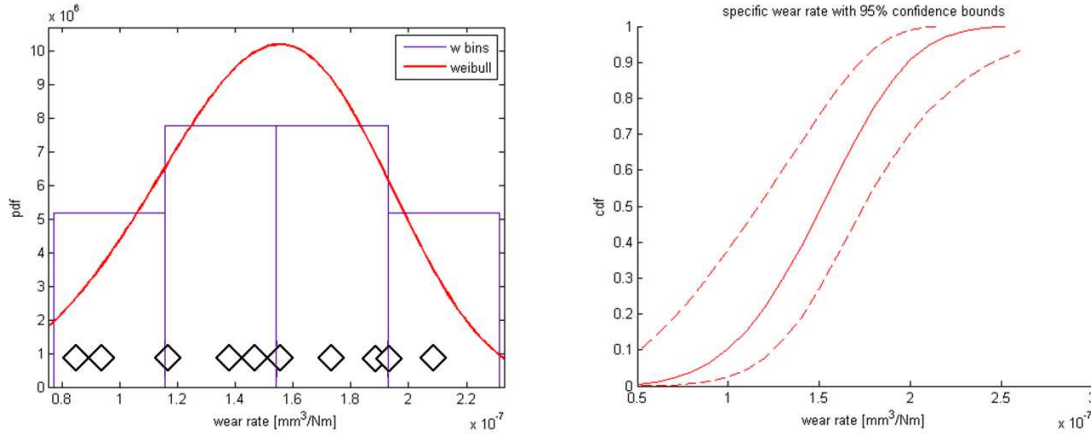


Figure 5.29: Left: Distribution of the total wear rate in Wear Test 6 : 1.74; 1.93; 1.16; 1.54; 1.87; 1.41; 1.48; 0.93; 0.83, 2.06E-7 mm³/Nm; Right: cumulative probability of wear rate and confidence bounds

The specific wear rates, from Wear Test 06, are shown in Figure 5.29 left together with the Weibull fit. In Figure 5.29 right, the cumulative density function is given together with the 95% confidence bounds. While Figure 5.28 is representative only for conditions in Wear Test 6, the more general Figure 5.29 can be used for other loads and sliding distances. This is discussed later in Chapter 6.

5.6. Fretting wear experiments

Fretting wear experiments are named Wear Tests 8 and 9 and are done on two testing apparatuses. The first apparatus, a more sophisticated one, was used to determine the wear behaviour as a function of contact displacement. The second apparatus was used to define the influence of oil on fretting wear. In both cases, the investigated material is CuNiAl, a bronze type of material used for standard CPP hubs.

5.6.1 Testing procedure for Wear Test 08

In Wear Test 8, a fretting apparatus shown in Figure 5.30 was used to simulate the linear fretting motion over a small stroke. This experiment was performed in an external institution by the order of the author. As the goal of the experiment was to determine the influence of the fretting amplitude on fretting wear behaviour of CuNiAl, the first level simulation was selected. A ball on a flat surface was selected for Wear Test 8 in order to gain more precise control over the fretting amplitude. The ball was moving over flat surface with 3Hz frequency. The material tested in this experiment is

CuNiAl against a 100Cr6 steel ball without any lubrication. As it was not possible to test a 42CrMo6 steel ball, the 100Cr6 steel ball with 10mm radius was used. These two materials have similar values for Young's modulus and Poisson's ratio, which both are important parameters in the calculation of Hertzian stresses.

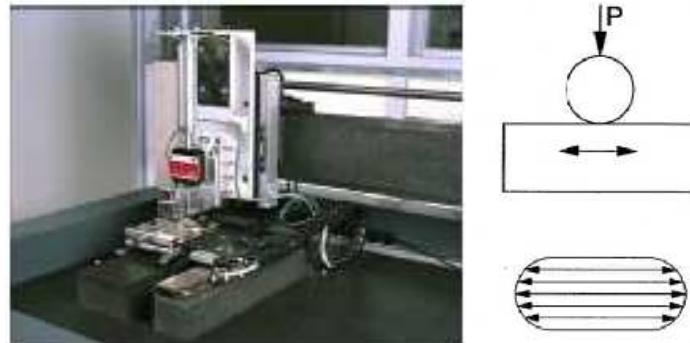


Figure 5.30: test apparatus and tested motion in the first experiment

The main parameters of Wear Test 8 are given in Table 5.7. The load that is used in the experiment was much higher than in all other experiments. However, this was unavoidable because of the point contact (a ball on a flat surface). Wear Test 8 consists of five tests (runs) of different fretting amplitudes (strokes). In Table 5.7, the load was presented as a maximal Hertzian pressure resulting from normal force in the contact.

Table 5.7: Values of parameters used in Wear Test 8

Wear Test 8	Force [N]	Max. Load [N/mm ²]	Radius of contact area [mm]	Amplitude [μm]	Number of cycles	Total distance [m]	Oil
8.1	1	242	0.044	100	50.000	10	No
8.2	1	242	0.044	250	20.000	10	No
8.3	1	242	0.044	500	10.000	10	No
8.4	1	242	0.044	750	6.700	10	No
8.5	1	242	0.044	1000	5.000	10	No

5.6.2 Testing procedure for Wear Test 9

After investigating the influence of displacement on fretting wear, the influence of oil and load was investigated on different apparatus. Figure 5.31 shows the testing apparatus and contact situation in Wear Test 9. The contact is achieved using the three block-shaped samples and the cone-shaped counter body with 25mm radius of curvature. Therefore, the contact between the samples and the counter body is a line contact. The cone is made from 42CrMo4 steel and rotates. The tested samples are in the form of blocks and made from CuNiAl. The cone is loaded with air pressure and standing on three blocks. Experiments done with oil are done with specimens fully immersed in ISO VG46 oil.

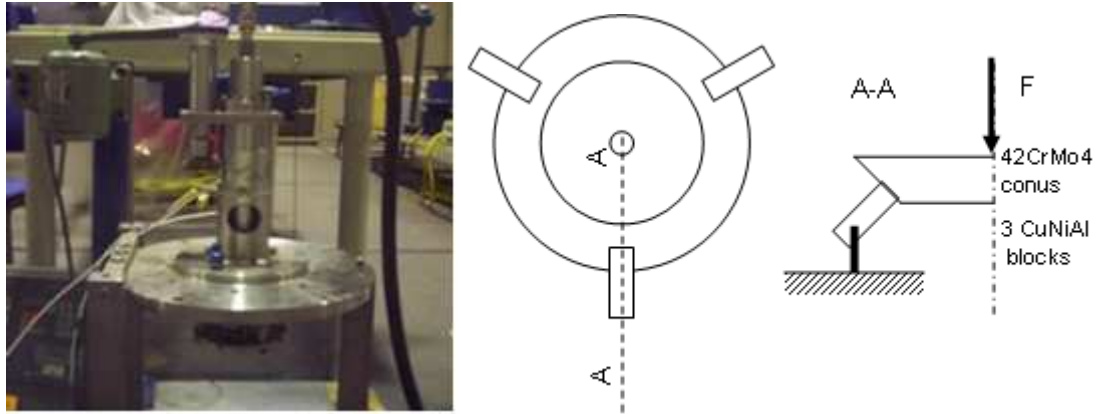


Figure 5.31: testing apparatus and contact geometry in Wear Test 9

The main parameters of Wear Test 9 are given in Table 5.8. Wear Test 9 consists of five tests (runs) of different fretting amplitudes, loads and the presence of lubrication. In Table 5.8, the load was presented as a maximal Hertzian pressure in the contact.

Table 5.8: Values of parameters used in Wear Test 9

Wear Test 9	Force [N]	Max Load [N/mm ²]	Contact half width [mm]	Amplitude [μm]	cycles	Total distance [m]	Oil
9.1	15.12	53.5	0.03	840	65.000	109.2	No
9.2	26.46	70.2	0.04	840	65.000	109.2	No
9.3	37.80	83.5	0.05	840	65.000	109.2	No
9.4	37.80	83.5	0.05	840	1.000.000	1680	Yes
9.5	37.80	83.5	0.05	385	1.000.000	770	Yes

The apparatus used in Wear Test 9 was simple to run for a large number of cycles and to investigate the influence of oil. However, the fretting amplitude was not as controllable as in the apparatus shown in Wear Test 8.

5.6.3 Results of fretting wear experiments

In both experiments, Wear Tests 8 and 9, wear is measured at the conclusion of the tests. However, in Wear Test 8, friction was measured continuously, while in Wear Test 9 that was not possible. Figure 5.32 shows the friction coefficient as a function of displacement measured in Wear Test 8 for five different runs. Different colours represent different cycles and the loops rotate clockwise. The fluctuations at the end of a stroke are artificial and come from the equipment. For the smallest stroke, fluctuations are also visible during the cycle. The reason for this might be a low actuating speed which reflected in stick-slip motion.

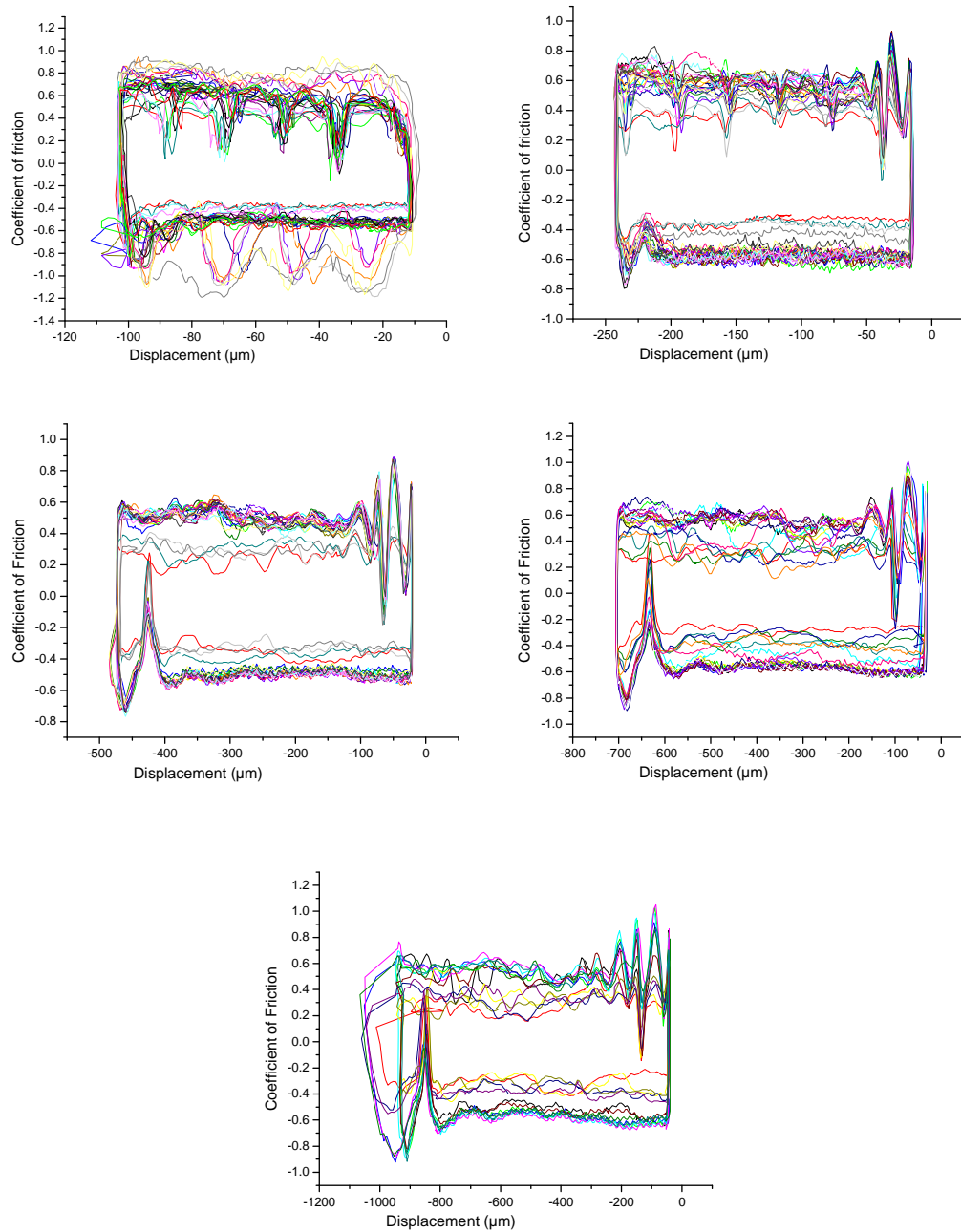


Figure 5.32: Fretting loops from Wear Test 8, pictures taken by Falex

In Wear Test 8, wear was measured as volume lost at the end of the experiments using a light profilometer². Figure 5.33 shows images of the measurements of lost volume. The measured results of lost volume are summarized in Table 5.9.

² A measuring instrument used to measure surface's profile in order to quantify its roughness.

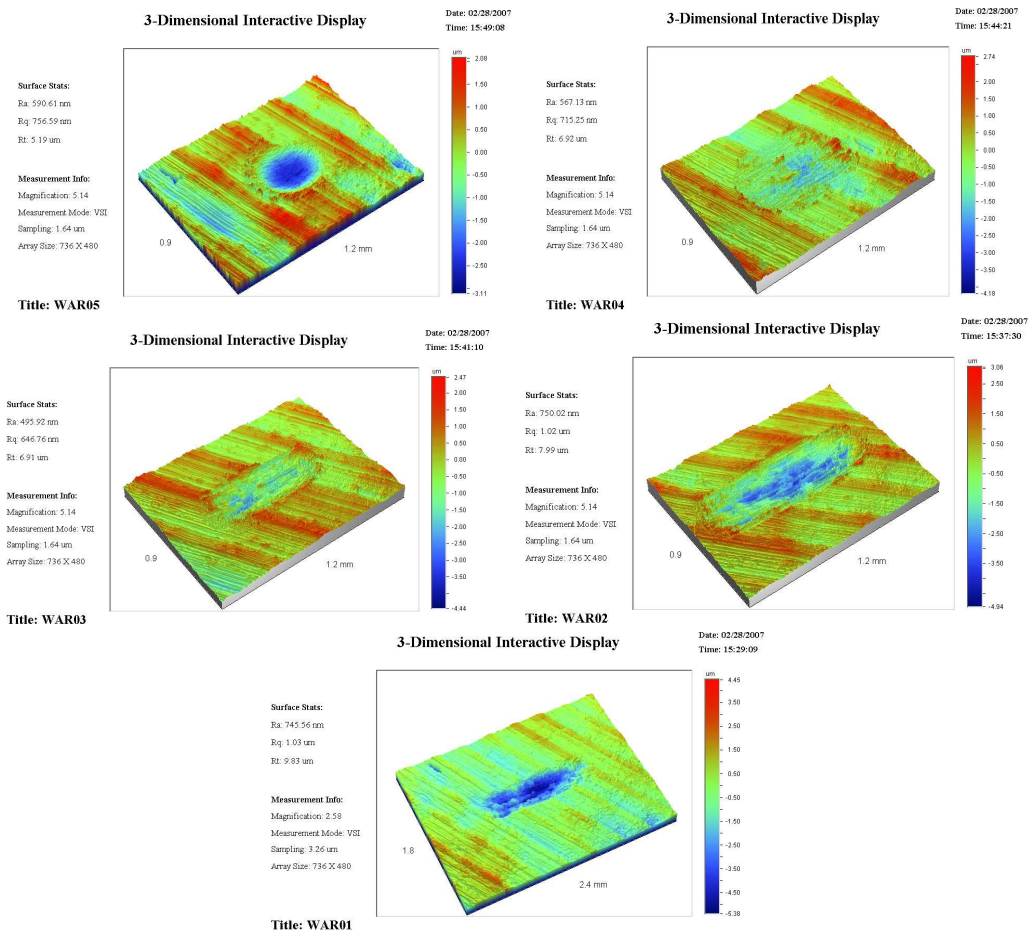


Figure 5.33: Wear Test 8: fretting wear scars in CuNiAl done with 100Cr6 steel ball with typical displacements of 100, 250, 500, 750, 1000 μ m. Picture taken by Falex

Table 5.9: Results of Wear Test 8 Source: External institute

Wear Test 8	Amplitude [μ m]	Lost volume [μ m ³]
8.1	100	142937
8.2	250	238180
8.3	500	150059
8.4	750	487709
8.5	1000	954724

In Wear Test 9, it was only possible to measure the weight loss of each sample at the end of the experiment. Table 5.10 shows the measured weight loss of each specimen in the test and their average value.

Table 5.10: weight lost of CuNiAl in Wear Test 9.

Wear Test 9	Weight loss [mg]				Oil
	Sample 1	Sample 2	Sample 3	average	
9.1	4.6	4.3	1.1	3.3	No
9.2	5.5	5.5	2.3	4.4	No
9.3	4.4	7.8	5.8	6.0	No
9.4	1.2	1.2	1.0	1.1	Yes
9.5	0.2	0.2	0.2	0.2	Yes

Figure 5.34 shows test specimens after the 9.2 experiment without oil (left) and 9.4 with the presence of oil (right).

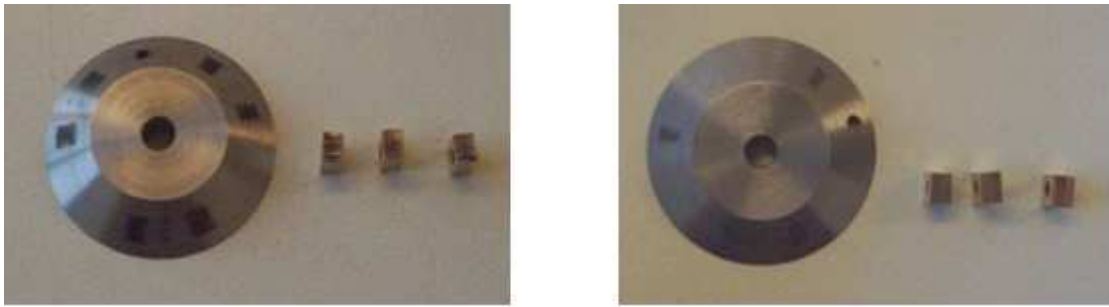


Figure 5.34: tested sample without oil (left) with oil (right)

5.7. Analysis of fretting wear experiments

In the discussion of Wear Tests 8 and 9, a specific wear rate (w) will be used. The specific wear rate was defined in Chapter 2 in Equation (2.5) and is calculated for the total sliding distance (S) done in the experiment for normal force (F):

$$w = \frac{V}{F \cdot S} \quad (5.3)$$

5.7.1 Influence of fretting amplitude

After doing Wear Test 8, it was possible to evaluate the influence of fretting amplitude on the amount of fretting wear. Table 5.11 shows the specific wear rate in Wear Test 8 and Figure 5.35 gives the graphical interpretation.

Table 5.11: specific wear rate in Wear Test 8		
Wear Test 8	Amplitude [μm]	w [mm^3/Nm]
8.1	100	1.43E-5
8.2	250	2.38E-5
8.3	500	1.50E-5
8.4	750	4.88E-5
8.5	1000	9.55E-5

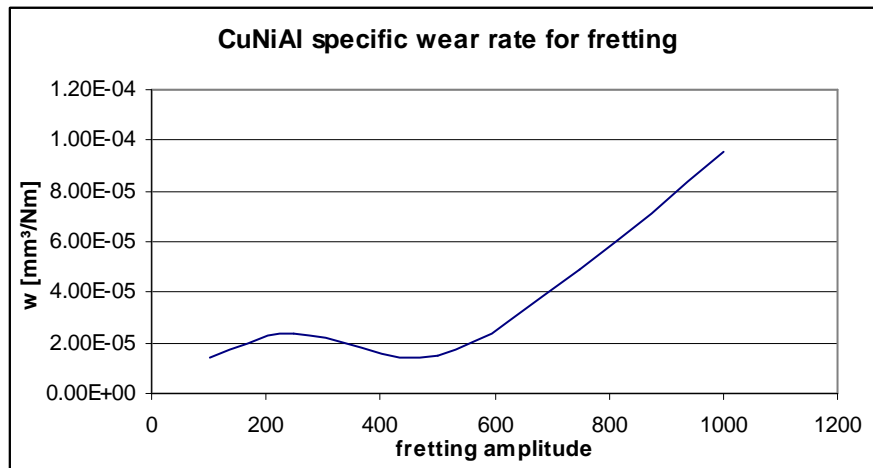


Figure 5.35: results for specific wear rate as a function of displacement in Wear Test 8

Results from Wear Test 8 indicate transition in specific wear rate for sliding amplitudes (roughly) above 500μm.

5.7.2 Influence of lubrication

In Wear Test 9, the influence of lubrication was investigated. Table 5.12 shows specific wear rate in Wear Test 9 as a function of lubrication. In examining the results, the presence of oil reduces specific wear rate by 100 times. Additionally, wear class as defined in Table 5.5 has been presented. According to the criteria defined in [Beek, 2004], this material selection does not fall into the hard wearing class, even not for the lubricated case.

Table 5.12: Specific wear rate in Wear Test 9

Wear Test 9	Oil	w [mm³/Nm]	Wear Class
9.1	No	2.55E-4	6
9.2	No	1.80E-4	6
9.3	No	1.90e-4	6
9.4	Yes	2.26E-6	4
9.5	Yes	0.89E-6	3

5.8. Discussion

In accordance with the goal, the main findings of wear experiments are presented in Chapter 5.5.4 and Chapter 5.5.7, whereby the seizure in a blade bearing and the wear distribution has been analyzed. The wear distribution and how to use it to asses the total wear in a blade bearing will be discussed in the following chapter. Here, the focus will be on seizure in a blade bearing and the relationship between the sliding and fretting wear.

In Chapter 5.5.4, large and temporary increases in wear rate and friction are detected for sliding wear. The increase of friction and wear could lead to the seizure of the bearing. Since the increase in wear rate occurs after an increase of friction, the reason

for seizure should be sought in a reason for the increase of friction. Friction can increase due to two reasons, increase of the friction coefficient or increase of the normal load. The friction coefficient can change due to a change in lubrication. The overlap of the contact area and sliding (or fretting) amplitude in a blade bearing is always maximal. Smaller overlap is beneficial for better lubrication since it allows more fresh oil in the contact. With maximal overlap the contact area stays isolated from the environment (oil in previous experiments) and it is likely that oil gets squeezed out of the contact area, particularly at higher contact pressures. This would result in lack of lubrication in the contact and increased friction and wear. The dependency on pressure was actually found in the experiments as a higher rate of occurrence of the phenomenon at higher loads.

In Chapter 5.5.2 higher presence of pitting was observed in Wear Test 5 samples than in Wear Test 7 samples. This was explained by larger contact area. For a smaller contact area it is easier for new oil to enter the contact.

In Chapter 2.8.4, it was explained how fretting wear can cause seizure of a bearing. Due to the large overlap of the contact area and fretting amplitude, worn out debris is unable to escape from the contact, and they react with the environment and cause seizure of a bearing (i.e. reduce the necessary clearance). Ultimately this would lead to an increase of the normal stress. However, this mechanism is not likely to occur in the previous experiments because it would show up as negative wear. This is possible to happen in a real CPP where sea water could enter the blade bearing and entrapped debris can oxidise.

The overlap of the contact area and motion amplitude in a blade bearing is always maximal, i.e. both for sliding and fretting motion. From that point of view, for seizure of a blade bearing, there is no substantial difference between fretting and sliding wear. However, due to its higher specific wear, the seizure of a CPP is more probable with the presence of fretting wear.

In comparing the results in Table 5.6 and Table 5.12, it can be seen that the specific wear rate for fretting wear is much higher than for sliding wear. The fretting wear will not only affect the total amount of wear, but it could also add to the seizure. Fretting in a blade bearing is dependent upon the shaft frequency, which is much higher than the frequency of sliding motion. If fretting wear is present, the seizure of a blade bearing is more probable and the seizure will occur more quickly than when only sliding wear is present. It should be remembered that in the same way as the fretting wear affects a blade bearing, fretting can also cause wear of the seal. This can result in the seizure of a CPP as explained below.

The results from Table 5.6 and Table 5.12 are from two different set-ups with two different contact geometries. It is possible that fretting wear in a blade bearing will have somewhat lower specific wear rate due to non-Hertzian contact and lower stresses. In order to definitively compare these two wear situations (sliding and fretting), it is recommendable to carry out experiments similar to sliding experiments, but with amplitude of fretting motion.

The question is how the seizure from experiments relates to a real application.

Maybe most importantly, in order to cause the seizure of the entire CPP mechanism, it is necessary that the seizure in the blade bearing occurs on at least two blade bearings simultaneously. This can be illustrated by doing a small analysis. For example, 20 bar is a necessary hydraulic pressure per blade (bearing) to actuate the pitch movement. Therefore, the actuating pressure is 20 bar times the number of blades, which for four blades gives 80 bars actuating pressure. As a rule of thumb, the maximum actuating pressure is usually limited to 120 bars. When friction is doubled in one blade bearing, it

results in 100 bars necessary actuating pressure. If friction is doubled in two blade bearings (i.e. seizure occurs simultaneously at two blade bearings), the necessary actuating pressure is 120 bars.

A further, perhaps more probable cause for a CPP to be unable to change the pitch can be seen in Wear Tests 8 and 9. The influence of lubrication on wear and friction is stunning. The wear rate increases 100 times when there is no lubrication and the friction coefficient goes as high as 0.8. In the lubricated contact, it is 0.08 to 0.1. If the seals (Figure 2.5) of a blade bearing fail to prevent water intrusion, the friction in the blade bearing will rise drastically and the CPP will be unable to perform its function, (i.e. change the pitch).

5.9. Conclusions

The main conclusions can be summarized as follows:

- Run in wear is present for material combinations used in a blade bearing of a CPP;
- In examining the appearance of wear scars for CuNiAl and 42CrMo4, the main wear mechanisms are abrasive and fatigue wear. Abrasive wear appears in the form of scoring, and fatigue in the form of pitting;
- PTFE coatings are not recommended for blade bearings;
- The best material combination is CuNiAl-42CrMo4 and CuNiAl-MnAl bronze. These two combinations fulfil hard wearing criteria;
- Sudden jumps in wear rate and friction probably occur due to the temporary lack of lubrication. These jumps may result in the seizure of a CPP;
- In order to avoid sudden jumps in wear rate, it is not advisable to have loads in blade bearing higher than 40 N/mm².
- Seizure of a CPP is more probable with higher loads and low CuNiAl hardness.
- The measurement of 10 wear depths for the same material, loads and total sliding distance, gives a (wide) distribution of results;
- With an increase of fretting amplitude, the fretting wear increases as well. The fretting amplitude can change the fretting specific wear rate four times;
- The most influential parameter on wear and friction of a blade bearing is its lubrication;
- Fretting wear appears to be more dangerous than sliding wear.

Acknowledgment:

Author would like to thank to Falex Tribology in Rotselaar, Belgium, for their contribution and to the University of Twente for the use of the testing apparatus described in Wear Test 9.

6. Field experience and total wear

The field experience related to usage of CPPs can be useful in several ways in determining the total wear of blade bearings. In the first place, to support the fretting hypothesis made in previous chapters. In the second place, to estimate the amount of pitch usage in real sailing conditions. The goal of the first part of this chapter is to investigate the presence of fretting in cases similar to the investigated case. For several propellers, similar to the investigated propeller (see Chapter 2.7), the prediction of fretting was made by comparing their spindle torque and friction torque. Afterwards, the service records were inspected for any trace of fretting related problems. However, service records are not sufficiently detailed and recorded problems do not always reflect the prediction of fretting. The second part of this chapter details the amount of pitch change used in service. The pitch position of one voyage of a ferry between Calais and Dover was monitored. In combining the pitch usage with the specific wear rate from Chapter 5, it was possible to estimate the total amount of wear during five years, which is the period between two overhauls. In the third part of this chapter, the influence of control strategy is examined. It was found that control strategies have a significant influence on the amount of total sliding distance and therefore on the amount of total wear. In the fourth part, fretting wear is quantified for a period of five years. It was found that the potential damage caused by fretting is twice the amount of damage caused by standard pitch control.

6.1. Service records on fretting wear

In previous chapters, it was found that fretting begins when the spindle torque overcomes the friction torque. For the investigated propeller, it reportedly suffered from fretting wear, as spindle torque exceeded friction torque. However, the question is whether the investigated propeller is a unique case of fretting damage with a unique ratio of spindle torque and friction torque. In order to answer this question, several propellers similar to the one investigated propeller are selected and their service records are inspected.

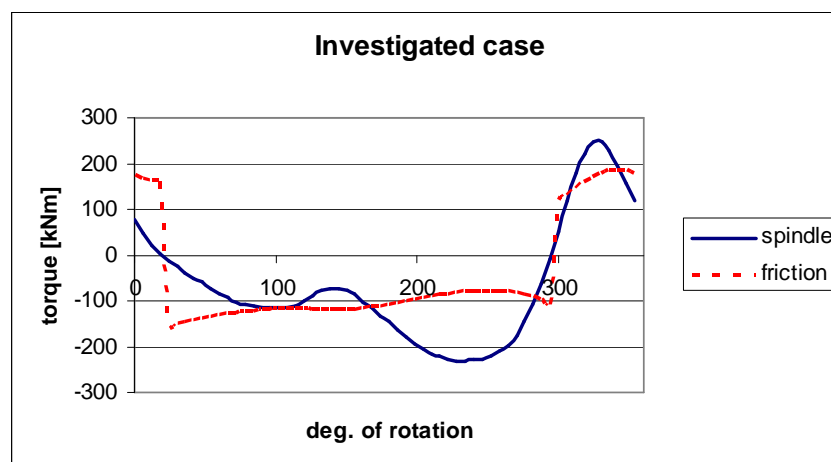


Figure 6.1: Calculated spindle and friction torque for the investigated case

The friction torque in blade bearing and blade spindle torque of the investigated case for design conditions are shown in Figure 6.1. Propellers similar to the one investigated were selected based on their diameter, load and speed. They are all from single screw vessels. These propellers are listed in Table 6.1 and they are called Cases A through H. Table 6.1 shows their operating data, dimensions, loads and geometry data.

Using the same procedure as for the investigated case, the friction torque and spindle torque are calculated for Cases A through H. Figure 6.2 through Figure 6.8 show spindle torque and friction torque in the blade bearing of Cases A through H for design conditions during one revolution. As proposed in Chapter 3, based on the ratio of spindle torque (M_{sp}) and friction torque (Q_{fr}), it is possible to determine the fretting coefficient (k_{fret}).

$$k_{fret}^{def} = M_{sp} / Q_{fr} \quad (6.1)$$

The maximum and minimum fretting coefficient for each case are calculated and listed in Table 6.2. The hypothesis is that fretting is present when the fretting coefficient is higher than one. By examining the values of the fretting coefficients, a prediction of fretting damage can be made. Cases in Table 6.2 are ranked by the danger of fretting, as well as Figure 6.2 through Figure 6.8. The value of the fretting coefficient is one criterion to assess the danger of fretting. The cases with the highest fretting coefficients have the highest danger of fretting. In addition to the actual value of the fretting coefficient, another important criterion is the number of times the spindle torque overcomes the friction torque. Due to the backlash, it is reasoned that it is more dangerous if spindle torque overcomes friction torque in positive and negative directions, than if it overcomes only in one direction. During one revolution, full motion through the backlash is possible only when the absolute value of fretting coefficient goes above 1 in both directions (positive and negative pitch). If it exceeds only in one direction, the fretting motion causes only a compression of the oil spring. As shown in Chapter 4, the amplitude of fretting motion is estimated to be 500 μ m with the effect of backlash while without backlash it is estimated to be 100 μ m.

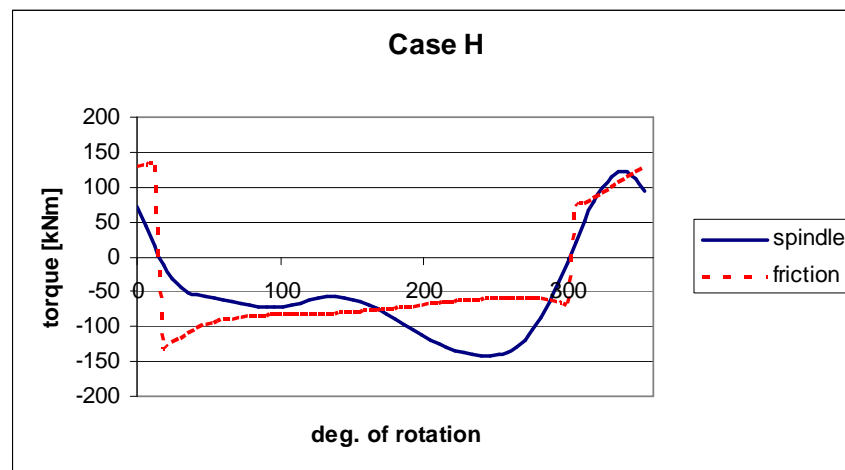


Figure 6.2: Calculated spindle and friction torque for Case H

Table 6.1: Investigated propeller and similar cases

Case (no. of orders)	Ship type	Power, M.C.R. [kW]	RPM, M.C.R. [1/min]	diameter [mm]	speed M.C.R. [kn]	Stress, M.C.R. [%]	C.o.g x[m]	C.o.g y[m]	C.o.g z[m]	cent. Fz [kN]	Fy [kN]	Qy [kNm]	Qz [kNm]	Prop. Skew [deg]	Max Rake [deg]
A (5)	Container	12355	100	6600	20.3	88.3	0.14	0.12	1.74	622	51.2	53	-51	40.5	-3.7
B (7)	Container	12240	105	6200	19.8	93.2	0.15	0.11	1.65	508	46	43.7	-33.7	31.5	0
C (2)	Container	27440	93	7700	24.5	106.9	0.29	0.23	1.93	1203	184	207	-202	45.1	5
D (3)	Tanker	15335	91	7700	16.2	99.5	0.06	0.05	2	786	25	21	-39	23.1	-2.2
E (6)	Ro-Ro	15540	113	6400	19.6	89.1	0.23	0.17	1.71	825	110	121	-87	46.3	-4.4
Investigated (10)	Container	23040	95	7000	26.2	91.6	0.36	0.19	1.83	813	83	266	-150	49.2	-4.9
G (1)	Tanker	8450	100	6300	16.3	72.7	0.05	0.06	1.64	420	14.1	9.3	-31.8	37.1	0
H (2)	Ro-Ro	16012	115	6600	20.1	90.9	0.21	0.15	1.68	742	91	90	-76.2	46.3	-4.26

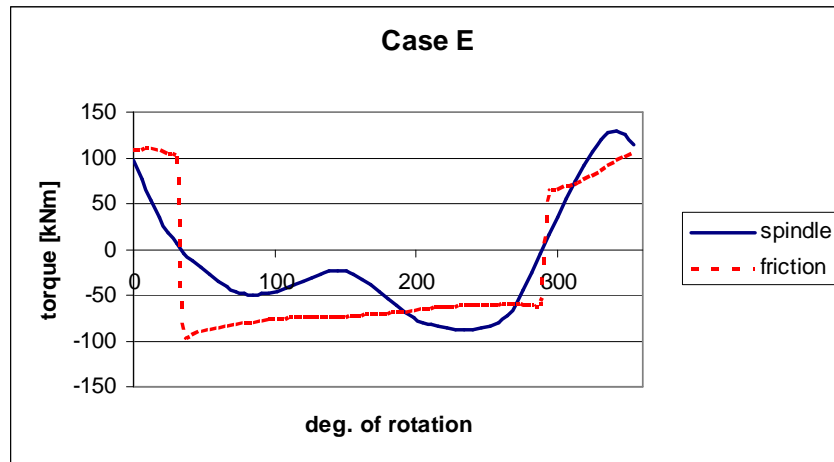


Figure 6.3: Calculated spindle and friction torque for Case E

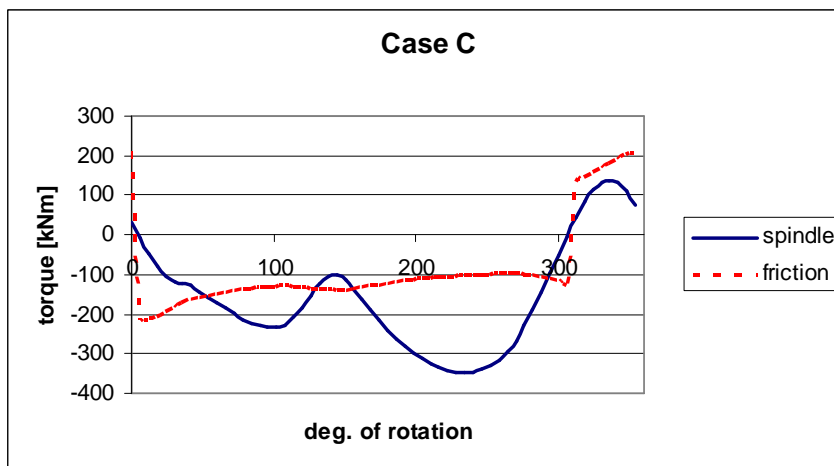


Figure 6.4: Calculated spindle and friction torque for Case C

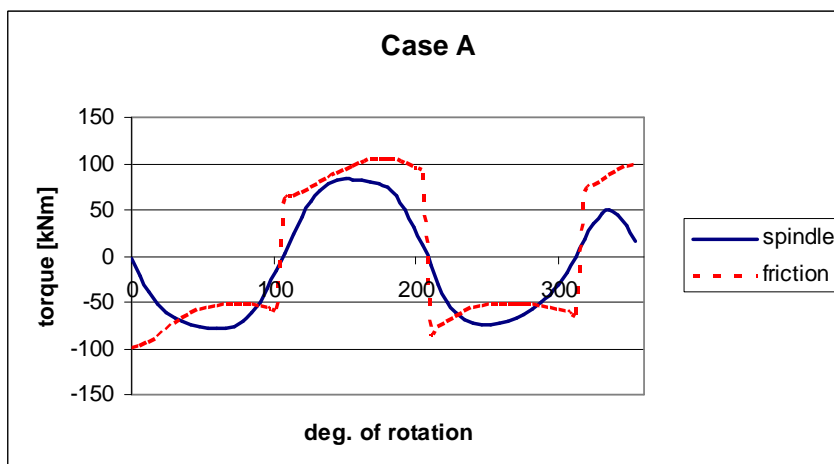


Figure 6.5: Calculated spindle and friction torque for Case A

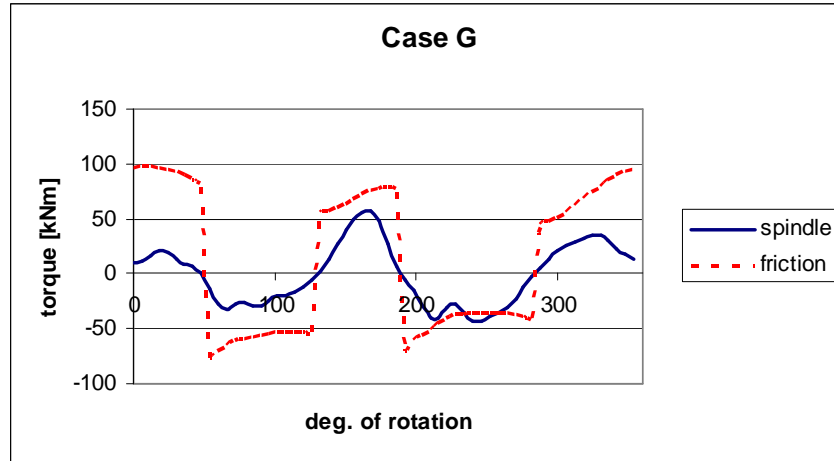


Figure 6.6: Calculated spindle and friction torque for Case G

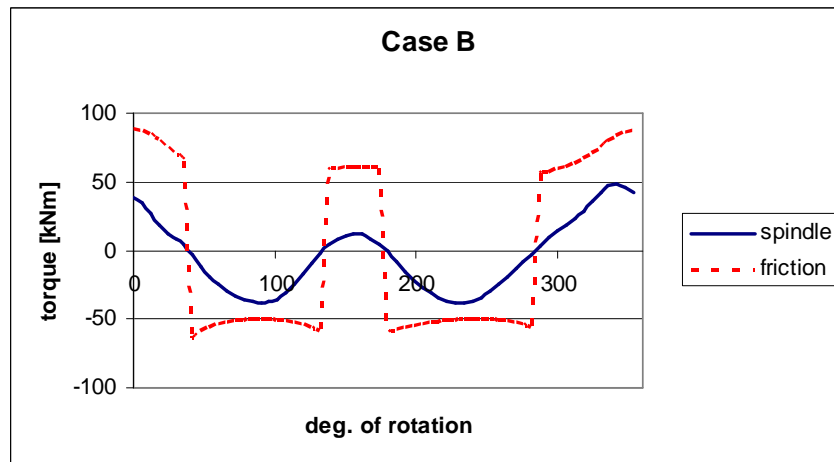


Figure 6.7: Calculated spindle and friction torque for Case B

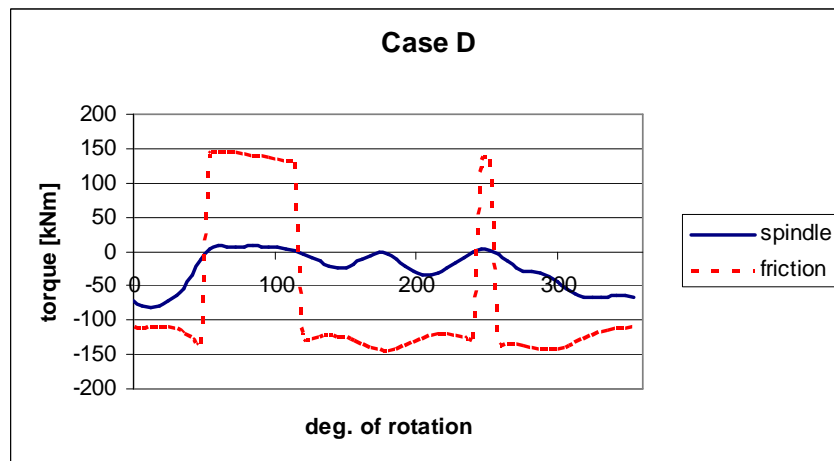


Figure 6.8: Calculated spindle and friction torque for Case D

Results indicate Cases H and E are most similar to the investigated case. For Cases C and A, the spindle torque exceeds friction torque only in a negative direction. The least dangerous are B and D, where the spindle torque does not exceed the friction torque. For Case G, the spindle torque overcomes friction only for a very short period. Following the discussion in Chapter 3 and 4, the influence of hydraulic pressure is neglected.

Table 6.2: Fretting coefficients for cases similar to the investigated case

Case	Min k_{fret}	Max k_{fret}
Investigated	-2.98	1.44
H	-2.35	1.14
E	-1.42	1.38
C	-3.44	0.78
A	-1.49	0.93
G	-1.22	0.75
B	-0.77	0.59
D	-0.75	0.06

The intention is to examine the service history of similar cases to determine if these similar cases also show any record of fretting. Ideally, service records would state the source of the failure, in this case fretting. Unfortunately, this is not the case as service records contain an occasional brief statement of the problem, brief description of work done and parts being replaced. Instead of searching for fretting, it is only possible to examine fretting related problems and parts that are affected by fretting. Fretting related problems can become manifest in the form of wear-out of parts and/or seizure of the CPP. Parts that are affected by fretting are blade bearings and/or seals at the blade foot. The seal of a blade bearing can be affected (wear) by fretting in the same way as the blade bearing. Moreover, because of the higher radius, the fretting amplitude is higher for the seal than for the blade bearing.

Table 6.3 shows extracts from a service history of CPP's that are similar to the investigated case. Service records are shown for each ship, so A (1) is Case A on the first ship of that series, A (2) is Case A on the second ship and so on. It should be noted that this is only the available service history of the manufacturer. It is possible that there is more in the records of the operator. Two things are immediately noticed. Firstly, there is no record of failure cause and failure symptom. Thus, in the records there is no mention of the word "fretting" and "seizure" or "worn out CPP". Secondly, for several cases there was a significant amount of recorded failures related to the intermediate disk in the blade bearing. Moreover, there was a record of placing additional disks to stiffen the contact and improve the sealing. There are two types of work done on intermediate disks; one is placing or mounting (m), and the second is replacing (r). Additionally, the table shows the percentage of sealing and blade bearing problems in relation to all problems.

Table 6.3: Service history of seal and blade bearing problems for similar cases

Case (ship)	Date of service	Type of service
A (1)	23.04.96	Seals
	20.10.96	Blade foot demounted, brought back to Drunen machined and back to ship
	No date	Disks (m) and seals
	No date	Disks (r) and seals

A (2)	10.10.96 03.11.98 30.08.03	Seals Disks (m) Seals
A (3)	20.12.96 22.12.98 12.01.01 14.06.03	Seals Disks (m) Seals and disks (r) Seals and disks (r)
A (4)	12.01.98 15.01.00	Disks (m) Seals
A (5)	12.02.98 10.11.00 30.06.05	Disks (m) Seals Disks (r) and seals

More than 50% of all problems related to seals and bearing problems

B (1)	10.09.98 19.02.01	Disks (m) Seals (r)
B (2)	26.06.96 23.01.01	Disks (m) Seals
B (3)	01.08.99	Disks (m)
B (4)	12.03.00	Disks (m)
B (5)	No date	Disks (m)
B (6)	04.11.97	Disks (m)
B (7)	23.06.97 25.09.99	Seals (r) Disks (m)

Around 25% of all problems related to seals and bearing problems

C (1)	15.07.00 No date	Seals (r) Seals (r)
C (2)	No date	Seals (r)

Around 10% of all problems related to seals and bearing problems

D (1)		No seal and disk problems reported
D (2)	21.10.99 16.05.06	Disks (m) Seals (r)
D (3)		No seal and disk problems reported

Around 5% of all problems related to seals and bearing problems

E (1)	06.07.06	Seals (r)
E (2)		No seal and disk problems reported
E (3)	17.01.00	Seals (r)
E (4)		No seal and disk problems reported
E (5)		No problems reported
E (6)		No problems reported

Around 10% of all problems related to seals and bearing problems

G		No seal and disk problems reported
H (1)		No seal and disk problems reported
H (2)		No seal and disk problems reported

The available service history indicates sealing and bearing problems with Case A propellers. Experience from the hub of Case A, 4C17-3A, showed the need for additional disks to stiffen the contact between blade foot and blade bearing. In later designs, this was solved with a somewhat thicker blade foot. It should be mentioned that replacing the seals and disks is a normal part of preventive maintenance. However, in the reports it is not indicated whether replacement was preventive or corrective. In examining the service records, Case A had the most serious problems. This could be explained if positive spindle torque had overcome the friction torque (Figure 6.5 suggests that just has not). Case A would then be the most dangerous case, because oscillations would have double rpm frequency. As shown in Chapter 3, the relationship between spindle torque and friction torque changes with service conditions, and it is entirely possible that for Case A, positive spindle torque overcame the friction torque during service.

Table 6.4: Risk of fretting and skew of the propeller

Case	skew	Fretting risk
Investigated	49.2	Highest
E	46.3	.
H	46.3	.
C	45.1	.
A	40.5	.
G	37.1	.
B	31.5	.
D	23.1	Lowest

Nevertheless, in examining Figure 6.1 through Figure 6.8 and Table 6.1 and Table 6.2, one interesting observation can be made. Table 6.4 shows cases from Table 6.1 listed by the risk of fretting same as in Table 6.2. It can be seen that the risk of fretting follows the skew angle of the propeller. The high skew propellers are more likely to suffer from fretting than low skew propellers, and the severity of the cases follows the skew of the propellers. Moreover, in a unique case of a recorded fretting problem, the investigated case has the biggest skew.

It is understandable that the danger of fretting follows the skew of a propeller. The influence of skew angle on spindle torque amplitude was investigated in Chapter 4.7.4. The hydrodynamic pressure distribution of high skew propellers is better and more equal than the pressure distribution for low skew propellers. The effect of a propeller's load distribution on fretting can be illustrated as a seesaw with two people sitting on each end. If the weight of each person is similar, it is easy to move the seesaw around

its canter point. If the difference in weight is significant, the load distribution is not equal, and it is difficult to move it.

The predicted most dangerous cases, Cases E and H do not have many records on wear related failures. Furthermore, Cases G, B and D also have very little record of wear related failures. This is in agreement with the estimated fretting danger. However, in the same archive, there is no clear record of fretting or wear related failures for the investigated CPPs. There is only a record of no pitch feedback. It can be stated that the current service records are not sufficient to investigate the wear related failures of a CPP in detail. In any case, field experience is valuable information, but the service records are not adequate to fully validate the work done in this thesis.

In the conclusion of Chapter 6.1, it can be stated that fretting probably occurs more than initially expected, but that it does not necessarily has to be catastrophic for the CPP. The investigated case is not unique, as there are other propellers where spindle torque overcomes the friction torque. However, it is the case with the highest ratio of spindle torque and friction torque, for both positive and negative values.

6.2. Total Wear

In order to estimate the total wear of a CPP, it is necessary to know how much pitch is being used in real service conditions. When the total amount of pitch change is known, the total sliding distance in the blade bearing will be known for a certain time period. In Chapter 5, the total wear was presented as a distribution. The total wear depth of blade bearings (h) can thus be calculated by combining the total sliding distance (S), specific wear rate (w) and load (σ) into the Archard equation:

$$h = w \cdot S \cdot \sigma \quad (6.2)$$

As stated in Chapter 5.1, the pitch change can be classified into small amplitude fretting motion, small amplitude sliding motion, and large amplitude sliding motion. The first type, small amplitude fretting motion, refers to unwilling vibrations caused by an oscillating spindle torque. The second two types, small amplitude and large amplitude sliding motion, refer to motion caused by controls and hydraulic systems. The small amplitude sliding motion would be the small pitch adjustments, which are relatively frequent (every 10 to 120 seconds) and have an amplitude of between 0.5 and 5 degrees. The exact figures depend upon many things, such as leakage, sealing, control strategy, etc. The largest amplitude of sliding motion is from full-pitch ahead to full-pitch astern, for example during the crash-ahead manoeuvre. The large adjustments in pitch may occur a few times a day.

In order to illustrate the wear limit of a CPP, a ferry from Dover to Calais will be used as a reference for the total amount of pitch change during one day. Figure 6.9 shows the recorded pitch position during one voyage. The sampling rate was 10Hz and the pitch position is shown as a percentage of the design pitch.

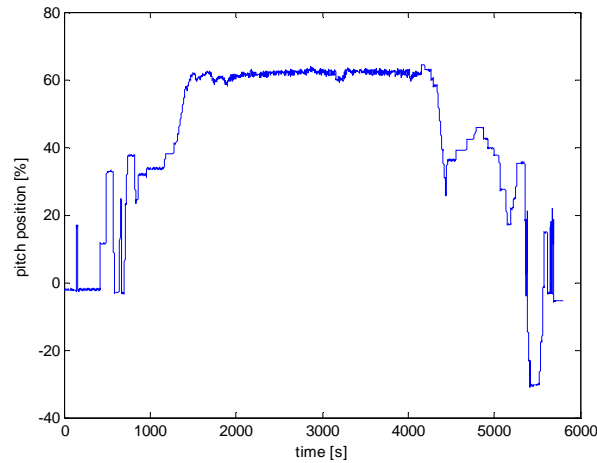


Figure 6.9: Pitch position during one voyage between Calais and Dover

As in any measurement, certain noise will be produced by it. In this case, it is difficult to distinguish between small amplitude sliding motion and noise. In order to exclude noise from the measured signal, using stepwise constant fitting, all changes lower than 0.5% pitch change will be considered noise since the resolution (the sensitivity of the pitch control and actuating system to small input changes) is between 0.5 and 1% pitch. The largest effect of the correction occurs for the period when there is no large pitch change, between 2000 and 4000 seconds. Figure 6.10 shows recorded and corrected pitch signals during a small period of time, in the period of no large pitch change.

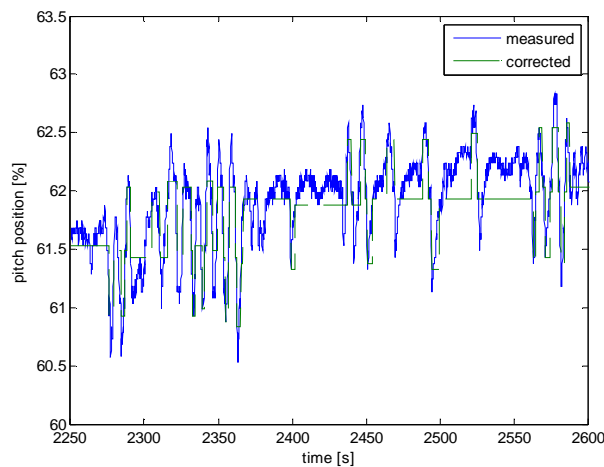


Figure 6.10: Corrected signal of pitch position

This procedure is very relevant for estimating the total amount of sliding distance. Figure 6.11 shows the total amount of sliding distance for the corrected and measured signals. The difference is approximately 2.5 times. It can be seen that the highest difference occurred between 2000 and 4000 seconds of the journey, (i.e. during free sailing ahead).

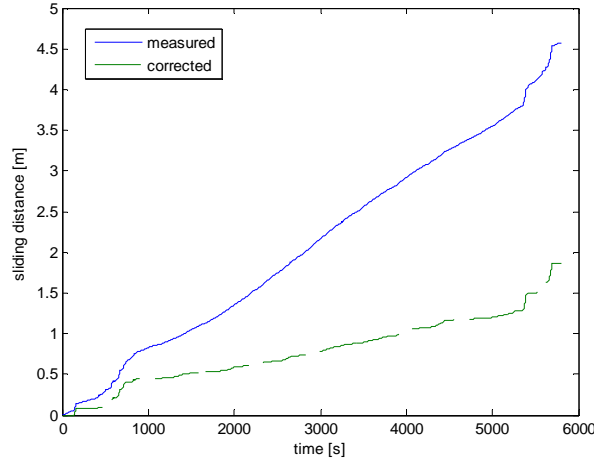


Figure 6.11: Total sum of pitch usage during one voyage; measured and corrected signal

During free sailing ahead, the motion made by hydraulics is small amplitude sliding motion and it is influenced by the control strategy. These small amplitude sliding motions apparently play a large role in determining the total sliding distance. Further information with respect to the influence of control system on total sliding distance can be found in 6.3. Summation of the changes in pitch position shown in Figure 6.9, using the corrected signal, yields a total pitch change of 9.54 times of the design pitch angle ($\varphi_d = 28$ deg). The total sliding distance is obtained by multiplying the design pitch angle with the blade bearing radius ($r = 0.392$ m):

$$S_{\text{corr}}^{\text{voy}} = 9.54 \cdot \frac{\varphi_d}{360} \cdot 2 \cdot \pi \cdot r \quad (6.3)$$

The total sliding distance for the corrected signal (dash green line) in Figure 6.11 is 1.83 meter sliding distance per voyage ($S_{\text{corr}}^{\text{voy}}$) from Calais to Dover. This ship makes around 10 voyages per day (n_{voy}) and operates approximately 340 days per year (n_{day}). The normal overhaul period is five years (n_y), and the total amount of sliding (S_{corr}) for five years is:

$$S_{\text{corr}} = S_{\text{corr}}^{\text{voy}} \cdot n_{\text{voy}} \cdot n_{\text{day}} \cdot n_y = 1.83 \cdot 10 \cdot 340 \cdot 5 = 31110 \text{ m} = 31.1 \text{ km} \quad (6.4)$$

It is possible to determine the allowable wear rate based on the maximum allowable wear, normal load and total sliding distance. The maximum normal load (σ_{max}) in the blade bearing is 21 N/mm² and the maximum allowable wear depth (h_a) is 200 μm, as defined in Chapter 2.10. This yields the allowable specific wear rate:

$$w_{\text{all}}^{\text{corr}} \leq \frac{h_a}{\sigma_{\text{max}} \cdot S_{\text{corr}}} \leq \frac{0.2}{21 \cdot 31110} \leq 3.06 \text{e-}7 \frac{\text{mm}^3}{\text{Nm}} \quad (6.5)$$

As in Chapter 5.5.7, the specific wear rates from Wear Test 06 are shown in Figure 6.12 (left) together with the Weibull fit. In Figure 6.12 (right), the cumulative density function is given together with 95% confidence bounds and, the maximum allowable specific wear rate from Equation (6.5).

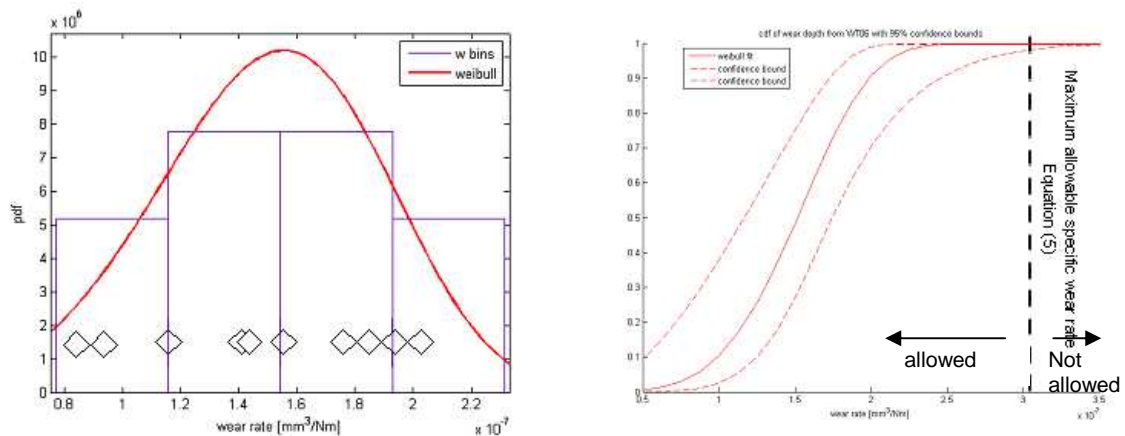


Figure 6.12: Left: Distribution of the total wear rate in Wear Test 6 : 1.74; 1.93; 1.16; 1.54; 1.87; 1.41; 1.48; 0.93; 0.83, 2.06 mm³/Nm; Right: cumulative probability of wear rate and confidence bounds

All wear rates from Wear Test 6 are lower than the maximum allowable wear rate. Even the lower confidence bound almost reaches 1 at the specific wear rate calculated in Equation (6.5). It is possible to say with 95% confidence that the possibility for a wear rate to exceed the allowable wear rate is less than 5%. There is very little chance that the propeller on this ferry will suffer from excessive wear under design conditions.

Another way to assess the allowable wear rate from Equation (6.5) is to compare it with the wear rate presented in Chapter 5.5.3, in Table 5.6. In Wear Test 4 it was found that the specific wear rate was 0.05E-6 mm³/Nm and the value from Equation (6.5) is considerably higher. The analysis done above indicates wear is not a problem for design conditions which include only small amplitude and big amplitude sliding motion, even if the non corrected pitch signal was used.

6.3. Influence of controls on total wear

The task of the propulsion plant control is a very complex one. There are three primary considerations:

- Meeting operational demands, such as acceleration, deceleration, manoeuvring, etc;
- Meeting safety demands, such as overspeed protection, prevent overload, etc; and
- Suppression of disturbances, avoiding strong fluctuations in speed and/or load.

There are also many other considerations to be taken into account, such as economy (maintenance and fuel), comfort, operational tasks, etc. There are numerous theoretical possibilities for defining control regimes. However, in present installations there are only two options for the controlling variable that comes out of the controller, the rpm demand and/or pitch (for systems with CPP).

A short description of a present control strategy for ships with CPPs is as follows. For systems with a CPP, there is a general control command, known as the combinatory curve, used to set both pitch and engine speed. The combinatory curve is used to define controlling variables (pitch and rpm), for part load and full speed ahead, without endangering the propulsion plant. Once the ship reaches demanded speed, all disturbances can be suppressed by controlling either the engine or pitch. However, in

order to reduce the wear of a CPP, the focus is on the engine and pitch is changed only when necessary.

Usually, in order to power the shaft generators, rpm is set constant and all disturbances are suppressed by controlling the engine load.

In order to reduce engine thermal load, a new control strategy was proposed in [Grimmelius, 2001]. Rather than using only one variable (pitch or fuel rack), it is possible to use multiple input and multiple output (MIMO) controllers that control the pitch and fuel rack simultaneously. In sea state six, it was calculated by simulation that the MIMO controller would cause a 5% amplitude of pitch change, with a frequency not higher than 0.1 Hz. Figure 6.13 shows results of the simulation of a MIMO controller made in [Grimmelius, 2001].

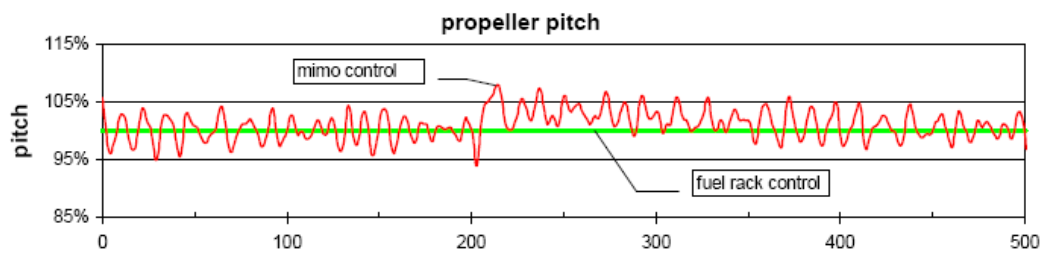


Figure 6.13: Simulation of active pitch control from [Grimmelius, 2001].

In order to estimate the influence of the MIMO behaviour controller on total wear, it will be assumed that the ship is sailing in a sea state lower than sea state six. Therefore, pitch oscillations will be assumed to have 3% amplitude with 0.1 Hz frequency. The 3% pitch oscillations will be superimposed (added) on the mean pitch shown in Figure 6.9 during free sailing ahead, (time between 1500 and 4200 seconds). During acceleration and de-acceleration the measured pitch value will be used since the pitch change was obvious and higher than the noise level. Figure 6.14 shows an estimated pitch position and total sliding distance using the MIMO behaviour controller during one voyage. A normal control strategy is assumed during manoeuvring and acceleration.

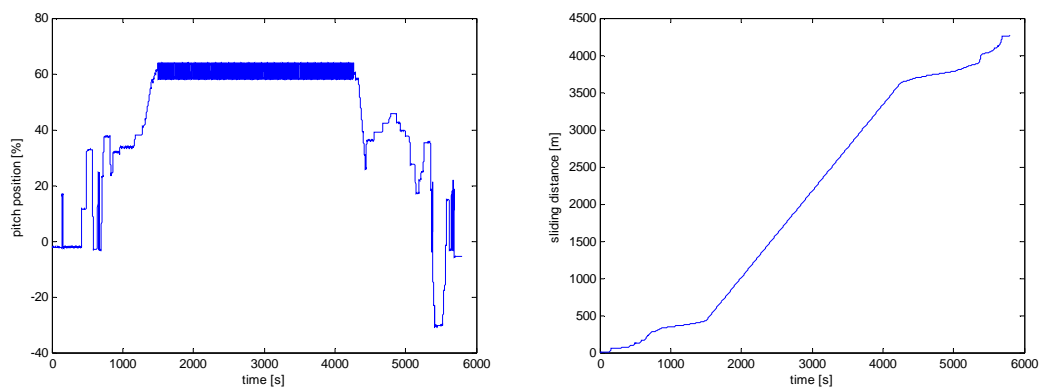


Figure 6.14: Estimated pitch usage with MIMO controller

The pitch usage increased more than four times with the MIMO behaviour controller. Therefore, it can be said that the active pitch control will cause four times more wear than the current control strategy. The total sliding distance per voyage (S_{MIMO}^{voy}) is 8.1 meters, which for five years gives a sliding distance of:

$$S_{MIMO} = S_{MIMO}^{voy} \cdot n_{voy} \cdot n_{day} \cdot n_y = 8.1 \cdot 10 \cdot 340 \cdot 5 = 137.7 \text{ km} \quad (6.6)$$

The allowable specific wear rate is:

$$w_{all}^{MIMO} \leq \frac{h_a}{\sigma_{max} \cdot S_{MIMO}} \leq \frac{0.2}{21 \cdot 137700} \leq 0.7e-7 \frac{\text{mm}^3}{\text{Nm}} \quad (6.7)$$

Using a MIMO controller, the allowable specific wear rate is extremely low for wear distribution shown in Figure 6.12. Based on results from Wear Test 6, as shown in Figure 6.15, there is less than 0.5% probability that the wear rate of the blade bearing will be lower than the allowable.

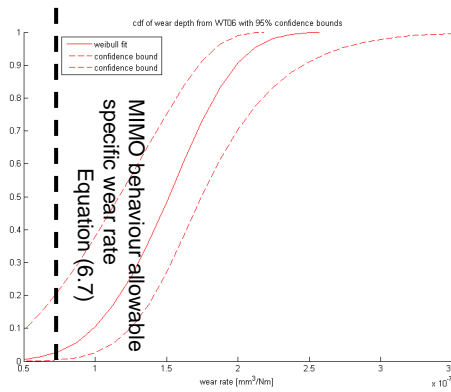


Figure 6.15: cumulative probability of wear rate with confidence bounds from Wear Test 6 and allowable specific wear rate for MIMO control from Equation (6.7).

However in Wear Test 4 and in Table 5.6, the measured specific wear rate is $0.05E-6 \text{ mm}^3/\text{Nm}$. This specific wear rate is lower than the allowable wear rate calculated in Equation (6.7). The difference in results between Wear Test 5 and 6, and Wear Test 4 was explained by the different hardness of CuNiAl material in Chapter 5.5.6. With currently available data, it is difficult to give a final answer whether the MIMO behaviour control strategy will cause excessive wear in the blade bearing. Therefore, it is recommended to do more tests to determine the variation in results for the correct CuNiAl hardness. It seems safe to state that CuNiAl of sufficient hardness is necessary to allow more frequent control.

6.4. Influence of fretting on total wear

The influence of fretting on total wear will be made for the case of a ferry travelling between Calais and Dover. For this ferry, the design rpm is 150 and it will be assumed that the fretting amplitude (d_{fret}) is $300\mu\text{m}$. This amplitude includes the effect of backlash and it is selected just for illustrative purpose. One voyage time (t_{voy}) is approximately 100 minutes and the total amount of fretting motion for one journey is:

$$S_{fret}^{voy} = 2 \cdot d_{fret} \cdot \text{rpm} \cdot t_{voy} = 2 \cdot 0.3 \cdot 150 \cdot 100 = 9 \text{ m} \quad (6.8)$$

Or in five years:

$$S_{\text{fret}} = S_{\text{fret}}^{\text{voy}} \cdot n_{\text{voy}} \cdot n_{\text{day}} \cdot n_y = 153 \text{ km} \quad (6.9)$$

The amount of sliding distance caused by fretting is approximately 6 times higher than sliding caused by standard pitch usage. If fretting is present, the total sliding distance per journey is:

$$S_{\text{tot}} = S_{\text{corr}}^{\text{voy}} + S_{\text{fret}}^{\text{voy}} = 1.83 + 9 = 10.83 \text{ m} \quad (6.10)$$

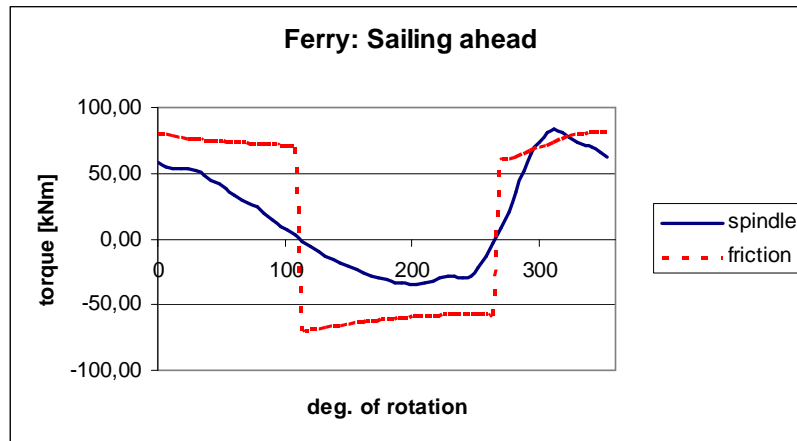


Figure 6.16: Friction torque and spindle torque of ferry's propeller

The total sliding distance is lower than for a MIMO behaviour controller, but considerably higher than for a case without fretting. For a propeller installed on the ferry, no fretting is expected. Nevertheless, in order to estimate the presence of fretting, Figure 6.16 shows friction torque and spindle torque of the propeller installed on the ferry. The maximum fretting coefficient is 1.13, and it is higher than one only for a short period, between 300 and 318 degrees of the blade's position. For this propeller no fretting is expected and 300 μ m fretting amplitude is selected only to illustrate the danger of fretting.

The variation of wake field is the main source of spindle torque oscillations. The investigated ferry is a two shaft vessel, and the wake field variation is lower than for single shaft vessels. For 1.13 fretting coefficient and for such a short period, the possibility of 300 μ m fretting amplitude seems highly unlikely and the chosen fretting amplitude is only for purposes of illustrating the fretting damage.

6.5. Discussion

The investigation done in Chapter 6.1 was inconclusive. The service records provide no hard information and are not suitable to verify the fretting hypothesis. However, it seems fretting may be present more often than initially believed. There is evidence of seal problems and there is possibility that it is related to fretting.

A ferry has been used as an example to estimate the total wear. It was a conservative choice since the pitch is used frequently and any estimate of wear is towards the safe side. In addition to the known parameters that influence wear, it was shown that the control strategy has a very influential role on the total amount of wear. Different control strategies yield different amounts of total sliding distance especially during free sailing ahead. This was already indicated in Figure 6.11 where measured and corrected pitch

signal differ by 2.5 times. The highest difference was during free sailing ahead, between 1500 and 4200 seconds of the voyage. If the measured signal was entirely correct, the total wear would be 2.5 times larger.

In addition, in Chapter 6.3 it was estimated that the usage of an advanced control strategy with multiple input and output signals (MIMO behaviour) would cause approximately 4 times more wear than the present solution, but this could be higher or lower (see [Vrijdag, 2009]).

The estimate of total wear depth depends upon the value of the specific wear rate. There are two sources of specific wear rate (w). The first source is Wear Test 6 and results presented in Chapter 5.5.7 where the wear depth was presented as a distribution, with a mean value of 0.085 mm for wear depth or $0.21\text{E-}6 \text{ mm}^3/\text{Nm}$ for specific wear rate. The distribution itself was an important finding that showed the spread of possible results. However, experiments done in Wear Test 6 were for material softer than the standard CuNiAl hardness. The other source is Wear Test 4 and Table 5.6 from Chapter 5.5.3, which resulted from experiments done for standard hardness. There, the wear rate is estimated to be $0.05\text{E-}6 \text{ mm}^3/\text{Nm}$. However, it was done on a limited number of samples and the spread of data has not been determined.

Using wear distribution from Chapter 5.5.7, into Chapter 6.2 it was shown that there is huge probability that the blade bearing will meet its demands, even for materials softer than allowed, providing that the standard control is used without fretting. However, the distribution of wear rate from Chapter 5.5.7 does not allow the use of the advance pitch control (MIMO behaviour) while results in Chapter 5.5.3, i.e. $w = 0.05\text{E-}6 \text{ mm}^3/\text{Nm}$, would allow it. In order to get more certainty it is recommended to repeat Wear Test 6 but for correct CuNiAl hardness.

In order to illustrate different influences on the total amount of wear in the blade bearing, the total amount of wear will be compared for standard control with sliding wear, MIMO behaviour control and, standard control with sliding and fretting wear. The total amount of wear will be calculated using the specific wear rate from Wear Test 4, keeping in mind that the allowable wear depth is $200\mu\text{m}$.

For the case of standard control where only small amplitude and big amplitude sliding motion is present the total wear depth is estimated:

$$h_s = w \cdot \sigma_{\max} \cdot S_{\text{corr}} = 0.54 \cdot 10^{-7} \cdot 21 \cdot 31100 = 35\mu\text{m} \quad (6.11)$$

For the case of a MIMO behaviour controller, the total wear depth is estimated as:

$$h_{\text{MIMO}} = w \cdot \sigma_{\max} \cdot S_{\text{MIMO}} = 0.54 \cdot 10^{-7} \cdot 21 \cdot 132700 = 150\mu\text{m} \quad (6.12)$$

For the case of a propeller experiencing fretting, the total distance is the sum of sliding distance from Equation (6.4) and fretting distance from Equation (6.9):

$$S_{\text{fret}}^{\text{tot}} = S_{\text{fret}} + S_{\text{corr}} = 153 + 31.1 = 184.1 \text{ km} \quad (6.13)$$

This yields the total wear depth:

$$h_{\text{fret}} = w \cdot \sigma_{\max} \cdot S_{\text{fret}}^{\text{tot}} = 0.54 \cdot 10^{-7} \cdot 21 \cdot 107600 = 209\mu\text{m} \quad (6.14)$$

The influence of fretting on total wear has been illustrated and it is quite significant. This is due to the rpm dependency of fretting. Although the displacement amplitude is small, the fretting motion is frequent, and during five years it provides a significant distance. Table 6.5 gives the estimated wear depth after 5 years caused by the different control regimes and the presence of fretting.

Table 6.5: The total amount of wear depth as a function of control strategy and presence of fretting wear ($w=0.54e-7$; $\sigma=21\text{N/mm}^2$).

Total wear depth [μm]	Control strategy	Wear
35	Standard	Sliding
150	MIMO Behaviour	Sliding
209	Standard	Sliding and fretting

Please note, in order to illustrate the influence of fretting on the total amount of wear in the blade bearing, the same specific wear rate was used for both, fretting wear and sliding wear. In Wear Test 8 and 9 it was found that the specific wear rate was higher for fretting wear than for sliding wear, the value from Wear Test 4. It is possible that the influence of fretting wear could be even higher. However, experiments done in Wear Test 8 and 9 had Hertzian contact geometry and, the loads were also higher than the load used in Equations (6.11), (6.12), and (6.14). Therefore, it is recommended to do further fretting tests with lower loads and non-Hertzian contact geometry.

A similar remark could be made for the total amount of wear calculated for sliding wear. In Equation (6.11) the value for specific wear rate was obtained from experiment done for the load of 48N/mm^2 while the maximum load in the blade bearing is 21N/mm^2 . Even if the specific wear rate would be lower for 21N/mm^2 then the estimate of total wear depth in Equation (6.11) would be more conservative and toward safer side.

6.6. Conclusions

Following the discussion in Chapter 6 following conclusion can be made:

- Sliding wear in combination with the present control strategy and under design conditions will not cause wear higher than allowable ($200\mu\text{m}$) between two overhauls (five years).
- Advance control strategies (MIMO behaviour) need require more experiments
- Fretting wear is a significant source of wear in blade bearing.

7. In retrospect

The background and motivation for the work undertaken in this thesis are presented in Chapter 1. They are followed by stating the goal of the research and the main questions related to the research. With respect to the goal, this thesis contributes to the better understanding of wear as a failure mechanism of a CPP. More specific main findings and contributions are:

- Sliding wear is less dangerous for a CPP than fretting wear
- Occurrence of fretting in a CPP is explained and a factor to quantify the effect was proposed
- The amplitude of fretting motion in a CPP was quantified and tested.
- An overall wear model was proposed to estimate the amount of wear in a CPP

The thesis sets a blueprint for evaluation of wear in CPP in service conditions. This was achieved by a wide multi-disciplinary research combining different technical sciences and engineering disciplines, such as tribology, mechanics, hydrodynamics, system integration, etc. The multi-disciplinary approach allowed the creation of a relationship between the skew of a propeller and fretting, controls and wear, ventilation and fretting, etc. Further, theoretical analysis was combined with set of tribology experiments to achieve the goal.

7.1. Discussion

In order to understand wear as a failure mechanism, it was necessary to define the wear related failures in a CPP. In Chapter 2, two failures of a CPP were described as wear related, namely, the worn out and seized CPP. A CPP is worn out when the amount of wear exceeds the allowable amount of wear. The allowable wear depth was defined as 200 μm , which is the sum of all tolerances in the mechanical assembly of a CPP. If the total amount of wear exceeds the allowable value, the mechanism of a CPP becomes too loose and inaccurate. On the other hand, a seized CPP, or a CPP that would suffer from seizure, would not be able to move and to change the pitch. In Chapter 2, after examining main wear mechanisms, it was realized that the fretting wear mechanism may cause entrapment of debris, which could lead to the seizure of a CPP. In Chapter 2.7, due to its intriguing fretting failure, one specific propeller was selected to be the investigated propeller. In conclusion of Chapter 2, the investigation was focused on the blade bearing of a CPP and on two wear situations, the sliding wear and fretting wear.

The multi-disciplinary approach presented in Chapter 1, includes aspects of wear related to the load, type and amount of motion, and tribology experiments. For the investigated CPP, the load in the blade bearing was analyzed in Chapter 3. After examining loads in the blade bearing for design conditions, it was realized that the blade spindle torque overcomes friction torque for design conditions. The moment when this happens ($M_{sp} > Q_{fr}$) was defined as the start of fretting motion. In Chapter 3, it was argued that in addition to the spindle torque and friction torque, the hydraulic pressure could also play a role in the total equilibrium of forces. However, the most conservative case was chosen by arbitrarily selecting the hydraulic pressure to be zero.

The hydraulic pressure can introduce an uncertainty in the analysis, but it should be looked at as a reaction force rather than as an action force. The influence of hydraulic pressure was also examined in Chapter 4 in order to reduce the uncertainty related to it. Later in Chapter 3, the theoretical fretting coefficient (k_{fret}) was introduced as the ratio of spindle torque and friction torque. This coefficient was not suitable for the investigation of self propulsion tests in heavy seas, as thrust was only available for the entire propeller instead of individual loads per blade. Investigations showed the importance of including the maximal values of blade spindle torque in design criteria. If only mean values of the spindle torque are considered, no fretting motion is predicted. In Chapter 3, it was shown that the fretting motion in the blade bearing is a combination of wakefield distribution and blade design. A wakefield with high variations in the wake factor is more likely to cause fretting motion, as is the case for large single screw vessels. In order to completely avoid fretting, the variations of spindle torque must be lower than the Coulomb friction torque. The draft of a ship was shown to be an important aspect and low draft situations are very dangerous for fretting in a CPP. In Chapter 3, the main step towards understanding the occurrence of fretting motion wear was made.

At the beginning of Chapter 4, the main aspects of friction behaviour were investigated. As an important statement, a sentence from [Persson, 2000] shows the complexity of friction behaviour. Persson states that “an exact treatment of the interaction between two solids needs to include microscopic effects on atomic level”. Since the interaction of solids in contact can apply to both friction and wear, the same remark can be made for wear behaviour. It is only natural that processes which depend on so many (microscopic) factors give a spread of results, even though the main (macroscopic) parameters are the same. The effect of this is visible in Chapter 5.5.7 where 10 samples exposed to same load and sliding distance give different results of total wear depth.

In Chapter 4, the main parameters that may influence the fretting motion were investigated. The fretting motion in the blade bearing of a CPP occurs when spindle torque of the blade overcomes the friction torque in the bearing. Other parameters that may significantly increase the fretting motion (maybe even become governing factors) are draught, skew, mass (size), ship form, and backlash in the mechanism. For design case, the amplitude of fretting motion in the blade bearing for the investigated propeller is approximately 100 μm . The influence of backlash on the amplitude of fretting motion is significant. The amplitude increases not only for the clearance in the bearing (backlash is 200 μm), but the body picks up additional speed and gives a total fretting amplitude of 500 μm . With respect to the uncertainty of influence of hydraulic holding pressure on fretting motion, it was found that the hydraulic holding pressure cannot oppose the fretting motion. In Chapter 1.7, one of the questions was whether the hydraulic pressure could be used to detect fretting. Theoretically, fretting motion in the blade bearing should create the motion of yoke and pressure pulses. However, it is not likely to be able to detect them in the OD box due to the long oil pipes. One of effects that can cause fretting is ventilation. Ventilation increases the spindle torque drastically, and as such, can introduce fretting motion.

In Chapter 5, a number of experiments were done to obtain specific wear rates resulting from pitch sliding and fretting motion. An increase of wear and friction was observed in sliding wear experiments for higher loads. The increase of friction may result in the inability to change the pitch, which would manifest as a seizure of a CPP. However, for loads below 48N/mm², the material combinations used in a CPP are found to have a satisfactory specific wear rate for sliding wear. The above mentioned spread of results

in Chapter 5.5.7 was an interesting observation. However, in order to gain more confidence in the distribution and spread of results, it is necessary to do more experiments. The influence of uncertainty in distribution was evident in evaluating allowable specific wear rates in Chapter 6.2.

Fretting wear experiments showed that the amplitude of fretting motion plays an important role in specific wear rate, but the most dominant is lubrication. Observed specific wear rates were by factor 100 lower for lubricated conditions.

The specific wear rate observed in fretting wear experiments is higher than the specific wear rate from sliding wear. However, there is a difference in the contact situation and loads between the sliding and fretting sets of wear experiments. It is not possible to estimate, with sufficient certainty, which one of the two wearing mechanisms, fretting or sliding, is more dangerous. In order to gain a definitive answer, it is recommendable to undertake fretting tests with amplitude of fretting motion. It is unclear as why the fretting wear would be more dangerous. The tangential stress on the surface is highest for the break away force, the moment of transition from stop to gross sliding. One possibility is that the fretting wear is more dangerous due to its frequent transitions from stop to go. Due to its vibrating nature, the break-away force is more frequent in the fretting situation than in sliding situation. For fretting, this may lead to higher tangential loads than for sliding. A further possibility is that with longer amplitude sliding, more oil can enter the contact in comparison with fretting motion.

Nevertheless, for a blade bearing, fretting motion is very dangerous due to its high frequency. In Chapter 6.5, it was shown that total amount of wear with fretting is four times higher than the amount of wear without fretting, even with the same specific wear rate. The presence of fretting may explain why some propellers suffer from quick and extensive wear in the blade bearing. Analysis undertaken in Chapter 6.5 was done for a relatively mild version of fretting wear, as the specific wear rate was the same as for sliding wear. The amplitude of fretting motion was 300 μm , although in Chapter 4 it was estimated that it can increase to 500 μm . Also, the calculation was for a case of good lubrication. In real CPP conditions, there is never perfect lubrication and a small intrusion of water is always expected. It is possible that fretting wear can cause ultimate failure of a CPP by exceeding the allowable wear, as hypothesized in Chapter 1.7. However, seizure of the blade bearing caused by fretting was not observed in this work. In order to provide a definitive answer, a fretting experiment with a larger non-Hertzian contact is recommendable. The discussion in Chapter 6 presented a possible technique to estimate the total wear by knowing the specific wear rate and the total usage of CPP. To estimate wear in real service conditions, it is proposed to use the total pitch sliding filtered for noise. For a full overview of the wear and condition of a CPP, it is suggested to monitor oil quality and the presence of water in it.

The entire work of this thesis outlines a blueprint for estimation of total wear of a CPP. This can be used to evaluate any future advanced pitch control strategies. The wear of blade bearings and other components of a CPP do not represent an obstacle for further development of CPPs. The problem might be in other components, such as counter balance valves and long oil pipes, which decreases the pitch actuating speed and CPP mechanism. If a higher wear resistance is needed, it is recommended that hard coatings, and not Teflon, be applied.

7.2. Recommendations

With respect to the work done, most important recommendations are:

- Fretting tests in combination with non-Hertzian contact and design load are recommended
- Repeat Wear Test 6 but with correct hardness and preferably do more tests to get confidence in the results
- Maintaining good lubrication is crucial. It is recommendable to develop better sealing and investigate the use of oils with higher tolerance on water presence
- Investigate hard-wearing coatings in blade bearing applications
- Reduce tolerances in blade bearing

Appendix A: The Project “DYLOPROPS”

Dyloprops is an acronym for: Dynamic Loads on Controllable Pitch Propellers in Service and the project was focused, as its name says, on dynamic loads on CPP in service conditions. The project team consisted of senior technical staff of Maritime Research Institute Netherlands, Delft Technical University, Royal Netherlands Naval College and Wärtsilä Netherlands. During four years the project covered the following items:

- dynamical behaviour of the controllable pitch propeller systems
- exploration of mechanical limits of a CPP
- improvement of simulation models of diesel engines
- exploration of thermal and mechanical limits of diesel engines
- better control algorithms
- investigation of loadings and phenomena while operating in heavy sea states
- new solutions for controllable pitch propeller construction

The external loads on the propeller were studied using an existing ship model of a fast container vessel. In this thesis measurement done in the project “Dyloprops” were used in Chapter 3 and Chapter 4.

Influence of ventilation on the blade spindle torque is presented in Chapter 4 with reference to experiments done in Dyloprops and results shown in [Beek, 2006]. The experimental results, unique in its sort indicated that heavy ventilation completely changes the size and character of the external load even when the propeller is not coming out of the water. A high importance was given to the occurrence of the amplification of the actuating forces in the dynamic overload of the propeller installation. Given the nature and unexpected occurrence the presence of ventilation could explain the phenomena. However it was also anticipated that this could not be solved by theoretical calculations. Therefore an extensive experimental program was carried out to verify the effects of ventilation or cavitation, first in calm water and later in waves.

The difference between cavitation and ventilation is that ventilation occurs due to air ingress at the propeller whereas cavitation occurs when the local pressure is below the vapour pressure. Experiments were carried out to verify the effects of ventilation in the vacuum tank under atmospheric pressure (without ventilation) and with scaled pressure, i.e. under cavitation and ventilating conditions. In this way a unique set of data was obtained which allows a first overview of the phenomena. Figure A.1 shows some of results made in those experiments.

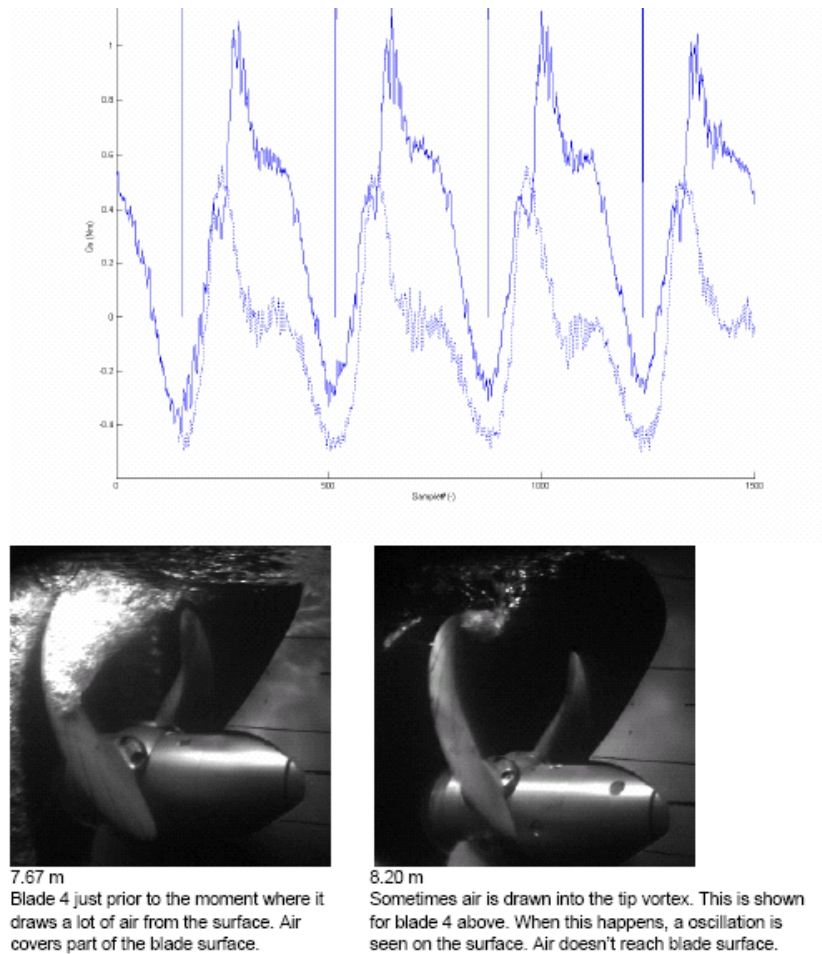


Figure A.1: Results of calm water tests with effect of cavitation and ventilation on actuating forces.
Source: [Beek, 2006]

In the course of the project, seakeeping tests are performed with a segmented model to explore the effects of the motions and flexural response on the propeller loading in waves. The seakeeping tests were used in Chapter 3 to analyze the fretting coefficient in service conditions. The purpose of the tests is to obtain a realistic and complete impression of the propeller (spindle) load variations that are experienced at sea. Additionally, measurements focus on the effects of ventilation and hull girder whipping and some results can be found in [Dallinga, 2006].

The tests are performed with a model of a fast, light-weight container ship. The wooden model was partially cut in a transverse way to adjust the stiffness. The aim was to model the natural frequency in the two-node bending; the flexural response of the model will be representative (although not the same) for that of the ship. By measuring both the flexural behaviour and the propeller response information is obtained on the direct relation between those two. The tests are performed in the seakeeping and manoeuvring basin of MARIN (Figure A.2) with a self-steering free-running model (Figure A.3).

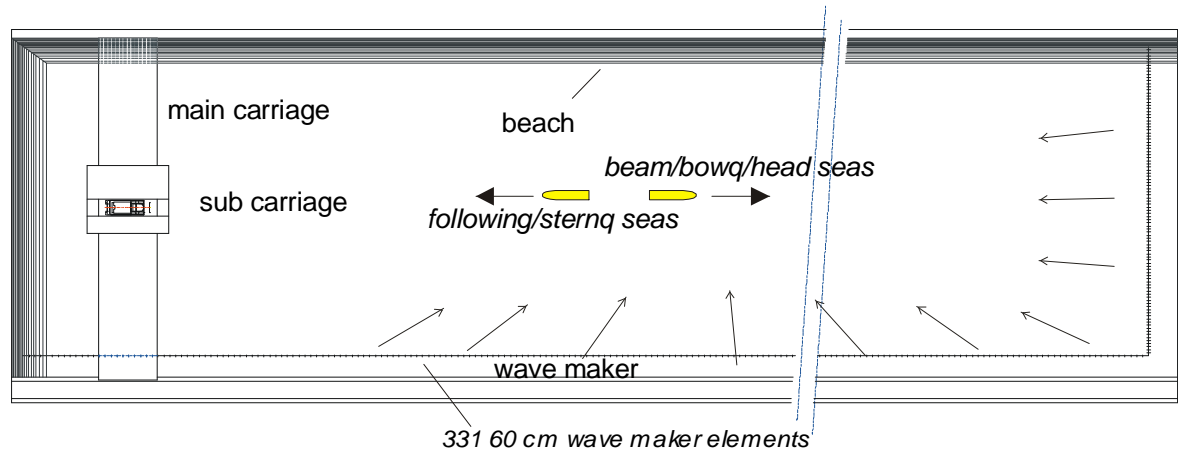


Figure A.2: Seakeeping basis used for tests.

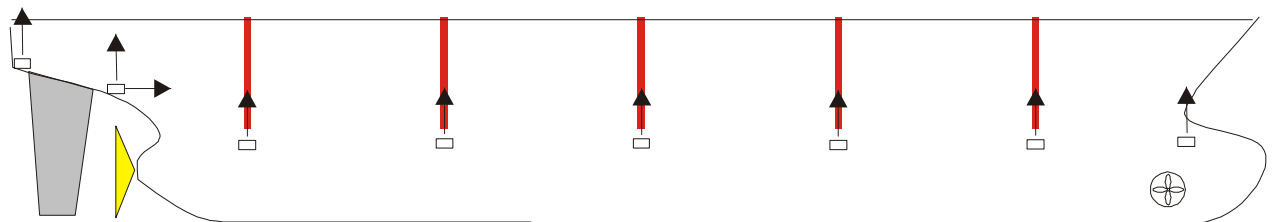


Figure A.3: Container ship model with acceleration sensors

The test comprises of variations in ship speed, heading, significant wave height and mean period which identified the most critical issues and situations. These experiments were completed by carrying out tests with a free running ship model in various wave conditions. While varying the wave conditions and direction the dynamic blade forces, thrust and torque were measured as well as motion and acceleration of the ship. The measurements contained:

- the rigid body motions;
- the bending moments and the whipping accelerations of both halves (4 vertical accelerations);
- mid ship bending moment;
- model speed,
- (fixed) propeller rpm;
- propeller thrust and torque;
- propeller blade forces and spindle torque;

- rudder angles
- loads on transverse thrusters in waves

Tests used in Chapter 3 and corresponding conditions are shown in Table A.1.

Table A.1: Seakeeping tests in irregular seas

Test no.	Wave Conditions			Speed [knots]	Spectrum type	Rpm
	Significant wave Height [m]	Peak Period [s]	Heading [deg]			
1	2.90	7.6	180	24.4	Jonswap	111
2	4.85	9.8	180	22.2		106
3	7.45	12.2	180	19.8		106
4	4.85	9.8	180	17.1		83
5	7.45	12.2	180	15.8		86-91
6	4.85	9.8	180	7.6		42
7	7.45	12.2	180	6.9		46
8	7.45	12.2	180	12.4		67-71
9	7.45	12.2	0	20.6		89
10	7.45	12.2	315	19.7		92
11	7.45	12.2	330	20.2		88
12	7.45	12.2	90	20.0		89
13	7.45	12.2	135	16.4		86
14*	2.90	7.6	180	25.1		108-104

Appendix B: Sensitivity analysis of LuGre friction model

Following text explores one dynamic friction model, the LuGre model, and its sensitivity on values of parameters used in the model. The LuGre friction model is defined as:

$$F_{fr} = \sigma_0 \cdot z + \sigma_1 \cdot \dot{z} + \sigma_2 \cdot \dot{x} \quad (B.1)$$

$$g(\dot{x}) = F_c + (F_s - F_c) e^{-(|\dot{x}|/v_s)^2} \quad (B.2)$$

$$\dot{z} = \dot{x} - \frac{\sigma_0 \cdot |\dot{x}|}{g(\dot{x})} \cdot z \quad (B.3)$$

A short description of LuGre friction model will be given here and for more details reader is referred to chapter 4.4.2 of this book. During pre-sliding, the actuating force is cancelled by a spring-damper system ($\sigma_0 \cdot z$ and $\sigma_1 \cdot \dot{z}$). For a very small (pre-sliding) velocity, the first part in (B.1) corresponds to hysteresis behaviour of the friction force and for gross sliding; it corresponds to the Stribeck behaviour. The second part of (B.1) provides damping of vibrations during the pre-sliding regime, and it vanishes for gross sliding. To visualize it, the average bending of asperities has a constant value ($z=\text{const.}$) for gross sliding. The third part of (B.1) corresponds to viscous friction. In this work viscous friction is assumed zero due to high load and low speed, i.e. $\sigma_2=0$.

Figure B.1, on the left side, shows the model which will be used in this sensitivity analysis. It is a body with mass m , actuated by force (F), and with the resisting friction force (F_{fr}). On the right side, Figure B.1 shows a MatLab Simulink version of the investigated model. The difference of actuating force (F) and friction force (F_{fr}) causes body to accelerate which results in the velocity and displacement of the body.

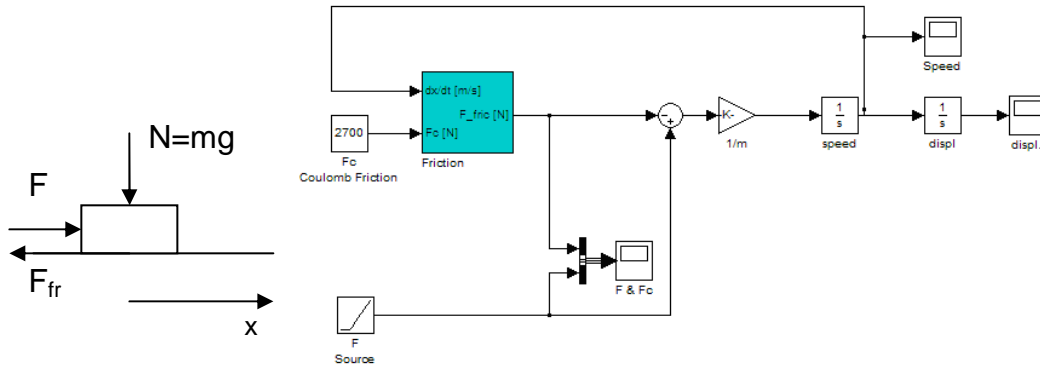


Figure B.1: Left: physical model; Right: Simulink model

The Coulomb friction force F_c is:

$$F_c = \mu \cdot N = \mu \cdot m \cdot g \quad (B.4)$$

The acceleration of body is:

$$m \cdot \ddot{x} = F - F_{fr} \quad (B.5)$$

It is assumed that body has a mass (m) of 2800 kg and friction coefficient (μ) is 0.1, these values have been chosen so that they match Coulomb friction from experiment in 4.3. The friction in the system is calculated using the LuGre friction model. Starting values for coefficients used to describe LuGre model have been chosen arbitrary and they are given in the Table B.1. Following analysis focuses on the influence of each parameter on the resulting friction force.

Table B.1: Starting values of LuGre parameters

Parameter	Value	Unit
σ_0	3e8	[N/m]
σ_1	400	[Ns/m]
σ_2	0	[Ns/m]
F_s	$1.1 \cdot F_c$	[N]
v_s	0.02	[m/s]

- Sensitivity of LuGre on solving method used in MatLab:

Firstly the model will be tested for the type of solving methods used in MatLab Simulink. Figure B.2 shows the comparison of friction force made using ODE45 and ODE23s solving method while all LuGre parameters are as in Table B.1. Apparently, oscillations of friction force with ODE45 are too high and this solving method is not suitable. It was observed that the solvers with the fixed step size require the step size of 0.00001 while the simulation is too slow and the oscillation of friction force is too high. As seen, the selection of proper solving method is important.

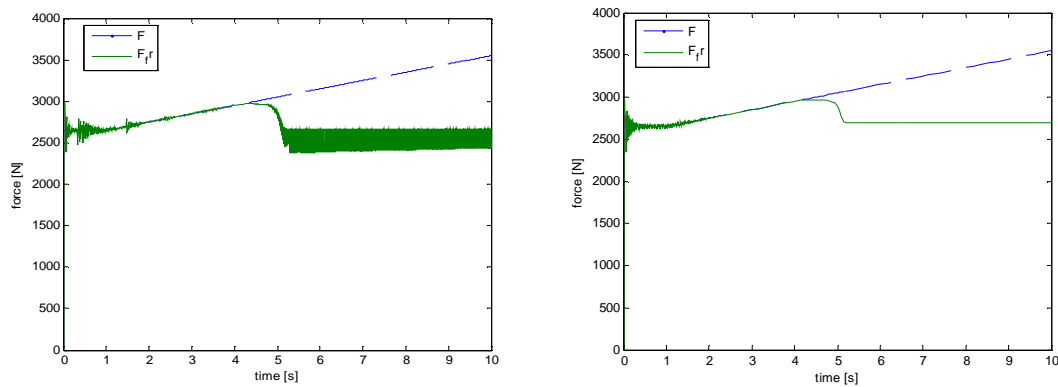


Figure B.2: ODE45 (left) and ODE23s (right)

- Sensitivity of LuGre on initial asperity displacement:

At the start of simulation, as it can be seen in Figure B.2, there is a vibration of friction force. It is reasoned this is due to the difference between the actuating and friction force at the start of simulation ($t=0$). After starting the simulation, the value for friction force oscillates for about two seconds. In order to reduce this effect there will be an initial value for asperity displacement (z_0). By doing so, the friction force will be modelled as a pre-strained spring. The initial value of asperity deflection is chosen so that when

multiplied with σ_0 it gives the resulting friction force which is equal to the actuating force (F) at the start of the simulation. The comparison of friction force as a function of the two initial deflections, zero and $0.8e-5$ meters, is shown in Figure B.3. The corresponding asperity deflection (z) during simulation is shown in the same figure below. The initial asperity displacement helped reducing the discontinuity but it did not abolish the oscillations of friction force.

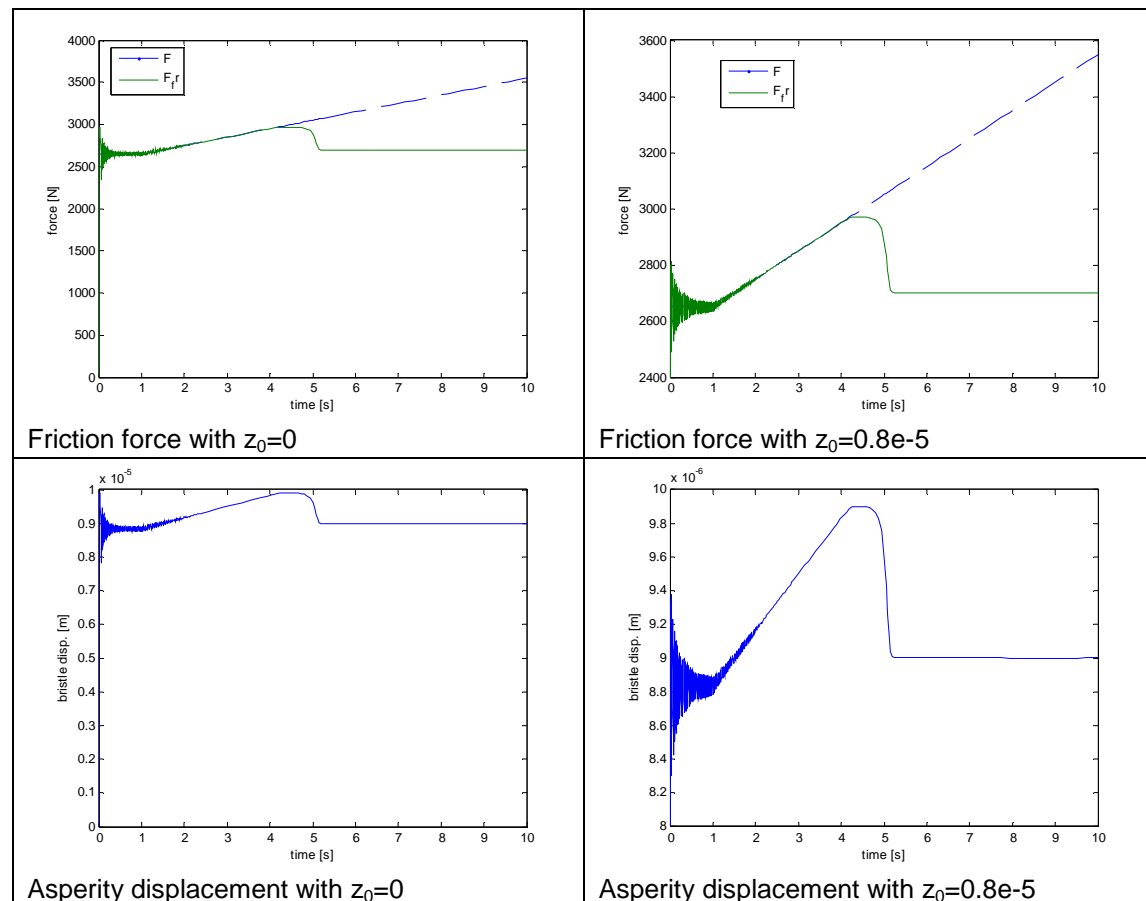


Figure B.3: Top: friction force and actuating force with and without z_0 . Bottom: total asperity displacement with and without z_0 .

- Sensitivity of LuGre on σ_0 :

It is obvious that the oscillation in friction force is caused by the oscillation in asperity displacement. In order to reduce the oscillation of asperity displacement it is necessary to increase the brittle stiffness. Figure B.4 shows the friction force and asperity displacement with asperity stiffness $\sigma_0 = 3e9$. Note the initial displacement z_0 had to be reduced by factor 10 since the stiffness was increased by factor 10. The increase of asperity stiffness helps to reduce the oscillations of friction force but it does not abolish them.

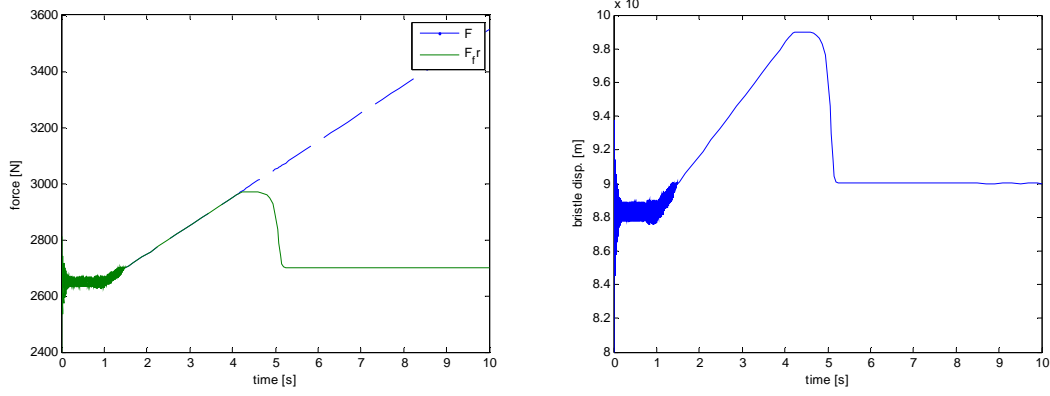


Figure B.4: Behaviour of friction force and asperity displacement with increased asperity stiffness

- Sensitivity of LuGre on σ_1 :

In order to reduce the duration of vibrations some damping is necessary. This can be achieved by increasing the damping coefficient σ_1 . Figure B.5 shows friction behaviour of investigated model for $\sigma_1=4e4$.

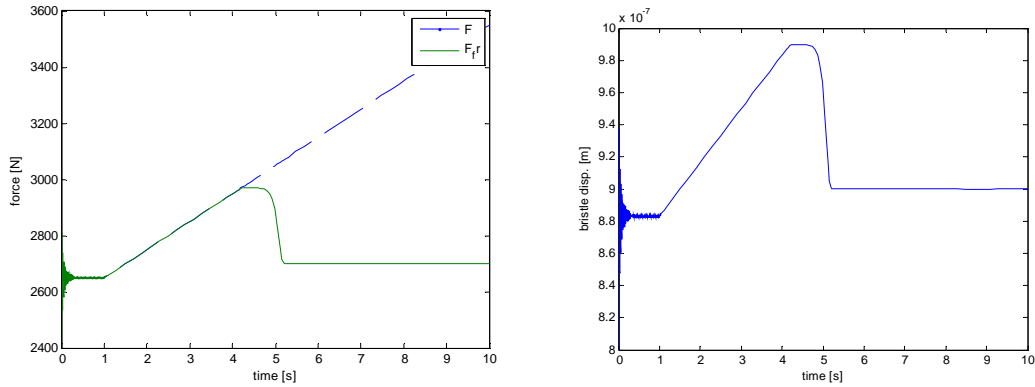


Figure B.5: Behaviour of friction force and asperity displacement with increased damping coefficient

- Sensitivity of LuGre on v_s :

In previous figures the transition from static to dynamic friction seemed too long, when compared with result in 4.3. In order to shorten the transition, the Stribeck factor (v_s) will be decreased. Figure B.6 shows the friction behaviour for $v_s=0.002$.

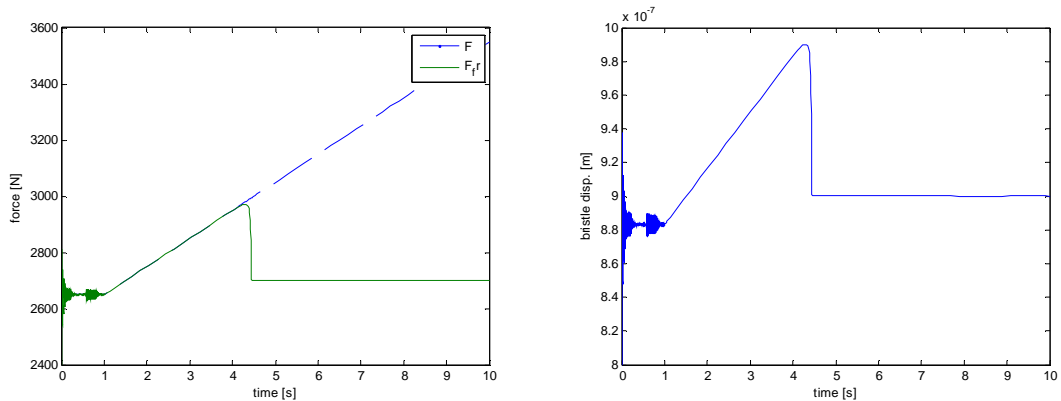


Figure B.6: Behaviour of friction force and asperity displacement with reduced damping coefficient

Note there was some additional vibration of friction force. This can be avoided by limiting the step size. The new maximal step size is 0.001.

All above mentioned parameters will have an effect on amount of the pre-sliding displacement. For instance, an increase of σ_0 reduces the pre-sliding displacement while an increase of v_s increases it. The final values of LuGre parameter are given in Chapter 4.4.2 and they are selected in order to simulate behaviour observed in Chapter 4.3. For more advance techniques of choosing right LuGre parameters, reader is directed to [Hensen, 2002].

Appendix C: Results of the Dyloporps seakeeping tests used in this work

Fourteen different seakeeping tests were used in Chapter 3 to estimate fretting in service conditions. These tests were done within the Dyloporps project and more about the testing procedure is in Appendix A. This appendix contains friction torque, spindle torque and distribution of fretting coefficient for each Test Case as well as the procedure used.

The calculation of friction torque and spindle torque is explained in Chapter 3. The theoretical value of friction torque and blade spindle torque is calculated for the conditions described in the test. Based on these theoretical values, the fretting coefficient is calculated as:

$$f_{\text{fret}} = \frac{Z \cdot M_{\text{sp}}}{T \cdot R_{0.7}} \quad (\text{C.1})$$

The critical value of fretting coefficient is the value at the moment when the blade spindle torque overcomes the friction torque. This moment is considered as the start of fretting. The blade spindle torque can overcome friction torque twice during one blade rotation, with its positive and negative value. It is argued that the full fretting occurs only when spindle torque overcomes friction twice during one rotation. In some test cases, theoretical calculation indicates the spindle torque does not overcome the friction. In order to calculate the critical fretting coefficient, the value of spindle torque is increased until it reaches the friction torque. Then the new value of critical fretting coefficient is calculated based on the ratio of increased spindle torque and thrust.

The fretting coefficient calculated from the ratio of measured spindle torque per blade and total thrust measured (f_{fret} in equation (3.47) in Chapter 3) will be compared with the critical (theoretical) fretting limit ($f_{\text{fret_critical}}$ in equation (3.48) in Chapter 3). The value of fretting coefficient will be calculated for maximum (positive and negative) values of blade spindle torque per each blade rotation. Afterwards, a distribution of maximal fretting coefficient will be made. It is reasoned that fretting occurs if the absolute value of maximal fretting coefficient is greater than the corresponding critical value.

For each Test Case, Figures C.1 through C.14 show:

- Calculated friction and spindle torque,
- Calculated fretting coefficient with the value of critical fretting coefficient
- Distribution of maximal and minimal fretting coefficients for positive and negative values of spindle torque observed in measurements.

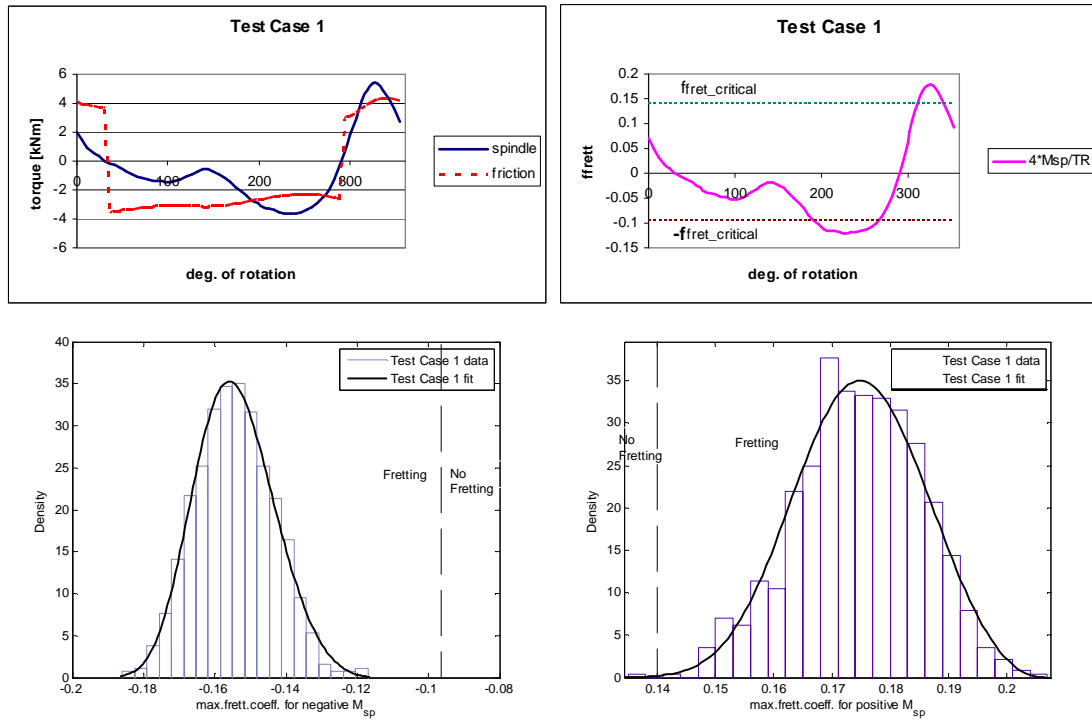


Figure C.1: Test Case 1: Top left: Calculated blade spindle torque and friction torque in the blade bearing; Top right: Calculated fretting coefficient during one rotation; Bottom left: minimum fretting coefficient for measured negative spindle torque; Bottom right: maximum fretting coefficient for measured positive spindle torque

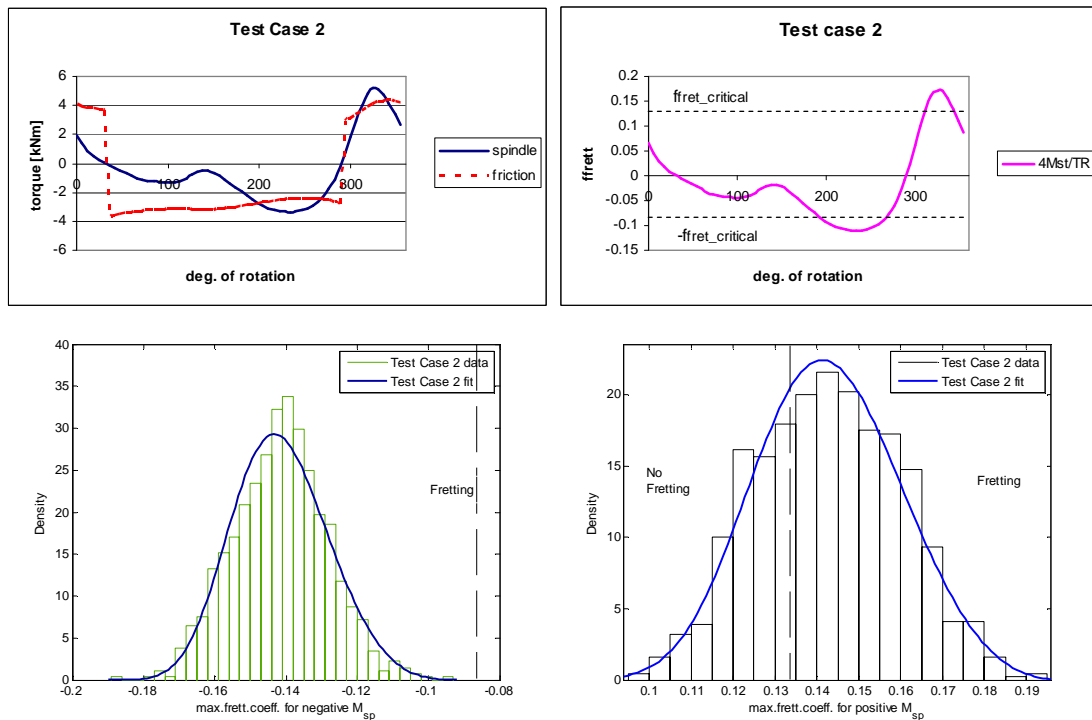


Figure C.2: Test Case 2: Top left: Calculated blade spindle torque and friction torque in the blade bearing; Top right: Calculated fretting coefficient during one rotation; Bottom left: minimum fretting coefficient for measured negative spindle torque; Bottom right: maximum fretting coefficient for measured positive spindle torque

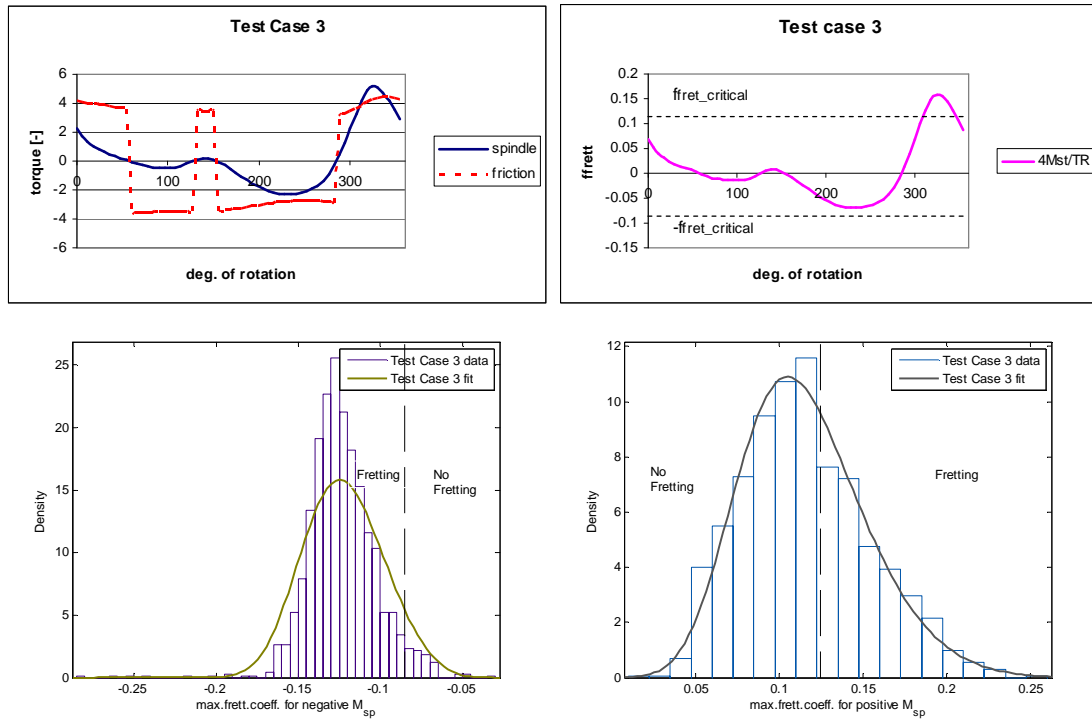


Figure C.3: Test Case 3: Top left: Calculated blade spindle torque and friction torque in the blade bearing; Top right: Calculated fretting coefficient during one rotation; Bottom left: minimum fretting coefficient for measured negative spindle torque; Bottom right: maximum fretting coefficient for measured positive spindle torque

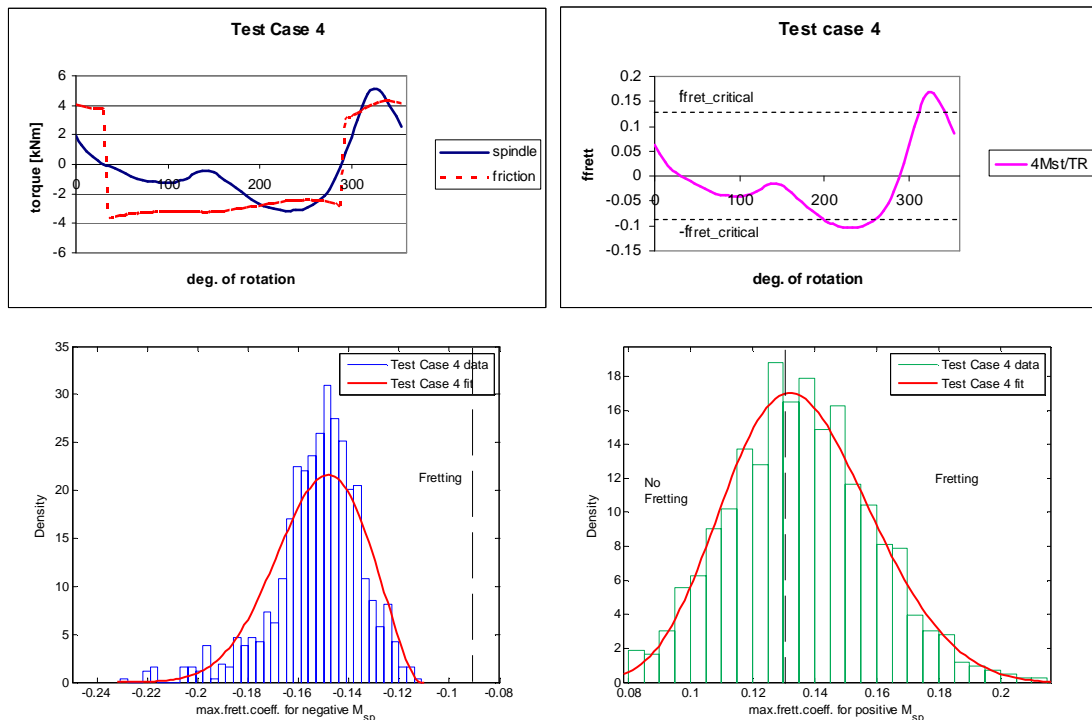


Figure C.4: Test Case 4: Top left: Calculated blade spindle torque and friction torque in the blade bearing; Top right: Calculated fretting coefficient during one rotation; Bottom left: minimum fretting coefficient for measured negative spindle torque; Bottom right: maximum fretting coefficient for measured positive spindle torque

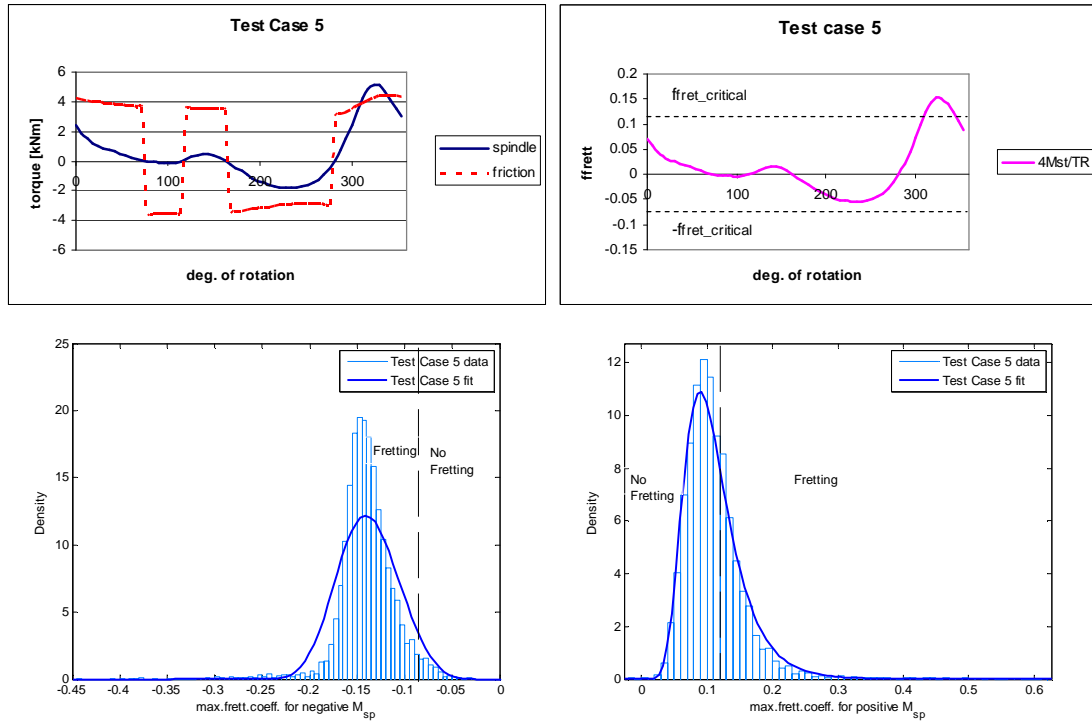


Figure C.5: Test Case 5: Top left: Calculated blade spindle torque and friction torque in the blade bearing; Top right: Calculated fretting coefficient during one rotation; Bottom left: minimum fretting coefficient for measured negative spindle torque; Bottom right: maximum fretting coefficient for measured positive spindle torque

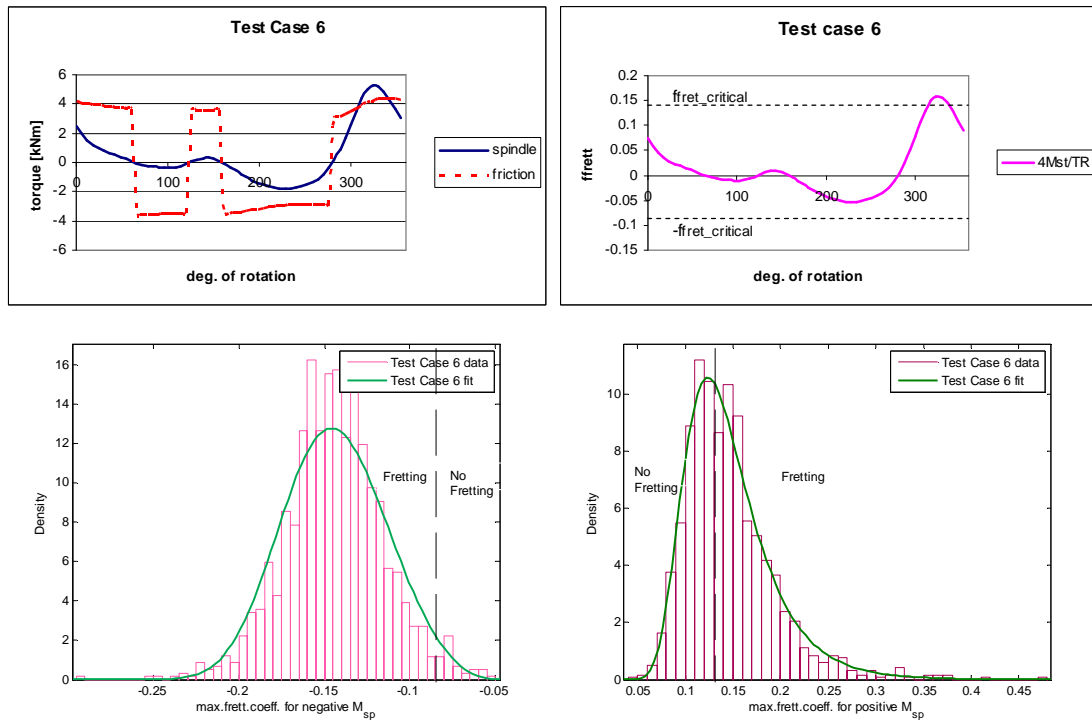


Figure C.6: Test Case 6: Top left: Calculated blade spindle torque and friction torque in the blade bearing; Top right: Calculated fretting coefficient during one rotation; Bottom left: minimum fretting coefficient for measured negative spindle torque; Bottom right: maximum fretting coefficient for measured positive spindle torque

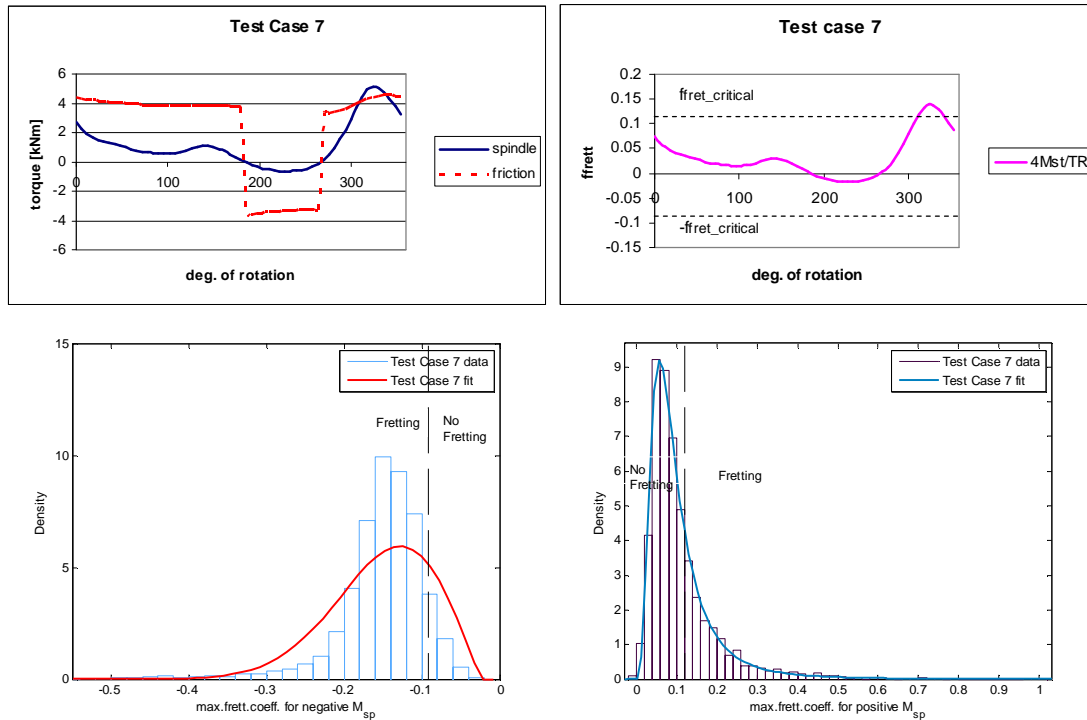


Figure C.7: Test Case 7: Top left: Calculated blade spindle torque and friction torque in the blade bearing; Top right: Calculated fretting coefficient during one rotation; Bottom left: minimum fretting coefficient for measured negative spindle torque; Bottom right: maximum fretting coefficient for measured positive spindle torque

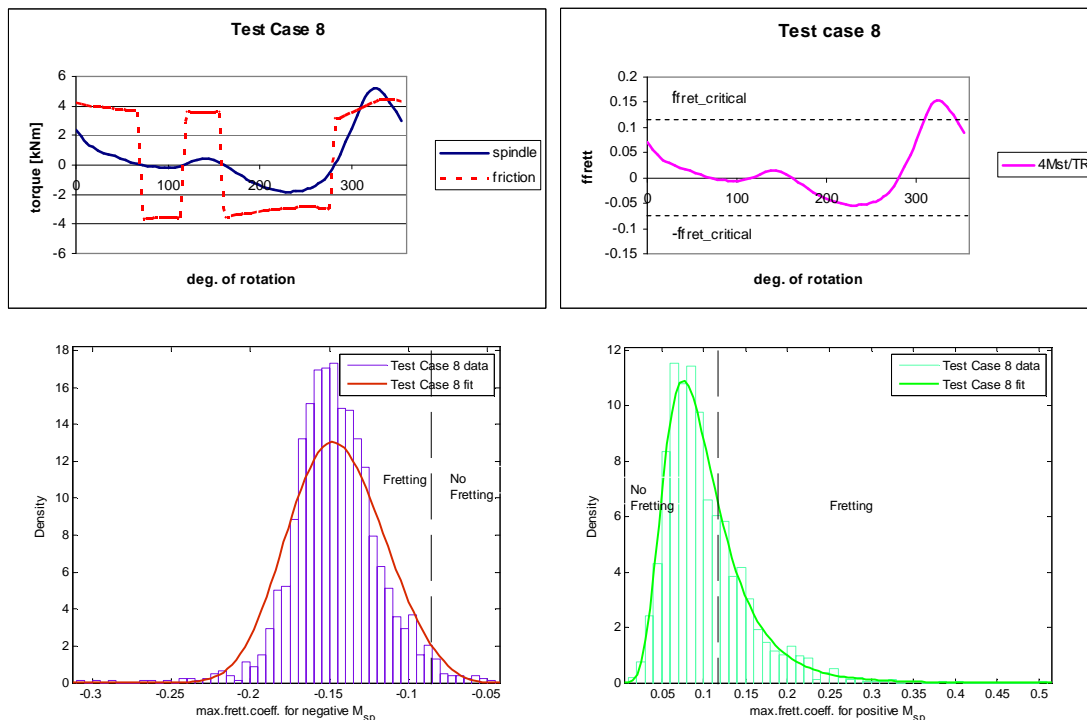


Figure C.8: Test Case 8: Top left: Calculated blade spindle torque and friction torque in the blade bearing; Top right: Calculated fretting coefficient during one rotation; Bottom left: minimum fretting coefficient for measured negative spindle torque; Bottom right: maximum fretting coefficient for measured positive spindle torque

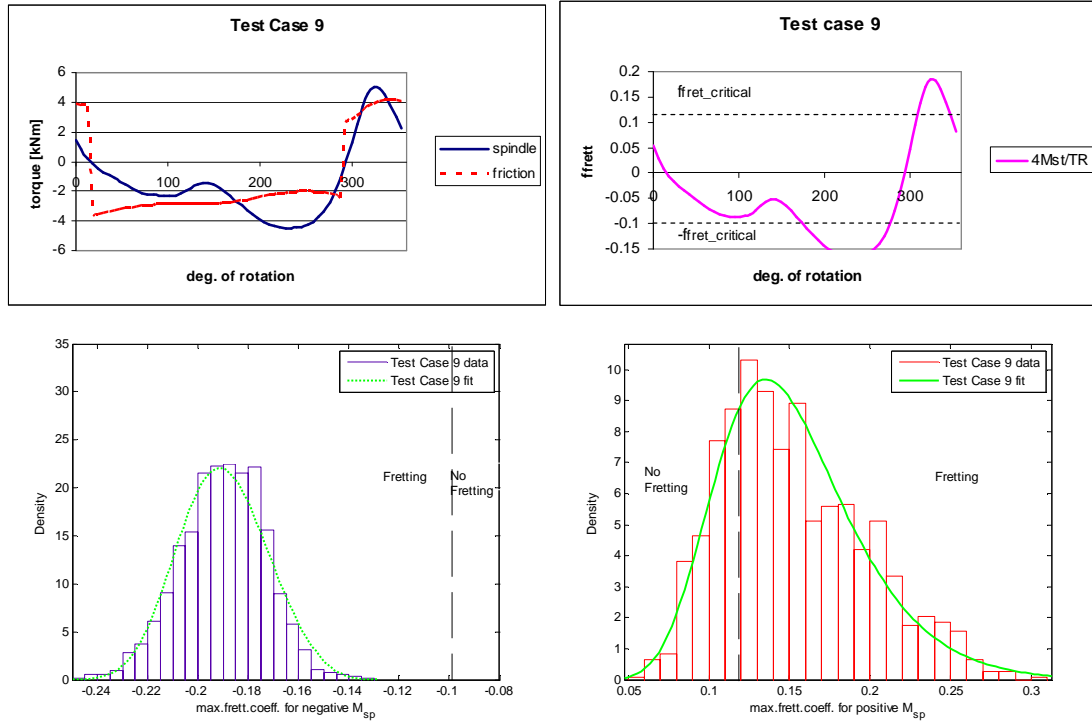


Figure C.9: Test Case 9: Top left: Calculated blade spindle torque and friction torque in the blade bearing; Top right: Calculated fretting coefficient during one rotation; Bottom left: minimum fretting coefficient for measured negative spindle torque; Bottom right: maximum fretting coefficient for measured positive spindle torque

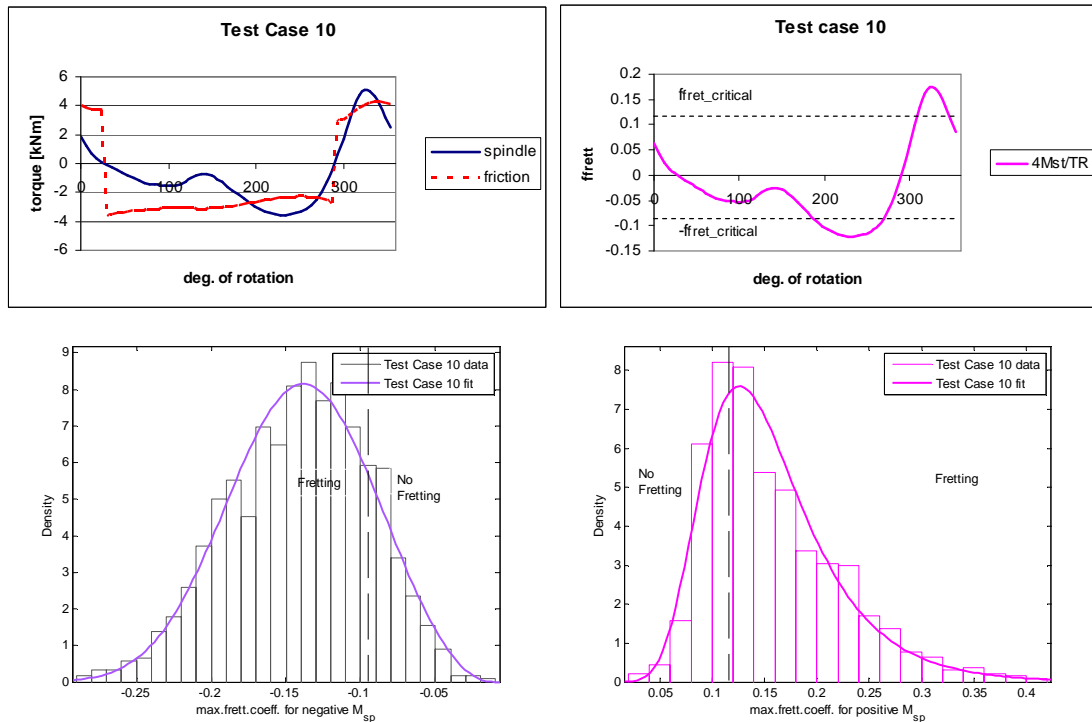


Figure C.10: Test Case 10: Top left: Calculated blade spindle torque and friction torque in the blade bearing; Top right: Calculated fretting coefficient during one rotation; Bottom left: minimum fretting coefficient for measured negative spindle torque; Bottom right: maximum fretting coefficient for measured positive spindle torque

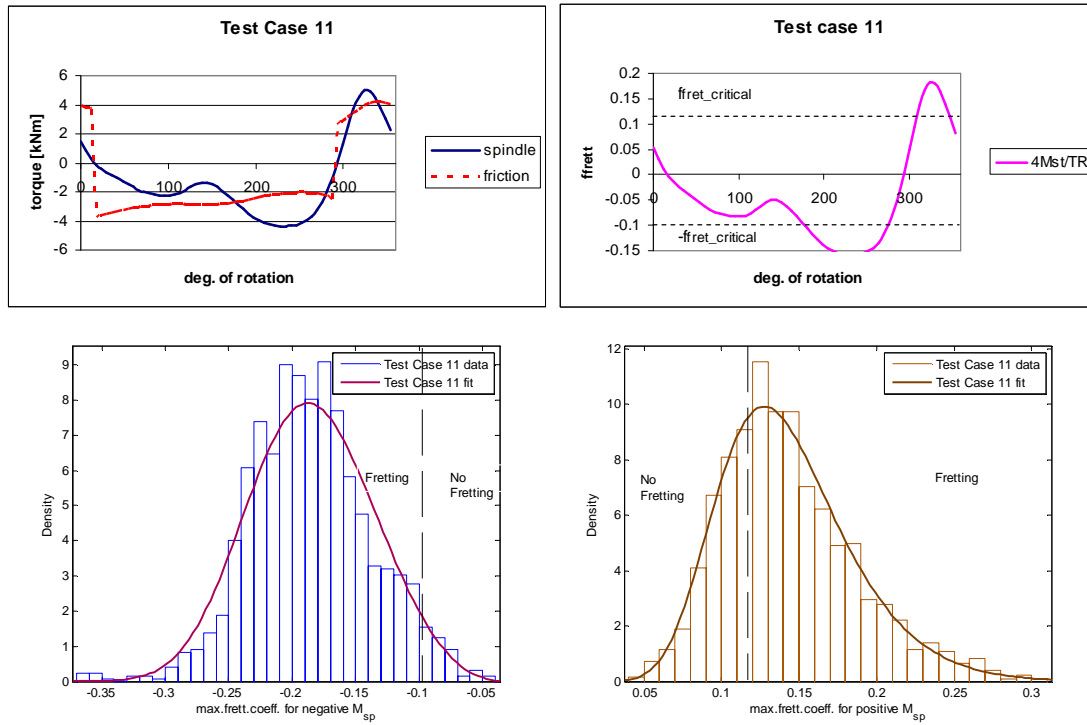


Figure C.11: Test Case 11: Top left: Calculated blade spindle torque and friction torque in the blade bearing; Top right: Calculated fretting coefficient during one rotation; Bottom left: minimum fretting coefficient for measured negative spindle torque; Bottom right: maximum fretting coefficient for measured positive spindle torque

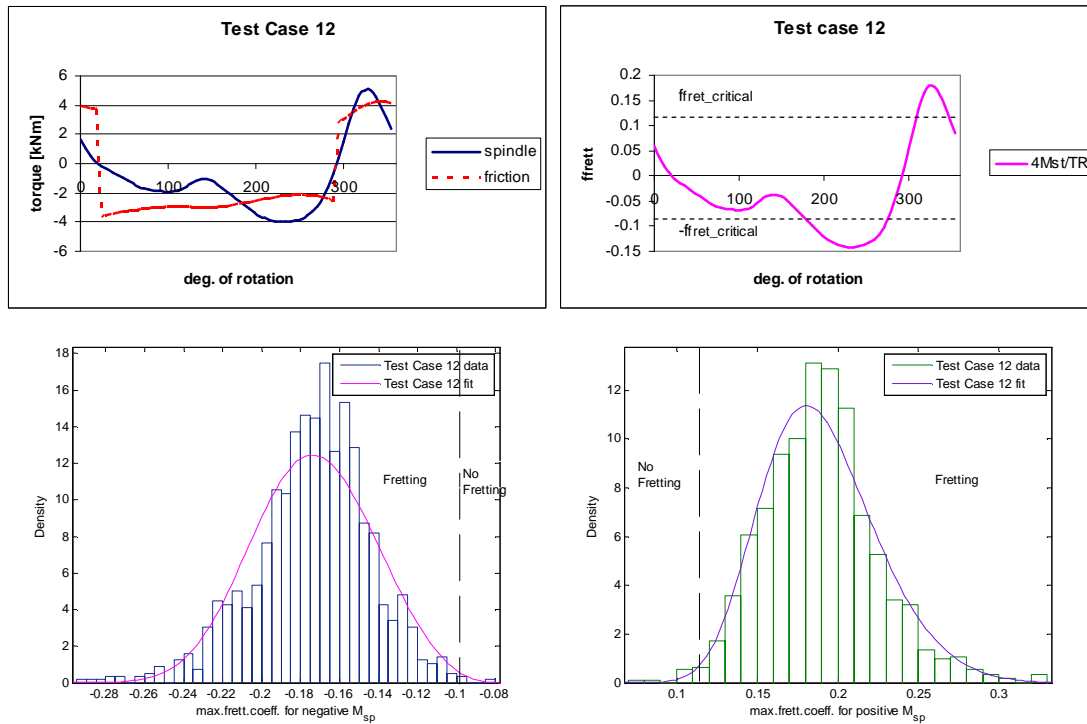


Figure C.12: Test Case 12: Top left: Calculated blade spindle torque and friction torque in the blade bearing; Top right: Calculated fretting coefficient during one rotation; Bottom left: minimum fretting coefficient for measured negative spindle torque; Bottom right: maximum fretting coefficient for measured positive spindle torque

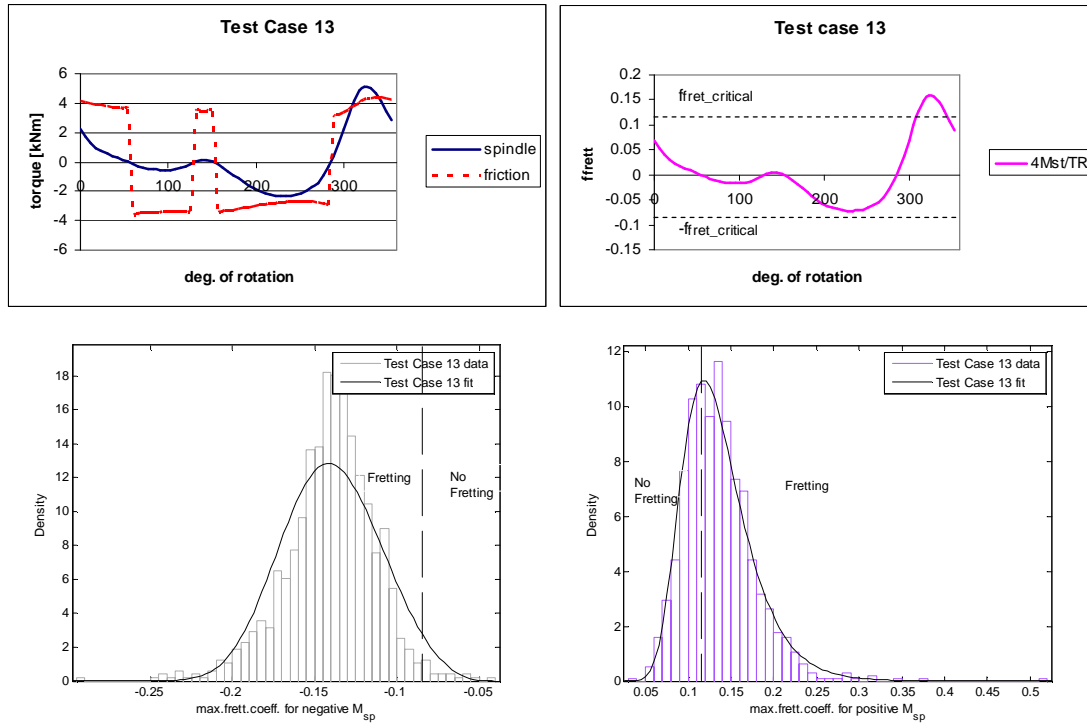


Figure C.13: Test Case 13: Top left: Calculated blade spindle torque and friction torque in the blade bearing; Top right: Calculated fretting coefficient during one rotation; Bottom left: minimum fretting coefficient for measured negative spindle torque; Bottom right: maximum fretting coefficient for measured positive spindle torque

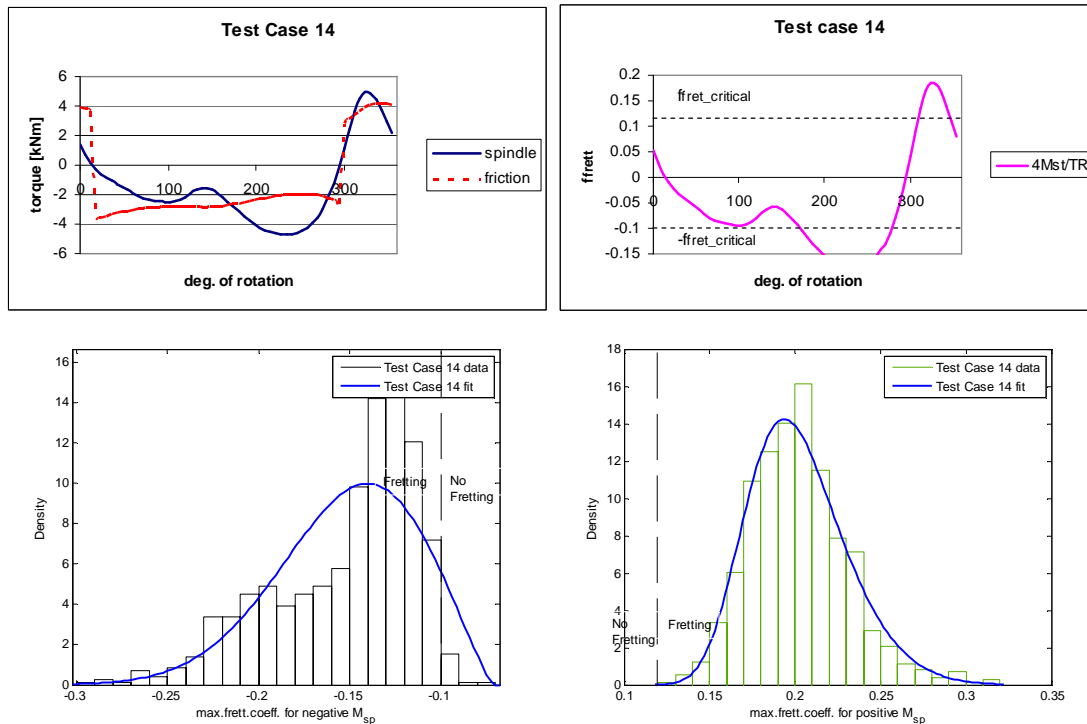


Figure C.14: Test Case 14: Top left: Calculated blade spindle torque and friction torque in the blade bearing; Top right: Calculated fretting coefficient during one rotation; Bottom left: minimum fretting coefficient for measured negative spindle torque; Bottom right: maximum fretting coefficient for measured positive spindle torque

Appendix D: Material properties

Properties of material used are listed in Table D.1 through Table D.3.

Table D. 1: Material properties of MnAl bronze

Material	MnAl bronze									
Composition [%]		Al	Si	Mn	Fe	Ni	Cu	Zn	Sn	Pb
	min	6.7		12	3	1.5	70	1.5		
	max	7.2	0.1	14	4	2.5	74	3.5	0.1	0.01
Density	7450 kg/m ³									
E modulus										
Poisson's ratio										
Yield stress	275 N/mm ²									
Tensile strength	640 N/mm ²									

Table D. 2: Material properties of CuNiAl

Material	CuNiAl									
Composition* [%]		Al	Si	Mn	Fe	Ni	Cu	Zn	Sn	Pb
	min	9		0.8	4.5	4.2	78.5			
	max	9.5	0.1	1.3	5.1	4.8	80.5	1	0.1	0.03
Density	7650 kg/m ³									
E modulus	121000 N/mm ²									
Poisson's ratio	0.33									
Yield stress	250 N/mm ²									
Tensile strength	650 N/mm ²									

*Other elements in composition min: 0.005%, max:0.063

Table D. 3: Material properties of 42CrMo4 steel

Material	42CrMo4
Composition [%]	Specified by standard: EN 10083-1
Density	7830 kg/m ³
E modulus	212 000 N/mm ²
Poisson's ratio	0.3
Yield stress	550 N/mm ²
Tensile strength	800 N/mm ²

Summary

This doctoral thesis focuses on the friction and wear and their mutual dependence in a Controllable Pitch Propeller (CPP) system. The goal of the research is to understand wear as a failure mechanism of a CPP. The motivation for the work done is not only to understand some of the failures in the past, but to evaluate the limits of a CPP for more demanding usage in a ship propulsion system. The blueprint for estimating wear in a CPP, developed in this research, can be used to estimate the total amount of wear caused by the more demanding pitch usage. Moreover, critical parameters affecting the wear and friction of a CPP have been made clear and together with recommendations they can be used for future development of a CPP.

In the beginning the challenge was to define which failures of a CPP are related to wear mechanisms. In Chapter 2 the main parts of a CPP are presented together with the main types of wear. Two types of failures have been related to wear mechanisms, namely excessive wear and seizure. These two wear mechanisms will make the pitch mechanism, more specifically the blade bearing, loose or stuck. Since wear is governed by loads, motions and type of materials in the contact, Chapters 3, 4, and 5 are focused on loads, motions and wear experiments.

In Chapter 3 a calculation of loads is presented for hydrodynamic, centrifugal, friction, and hydraulic forces. Based on an analysis of forces and their equilibrium, the start of fretting motion was explained as the moment when the blade spindle torque overcomes the friction torque in a blade bearing. Further, a theoretical fretting coefficient has been defined. The theoretical fretting coefficient was modified in order to investigate the influence of service conditions on fretting motion. The self-propulsion measurements, in different service conditions, were done as a part of the DYLOPROPS project, more about that project and measurements can be found in Appendix A.

In Chapter 4 the amplitude of fretting motion was investigated using static and dynamic friction models. Also, critical parameters have been investigated and clearance in the blade bearing was found to be an important factor on the amplitude of fretting motions.

In Chapter 5 two types of wear experiments are reported, namely sliding and fretting wear experiments. The sliding experiments are done for four different material combinations including two coatings. A temporary jump in wear rate and friction was recorded in sliding experiments for higher loads during stable wear period. In fretting wear experiments the importance of lubrication was shown. The specific wear rate was found to be two orders higher for contact without oil than for a contact with presence of oil.

In Chapter 6 a synthesis of the work done was made. The conclusions and data from previous chapters have been used to obtain a total wear model of a blade bearing. Using the model, wear in a blade bearing was quantified for the current control setting without effect of fretting, with effect of fretting and with an advanced control system requiring higher pitch usage. The main conclusions and recommendations of the work done in this thesis can be found in Chapter 7.

Samenvatting

Dit proefschrift richt zich op de wrijving en slijtage en hun onderlinge afhankelijkheid in een verstelbare schroef (Controllable Pitch Propeller: CPP) systeem. Het doel van het onderzoek is om slijtage te begrijpen als een storingsmechanisme van een CPP. De motivatie voor het verrichte werk is niet alleen om een aantal in het verleden opgetreden faalgevallen te begrijpen, maar ook om de grenzen van een CPP voor een meer veeleisend gebruik van de voortstuwing van schepen te evalueren. De blauwdruk voor het schatten van slijtage in een CPP, ontwikkeld in dit onderzoek, kan worden gebruikt om een schatting te maken van de totale slijtage veroorzaakt door een meer veeleisend gebruik van de spoedverstelling. Bovendien zijn kritische parameters die de slijtage en wrijving oorzaken bij een CPP duidelijk gemaakt en samen met de aanbevelingen kunnen zij worden gebruikt voor de toekomstige ontwikkeling van een CPP.

In het begin was de uitdaging om falen van een CPP te definiëren dat gerelateerd is aan slijtage. In hoofdstuk 2 zijn de belangrijkste onderdelen van een CPP gepresenteerd samen met de belangrijkste mechanismen van slijtage. Twee soorten storingen zijn gerelateerd aan slijtage, namelijk overmatige slijtage en vastlopen. Deze twee slijtage mechanismen maken dat het spoedverstellingsmechanisme, meer specifiek het bladlager, los of vast komt te zitten. Aangezien slijtage wordt beheerst door belastingen, bewegingen en het type van materialen in de contactzone, zijn de hoofdstukken 3, 4 en 5 gericht op belastingen, bewegingen en slijtage experimenten. In hoofdstuk 3 is een berekening van de belasting gepresenteerd voor hydrodynamische, centrifugale, wrijvings-, en hydraulische krachten. Gebaseerd op een analyse van krachten en hun evenwicht, is het begin van de fretting beweging verklaard als het moment waarop het spindle koppel het wrijvingskoppel overwint in een bladlager. Verder is er een theoretische fretting coëfficiënt gedefinieerd. De theoretische fretting coëfficiënt werd aangepast om de invloed van de dienstomstandigheden te onderzoeken. De voortstuwingsmetingen met modelschroef werden in verschillende condities gedaan als onderdeel van het DYLOPROPS project, meer over dat project en de metingen is te vinden in Bijlage A.

In hoofdstuk 4 is de amplitude van de fretting beweging onderzocht met behulp van statische en dynamische wrijvingsmodellen. Ook werden kritische parameters onderzocht en de speling in het bladlager werd als een belangrijke invloed op de amplitude van de fretting beweging aangemerkt.

In hoofdstuk 5 worden twee type slijtage experimenten gerapporteerd, namelijk een glijdend experiment en een fretting slijtage experiment. Het glijdende experiment is uitgevoerd voor vier verschillende combinaties van materialen, waaronder twee coatings. Tijdens een stabiel dragende periode voor hoge belastingen in de glijdende experimenten werd een tijdelijke toename in slijtagesnelheid en wrijving gemeten. In het fretting slijtage experiment werd het belang van smering aangetoond. De specifieke slijtagesnelheid voor contact zonder olie is twee ordegrootte hoger dan met olie.

In hoofdstuk 6 is een synthese van het verrichte werk gemaakt. De conclusies en gegevens uit eerdere hoofdstukken zijn gebruikt om tot het totale slijtage model van een bladlager te komen. Met behulp van het model werd slijtage in een bladlager gekwantificeerd voor de huidige besturingsinstellingen, zonder effect van fretting, met effect van fretting en met een geavanceerd besturingssysteem waarbij meer

spoedverstelling vereist is. De belangrijkste conclusies en aanbevelingen van het werk dat in dit onderzoek is verricht zijn te vinden in hoofdstuk 7.

Reference:

Al-Bender, 2004

- F. Al-Bender; V. Lampaert; J. Swevers: "Modeling of dry sliding friction dynamics: From heuristic models to physically motivated models and back" Chaos, 2004, No: 14(2) pp: 446-459

Archard, 1953

- J. F. Archard: "Contact and Rubbing of Flat Surfaces" Jurnal of Applied Physics, 1953, No: 8(14) pp: 981-988

Bakker, 2005

- J. Bakker: "Modelling of a CPP", MSc thesis, TU Delft, Delft 2005

Bakker, 2006

- J. Bakker, A. Wesselink: "The Use of Non-linear Models in the Analysis of CPP Actuator Behaviour"; 2006, WMTC Conference

Barbey, 1982

- NSWC: "Summary report of the controllable pitch propeller research program"; Report No: DTNSRDC-81/065, July 1982

Bayer, 1994

- R.G. Bayer: "Mechanical Wear Prediction and Prevention"; 1994, Marcel Dekker

Beek, 1976

- G.H.M. Beek, J. Heidemans: Strength considerations in controllable pitch propeller design; Proceedings of 3rd Lips Propeller Symposium, May 1976; pp: 329-341.

Beek, 2004

- A. Beek: "Machine lifetime performance and reliability"; 2004, Technical University Delft, ISBN: 90-3700-208-0

Beek, 2006

- T. van Beek; T. van Terwisga: "Ventilation or cavitation: An experimental study to determine dynamic loads on controllable pitch propellers"; 2006, Sixth International Symposium on Cavitation, CAV2006, Wageningen

Bliman, 1995

- P.A. Bliman, M. Sorine: "Easy to use realistic dry friction models for automatic control"; Proceedings of 3rd European Control Conference, Rome 1995, pp: 3788-3794

Bosswell, 1971

- R.J. Bosswell: "Design, cavitation, and open water performance of a series of research skewed propellers", NSRDC, 1971, Report number: 3339

Bowden, 1950

- F.P. Bowden; D. Tabor: "The friction and lubrication of solids"; Oxford Univesity Press, Oxford 1950

Canudas de Wit, 1995

- C. Canudas de Wit; H. Olsson; K.J. Astrom; P. Lischinsky: "A new model for control systems with friction"; Transactions on Automatic Control, 1995, No: 40(3), pp: 419-425

Carlton, 2007

- J. Carlton: "Marine propellers and propulsion"; Elsevier, Oxford 2007

Czichos, 1978

- H. Czichos: "A System Approach to the Science and Technology of Friction, Wear, and Lubrication"; Elsevier, 1978

Dahl, 1968

- P. Dahl: "A solid friction model"; Technical report TOR-0158(3107-18)-1, 1968, The Aerospace Corporation, El Segundo, CA, USA

Dallinga, 2006

- R. Dallinga: Bow Flare Slamming of Container Ships and its Impact on Operational stability; RINA Conference, Design & Operation of Container Ships; London 2006.

Dowson, 1998

- D. Dowson: "History of Tribology"; 1998, John Willey and sons

Dupont, 2002

- P. Dupont; V. Hayward; B. Armstrong; F. Altpeter: "Single state elastoplastic friction models"; Transactions on Automatic Control, 2002, No: 47(5), pp: 787-792

Faraz, 2001

- A. Faraz, S. Payandeh: Towards approximated models of coulomb frictional moments; Journal of Engineering Mathematics, Volume 40, Number 3, July 2001, pp. 283-296(14)

Grimmelius, 2005

- H.T. Grimmelius: "Condition monitoring for marine refrigeration plants: based on process model"; 2005, Delft University Press

Grimmelius, 2001

- H.T. Grimmelius, D. Stapersma: "The Impact of Propulsion Plant Control on Diesel Engine Thermal Loading"; 2001, CIMAC Conference

Hensen, 2002

- R.H.A. Hensen: "Controlled mechanical systems with friction"; PhD thesis TU Eindhoven, Eindhoven 2002

Jelali, 2003

- M. Jelali; A. Kroll: "Hydraulic servo systems: modelling, identification and control"; Springer, London 2003

Johannes, 1973

- V.I. Johannes; M.A. Green; C.A. Brockley: "The role of the rate of application of the tangential force in determining the static friction coefficient"; Wear, 1973, No:24 pp: 381-385

Karnopp, 1985

- D. Karnopp: "Computer simulation of slip-stick friction in mechanical dynamic system", 1985, Journal of Dynamic Systems, Measurement, and Control; No:107(1); pp:100-103

Meshabi, 2005

- A. Meshabi (editor), D. Clark (editor): Proceedings of the 24th ITTC 2005, Edinburgh September 2005, Volume I, pp 89-94

Mindlin, 1953

- R.D. Mindlin: "Elastic spheres in contact under varying oblique forces"; 1953, Journal of Applied Mechanics, 20, pp: 327-344

Olsson, 1997

- H. Olsson; K.J. Astrom; C. Canudas de Wit; M. Gafvert; P. Lischinsky: "Friction models and friction compensation"; European Journal of Control, 1998, No:4 pp: 176-195

Oossanen, 1970

- P. van Oossanen: Calculation of performance and cavitation characteristics of propellers including effects of non-uniform flow and viscosity"; MARIN, 1970, Publication number: 457

Palmgren, 1945

- A. Palmgren: "Ball and roller bearing engineering"; 1945, SKF Industries

Parlitz, 2004

- U. Parlitz; A. Hornstain; D. Engster; F. Al-Bender; V. Lampaert; T. Tjahjowidodo; S.D. Fassois; D. Rizos; C.X. Wong; K. Worden; G. Manson: "Identification of pre-sliding friction dynamics"; Chaos, 2004, No: 14(2), pp: 420-430

Persson, 2000

- B.N. Persson: "Sliding friction: physical principles and applications"; Springer, Berlin 2000

Pronk, 1980

- C. Pronk: "Blade spindle torque and off-design behaviour of controllable pitch propellers", Graduation thesis TU Delft, Delft 1980

Raboniwicz, 1951

- E. Rabinowicz: The nature of the static and kinetic coefficients of friction"; Journal of applied physics, 1951, No: 22(11) pp: 1373-79

Rabinowicz, 1965

- E. Rabinowicz: "Friction and Wear of Materials"; 1965, John Willey and sons

Reynolds, 1886

- O. Reynolds: "On the Theory of Lubrication and its application to Mr. Beauchamp Tower's Experiments, Including an Experimental Determination of the Viscosity of Olive Oil"; 1886, Phil. Transactions, Royal Society London, No: 177(1), pp: 157-234

Stachowiak, 2005

- G. Stachowiak, A.W. Batchelor: "Engineering Tribology"; 2005, Butterworth-Heinemann

Stribeck, 1903

- R. Stribeck: Die Wesentlichen Eigenschaften der Gleit und Rollenlager"; Berlin 1903

Vrijdag, 2005

- A. Vrijdag, D. Stapersma, T.J.C. van Terwisga: "Cavitation Inception in Operational conditions"; 2005, Proceedings of the 4th International Conference on Computer and IT Applications in Maritime Industries COMPIT 2005; pp: 1-15

Vrijdag, 2009

- A. Vrijdag: "Control of Propeller Cavitation in Operational Conditions"; PhD Thesis 2009, TU Delft, Published by: VSSD

Weibull, 1939

- W. Weibull: "A statistical theory of the strength of materials"; 1939 Proceedings of the Royal Swedish Academy, Vol 151

Williams, 1994

- J.A. Williams: "Engineering Tribology"; 1994, Oxford University Press

Wind, 1978

- J. Wind: "Hub size selection criteria for controllable pitch propellers as a means to ensure system integrity"; Naval engineers journal 1978, No: 90(4) pp:49-61

Worden, 2007

- K. Worden; C.X. Wong; U. Parlitz; A. Hornstein; D. Engster; T. Tjahjowidodo; F. Al-Bender; D.D. Rizos; S.D. Fassois: "Identification of pre-sliding friction and sliding friction dynamics: Grey box and black box models", Mechanical Systems and Signal Processing, 2007, No: 21(1) pp:514-534

Wulpi, 1999

- D.J. Wulpi: "Understanding how components fail"; 1999 ASM International

Zaretsky, 2000

- E.V. Zaretsky; J.V. Poplawski; C.R. Miller: “Rolling bearing life prediction-past present and future”, 2000, NASA Glenn Research Centre; Report: E-12178; NAS 1.15:210529; NASA/TM-2000-210529

Curriculum Vitae and List of Publications:

Milinko Godjevac, born on 9th November 1975 in Belgrade, Serbia

1990-1994	Electro technical High School “Nikola Tesla”, Belgrade
1995-2004	Dipl. Ing. Naval Architect, University of Belgrade, Faculty of Mechanical Engineering, Belgrade
2004-2006	PhD candidate at Delft University of Technology, Delft
2006-	Research Engineer in Wartsila Netherlands, Drunen

Publications:

- M. Godjevac, T. van Beek, H. Grimmelius, D. Stapersma: “Wear mechanism of a CPP”, WMTC Conference, London (March 2006)
- M. Godjevac, van Beek, T., Grimmelius, H. T., Tinga, T. and Stapersma, D. Prediction of fretting motion in a controllable pitch propeller during service. *Proc. IMechE, Part M: J. Engineering for the Maritime Environment*, 2009, 223 (7), 541-560. DOI 10.1243/14750902JEME128